Nickel–Metal Hydride: Metal Hydrides

PHL Notten, Philips Research Laboratories, Eindhoven, The Netherlands, and Eindhoven University of Technology, Eindhoven, The Netherlands
M Latroche, CMTR-ICMPE, UMR 7182, CNRs, Thiais, France

Introduction

Many potential applications have been suggested since the discovery of hydride-forming metals and related intermetallic compounds, ranging from hydrogen purification membranes, and hydrogen sensors to hydrogen-driven heat pumps. To date, however, only one application has proven its widespread commercial feasibility. The application of hydride-forming compounds to the electrochemical field of rechargeable batteries has become a major success over the past decade. Indeed, nickel–metal hydride (Ni–MH) batteries have become one of the leading battery systems in portable electronics and its use is rapidly expanding to other fields such as, the hybrid electrical vehicles (HEVs). This is, among other things, due to their high storage capacity, good rate capability, reliability, environmental friendliness, and low cost.

The discovery in the late 1960s at the Dutch Philips Research Laboratories that the intermetallic compound $LaNi_5$ was able to absorb reversibly large amounts of hydrogen gas has initiated this tremendous technical and commercial success. Soon after this discovery it was realized that electrodes made of this type of hydride-forming materials would be highly favorable as electrochemical energy storage medium and could become a serious alternative for the frequently used nickel–cadmium (Ni–Cd) batteries. It took, however, until the late 1980s before Ni–MH batteries had turned into a mature and reliable battery system and, subsequently, had become widely accepted in our present-day portable society. The reason for this long introduction time was related to the fact that the thermodynamic properties and the cycle-life performance of the parent compound $LaNi_5$ in the required alkaline electrochemical environment were rather poor. The development at the Philips Research Laboratories of electrochemically stable multicomponent, AB_5-type hydride-forming, compounds eventually solved this serious problem and accomplished the required breakthrough, needed for the realization of Ni–MH batteries. For many years now, commercial Ni–MH batteries have employed mischmetal-based, AB_5-type hydride-forming, compounds as negative electrode material but, nowadays, new compounds are developed, leading to a promising future for these alkaline-type batteries.

In this article the materials research making the Ni–MH battery feasible is reviewed. First, the basic electrochemical principles underlying the energy storage reactions and the various side reactions, occurring during (over)charging and (over)discharging, and open-circuit conditions are highlighted. Subsequently, the properties of hydride-forming materials are outlined in detail, including the crystallographic and electrochemical characteristics of both stoichiometric and nonstoichiometric, intermetallic, AB_{5+x} compounds. Taking into consideration the near future some points regarding the potentially new materials, offering, for example, high potentials as far as energy density is concerned are discussed. For the crystallographic and electrochemical properties of the second (nickel) electrode inside Ni–MH batteries, the reader is referred to the excellent review written by J. McBreen.

Basic Principles of Ni–MH Batteries

Energy Storage Reactions

A schematic representation of a Ni–MH battery, containing a hydride-forming (MH) electrode and a nickel electrode, is shown in Figure 1. A separator electrically insulates the electrodes. Both separator and electrodes are impregnated with a strong alkaline solution (usually of the order of $7\,\mathrm{mol\,L^{-1}}$ KOH) that provides for the ionic conductivity between the two electrodes. The overall electrochemical reactions, occurring at both electrodes during charging (ch) and discharging (d) can, in their most simplified form, be represented by

$$Ni(OH)_2 + OH^- \underset{d}{\overset{ch}{\leftrightarrow}} NiOOH + H_2O + e^- \qquad [I]$$

$$M + H_2O + e^- \underset{d}{\overset{ch}{\leftrightarrow}} MH + OH^- \qquad [II]$$

During charging divalent Ni(II) is oxidized into the trivalent Ni(III) state and water is reduced to hydrogen atoms at the metal (M) electrode, which are, subsequently, absorbed by the hydride-forming compound. The reverse reactions take place during discharging. The net effect of this reaction sequence is that hydrogen is transported from one electrode to the other. The reaction takes place without any water consumption preventing any drying of the battery contrary to Ni–Cd batteries. It should be noted that the hydrogen stored in the MH electrode is in equilibrium with that in the gas phase.

In general, exponential relationships between the partial anodic/cathodic currents and the applied electrode

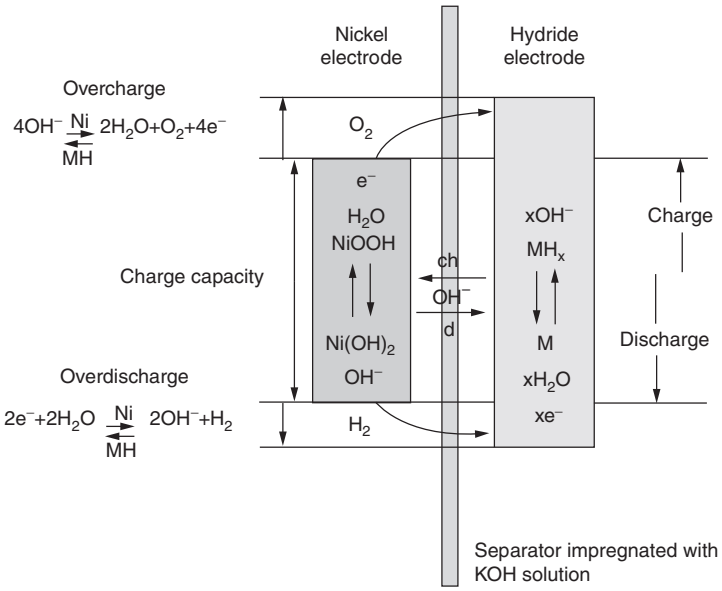

Figure 1 The concept of a sealed rechargeable Ni–MH battery seen from a schematic point of view. Reproduced with permission from Notten PHL (1994) In: Grandjean F, Long GJ, and Buschow KHJ (eds.) *Rechargeable Nickel–Metal Hydride Batteries: A Successful New Concept*, ch. 7, vol. 281, p. 151. NATO ASI Series E. London, ISBN 0-7923-3299-7.

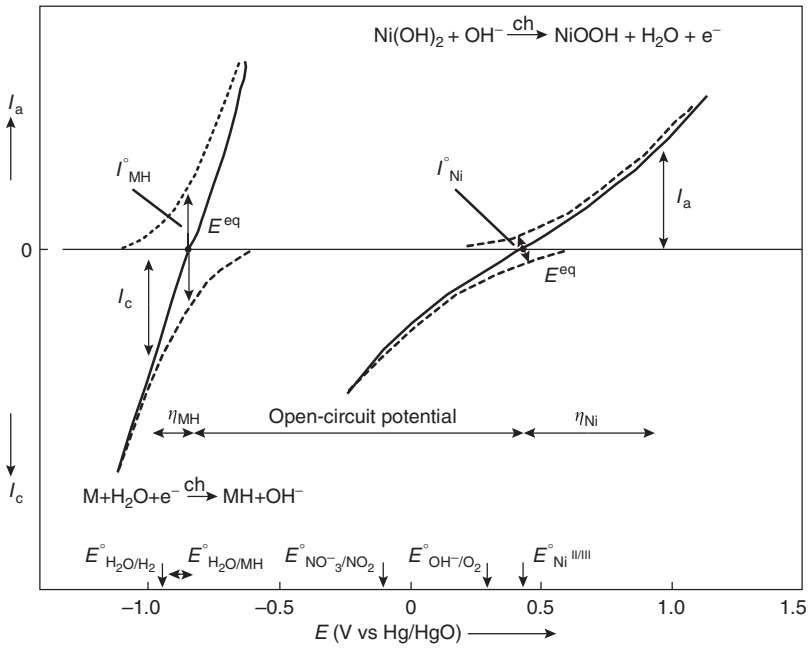

Figure 2 Schematic representation of the current–potential curves for a Ni and MH electrode (solid lines), assuming kinetically controlled charge transfer reactions. The partial anodic and cathodic reactions are indicated as dashed lines. The exchange currents (I°) are defined at the equilibrium potentials (E^{eq}). Potentials are given with respect to an Hg/HgO reference electrode. Besides the redox potentials (E°) of the main electrode reactions, those of some side reactions are also indicated. Reproduced with permission from Notten PHL (1994) In: Grandjean F, Long GJ, and Buschow KHJ (eds.) *Rechargeable Nickel–Metal hydride Batteries: A successful New Concept*, ch. 7, vol. 281, p. 151. NATO ASI Series E. London, ISBN 0-7923-3299-7.

potential are observed under kinetically controlled conditions, as is schematically depicted in Figure 2 (dashed curves). The potential scale is given with respect to an Hg/HgO reference electrode. The equilibrium potential of the nickel electrode under standard conditions is more positive ($E^{eq}_{Ni} = +439$ mV) than that of the MH electrode (E^{eq}_{MH}) – depends on the partial hydrogen pressure of the hydride-forming materials, according to

$$MH + MH \rightarrow 2M + H_2 \uparrow \qquad [III]$$

Because the preferred partial hydrogen pressure of MH electrode materials is of the order of up to a few 0.01 bars, E^{eq}_{MH} ranges generally between −930 and −860 mV. This implies that the theoretical open-circuit potential of a Ni–MH battery is approximately 1.3 V ($E_{Ni-MH} = E_{Ni} - E_{MH}$), indeed similar to that of Ni–Cd batteries, making these two aqueous battery systems very compatible.

During galvanostatic charging with a constant current an overpotential (η) will be established at both electrodes. The magnitude of each overpotential component (η_{Ni} and η_{MH} in **Figure 2**) is determined by the kinetics of the charge transfer reactions. An electrochemical measure for the kinetics of a charge transfer reaction is generally considered to be the exchange current I^o, which is defined at the equilibrium potential, E^{eq}, at which the partial anodic current equals the partial cathodic current (see **Figure 2**). In the case of the Ni electrode, I^o_{Ni} is reported to be relatively low, which implies that at a given constant anodic current, I^a_{Ni}, the established overpotential at the Ni electrode is relatively high (**Figure 2**). In contrast, the kinetics of the MH electrode is reported to be strongly dependent on the materials composition. Assuming a highly electrocatalytic hydride-forming compound, this implies that the current–potential curves, characteristic for the MH electrode, are very steep in comparison to those for the nickel electrode, resulting in a much smaller value for η_{MH} at the same cathodic current I^c_{MH}, as is schematically shown in **Figure 2**. It is evident that the battery voltage under current flow is a summation of the open-circuit potential and the various overpotential contributions, including the ohmic potential drop (η_{IR}) caused by the electrical resistance of the electrolyte (R_e). The reverse processes occur during discharging, resulting in cell voltage lower than 1.3 V.

Side Reactions

To ensure the well functioning of sealed rechargeable Ni–MH batteries under a wide variety of operating conditions, the nickel electrode is designed to be the capacity-determining electrode, as is schematically depicted in **Figure 1**. Such a configuration forces side reactions to occur at the nickel electrode both during overcharging and overdischarging.

Overcharging

During overcharging OH^- ions are oxidized at potentials more positive with respect to the standard redox potential of the OH^-/O_2 redox couple (about 0.3 V with respect to Hg/HgO reference in **Figure 2**) and oxygen evolution is induced at the nickel electrode, according to

$$4OH^- \xrightarrow{Ni} O_2 + 2H_2O + 4e^- \qquad [IV]$$

As a result, the partial oxygen pressure inside the sealed cell starts to rise. Advantageously, oxygen can be transported to the MH electrode, where it can be reduced at the MH/electrolyte interface at the expense of the hydride-formation reaction [II] according to

$$O_2 + 2H_2O + 4e^- \xrightarrow{MH} 4OH^- \qquad [V]$$

Both the oxygen evolution and the so-called oxygen recombination reaction are schematically represented in **Figure 3**. Because the overpotential for the recombination reaction at the MH electrode is relatively high, it has been argued that its rate is most probably transport-controlled by the oxygen supply through the electrolyte. The oxygen recombination mechanism ensures that the partial oxygen pressure inside the Ni–MH battery will be maintained low. It should be noted that both oxygen and hydrogen gas are present during overcharging as has recently been analyzed and simulated.

Although thermodynamically more favorable ($E^o_{Ni} > E^o_{O2}$), the parasitic oxygen evolution reaction (eqn [IV]) only takes place at significant rates at more positive potentials than the voltage range at which the basic nickel reaction generally occurs (eqn [I]). This is fortunately due to the much poorer kinetics of the oxygen evolution reaction ($I^o_{O2} < I^o_{Ni}$) compared to those of the nickel reaction. This generally results in a rather sharp increase of the battery voltage at the end of the charging process, at the point where the overcharging process takes over. This is indeed confirmed experimentally, as **Figure 4** reveals. It is also clear from this figure that the pressure inside the battery sharply rises at the end of the charging process, around 100% state-of-charge (SoC), and tends to level off at higher SoC. This pressure rise is, in fact, dictated by the competition of the oxygen evolution reaction and the nickel reaction and is found to be strongly dependent on the rate at which the Ni–MH battery is charged. Besides the gas pressure build-up inside Ni–MH batteries, the development of the battery temperature is also of considerable importance and influences the thermodynamics and kinetics of the various processes. In addition, the temperature may also induce secondary effects, such as a reduced cycle life.

The formation of heat (W) inside a Ni–MH battery can be represented by

$$W_{Ni-MH} = \left\{ \sum \left[\frac{-I_i T \Delta S_i}{F} \right] + \sum I_i |\eta_i| + I^2_{Ni-MH} R_e \right\} \qquad [1]$$

where I_i are the partial currents flowing through the battery with $I_{Ni-MH} = \Sigma I_i$, T is the temperature, and F is the Faraday constant. The factors, which contribute to the heat evolution during current flow, can be easily recognized in eqn [1]: the entropy changes (ΔS_i) brought about by the various electrochemical reactions (i), the

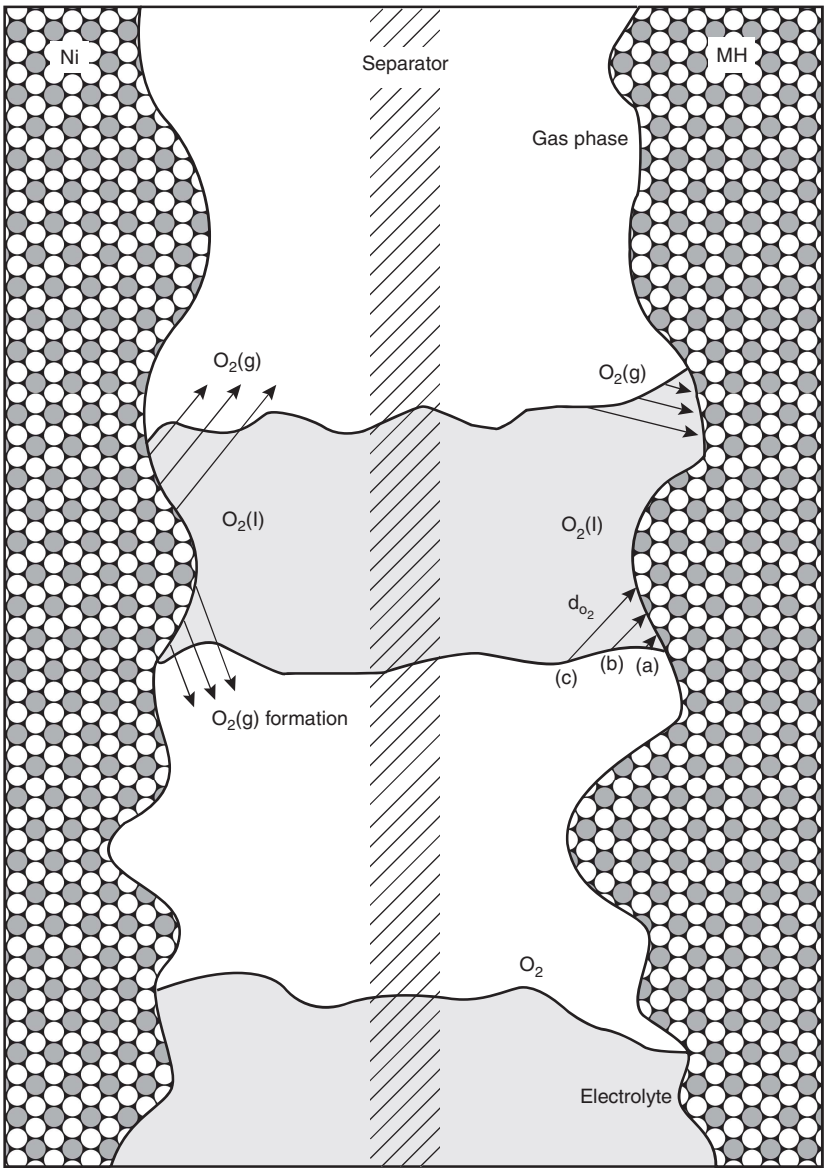

Figure 3 Schematic representation of the oxygen recombination cycle. Oxygen formation is initiated at the nickel electrode/electrolyte interface. Small gas bubbles are formed and the gas will be transported to the gas phase. Recombination starts by redissolution of oxygen in the electrolyte and will subsequently be reduced at the MH electrode/electrolyte interface. The recombination rate strongly depends on the diffusion layer thickness, through which oxygen has to be transported and is most favorable at the three-phase boundaries, as is schematically indicated by arrows (a)–(c).

various overpotential components (η_i), and the internal battery resistance (R_e). As long as the basic electrochemical reactions (eqns [I] and [II]) proceed inside the battery, the overpotentials established at both the nickel and MH electrode are relatively small (see **Figure 2**). This implies that the heat contribution, resulting from the electrode reactions, is limited, resulting, in turn, in a rather moderate temperature rise (**Figure 4**). However, this situation changes drastically as soon as the oxygen recombination cycle at the MH electrode starts to occur. Because the MH electrode potential is at least 1 V more negative with respect to the standard redox potential of the OH^-/O_2 couple, this implies that the established overpotential for the oxygen recombination reaction is extremely high (>1.2 V). Considering eqn [1], it is expected that the heat evolution inside a battery will sharply increase as soon as the oxygen recombination cycle starts. This is indeed in agreement with the pronounced temperature increase found during overcharging in the experiments (see **Figure 4**) and has been confirmed by simulations. As a result of this severe temperature increase the voltage tends to decrease during overcharging. This so-called $-\Delta V/dt$ effect is often used as signal to terminate the charging process.

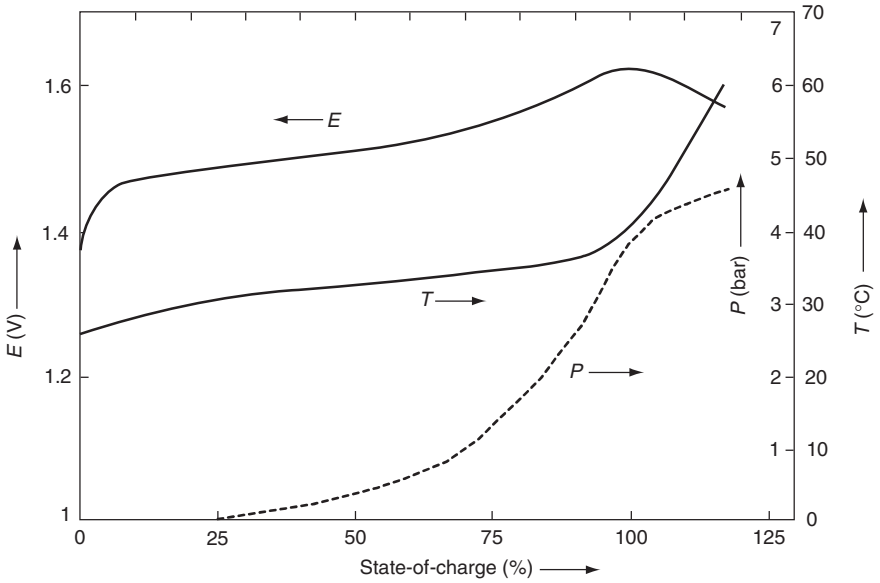

Figure 4 Development of the cell voltage (E), the internal gas pressure (P), and the cell temperature (T) as a function of state-of-charge (SoC) for a Ni–MH battery during charging and overcharging with a high (3 A) current, that is, the battery is fully charged within 20 min. Note that during overcharging the temperature increases sharply and, consequently, the battery voltage decreases. Reproduced with permission from Notten PHL (1994) In: Grandjean F, Long GJ, and Buschow KHJ (eds.) *Rechargeable Nickel–Metal Hydride Batteries: A Successful New Concept*, ch. 7, vol. 281, p. 151. NATO ASI Series E. London, ISBN 0-7923-3299-7.

Overdischarging

Protection against overdischarging is another factor of importance, especially when Ni–MH batteries, which inevitably reveal small differences in storage capacities, are used in series. This implies that some batteries are already completely discharged while others contain small amounts of electrical energy. Continuation of the discharge process induces overdischarging to occur of the already fully discharged batteries. Under these circumstances, water is forced to be reduced at the nickel electrode, according to

$$2H_2O + 2e^- \xrightarrow{Ni} 2OH^- + H_2 \qquad [VI]$$

which also results in a pressure build-up inside the battery when no precautions are taken (see also **Figure 1**). As the (electro)chemical affinity of the metal hydride (MH) electrode toward hydrogen gas is, in principle, excellent, it is evident that this gas can be again converted into water at the MH electrode during overdischarging, according to

$$H_2 + 2OH^- \xrightarrow{MH} 2H_2O + 2e^- \qquad [VII]$$

or through a dissociative absorption reaction. Considering the similar nature of reactions [VI] and [VII], a cell voltage of close to 0 V is to be expected during overdischarging. The experimental result of such a process is shown in **Figure 5** and is in agreement with these expectations. During normal discharging, the battery voltage is located around 1.2 V and drops indeed toward an inverted voltage of −0.2 V when the overdischarging reactions take over. **Figure 5** also reveals that the pressure rise due to hydrogen evolution may be considerable, indicating that hydrogen recombination is not very favorable in this case. In the example given, the pressure was quickly built up to the critical level of approximately 20 bar, (1 bar = 10^5 Pa). At that level, the safety vent was forced to open, which can be recognized on the small pressure decrease. Conclusively, monitoring the voltage(s) of individual cells or groups of cells is essential in order to protect these against severe (over)discharging, which is especially important for specific applications as (H)EV.

A detailed mechanistic and kinetic study of the complex overdischarging reactions, occurring inside Ni–MH batteries, has recently been reported by A. Belfadhel-Ayeb and coworkers. It was concluded that the hydrogen evolution reaction at the nickel electrode occurs through the so-called Volmer–Heyrovsky mechanism and that the rate is characterized by two different Tafel slopes. The reaction order of hydrogen recombination reaction was found to be 0.5 and temperature independent in the whole temperature range investigated, indicating that dissociation of hydrogen molecules at the MH electrode is the rate-determining step.

Self-discharge

It is well known that charged Ni–MH batteries, similar to Ni–Cd and lithium-ion batteries, lose their stored energy

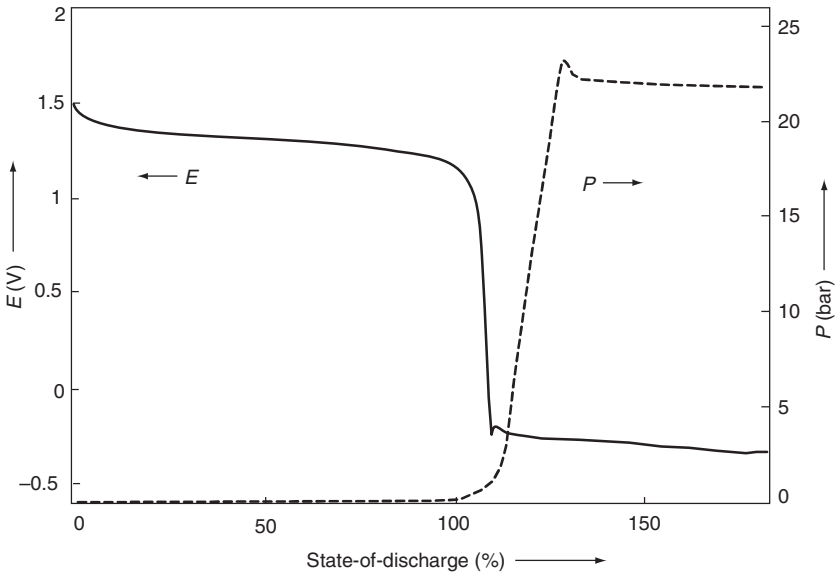

Figure 5 Experimental result of the development of the cell voltage (*E*) and internal gas pressure (*P*) as a function of state-of-discharge for a Ni–MH battery during discharging and overdischarging. Reproduced with permission from Notten PHL (1994) In: Grandjean F, Long GJ, and Buschow KHJ (eds.) *Rechargeable Nickel–Metal Hydride Batteries: A Successful New Concept*, ch. 7, vol. 281, p. 151. NATO ASI Series E. London, ISBN 0-7923-3299-7.

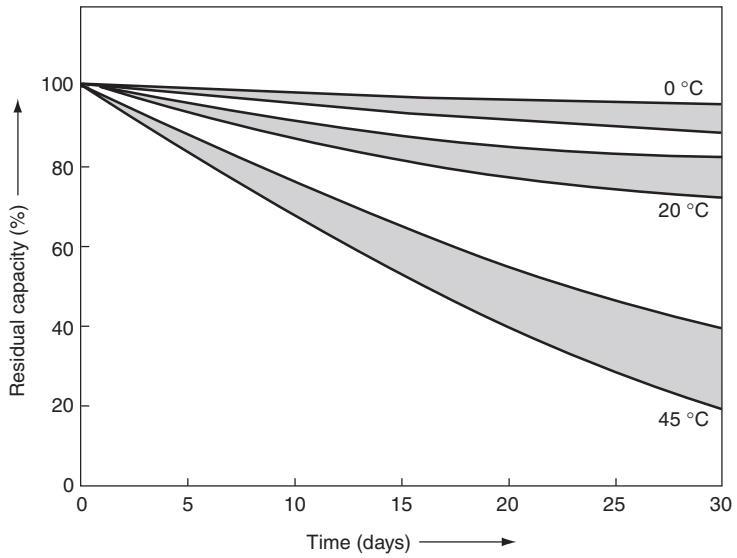

Figure 6 Self-discharge characteristics of a Ni–MH battery at various temperatures. Gray regions indicate the spread between different batteries. Reproduced with permission from Notten PHL (1994) In: Grandjean F, Long GJ, and Buschow KHJ (eds.) *Rechargeable Nickel–Metal Hydride Batteries: A Successful New Concept*, ch. 7, vol. 281, p. 151. NATO ASI Series E. London, ISBN 0-7923-3299-7.

under open-circuit conditions to a certain extent. Typical self-discharge rates are of the order of 1% of the nominal storage capacity per day. These rates, however, strongly depend on the external conditions, such as state-of-charge and temperature. Figure 6 shows that the self-discharge rate increases significantly at higher temperatures.

Various mechanisms contribute to the overall self-discharge rate. These mechanisms are all electrochemical in nature. The most important mechanisms, contributing to the overall self-discharge rate, are as follows:

(i) Owing to the more positive redox potential of the nickel electrode ($+439\,\text{mV}$) compared to that of the competing oxygen evolution reaction ($+300\,\text{mV}$; see Figure 2), trivalent Ni^{III} is thermodynamically unstable in an aqueous environment. Consequently, nickel oxyhydroxide (NiOOH) will,

under open-circuit conditions, be reduced by hydroxyl ions according to

$$NiOOH + H_2O + e^- \rightarrow Ni(OH)_2 + OH^- \qquad [VIII]$$

$$4OH^- \xrightarrow{Ni} O_2 + 2H_2O + 4e^- \qquad [IX]$$

The electrons released by the OH^- ions are transferred to the nickel electrode at the nickel electrode/electrolyte interface. Although the Ni(III) species are principally unstable, electrical charge can, however, relatively long be stored in the nickel electrode due to the fact that the kinetics of the oxygen evolution reaction are fortunately rather poor. Subsequently, the produced oxygen gas will be transported to the MH electrode, where it can be reconverted into OH^- ions at the expense of charge stored in the MH electrode, that is,

$$O_2 + 2H_2O + 4e^- \xrightarrow{MH} 4OH^- \qquad [X]$$

$$MH + OH^- \rightarrow M + H_2O + e^- \qquad [XI]$$

These reactions also occur at the open-circuit potential at the MH electrode. The ultimate result is that the chemical energy stored in both the nickel and MH electrode is slowly released through an oxygen gas-phase shunt.

(ii) A different type of gas-phase shunt is initiated by the MH electrode and is caused by the presence of hydrogen gas inside the battery. As the storage capacity of the MH electrode is considerably larger than that of the nickel electrode (**Figure 1**) and the MH electrode contains a certain amount of 'precharge' in the form of a metal hydride, a minimum partial hydrogen pressure is established inside the Ni–MH battery, according to the chemical equilibrium

$$MH \leftrightarrow M + \tfrac{1}{2}H_2 \qquad [XII]$$

As a result, hydrogen is inevitably in contact with the nickel electrode. Because the standard redox potential of the H_2/H_2O redox couple is much more negative than that of the Ni(II)/Ni(III) couple (**Figure 2**), hydrogen can in principle be oxidized at the nickel electrode, whereas the nickel electrode is simultaneously reduced, according to

$$H_2 + 2OH^- \xrightarrow{Ni} 2H_2O + 2e^- \qquad [XIII]$$

$$NiOOH + H_2O + e^- \rightarrow Ni(OH)_2 + OH^- \qquad [XIV]$$

The overall electrochemical process occurs again under open-circuit, electroless, conditions at the nickel electrode and will be strongly influenced by the partial hydrogen pressure inside the battery. It has indeed been reported that the self-discharge rate at the nickel electrode is proportional to the partial hydrogen pressure. According to eqns [XII] and [XIV], the chemical energy stored in both the MH and nickel electrode is 'wasted' by a hydrogen gas-phase shunt and can no longer be employed for useful energy supply.

(iii) A third possible self-discharge mechanism is related to the fabrication process of the nickel electrode. This electrode is often prepared by electrolytic reduction of an acidic salt electrolyte, for example, nickel nitrate ($Ni(NO_3)_2$). During this process NO_3^- ions are reduced to NH_4^+ ions. This results in a significant increase in pH near the electrode/electrolyte interface. Because the solubility product of nickel hydroxide ($Ni(OH)_2$) exceeds, nickel hydroxide will subsequently precipitate on the substrate. A consequence of this process is that a certain amount of nitrate ions are inevitably incorporated in the nickel electrodes, which can be leached out during the battery cycle-life. These NO_3^- ions, dissolved in the electrolyte, form the basis of this third self-discharge mechanism. These ionic species can be reduced to lower oxidation states. It is generally assumed that a so-called nitrate/nitrite shuttle is operative in alkaline rechargeable batteries. Because the standard redox potential of the nitrate/nitrite redox couple is much more positive than that of the MH electrode ($E^{\circ}_{NO_2^-/NO_3^-} = -91$ mV vs Hg/HgO; see also **Figure 2**), NO_3^- ions can be reduced at the MH electrode under open-circuit conditions, according to

$$NO_3^- + H_2O + 2e^- \xrightarrow{MH} NO_2^- + 2OH^- \qquad [XV]$$

$$MH + OH^- \rightarrow M + H_2O + e^- \qquad [XVI]$$

The produced nitrite ions can diffuse to the nickel electrode and can be reconverted into nitrate while nickel oxyhydroxide is simultaneously reduced, according to

$$NO_2^- + 2OH^- \xrightarrow{Ni} NO_3^- + H_2O + 2e^- \qquad [XVII]$$

$$NiOOH + H_2O + e^- \rightarrow Ni(OH)_2 + OH^- \qquad [XVIII]$$

This reaction sequence can proceed continuously because the electroactive nitrate and nitrite species are continuously produced at both electrodes and are not effectively consumed. The final result is again that charge stored in both the MH and nickel electrode is consumed and is no longer available for useful energy supply.

Hydride-Forming Electrode Materials

AB_5-Type Compounds

Structural properties

The first intermetallic compound tested as negative electrode for Ni–MH batteries was $LaNi_5$ in the early 1970s. Since this very first work, several improvements have been achieved relating to hydride-forming materials. For about two decades, all the negative electrode materials used in Ni–MH batteries are based on $LaNi_5$-type compounds.

The crystallographic properties of $LaNi_5$ were first reported by H. Nowotny. This phase crystallizes in the $CaCu_5$-type hexagonal structure (*P6/mmm* space group) with La(1*a*) in (0,0,0), Ni(2*c*) in (1/3,2/3,0), and Ni(3*g*) in (1/2,0,1/2) (**Figure 7**). The structure can be seen as a stacking of planes containing both lanthanum and nickel hexagonal rings for $z = 0$ and only nickel hexagonal ring for $z = 1/2$. $LaNi_5$ alloy exhibited very high equilibrium pressure (0.17 MPa) and very poor cycle life to be used in practical batteries. Such a poor behavior is illustrated in **Figure 8** where the storage capacity of $LaNi_5$ is shown as a function of the number of electrochemical charge/discharge cycles. Despite a rather high initial specific capacity ($\sim$372 mAh g^{-1}), only 12% are recovered after 400 cycles. The insets in **Figure 8** show that the origin of this poor cycle life is related to a combination of particle size reduction, induced by repeated hydrogen absorption/desorption, and surface oxidation at the electrode/electrolyte interface. Such difficulties can be overcome by preparing the so-called pseudobinary alloys.

Several research groups have investigated the evolution of the plateau pressure as a function of the substituting elements. It was demonstrated that a linear relation exists between the intermetallic cell volume and the logarithm of the plateau pressure. This so-called geometrical model has been widely applied for adapting the plateau pressure of the compound to the application needs. Such behavior is illustrated in **Figure 9** for various substituting atoms either on the nickel or on the lanthanum sublattice. A practical plateau pressure around 10^{-3} MPa suitable for electrochemical applications can be easily achieved by substituting nickel with other elements such as aluminum, manganese, or cobalt. Fortunately, aging problems in electrochemical medium may also be solved by making appropriate substitutions. Capacity loss upon cycling is generally attributed to the decomposition of the alloys into lanthanum hydroxide ($La(OH)_3$) and nickel particles in concentrated potassium hydroxide. J. J. G. Willems at the Philips Research Laboratories obtained real improvements in terms of cycle life in the 1980s by adding cobalt to the nickel sublattice. Indeed, as can be seen in **Figure 10**, the cycle life of a cobalt-substituted compound ($La_{0.8}Nd_{0.2}Ni_{2.4}Co_{2.5}Si_{0.1}$) exhibits a stable reversible electrochemical capacity over 400 cycles, keeping about 86% of its initial value. The insets show that the electrodes hardly reveal any particle cracking and surface oxidation upon electrochemical cycling. Since then, numerous substitutions have been tempted, using various elements in order to obtain more efficient negative electrode materials.

Both lanthanum and nickel atoms can be substituted by other elements preserving the hexagonal $LaNi_5$ parent

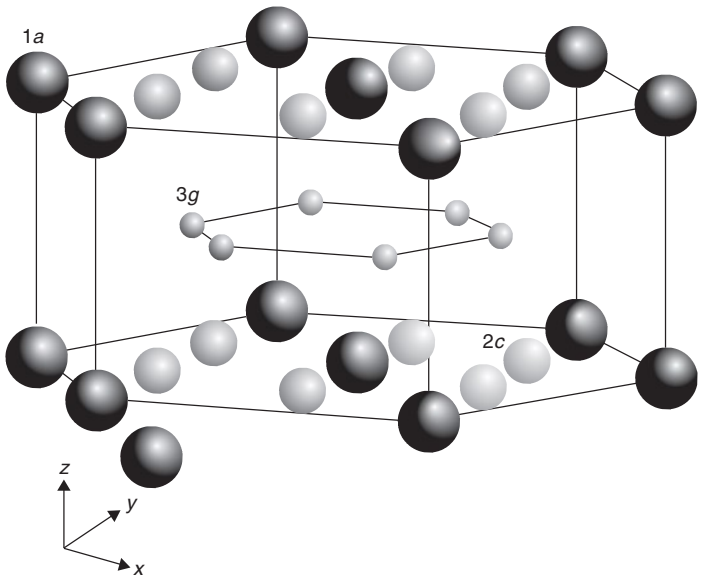

Figure 7 Crystal structure of $LaNi_5$ ($CaCu_5$-type hexagonal structure; *P6/mmm* space group) with La(1*a*) in (0,0,0) (in black), Ni(2*c*) in (1/3,2/3,0) (in dark gray), and Ni(3*g*) in (1/2,0,1/2) (in light gray).

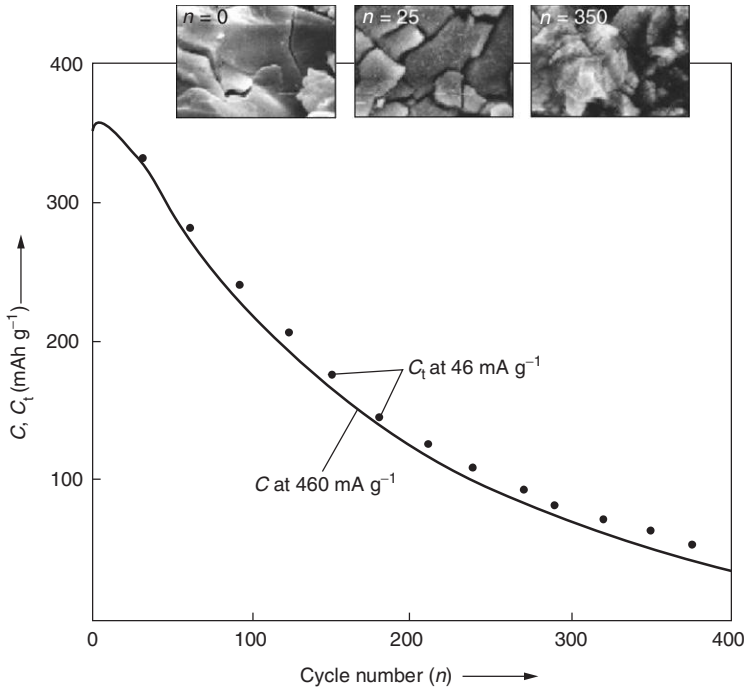

Figure 8 Electrochemical specific storage capacity as a function of the number of full charge and discharge cycles for a $LaNi_5$ electrode at room temperature. The photographs reveal the electrode surface after various, cycles ($n = 0, 25, 350$).

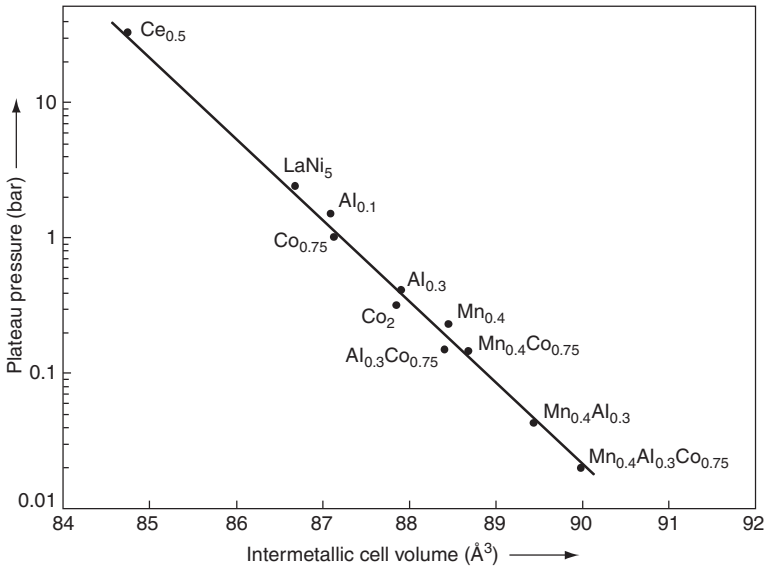

Figure 9 Linear dependence of the plateau pressure as a function of the intermetallic cell volume for various $La_{1-y}R_yNi_{5-x}M_x$ compounds at room temperature. Reproduced with permission from Notten PHL, Ouwerkerk M, van Hal H, Beelen D, Keur W, Zhou J, and Feil H (2004) High energy density strategies: From hydride-forming materials research to battery integration. *Journal of Power Sources* 129(1): 10.

structure. Lanthanum can be easily replaced by $4f$ elements in the whole range of concentration, leading to a complete solid solution for the rare earth site. Using this property, lanthanum can be easily replaced by cheaper natural mixture of rare earth, generally denoted as Mischmetal (Mm). On the nickel side, the substitution can be total for some neighboring elements but it is usually limited to a given range depending on the nature and the atomic radius of the substituting element. For example, the solid solution $LaNi_{5-x}M_x$ is complete for M = Co, Pt, or Cu but partial for Sn ($x \leqslant 0.5$), Si ($x \leqslant 0.6$), Fe ($x \leqslant 1.2$), Al ($x \leqslant 1.3$), or Mn ($x \leqslant 2.2$).

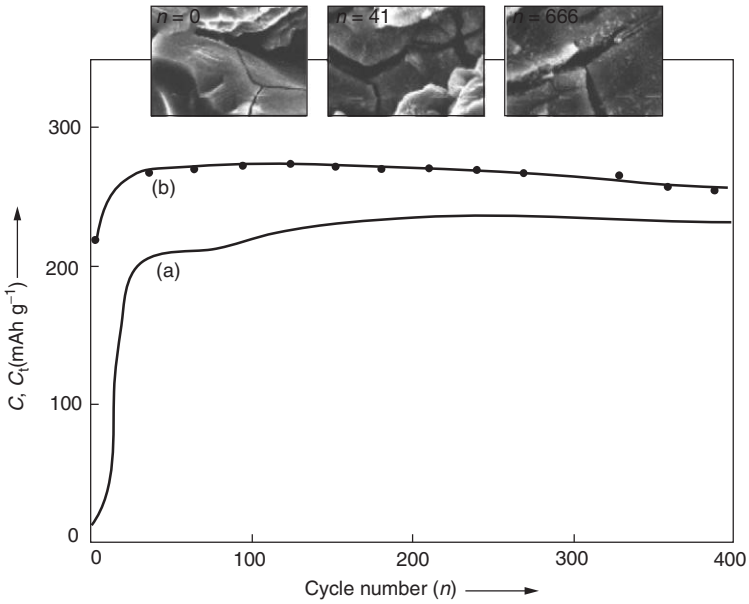

Figure 10 Cycle life plot of a $La_{0.8}Nd_{0.2}Ni_{2.4}Co_{2.5}Si_{0.1}$ electrode charged and discharged at room temperature with 350 mA g^{-1} (a) and additionally discharged at 35 mA g^{-1} every 30 cycles (b). The photographs indicate the electrode surfaces at various cycle numbers (n).

On the nickel sublattice, substitutions may occur on both sites 2*c* and 3*g* (Figure 7). On the basis of the scattering contrast between the nickel and the M element, the substitution rate between these two sites can be determined by classical X-ray or neutron powder diffraction experiments in the case of single-substituted compounds ($LaNi_{5-x}M_x$). Refined site occupancy factors of satisfactory precision were obtained by neutron powder diffraction on mono-substituted compounds such as $LaNi_{5-x}M_x$ (M = Mn, Al), (M = Al, Si, Cu), (M = Sn), and $LaNi_4Co$. The results show that manganese and cobalt have a slight, and aluminum, silicon, and tin a strong preference for site 3*g*, whereas copper has a slight preference for site 2*c*. As a general rule, it is observed that the larger atoms occupy preferentially site 3*g*, which presents more space to fit them, whereas atoms of size close to that of nickel substitute almost randomly on both sites.

Besides the mono-substituted compounds, many studies have been devoted to multisubstituted compounds. Numerous substitution schemes have been tested and good performances were empirically obtained by, for example, M. Ikoma and coworkers using the alloy composition $MmNi_{3.55}Mn_{0.4}Al_{0.3}Co_{0.75}$. Such Mm-based alloys are nowadays commonly used in commercial batteries, exhibiting a reversible specific capacity of about 320 mAh g^{-1}. Site occupancy factors on the multisubstituted compound $LaNi_{3.55}Mn_{0.4}Al_{0.3}Co_{0.75}$ have been investigated by J.-M. Joubert and coworkers. However, the individual occupancy factors of the metal constituents, such as nickel, manganese, aluminum, and cobalt, on the two available atom sites cannot be refined in an independent manner from a single diffraction experiment. Therefore, the distribution of the substituting elements such as manganese, aluminum, and cobalt was determined from synchrotron powder diffraction experiments by using the diffraction contrast produced by the anomalous dispersion effect. Joint Rietveld refinements on four different diffraction patterns have shown that the larger aluminum and manganese atoms occupy almost exclusively site 3*g*, whereas cobalt is distributed over sites 2*c* and 3*g*, with a slight preference for site 3*g*. From these results, it can be concluded that the distribution of atoms in multisubstituted compounds is not very different from that observed for the equivalent mono-substituted alloys.

Structural properties of metal hydrides

Upon hydrogenation, the intermetallic phase transforms itself into a metal hydride. This exothermic reaction can usually well be characterized by the so-called pressure composition temperature (PCT) isotherms. Such PCT curves exhibit a characteristic plateau pressure that corresponds to the progressive transformation from the hydrogen-poor α-phase, into the hydrogen-rich β-phase. The metallic framework is usually preserved at the transition but, due to hydrogen absorption, the cell volume of the β-phase is much larger than that of the α-phase. Typical values up to $\Delta V/V = 25\%$ are commonly observed for $LaNi_5$-type materials. Thus, huge constraints are involved by this volume expansion leading to an important decrepitation (see, e.g., Figure 8) and creating new fresh surfaces susceptible to electrochemical corrosion. Moreover, as the strains are not equal in all crystallographic directions, it is common to observe

anisotropic line broadening in the diffraction patterns of metallic hydrides.

Much research has been carried out on the structural properties of metal hydrides, although crystallographic studies are rather difficult for these materials: (1) neutron diffraction should be used instead of classical X-ray diffraction to locate hydrogen atoms (deuterium is usually preferred to lower the incoherent scattering); (2) due to the large value of $\Delta V/V$ that occurs during absorption, powderization of the material occurs at the α/β transition, which does not permit single crystal studies; (3) due to the constraints generated during this process, severe line broadening is commonly observed in the diffraction patterns leading to complex anisotropic modeling of the line width.

Anisotropic diffraction line broadening effects due to hydrogen absorption have been studied both ex situ and in situ. Such effects can be successfully solved by modified Rietveld refinement methods. Anisotropic line broadening in hydrogen cycled hexagonal $LaNi_5$ and substitutional derivatives has also been studied by means of synchrotron powder diffraction. The data have been analyzed by a local lattice parameter variation implemented in a Rietveld code and by an individual profile fitting using a dislocation line broadening model. The misfit of the lattice parameters between the intermetallic compounds and their hydrides activates two main dislocation systems. As a function of the nickel substitution by other elements, two main effects were observed: (1) the decrease or disappearance of the broadening related to the decrease of the total dislocation density and (2) the change of the anisotropy of the broadening related to the change of the nature of the dislocation system involved. The latter effect was attributed to a modification of the hydride precipitate shape.

In AB_5 compounds, hydrogen usually occupies tetrahedral sites that can be differentiated according to the nature of the site-forming atoms, that is, A_2B_2, AB_3, or B_4 where A and B define the atoms at the corners of the tetrahedron. However, some authors also report on the possible occupation of octahedral sites (especially site $3f$ in $P6/mmm$ space group). C. Lartigue and coworkers carefully investigated the structure at different concentrations of deuterium. They found evidence for a superstructure leading to a doubling of the c-axis, a hydrogen ordering, and a new description of the structure in space group $P6_3mc$ with seven interstitial sites for deuterium.

The consequences of metallic sublattice substitution on the structural hydride properties have been also widely investigated. It is generally observed that for pseudobinary compounds $LaNi_{5-x}M_x$ (M = Al, Mn, Cu), the symmetry of the intermetallic ($P6/mmm$) is preserved upon hydrogenation. The hydride can be described using a four-site structural model: $4h$ (B_4); $6m$ (A_2B_2); $12n$ (AB_3); and $12o$ (AB_3), as shown in **Figure 11**. From these studies, the lower capacities observed for pseudobinary-substituted compounds are attributed to a poorer filling of all the tetrahedral sites. Structural analysis of the multisubstituted deuteride $LaNi_{3.55}Mn_{0.4}Al_{0.3}Co_{0.75}$ has also been determined by neutron diffraction. It shows the same structure than the single-substituted deuterides, without symmetry lowering.

For some substituting atoms, deviations from the original metallic lattice are observed. For example, in the $LaNi_{5-x}Co_x$ system, two different hydrides are reported for $x \geq 0.1$. For $x = 1$, the first hydride (the so-called γ-phase with 4.4 H mol^{-1}) is correctly described in the $P6/mmm$ structure but the fully charged hydride $LaNi_4CoD_{6.1}$ (β-phase) is better described in the $P6_3mc$ structure, with a doubling of the c-parameter. More recently, the pseudobinary system $LaNi_{5-x}Sn_x$ has been investigated by Joubert and coworkers within the range $0.2 \leqslant x \leqslant 0.5$. For $x = 0.4$ and $x = 0.5$, the deuteride crystal

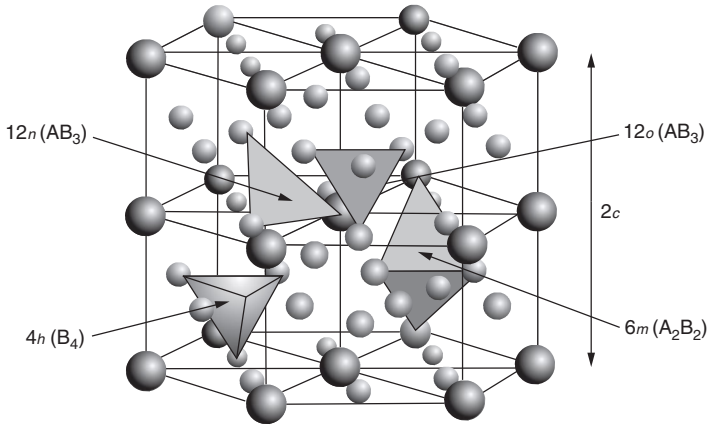

Figure 11 Crystal structure of pseudobinary metallic hydrides adopting the four-site structural model. Hydrogen sites are shown as tetrahedrons. The cell has been doubled along the c-axis only for sake of clarity.

structures are close to that of other metal-substituted $LaNi_5$ deuterides but for $x = 0.2$ a symmetry decrease to noncentro-symmetric space group *P6 mm* was observed and explained by partial deuterium ordering.

The necessity of substituting nickel by cobalt to obtain improved material upon electrochemical cycling has been reported very early. It is most likely that the benefit brought about by this element is connected to the mentioned formation of an intermediate γ-hydride. It is believed that in the three-substituted alloy $LaNi_{3.55}Mn_{0.4}Al_{0.3}Co_{0.75}$, this intermediate γ-hydride disappears for the benefit of a wider β-branch. However, cobalt remains highly expensive: its 10% weight in the alloy represents about 40% of the cost of the alloy. Therefore, a lot of work has been devoted to the reduction of this element in the electrode material. In situ studies on working electrodes using powder neutron diffraction have been performed on these electrode materials. This technique is very powerful since it allows a bulk analysis of the working electrode in a configuration very close to that of real commercial batteries. Using such in situ technique, two potential negative electrode materials with 5 and 10 wt% of cobalt have been investigated. For the cobalt-rich alloy, the existence of the intermediate γ-phase was reported. This γ-phase, with an intermediate cell volume and a capacity of 3–3.5 H mol^{-1}, plays probably a very important role in the strain distribution within the grain. It is believed that this phase is metastable and it exists only at the interface between the α- and β-phase. This interesting feature is related to volume expansion. Indeed, an intermediate hydride implies a two-step process in the discrete volume expansion (α→γ, γ→β) allowing the system to reduce the strains and therefore to limit the decrepitating process.

Nonstoichiometric AB_{5+y} Compounds

Besides the stoichiometric compound, careful examination of the lanthanum–nickel phase diagram shows an existence domain from $LaNi_{4.85}$ to $LaNi_{5.4}$ at about 1543 K. For the nickel-poor (under-stoichiometric) compositions, random substitutions of nickel by lanthanum were originally proposed to explain the non-stoichiometry but more recent works propose a lower limit of $LaNi_{4.88}$ and assumed the simultaneous occurrence of both lanthanum atoms and vacancies on the nickel sites. The over-stoichiometry in $LaNi_{5+y}$ has been interpreted by the presence of randomly distributed nickel atom dumbbells occupying site 2*e* in *P6/mmm* space group oriented along the *c*-axis and replacing lanthanum atoms. Moreover, the nickel atoms forming a hexagon in the $z = 0$ plane around the dumbbell are no longer on site 2 *c* but shrink into position 6 *l* (**Figure 12**). Accordingly, the stoichiometry is better described as $La_{1-t}Ni_{5+2t}$ with $t = y/(7 + y)$ that corresponds to the real number of atoms lying in the crystallographic cell.

A challenging crystallographic problem is encountered when investigating the structural properties of substituted over-stoichiometric $La(Ni_{1-x}M_x)_{5+y}$ compounds. In this case, there are two additional sites 6 *l* (0.28,0.56,0) and 2*e* (0,0,0.30) that can be occupied either by nickel atoms or by the substituting M atoms. Such structure determination has been achieved for M = Cu using neutron and anomalous synchrotron powder diffraction joint refinements, and for M = Mn using powder neutron diffraction data. For the copper compounds, the 2*e* and 6 *l* positions are only made of nickel for $y = 0.4$, whereas for larger *y* values, $y = 0.8$ and 1.0, these crystallographic positions begin to be occupied by copper.

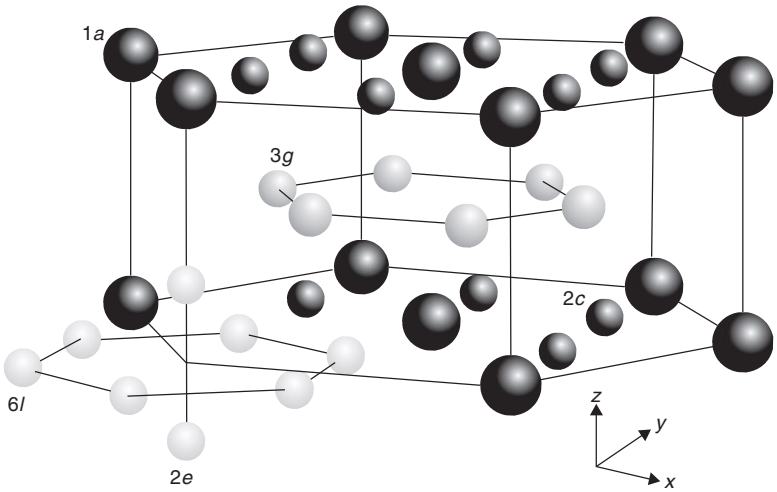

Figure 12 Crystal structure of $LaNi_5$ ($CaCu_5$-type hexagonal structure; *P6/mmm* space group) with La(1*a*) (in black), Ni(2 *c*) (in dark gray), Ni(3 *g*) (in light gray), Ni(6*l*), and Ni(2*e*) (in white). The nickel dumbbell lying along the *c*-axis is shown surrounded by the six nickel atoms that shrink around it.

For the manganese compounds, a clear preference of the manganese atoms for site $3g$ is observed and site $2c$ is almost pure nickel. Besides, the dumbbell site ($2e$) is found to be occupied by manganese only, whereas site $6l$ is made of nickel for $y = 0.14$ but contains 25% of manganese for $y = 0.5$. This shows that, according to the nature of the substituting atoms, the composition of the dumbbells can be very different.

Although the crystallographic structure of the stoichiometric hydride $LaNi_5H_p$ has been studied in detail in the past, investigations of over-stoichiometric hydrides $LaNi_{5+y}H_p$ are to be done. Because commercial alloys used in electrode materials are nowadays over-stoichiometric, the effect of over-stoichiometry on the nature and the occupancy of the various sites occupied by hydrogen (deuterium) as a function of the stoichiometry y have been recently studied. It was found that, as for stoichiometric $LaNi_5$, deuterium ordering related to the doubling of the c-axis occurs for $y = 0$ and 0.2 but this effect is no more observed for $y = 0.4$. However, it can be expected at higher pressure (i.e., larger concentration) for this latter compound.

Cycle life and price form one of the important issues when using such materials as negative electrodes in Ni–MH battery. Willems showed how the corrosion process was directly related to the cycling effect and could be well explained by the volume expansion observed during hydrogen absorption. P. H. L. Notten and coworkers have shown that the predominant factor was the so-called discrete lattice expansion between the α_{max} and the β_{min} phases, that is, the actual volume expansion occurring at the pressure plateau. This has been proven for over-stoichiometric $La(Ni_{1-x}Cu_x)_{5+y}$ and $La(Ni_{1-x}Mn_x)_{5+y}$ compounds for which excellent cycle lives were found. **Figure 13** indeed shows that the electrodes are becoming much more stable with increasing degree of nonstoichiometry. The increased corrosion stability was attributed to the much smaller discrete lattice expansion upon hydrogenation, resulting in a much lower degree of decrepitating. The photographs in **Figure 13** reveal that the particle size of the $AB_{5.4}$ compound is much larger than that of the corresponding $AB_{5.0}$ compound. This result shows that cobalt-free and electrochemically stable AB_5-type materials could be designed by adopting the nonstoichiometric strategy. Similar results have been reported for cobalt-free, manganese-based, nonstoichiometric compounds.

More recently, both the increase of stoichiometry and the part reduction of cobalt were further investigated. Good cycle life performance was also obtained with materials containing low cobalt contents without drastically reducing the capacity. Again, such benefit could be attributed to a combination of the stoichiometric impact and the occurrence of the intermediate γ-phase as has been concluded from electrochemical in situ studies.

For the past 20 years, the metallic hydrides used as negative electrode in Ni–MH batteries were almost exclusively AB_5-type-substituted compounds. The initial aim for substitution was to adapt the equilibrium pressure but it was shown very early that it also protects the electrode materials in the alkaline medium. This latter point has been particularly investigated using very

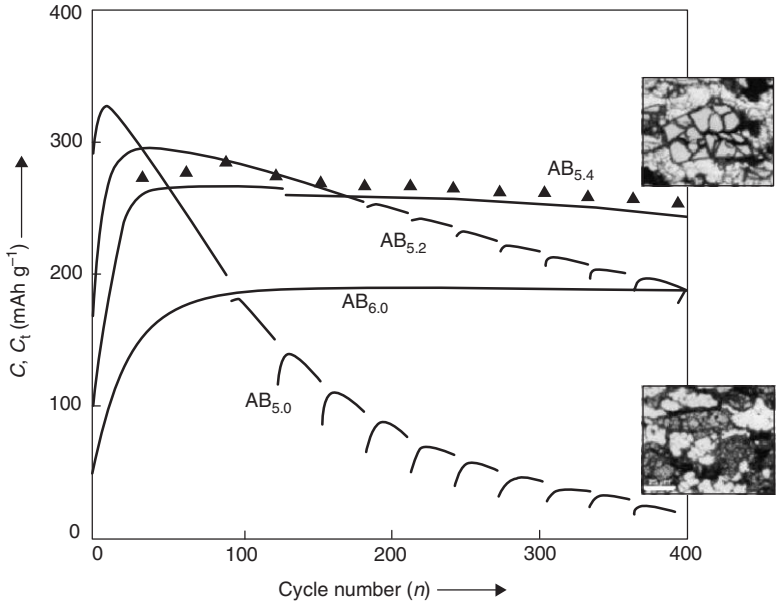

Figure 13 Cycle life plots of some nonstoichiometric AB_{5+x} alloys with constant Cu content ($LaNi_{x-1}Cu$) discharged with 350 mA g^{-1} and additionally discharged at 35 mA g^{-1} for $LaNi_{4.4}Cu$ (triangles). The photograph reveals the polished cross-section of the $AB_{5.0}$ (lower photo) and $AB_{5.4}$ (upper photo) electrode after 400 charge/discharge cycles.

different atomic elements, stoichiometry and substituting scheme, and leading to very complex formula, such as $(LaCePrNd)(NiAlMnCo)_{5+y}$. Most of the corrosion process is attributed to the decrepitation that occurs during the α/β (or $\alpha/\gamma/\beta$) transition along the phase transformation plateau pressure. Deep efforts have been made to understand how the crystallographic structures of each phase can coherently coexist within the grain and how strains are generated at the interface. Knowledge of the different crystallographic structures of each phase is of particular interest with the aim of finding the crystallographic forms leading to the smallest defect generation at the interface.

Other Metallic Compounds Suitable for Electrochemical Application

AB_2 compounds

Hydride-forming compounds with increased weight capacity with respect to AB_5 compounds have been explored in order to satisfy the demand of high-capacity accumulators for portable devices and (hybrid) electric vehicles. Although research and development on AB_5 compounds had to focus mainly on corrosion resistance, research on AB_2 compounds had to face at the same time several problems such as (1) difficulties to prepare single-phase compounds, (2) adaptation of the equilibrium pressure, (3) passivation and slow activation, and (4) corrosion.

Laves phases are intermetallic compounds with AB_2 stoichiometry, crystallizing among one of three following structure types: $MgCu_2$ (cubic), $MgZn_2$ or $MgNi_2$ (hexagonal). The criterion for the existence of such phases is mainly geometric. As a matter of fact, the Laves phases correspond to a compact stacking for atomic radius ratio $R_A/R_B = 1.225$. They belong to the topologically close-packed structure class and, as a consequence, are characterized by the unique presence of tetrahedral interstices and Fanck–Kasper coordination polyhedra. The three different crystal structures can be described as different stacking modes of this polyhedron. Electronic factors play a key role in determining in which structure type the Laves phase will crystallize. In ternary systems $A(B_{1-x}B'_x)_2$, the change of electronic concentration induced by the B' atom substitution can lead to changes in the crystal structure of the binary AB_2 compound. In the C14 crystal structure, where two different sites are available for the B element, no preferential occupancy for B-substituting elements is observed, as reported, for example, in iron- and nickel-substituted $ZrCr_2$ compounds. Concerning nonstoichiometric phenomena in AB_2-based compounds, both values higher or lower than the 1:2 ideal ratio have been observed in some systems, leading to compositional homogeneity domains. As an example, C14 phase in Ti–Mn extends from 60 to 70 at% manganese. The titanium-rich compound $TiMn_{1.5}$ has been described by a partial titanium substitution on manganese sites, which can be expressed in terms of AB_2 notation as $Ti(Ti_{0.1}Mn_{0.9})_2$.

The crystal structures of AB_2 intermetallic compounds are generally conserved after hydrogenation. Hydrogen may occupy interstitial tetrahedral sites with environment A_2B_2, AB_3, and B_4, the number of which is the same in C14 or C15 structures. A_2B_2 sites are the most occupied sites because they are the largest and, owing to their high coordination with A-type elements, present the strongest affinity for hydrogen. Only in rare cases, for fully charged $ZrV_2D_{4.5}$ or $ZrCr_2D_{3.8}$, AB_3 sites begin to be filled up. The case of C14 hydrides is more complicated because four distinct A_2B_2 positions are available. It has been shown that occupancies of these sites are significantly different in spite of their same nearest neighbor environment.

AB compounds

AB intermetallic compounds are able to absorb between 2 and 3 H mol^{-1} by the solid–gas reaction method. Major interest was focused on titanium- and zirconium-based AB alloys due to their high hydrogen storage capacity, low specific weight, and reasonable cost. The reversible hydrides of TiNi and TiFe were discovered in the early 1970s. They constitute today the AB-type compounds with the most interesting hydrogenation properties.

The most interesting AB compounds regarding hydrogen storage capacity and stability are the titanium-based alloys (TiFe, TiCo, and TiNi) and the zirconium-based alloys (ZrNi and ZrCo). TiFe, TiCo, and ZrCo crystallize in the highly symmetrical CsCl-type cubic structure, whereas ZrNi has a CrB-type orthorhombic structure. The case of TiNi is particular since it presents a martensitic transformation around room temperature that is responsible for its remarkable shape memory behavior. The high temperature phase (austenite) exhibits a CsCl-type structure that transforms on cooling into a monoclinic $P2_1/m$ structure (martensite). The martensitic transformation is strongly sensitive to metallurgical properties such as alloy stoichiometry, secondary phases, internal stresses, and thermal history. The transformation temperature can also be modified by substitutions of titanium and nickel by other transition metals or aluminum. For instance, it decreases when replacing titanium by aluminum and manganese, or nickel by cobalt and iron, but increases when substituting zirconium by titanium, or gold by nickel. It has been reported that the progressive replacement of titanium by zirconium, which is of particular interest as concerns the hydrogenation properties of TiNi, increases gradually the martensitic transformation temperature till a maximum value of $\sim 250\,^{\circ}C$ for a 50 at% substitution level.

Upon hydrogenation most of the AB compounds preserve their metal structure. For example, TiFe forms two stable hydrides with compositions TiFeH and $TiFeH_{1.9}$, for which the CsCl-type structure of the metallic sublattice is retained. On the contrary, ZrCo, which has a CsCl-type cubic structure, forms a trihydride that exhibits an orthorhombic metal sublattice. The case of ZrNi, with a CrB-type structure, is more complex. Two hydrides with compositions ZrNiH and $ZrNiH_3$ are formed. The first one induces a distortion from an orthorhombic to a triclinic structure, whereas the second one causes reversion to the orthorhombic structure. Austenitic TiNi forms, upon hydrogenation, a unique TiNiH tetragonal hydride with space group $I4/mmm$, as determined by X-ray and neutron diffraction. It can be observed that the initial CsCl structure of the metal sublattice is slightly deformed, apart from the normal hydrogen-induced expansion. The lower hydrogen storage capability of cubic-TiNi (1.4 H mol^{-1}) with respect to the isostructural TiFe (2 H mol^{-1}) has been attributed to the different strengths of Ti–Ni and Ti–Fe bonds. This would induce distinct lattice distortions between the two systems, enabling the occupancy of A_2B_4 and A_4B_2 octahedral sites for TiFe but only A_4B_2 sites for cubic-TiNi. Contrary to AB_5 and AB_2 compounds, hydrogen occupies octahedral sites in most AB compounds. Finally, regarding martensitic TiNi, no crystal structure of the hydride has been reported yet.

AB_{3-4} compounds

Besides the classical AB_n compounds ($n = 5$, 2, or 1), other promising families also have to be considered. Looking at the La–Ni phase diagram between 75 and 80 at% of nickel, one can observe the presence of three phases: $LaNi_3$, La_2Ni_7, and La_5Ni_{19}. Although the electrochemical properties of these binary compounds are poorly interesting, increasing interest is recently raised for these systems due to the possibility to form ternary compounds in the A–Mg–Ni system (A: rare earths). These phases are usually obtained by reaction of a mixture of $MgNi_2$ and ANi_5 intermetallic compounds or by direct reaction of the pure elements. Both magnesium and lanthanum elements are good hydride-forming compounds and this type of ternary alloy absorbs and desorbs readily hydrogen at room temperature. The possibility to prepare magnesium-containing ternary intermetallic compounds allows decreasing the molar mass and therefore significantly increasing the electrochemical storage capacity of such electrode materials.

The A–Mg–Ni system was investigated by K. Kadir and coworkers in the late 1990s. They reported the existence of ternary AMg_2Ni_9 compounds with various rare earths (lanthanum to gadolinium). The authors showed that such compounds adopt the $PuNi_3$-type structure. Among the two available plutonium sites (3*a* and 6*c* in $R\bar{3}m$ space group), the magnesium atoms lie exclusively on the 6*c* site and AMg_2Ni_9 can be seen as ternary compounds built from stacking ANi_5 (Haucke phase) and $MgNi_2$ (Laves phase) units along the *c*-axis as illustrated in Figure 14. Many substitutions have been studied either on the A-site (3*a*, by calcium and yttrium), on the magnesium site (6*c*, by calcium, titanium, and yttrium), or on the nickel sublattice (by aluminum or manganese).

Despite real improvement regarding capacities, this class of AB_3 compounds remain far to fulfill the criteria necessary for electrode materials especially concerning cycle lives. However, a breakthrough was achieved by T. Kohno and coworkers with $La_{0.7}Mg_{0.3}Ni_{2.8}Co_{0.5}$. This phase shows a much larger specific capacity (410 mAh g^{-1}) than commonly found for $LaNi_5$-type compounds. This $AB_{3.3}$ alloy leads to improved charge–discharge capability of the negative electrode with reasonable cycle life. This was confirmed by R. Tang and coworkers who prepared a Mischmetal-based compound $Mm_{0.7}Mg_{0.2}Ni_{2.8}Co_{0.6}$ (Mm = 87 wt% La, 6 wt% Ce, 4 wt% Pr, 2.5 wt% Nd). They observed a mixing of two phases: $LaNi_5$-type and $La_5Mg_2Ni_{21}$ (AB_3-type). They report 380 mAh g^{-1} for this composite material with 82.5% of reversible specific capacity remaining after 100 cycles. It is worthwhile to note that, contrary to classical $LaNi_5$-type material, a mixture of two phases is commonly observed in these electrode materials depending on the value of x ($3 \leqslant x \leqslant 4$) in this AB$x$ system. From these results, many works have been carried out on these compounds investigating the influence of stoichiometry (x) and composition (A = La, Ce, Mm, Mg; B = Ni, Mn, Co, Al).

Recently, these phases have been crystallographically described by H. Hayakawa and coworkers. They showed that these systems have layered structures and show polytypism that originates from differences in the stacking of the units composed of m AB_5-type layers with one AB_2-type layer along the *c*-axis. A wide variety of layered structures can be formed depending on m. They can be described by the general formula $La_{m+1}MgNi_{5m+4}$ with $m = 0$, 1, 2, 3,.... In all cases, magnesium cannot substitute the rare earth in the AB_5-type layer but this atom enters the lanthanum site of the AB_2 unit allowing both reduction of the molar mass and stabilization of the structure by reducing the strains generated by AB_5 units stacking along the *c*-axis.

To our knowledge, there are only a few papers reporting the crystal structure of such ternary hydrides. The crystallographic properties of two deuterides $LaY_2Ni_9D_{12.8}$ and $CeY_2Ni_9D_{7.7}$ have been determined recently. It was shown that the symmetry of the parent compounds is preserved upon deuteration. However, significant differences are noticed between the lanthanum and cerium compound. The lanthanum compound exhibits an isotropic cell volume expansion when loaded with deuterium related to occupation of both AB_5 and

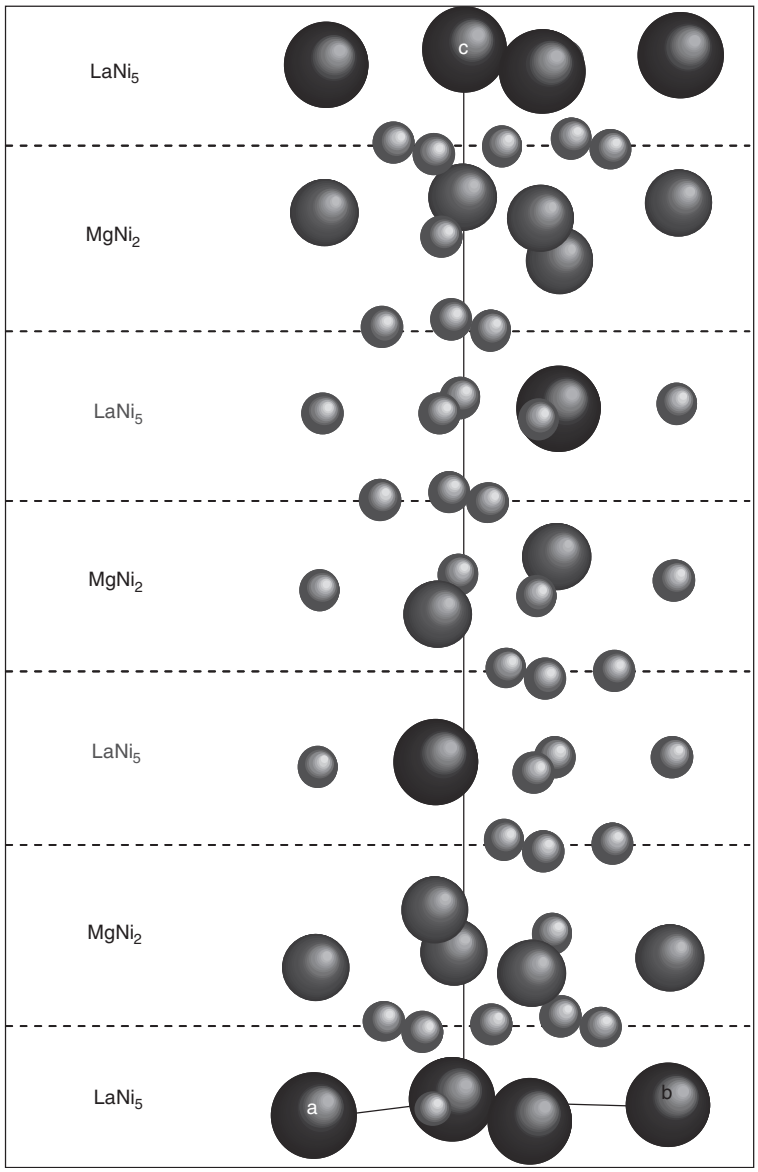

Figure 14 Crystal structure of LaY_2Ni_9 ($R\bar{3}m$ space group) with La (large spheres), Mg (middle spheres), and Ni (small spheres). The structure can be seen as a stacking of RNi_5 and $MgNi_2$ units along the *c*-axis. The dotted lines show the boundary between the different units and are a guide to the eyes.

AB_2 units. For the cerium compound, a large anisotropic volume expansion is observed and attributed to the exclusive occupation of AB_2 units by deuterium. Moreover, this latter compound exhibits a valence change for cerium leading to a heterogeneous mixed valence state of this element upon deuteration than was successfully related to the different hydrogen environment of both cerium atoms lying on sites 3*a* and 6*c*.

Similar effects have been reported recently by R. V. Denys and coworkers for the La–Mg–Ni system. Investigating the hydrogen storage properties of the $La_{1-x}Mg_x(Ni_{1-y}(Mn,Al)_y)_3$ systems, these authors observed that in $LaNi_3D_3$ hydrogen is preferentially located within the AB_2 units involving a huge uniaxial expansion (60%) along the *c*-axis. By partial substitution of lanthanum within the AB_2 units, magnesium causes an isotropic expansion in $La_{0.67}Mg_{0.33}Ni_3D_4$ preserving the metal sublattice without major modifications. Therefore, it can be concluded that magnesium substitution leads to a substantial increase of the reversible hydrogenation capacity and an enhanced stability against hydrogenation-induced amorphization.

Magnesium-based compounds

Evidently, the Holy Grail in hydrogen storage materials is to make use of very light-weight materials. Magnesium-based compounds offer this potential. Efforts have therefore been put into this research subject for a

long period. However, an important drawback of magnesium hydrides appeared to be the extremely poor (de)hydrogenation kinetics. Since the discovery that nanostructured materials might have a positive impact on these properties, renewed interest was put into these materials. In particular, ball-milling was successfully adopted by the Iwakura group to create interesting electrode materials. Reversible storage capacities up to 1080 mAh g^{-1} have been reported.

Resulting from 'switchable mirror' research, magnesium-based thin film electrodes, having a specific crystallographic structure, were recently found to combine interesting optical properties with strikingly high reversible hydrogen contents. The hydrogen storage capacity of these fluorite-structured compounds was shown to have a much larger reversible electrochemical storage capacity with respect to mischmetal-based AB_5 compounds in both thin film and bulk form. Comparing the extracted charge of a fully hydrogenated AB_5-type hydride-forming electrode (curve (a) in **Figure 15**) with that of a fluorite-stabilized magnesium-compound reveals that the latter has a more than four times higher storage capacity (curve (b)). In addition, the rates at which hydrogen can be electrochemically loaded and removed were substantial, making these fluorite-stabilized materials very interesting.

Indeed, specific fluorite-type of magnesium-based compounds alloyed with scandium has been studied electrochemically with compositions ranging from 50 to 100 at%. It was found that the favorable discharge kinetics was retained up to 80 at% magnesium. The improvement of the (de)hydriding kinetics compared to pure magnesium has been attributed to the more open fluorite structure of scandium hydride instead of the more compact rutile structure of conventional magnesium hydrides.

The fluorite structure was confirmed for the compositions $Mg_{65}Sc_{35}$ and $Mg_{75}Sc_{25}$ by ex situ X-ray diffraction (XRD). Recently, the crystal structure of a palladium-containing $Mg_{65}Sc_{35}$ compound has been studied upon hydrogenation by neutron diffraction. The metallic phase adopts a pseudo-CsCl-type structure. When hydrogenated, the structure changes from pseudo-CsCl to FCC involving an elongation along the *c*-axis and shrinkage along the *a*-axis. Upon deuteration, a two-phase domain is subsequently observed between 0.85 and 1.55 D/metal with two hydrides in equilibrium. Above this value, an increasing branch appears in the isotherm, leading to fully occupied tetrahedral sites and partially filled octahedral sites. It has been argued that the interstitial hydrogen is highly mobile, due to the large partially occupied octahedral sites favorably influencing the transportation properties. Using proton nuclear magnetic resonance (NMR), the crystallography has recently indeed proven to be responsible for the beneficial transportation properties of the fluorite-structured magnesium compounds; the frequency hopping rate for the fluorite-structured compounds at the relevant temperatures was found to be many orders of magnitude higher than that of the rutile-structured material. The hydrogenation reaction is fully reversible in the range 0.85 and 2.25 H per metal and thermal desorption of the

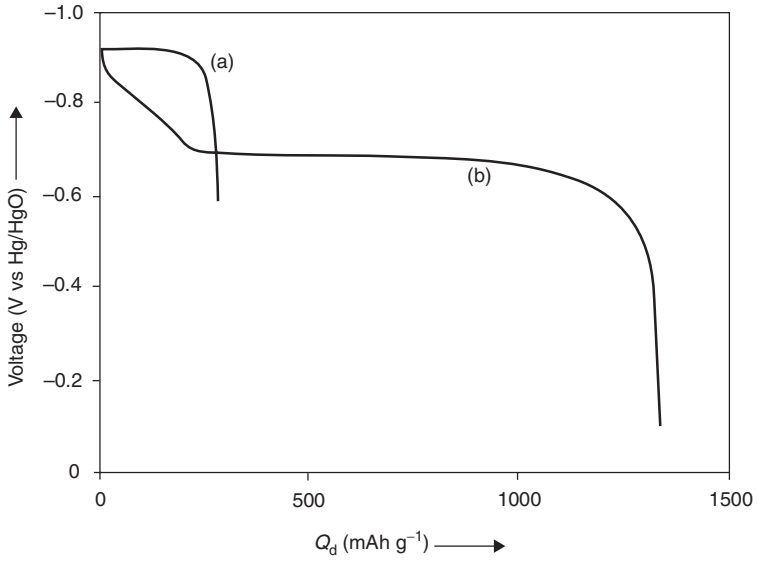

Figure 15 Comparison of galvanostatic discharge curves for a conventional AB_5-type electrode (curve (a)) and a fluorite-structured, magnesium-based, electrode with composition $Mg_{0.72}Sc_{0.28}(Pd_{0.012+}Rh_{0.012})$ (curve (b)) Reproduced with permission from Notten PHL, Ouwerkerk M, van Hal H, Beelen D, Keur W, Zhou J, and Feil H (2004) High energy density strategies: From hydride-forming materials research to battery integration. *Journal of Power Sources* 129(1): 10.

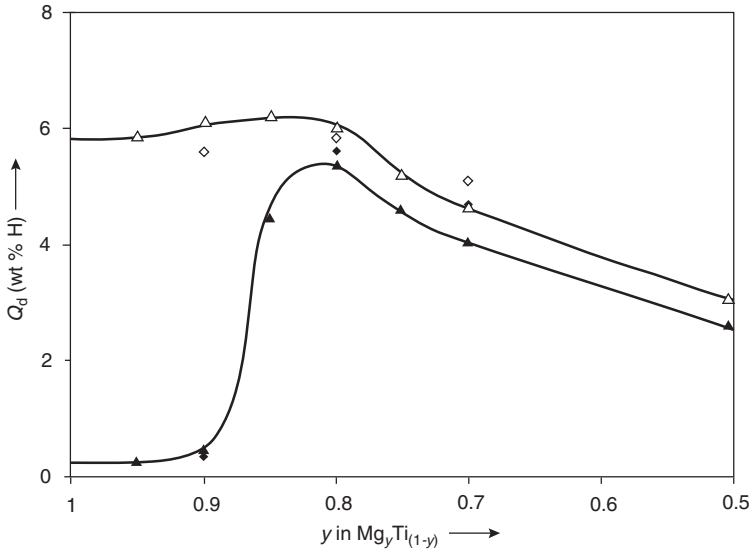

Figure 16 Electrochemically determined reversible hydrogen storage capacity at room temperature as a function of magnesium content in Mg–Ti thin film electrodes.

sample below 0.7 H per metal leads to decomposition into scandium dihydride (ScH_2) and magnesium.

As scandium is rather expensive, attempts to find cheaper substitutes were recently undertaken. Both titanium and vanadium form dihydrides with the same fluorite structure as scandium dihydride and were therefore argued to be probable candidates. Experiments performed with $Mg_{80}Ti_{20}$ and $Mg_{80}V_{20}$ thin film electrodes indeed showed a similar dramatic improvement of the discharge (dehydrogenation) kinetics compared to pure magnesium hydride (MgH_2). A more elaborate study on the Mg–Ti system (Figure 16) revealed that the composition dependence of the hydrogen storage capacity was quite similar to that of the Mg–Sc system, also showing a maximum around 80 at% magnesium. The crystal structure of the resulting hydride therefore also seems to play a crucial role in determining the (de)-hydrogenation kinetics for this interesting new class of hydrogen storage materials.

Electrochemical storage capacities substantially more than 1500 mAh g^{-1} have been reported for the Mg–Ti system at room temperature. This corresponds to reversible hydrogen contents of around 6 wt% (Figure 16). In addition, it has recently been shown that these meta-stable materials cannot only be made by thin film evaporation and sputtering techniques but also by mechanical milling, although it should be noted that the authors have not yet succeeded in producing the pure electroactive phase.

Although various problems, such as electrode degradation and materials cost, have to be improved drastically, this new class of magnesium materials are not only interesting for future electrochemical battery applications but might also offer interesting storage properties for fuel cell applications for which hydrogen needs to be stored through the gas phase. A hydrogen content of about 6 wt% approaches the requirements set by the US Department of Energy, essential to make the hydrogen economy feasible.

Comparison between the various compounds

Despite presenting larger intrinsic hydrogen absorption capacities than AB_5-type compounds, AB_2 Laves phases have not yet been developed as industrial electrode materials (some authors claim, however, that multiphase AB_2-based alloys reach improved properties compared to AB_5 compounds under industrial conditions). Obtaining single-phase material remains far more difficult than for AB_5 compounds. Though adaptation of the plateau pressure to the application need can be easily achieved, the AB_2 compounds suffer from poor activation, severe surface degradation, and corrosion. One of the reasons for this is, as compared to AB_5 compounds, the higher content in hydrogen but also highly oxidation-sensitive A-elements.

AB compounds are, at present, the least adapted intermetallic compounds for electrochemical applications. Only TiNi-based alloys exhibit some promising performances for rechargeable batteries. TiNi-based alloys possess also a complicated metallurgy due to the easy formation of secondary phases and the difficulty to control the temperature of the martensitic transformation. However, TiNi-based alloys present considerable interest, especially concerning the high electrochemical activity of austenite-TiNi and the high storage capacities of Ti–Ni–Zr martensitic alloys.

AB_5-type alloys have shown their ability to electrochemically store large amounts of hydrogen. They have been worldwide used as negative electrode materials in

Ni–MH batteries. Best compromise in terms of capacity, cycle life, kinetics, and cost was achieved with Mischmetal-containing, multisubstituted, low cobalt-content, over-stoichiometric $LaNi_5$-type compounds. Such complex metallurgical state reflects all the research that has been carried out in order to design highly efficient materials suitable for the development of batteries with high-energy density and friendly environment.

The new generations of Ni–MH batteries are now made from AB_{3-4}-type composite materials obtained from rare earths, magnesium, and transition metals – mainly nickel (with aluminum), manganese, and cobalt. These electrode materials have been commercialized since 2004 by battery manufacturers such as Sanyo Electric Co., Ltd. that has announced AA size (2700 mAh) and AAA size (1000 mAh) Ni–MH batteries. Such high capacities were achieved by adopting what Sanyo called 'Superlattice Alloy Technology', in fact an AB_{3-4}-type structural material for the negative electrode.

Finally, magnesium-based compounds adopting a fluorite structure might offer interesting potentials for future lightweight hydrogen (electrode) storage materials. These materials might induce the development of a new generation of even higher energy density Ni–MH batteries, making the competition with lithium-ion batteries even more interesting.

Nomenclature

Symbols and Units

C	specific electrochemical storage capacity ($mAh\,g^{-1}$)
E	potential (V)
E^{eq}	equilibrium potential (V)
E_{MH}	electrode potential MH electrode (V)
E_{Ni}	electrode potential Ni electrode (V)
E_{Ni-MH}	battery voltage (V)
E^o	redox potential (V)
F	Faraday constant ($As\,eq^{-1}$)
I_a	anodic current (A)
I_c	cathodic current (A)
I^o	exchange current (A)
n	number of electrons in electrochemical reactions
P_{H_2}	partial hydrogen pressure (Pa)
Q_d	discharge capacity $mAh\,g^{-1}$
R	gas constant ($J\,Mol^{-1}\,K^{-1}$)
R_A	radius atom A
R_B	radius atom B
R_e	electrolyte resistance (Ω)
T	temperature (K)
W	formation of heat (W)
W_{Ni-MH}	heat evolution Ni–MH batteries (W)
ΔS	entropy change ($J\,Mol^{-1}\,K^{-1}$)
η	overpotential (V)

Abbreviations and Acronyms

FCC	face-centered cubic
HEV	hybrid electrical vehicle
NMR	nuclear magnetic resonance
PCT	pressure composition temperature
P(H)EV	plug-in (hybrid) electrical vehicle
SoC	state-of-charge

See also: **Applications – Transportation:** Electric Vehicle: Batteries; **Batteries:** Capacity; Energy; Modeling; Self-Discharge; **Batteries and Fuel Cells:** Power; **Chemistry, Electrochemistry, and Electrochemical Applications:** Oxygen; **Electrochemical Theory:** Hydrogen Evolution; Kinetics; Oxygen Evolution; Thermodynamics; **Energy:** Hydrogen Economy; **History:** Electrochemistry; Secondary Batteries; **Measurement Methods:** Structural Properties: X-Ray and Neutron Diffraction; **Secondary Batteries:** Overview; **Secondary Batteries – Nickel Systems:** Nickel–Metal Hydride: Overview.

Further Reading

Achard J-C, Dianoux A-J, Lartigue C, Percheron-Guégan A, and Tasset F (1982) In: McCarthy GJ, Silber HB, and Rhyne JJ (eds.) *The Rare Earths in Modern Science and Technology*, vol. 3, p. 481, New York: Plenum Press.

Ayeb A, Otten WM, Mank AJG, and Notten PHL (2006) The hydrogen evolution and recombination kinetics inside sealed Nickel-Metal Hydride batteries. *Journal of the Electrochemical Society* 153: A2055.

Boter PA (1977) Rechargeable Electrochemical Cell. US Patent 4,004,943.

Denys RV, Yartys VA, Sato M, Delaplane RG, and Riabov AB (2007) Hydrogen storage properties and structure of $La_{1-x}Mg_x(Ni_{1-y}Mn_y)_3$ intermetallics and their hydrides. *Journal of Alloys and Compounds* 446–447: 166–172.

Fruchart D, Soubeyroux J-L, and Hempelmann R (1984) Neutron diffraction in $Ti_{1.2}Mn_{1.8}$ deuteride: Structural and magnetic aspects. *Journal of the Less-Common Metals* 99: 307.

Iwakura C, Inoue H, Furukawa N, and Nohara S (2003) Research and Development of Mg-based hydrogen storage alloys for intended use in nickel-metal hydride batteries. *Electrochemistry* 71: 776.

Joubert J-M, Latroche M, Cerný R, Bowman RC Jr., Percheron-Guégan A, and Yvon K (1999) Crystallographic study of $LaNi_{5-x}Sn_x$ ($0.2 <= x <= 0.5$) compounds and their hydrides. *Journal of Alloys and Compounds* 293–295: 124.

Justi EW, Ewe HH, Kalberlah AW, Saridakis NM, and Schaefer MH (1970) Electrocatalysis in the nickel-titanium system. *Energy Conversion* 10: 183.

Kadir K, Sakai T, and Uehara I (1997) Synthesis and structure determination of a new series of hydrogen storage alloys; RMg_2Ni_9 (R = La, Ce, Pr, Nd, Sm and Gd) built from $MgNi_2$ Laves-type layers alternating with AB5 layers. *Journal of Alloys and Compounds* 257: 115.

Kalisvaart WP and Notten PHL (2008) Mechanical alloying and electrochemical hydrogen storage of Mg-based systems. *Journal of Materials Research* 23: 2179.

Kohno T, Yoshida H, Kawashima F, et al. (2000) Hydrogen storage properties of new ternary system alloys: La_2MgNi_9, $La_5Mg_2Ni_{23}$, La_3MgNi_{14}. *Journal of Alloys and Compounds* 311: L5.

Lartigue C, Percheron-Guégan A, Achard J-C, and Tasset F (1980) Thermodynamic and structural properties of LaNi5-xMnx compounds and their related hydrides. *Journal of the Less-Common Metals* 75: 23.

Latroche M, Joubert J-M, Percheron-Guégan A, and Notten PHL (1999) Crystal structure of non-stoichiometric copper substituted La(Ni1-zCuz)x compounds studied by neutron and synchrotron anomalous powder diffraction. *Journal of Solid State Chemistry* 146: 313.

Latroche M, Paul-Boncour V, and Percheron-Guegan A (2004) Structural properties of two deuterides LaY2Ni9D12.8 and CeY2Ni9D7.7 determined by neutron powder diffraction and X-ray absorption spectroscopy. *Journal of Solid State Chemistry* 177: 2542.

Mank AJG, Ayeb A, Krusemann PVE, and Notten PHL (2005) In situ Raman analyses of gas formation in NiMH batteries. *Applied Spectroscopy* 59: 101–106.

Matsumoto I and Ikoma M (1988) Metal hydride electrode for high energy density Sealed nickel-hydrogen battery, power sources. *Proceedings of the 16th International Power Sources Symposium* vol. 12: p. 203.

McBreen J (1990) *Modern Aspects of Electrochemistry* 21: 29.

Niessen RAH and Notten PHL (2005) Electrochemical hydrogen storage characteristics of thin film MgX (X = Sc, Ti, V, Cr) compounds. *Electrochemical and Solid-State Letters* 8: A534.

Noréus D, Werner P-E, Alasafi K, and Schmidt-Ihn E (1985) Structural studies of TiNiH. *International Journal of Hydrogen Energy* 10: 547.

Notten PHL (1994) In: Grandjean F, Long GJ, and Buschow KHJ, (eds.) *Rechargeable Nickel–Metal Hydride Batteries: A Successful New Concept*, ch. 7 in NATO ASI Series E, vol. 281, p. 151. London, ISBN 0-7923-3299-7.

Notten PHL and Hokkeling P (1991) Double-phase hydride-forming compounds: A new class of highly electrocatalytic materials. *Journal of the Electrochemical Society* 138: 1877.

Notten PHL, Daams JLC, De Veirman AEM, and Staals AA (1994) In situ X-ray diffraction: A useful tool to investigate hydride formation reactions. *Journal of Alloys and Compounds* 209: 85.

Notten PHL, Einerhand REF, and Daams JLC (1994) On the nature of the electrochemical cycling stability of non-stoichiometric LaNi5-based hydride-forming compounds: Part I Crystallography and electrochemistry and Part II X-ray diffractiometry. *Journal of Alloys and Compounds* 210: 221, 233.

Notten PHL, Kruijt WS, and Bergveld HJ (1998a) *Battery Management Systems: Design by Modeling*. London: Kluwer Academic Publishers ISBN 1-4020-0832-5.

Notten PHL, Kruijt WS, and Bergveld HJ (1998b) Electronic network modeling of rechargeable batteries. *Journal of the Electrochemical Society* 145: 3774.

Notten PHL, Ouwerkerk M, van Hal H, et al. (2004) High energy density strategies: from hydride-forming materials research to battery integration. *Journal of Power Sources* 129: 45.

Notten PHL, Verbitskiy E, Kruijt WS, and Bergveld HJ (2005) The oxygen evolution and recombination kinetics in sealed rechargeable, Ni-based batteries. *Journal of the Electrochemical Society* 152: A1423.

Reilly JJ and Wiswall RH (1974) Formation and properties of iron titanium hydride. *Inorganic Chemistry* 13: 218.

van Deutekom HJH (1980/1982) Rechargeable Electrochemical Cell. US Patent 4,214,043, 4,312,928.

Willems JJG (1984) *Philips Journal of Research* 39: 1.

Zijlstra H and Westendorp FF (1969) Influence of hydrogen on magnetic properties of SmCo5. *Solid State Communications* 7: 857.

Nickel–Metal Hydride: Overview

B Hariprakash, Indocel Technologies Private Limited, Bangalore, India
AK Shukla, Indian Institute of Science, Bangalore, India
S Venugoplan, ISRO Satellite Centre, Bangalore, India

Introduction

There is a persistent effort to develop high-energy, high-power-density, and low-cost rechargeable batteries to meet the ever-increasing needs for spacecrafts, defense, communication, electric vehicles (EVs), power tools, and other home appliances. Nickel–metal hydride (Ni–MH) batteries that use hydrogen storage alloys as the negative electrode material have drawn increased attention owing to their higher energy density, both in terms of weight and volume, improved high-rate capability, and high tolerance to overdischarge. Furthermore, sealed Ni–MH cells can be easily constructed because oxygen and hydrogen gases that evolve during their overcharge and overdischarge, respectively, are effectively consumed allowing prismatic design with superior packaging and heat management capabilities. These batteries are also free from dendrite formation and memory effect due to recrystallization and are devoid of toxic materials such as lead, cadmium, mercury, and asbestos.

Similar to the nickel–cadmium (Ni–Cd) system, Ni–MH cells also use nickel positive plates with nickel oxyhydroxide (NiOOH) as the active material and an aqueous potassium hydroxide electrolyte. The main difference is that the active material in the negative plate is hydrogen absorbed in a metal alloy. The metal alloys in which hydrogen is stored fall mainly into two categories: (1) the AB_5 alloys based on mixtures of nickel and rare earth and (2) the AB_2 alloys based on nickel commonly blended with titanium, vanadium, and zirconium. It is found that although AB_2-type alloys yield superior energy storage densities, the AB_5 alloys are able to hold hydrogen better, thus lowering the self-discharge rate of the battery. Besides, AB_5 alloys happen to be less expensive and easier to use.

At present, most commercial Ni–MH batteries either use AB_5-type $MmNi_{3.2}Co_{1.0}Mn_{0.6}Al_{0.11}Mo_{0.09}$ (Mm = misch metal: 25 wt% La, 50 wt% Ce, 7 wt% Pr, 18 wt% Nd) or use AB_2-type $Ti_{0.51}Zr_{0.49}V_{0.70}Ni_{1.18}Cr_{0.12}$ alloys; AB_5- and AB_2-type alloys have different crystal structures wherein A and B sites are occupied by mixtures of elements. The commonly used misch-metal alloys are capable of delivering a specific capacity of only $\sim$300 Ah kg^{-1}. Although these alloys utilize Ovshinsky's concept of disorder, they cannot be compared with commercial Ovonic transition metal alloys that approach a specific capacity of $\sim$400 Ah kg^{-1} and provide 80 Wh kg^{-1} of specific energy at cell level. This jump is only considered as a first threshold to the projected specific capacity value of 700–1000 Ah kg^{-1} in future phases. Magnesium-based alloys have been projected as excellent materials for MH electrodes with specific capacity values as high as 1000 Ah kg^{-1}. However, these alloys are prone to corrosion in alkaline environment. The major problems associated with these alloys are the sluggish hydriding kinetics at room temperature and oxidation of the material under ambient environmental conditions.

Operating Principle of a Nickel–Metal Hydride Battery

Figure 1 depicts the operating principle of a sealed rechargeable Ni–MH cell. In the cell, nickel hydroxide $Ni(OH)_2$ at the positive electrode is oxidized to nickel oxyhydroxide on charge and reduced back to nickel hydroxide during discharge. During charge, at the MH negative electrode, reduction of water produces atomic, adsorbed hydrogen that diffuses into the lattice of the intermetallic alloy to form a metal hydride. A reverse reaction takes place during discharge. Accordingly, the electrochemical reactions occurring in a Ni–MH cell can be represented as follows:

$$NiOOH + MH \underset{\text{charge}}{\overset{\text{discharge}}{\leftrightarrows}} Ni(OH)_2 + M \quad (E_{cell} = 1.32 \text{ V vs SHE}) \qquad [I]$$

The charge–discharge reactions in a Ni–MH battery proceed via a homogeneous solid-state mechanism through proton transfer between nickel hydroxide and hydrogen storage alloy, which distinguishes this battery from nickel–cadmium batteries, in which the anode reaction proceeds through a dissolution–precipitation mechanism. Accordingly, many of the performance deficiencies, such as (a) changes in crystallography, (b) changes in mechanical integrity, (c) changes in surface morphology of the electrode as a result of dissolution and recrystallization, and (d) reduced electrical conductivity in the oxidized state, are eliminated in the Ni–MH system permitting more compact assembly, longer cycle life, and the possibility to realize an all solid-state battery using a proton-conducting solid electrolyte.

As in the nickel–cadmium cell, the electrolyte is concentrated aqueous potassium hydroxide. But there is no net change in the electrolyte quantity or concentration

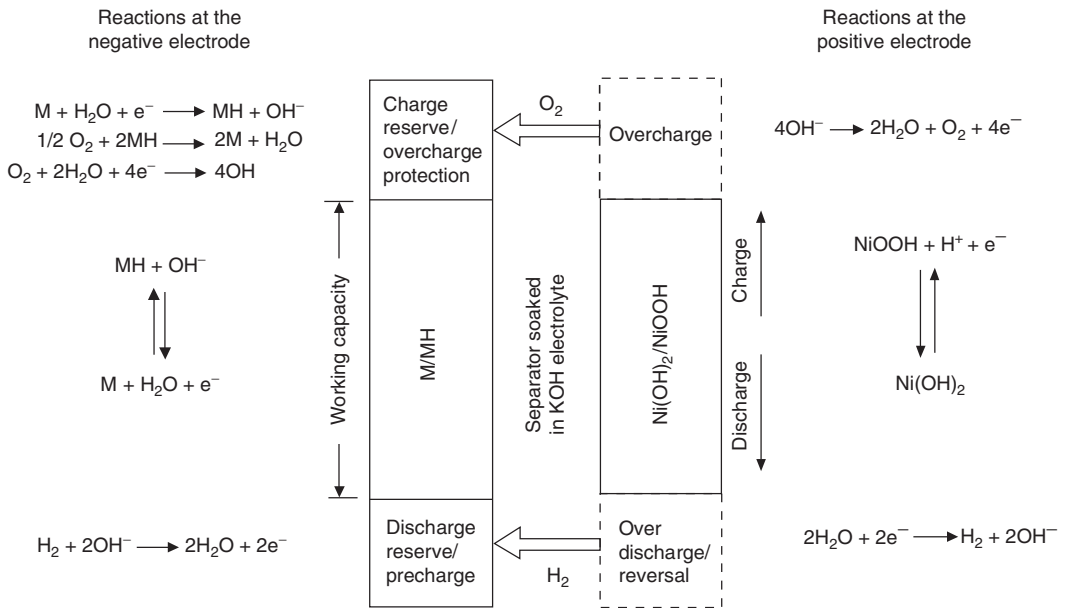

Figure 1 Operating principle of a sealed Ni–MH cell. Reproduced from Shukla AK, Venugopalan S, and Hariprakash B (2001) Nickel-based rechargeable batteries. *Journal of Power Sources* 100: 125–148.

over the charge–discharge cycles. This is an attractive feature of Ni–MH batteries over nickel–cadmium batteries in which water is generated during charge and consumed during discharge. On the down-side, Ni–MH batteries deliver less power, have a faster self-discharge, and are less tolerant to overcharge (like the nickel–cadmium batteries).

Because the nickel oxide electrode is thermodynamically unstable in the cell environment, oxygen evolution occurs at this electrode as a parallel and competing reaction. The parasitic reactions during cell charge are

$$4OH^- \rightarrow 2H_2O + O_2 + 4e^- \qquad [II]$$

and

$$MH + MH \rightarrow 2M + H_2\uparrow \qquad [III]$$

To ensure proper functioning of a sealed Ni–MH cell under varying conditions, it is designed to be limited by the positive electrode with negative to positive capacity ratio varying between 1.5 and 2. Typically, the discharge reserve is kept at about 20% of the positive capacity. Accordingly, oxygen evolution occurs at the positive electrode during overcharging, which diffuses to metal hydride electrode and combines to form water as shown in the following:

$$4OH^- \rightarrow 2H_2O + O_2 + 4e^- \qquad [IV]$$

$$M + H_2O + e^- \rightarrow MH + OH^- \qquad [V]$$

$$4MH + O_2 \rightarrow 4M + 2H_2O \qquad [VI]$$

Under deep discharge conditions, owing to inevitable differences in storage capacities of series-connected cells in a Ni–MH battery, hydrogen evolution occurs at the positive electrode and it is oxidized to water at the MH electrode. Accordingly, there are recombination mechanisms for both hydrogen and oxygen gases evolved during overdischarge and overcharge, respectively, which facilitate sealed operation of the Ni–MH cells. The following reactions occur during the cell overdischarge:

$$H_2O + e^- \rightarrow \tfrac{1}{2}H_2 + OH^- \qquad [VII]$$

and

$$\tfrac{1}{2}H_2 + OH^- \rightarrow H_2O + e^- \qquad [VIII]$$

Accordingly, there is no net change in the electrolyte concentration or quantity in the cell. Maintenance of electrolyte concentration results in good gas recombination, good high- and low-temperature operations, and good resistance to cycle-life limitations caused by corrosion and swelling. Akin to Ni–Cd cells, the temperature coefficient of electromotive force (EMF) (dE/dT factor) happens to be negative for Ni–MH cells (*see* **Secondary Batteries – Nickel Systems:** Nickel–Cadmium: Overview).

Performance Characteristics

Nickel–metal hydride cells are generally available in 'AA', 'sub-C', and 'C' sizes. Prismatic cells up to 250 Ah are manufactured for EV application by Ovonic Battery Company (USA) and Gold Peak Industries (Hong Kong). The capacity that can be obtained from a Ni–MH cell is about two times of an equivalently sized Ni–Cd cell. Nickel–metal hydride cells can operate in the temperature range of −20 to 45 °C. But above 45 °C, the charge efficiency falls steeply. The charge efficiency of Ni–MH cell is better than that of Ni–Cd cells for charge rates between $C/10$ and $C/20$ at 20 °C. The voltage and temperature profiles during charge at various rates are shown in **Figure 2**, and typical voltage profiles during cell charge at different temperatures are depicted in **Figure 3**. The internal pressure of the cell is generally observed to be below 50 psi for $C/10$ charge at 20 °C. The typical profiles of internal pressure during charge at various rates are shown in **Figure 4**. The cell pressure increases both at higher charge rates and at higher temperatures. Cylindrical cells are provided with a safety vent operating at around 400 psi. Because of the endothermic nature of the discharge process, the heat evolved during discharge is relatively less than Ni–Cd cells at discharge rates below 1 *C*. Joule heating masks the cooling because of endothermic desorption of hydrogen during discharge. Nickel–metal hydride cells can be discharged even at 5 *C* rate. The dependence of the discharge rate and the discharge capacity is depicted in **Figure 5** and the effect of temperature on available capacity is shown in **Figure 6**.

The absorption of hydrogen during charge is an exothermic process. But the rise in temperature becomes noticeable only from the point where oxygen recombination begins to occur. During hydriding, the electronic conductivity of metal hydride decreases. If the overcharge is controlled, then the heat generation in the cells happens to be mainly due to Joule heating. Cells can be charged at 1 *C* rate. The inflection of charge voltage is considered to be the most appropriate method for preventing overcharge and it improves the cycle life of the cell. A cycle life >1000 cycles at 100% depth of discharge (DoD) has been demonstrated. Cycling at $C/3$ (charge for 65 min and $C/1.6$ discharge for 35 min) at 40% DoD with an overcharge factor of 1.02 at 22 °C has been demonstrated for over 8000 cycles. Under similar conditions, a Ni–H_2 cell requires 1.1 overcharge factors. Nickel–metal hydride cells have a higher rate of self-discharge in relation to Ni–Cd cells.

Highly facile oxygen recombination reaction at MH alloy electrode can accelerate the decomposition of positive active material and gaseous hydrogen in equilibrium with the metal hydride alloy can reduce the charged positive electrode as shown below:

$$2NiOOH + H_2 \rightarrow 2Ni(OH)_2 \qquad [IX]$$

It is noteworthy that hydrogen oxidation is inhibited by anodically formed $Ni(OH)_2$/NiOOH. But cathodically deposited nickel hydroxide does not inhibit the reaction to the same degree. Shuttle reactions owing to the presence of impurities, such as nitrate present in the electrodes and the electrolyte, contribute to self-discharge to a significant extent in a fresh cell.

Oxidation of organic impurities that are extracted or leached out from the separator at the positive electrode also contributes to self-discharge process. Metal ions leached out from the MH alloy may have adverse reaction at the positive electrode. It is reported that the main contributing factor to the decomposition of conventional polyamide separator is the production of ammonia and amine, which participate in shuttle reactions similar to NO_3^- ions in Ni–Cd battery (*see* the section

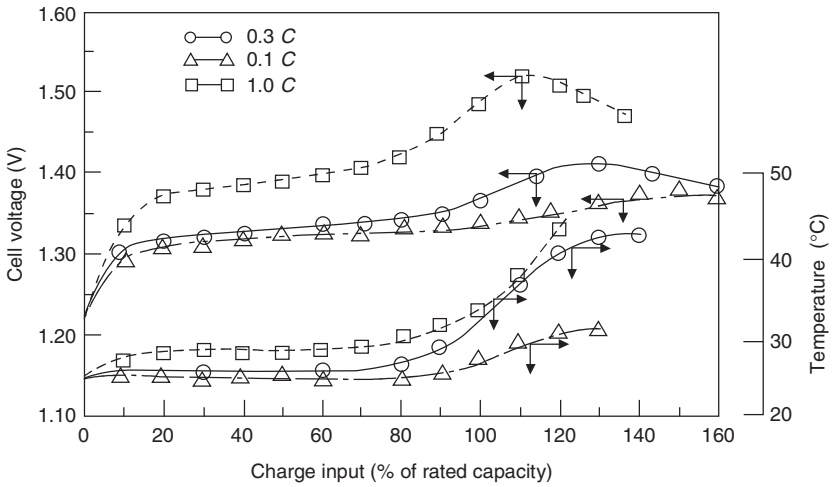

Figure 2 Typical voltage and temperature profiles for a Ni–MH cell during its charging at various rates. Reproduced from Shukla AK, Venugopalan S, and Hariprakash B (2001) Nickel-based rechargeable batteries. *Journal of Power Sources* 100: 125–148.

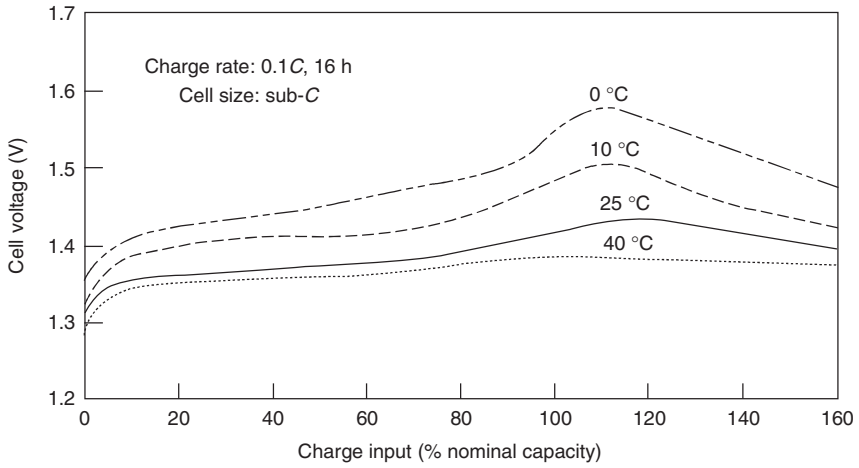

Figure 3 Voltage profiles for a Ni–MH cell during its charging at different temperatures. Reproduced from Shukla AK, Venugopalan S, and Hariprakash B (2001) Nickel-based rechargeable batteries. *Journal of Power Sources* 100: 125–148.

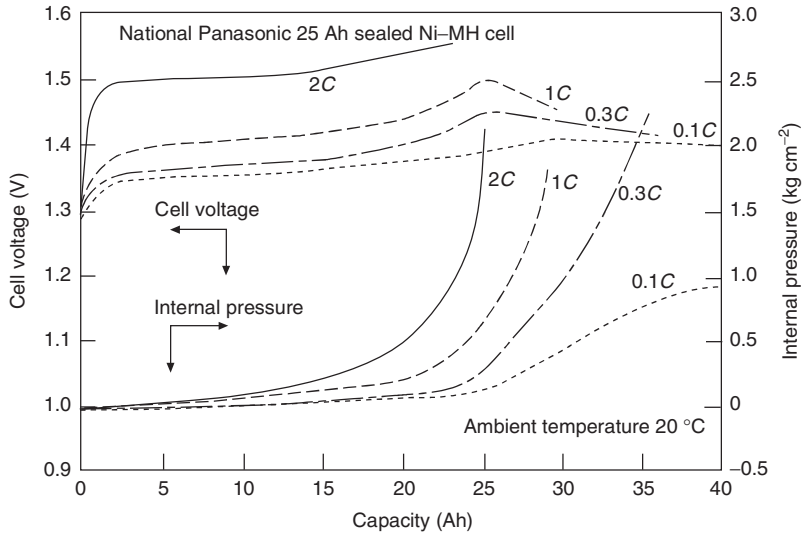

Figure 4 Pressure profiles for a Ni–MH cell during its charging at various rates. Reproduced from Shukla AK, Venugopalan S, and Hariprakash B (2001) Nickel-based rechargeable batteries. *Journal of Power Sources* 100: 125–148.

under **Secondary Batteries – Nickel Systems:** Nickel–Cadmium: Overview). The charge retention can be drastically improved by using chemically stable separators such as sulfonated polypropylene. **Figure 7** depicts the comparison of charge retention characteristics of Ni–MH cells while using different separator materials. Addition of aluminum and zirconium improves the charge retention in AB_5-type alloys.

Current Status, Opportunities, and Challenges

A very common problem with hydrogen storage materials is severe volume expansion during charge–discharge process, leading to cracking and pulverization of the alloy and making it amenable to oxidation. In addition, dissolution of the alloy in the electrolyte contributes to capacity decay. Present materials science strategies are concentrated in combining different phases and microstructures to overcome shortcomings associated with the bulk metal hydrides. To increase rate capability, materials with high surface area are being produced by powder metallurgy, mechanical alloying, and chemical/electrochemical etching. All the materials with high surface area invariably suffer from lower cycle life owing to the increased oxidation of their surfaces. Metal hydride electrodes are susceptible to widespread cracking and irreversible oxidation, which affect their cycle life, stability, and rate capability. Metallurgical processes such as encapsulation (electroless plating of copper and nickel),

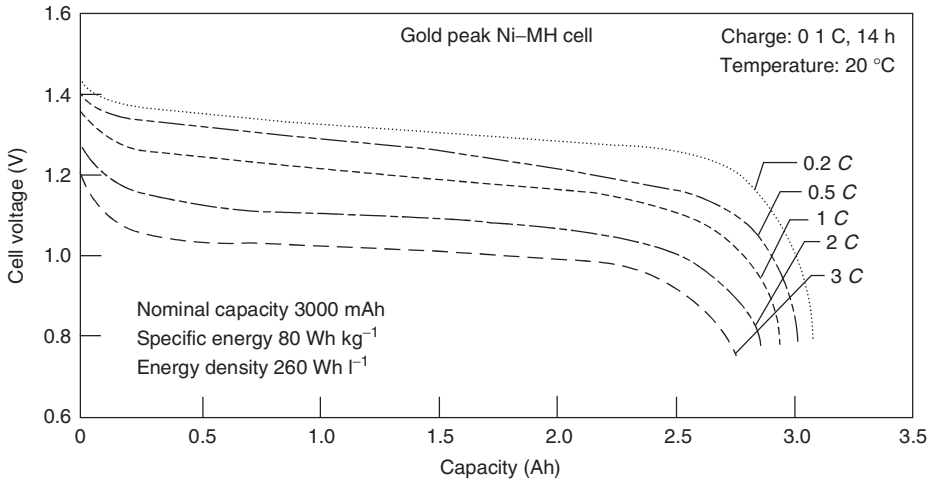

Figure 5 Effect of discharge rates on the capacity of a Ni–MH cell. Reproduced from Shukla AK, Venugopalan S, and Hariprakash B (2001) Nickel-based rechargeable batteries. *Journal of Power Sources* 100: 125–148.

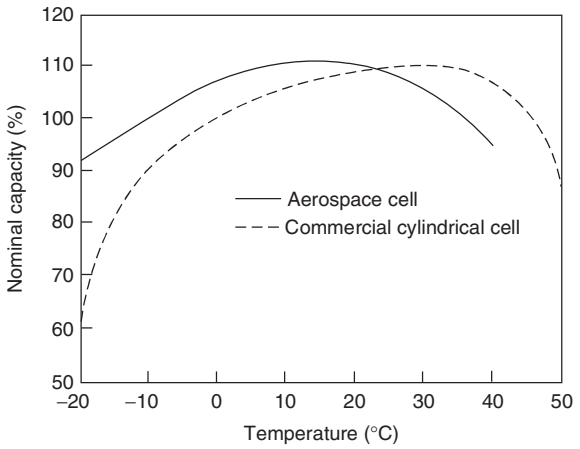

Figure 6 Effect of temperatures on the capacity of Ni–MH cells. Reproduced from Shukla AK, Venugopalan S, and Hariprakash B (2001) Nickel-based rechargeable batteries. *Journal of Power Sources* 100: 125–148.

doping with palladium and cerium, rapid solidification, and macroalloying have shown only a limited success in reducing the rate of degradation. Pure $LaNi_5$ electrodes in contact with potassium hydroxide vapor undergo brittle fracture during hydriding, resulting in rapid decay of capacity with cycling. Cobalt addition with aluminum or silicon has been found to significantly improve the cycling behavior of Ni–MH cells. Laboratories around the world have exhausted nearly all the elements in the periodic table to synthesize various AB_2 and AB_5 alloys in their efforts to improve the cycle life and capacity of metal hydride cells.

The major problem with metal hydride electrodes is that the function of the alloying elements either acting alone or in combination with other alloying elements cannot be predicted with certainty. Conventional AB_5 and AB_2 alloys based on $LaNi_5$ and (Ti, Zr)Ni_2 have relatively low coulombic capacity values between 300 and 450 Ah kg^{-1} and, hence, the present-day research has focused on alloys such as $TiZrNi_2$ and Mg_2Ni as low-cost, lightweight, and safer alternatives. In order to increase the energy density of the Ni–MH battery, it is mandatory to improve the performance of metal hydride electrodes. With a combination of modifications in the alloy composition and new methods of electrode preparation, discharge capacities between 630 and 780 Ah kg^{-1} have been achieved at a discharge current density of 50 A kg^{-1} for the magnesium-based $Mg_{1.9}Al_{0.1}Ni_{0.8}Co_{0.1}Mn_{0.1}$ alloy electrodes. An amorphous structure appears to be central in achieving high discharge capacities. These results indicate that the kinetics of hydriding/dehydriding reactions of magnesium-based alloy electrodes can be greatly improved by ball milling and chemical coating. Efforts are therefore being directed toward maintaining particle-to-particle electrical contact by the use of polymer binders, compaction of porous nickel foam, surface plating, and doping and compaction with conductive powders.

The specific energy of Ni–MH batteries can vary from 40 to 110 Wh kg^{-1} depending on the requirement. For example, where device runtime is paramount, Ni–MH batteries need not have high-power capability. On the other hand, for extremely high power charge and discharge requirements, factors that affect the specific energy of Ni–MH batteries are: (a) extra current collection, (b) high N/P ratios (proportion of excess negative electrode capacity to positive electrode capacity), and (c) specific cell design and construction.

Table 1 presents evolution in specific energy values of Ni–MH batteries during the last 10 years in consumer cylindrical Ni–MH cells for portable power. The specific energy of Ni–MH batteries is kept between 90 and 110 Wh kg^{-1} for portable power applications, between 65 and 80 Wh kg^{-1} for EV batteries, and between 45 and

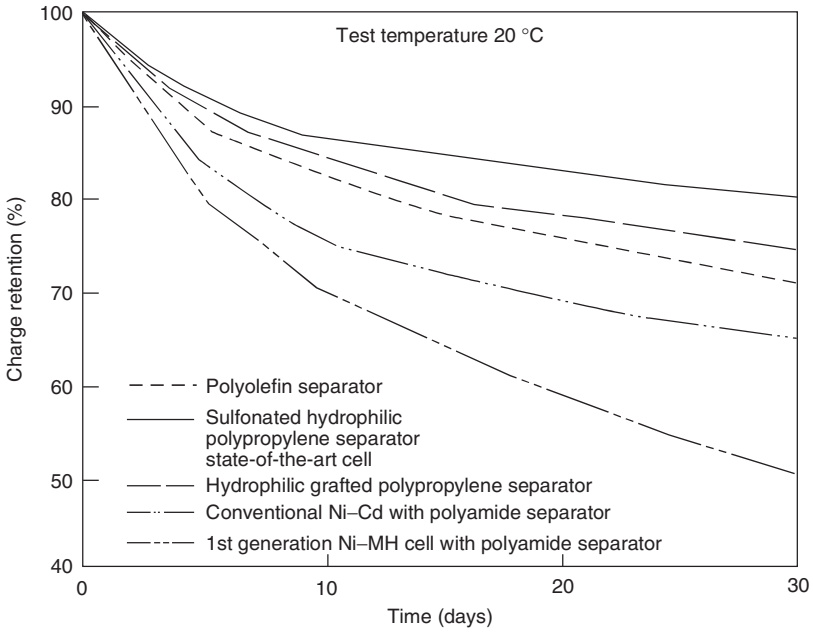

Figure 7 A comparison of charge retention characteristics of Ni–MH cells with different separators. Reproduced from Shukla AK, Venugopalan S, and Hariprakash B (2001) Nickel-based rechargeable batteries. *Journal of Power Sources* 100: 125–148.

Table 1 Evolution in specific energy and energy density values of Ni–MH batteries

Year	*Specific energy (Wh kg^{-1})*	*Energy density (Wh L^{-1})*	*Ni–MH AA cell capacity (mAh)*
1991	*54*	*190*	*1100*
1993	70	235	1400
1996	80	255	1600
2000	92	300	1900
2002	95	345	2100
2003	102	385	2300
2005	107	428	2600

Source: Reproduced from Fetcenko MA, Ovshinsky SR, Reichman B, et al. (2007) Recent advances in NiMH battery technology. *Journal of Power Sources* 165: 544–551.

60 Wh kg^{-1} for hybrid electric vehicle (HEV) and other high-power applications. Although gravimetric energy density is imperative for advanced battery technologies, in many cases volumetric energy density (Wh L^{-1}) happens to be more important. It has been possible to achieve energy density values as high as 420 Wh L^{-1}. Cost reduction is at the center stage of Ni–MH battery development. In recent years, high-volume battery production has pushed the cost of Ni–MH batteries below that of Ni–Cd batteries.

Table 2 shows the evolution in the specific-power values of Ni–MH batteries. Persistent efforts to engineer the surface oxide have vastly improved the low-temperature performance. The oxide forms a support matrix on ultrafine metallic catalysts but contains insufficient pore structure to allow rapid transfer of reactants at low temperatures. By realizing increased porosity and specifically sized pore channels, low-temperature power density of Ni–MH batteries has increased from practically zero at -30 °C to over 300 W kg^{-1}. Excellent high-temperature performance was obtained for a cobalt-rich zinc-poor powder containing coprecipitated calcium and magnesium. Nickel–metal hydride battery charging efficiency at 65 °C was increased from 36% to 85% by formulating the nickel hydroxide active material so as to suppress oxygen evolution. By introducing extremely small metallic nickel alloy inclusions throughout the surface oxide of the metal hydride alloy by the method of preferential corrosion, the catalytic activity was significantly increased through reduced charge transfer resistance and a specific power of 1900 W kg^{-1} was attained.

Conclusions

The performance of Ni–MH batteries has seen continuous improvements over the years since their inception in 1991 through a variety of novel approaches such as high-density negative electrodes, thinner separators, upgraded positive electrodes, and improved packaging efficiencies. At present, Ni–MH batteries are being produced in high volumes for portable power applications with an annual worldwide production of over 1 billion cells. Nickel–metal hydride batteries have now become proven power source for HEVs. In addition to the essential performance targets of energy, power, cycle life, and operating temperatures, flexible vehicle packaging, easy application to series and series/parallel strings,

Table 2 Evolution in specific power values of Ni–MH batteries

State of charge	*Specific power (W kg^{-1})*						
	1991	*1993*	*1996*	*1999*	*2000*	*2002*	*2003*
100	170	340	770	1060	1280	1650	1780
80	150	330	710	1000	1290	1900	1990
50	140	320	630	950	1280	1880	1960
20	120	260	500	800	1090	1580	1630

Source: Reproduced from Fetcenko MA, Ovshinsky SR, Reichman B, et al. (2007) Recent advances in NiMH battery technology. *Journal of Power Sources* 165: 544–551.

choice of cylindrical/prismatic cells, safety, tolerance to electrical and mechanical abuse, maintenance-free operation, ability to utilize regenerative braking energy, simple and less expensive charging and electronic control circuits, and environmentally acceptable and recyclable materials have established the eminence of Ni–MH batteries. However, the declining costs and mounting performances of secondary lithium batteries are threatening to replace Ni–MH batteries.

Nomenclature

Symbols and Units

C	rate capacity
E	voltage
E_{cell}	cell voltage
T	temperature

Abbreviations and Acronyms

DoD	depth of discharge
EMF	electromotive force
EV	electric vehicle
HEV	hybrid electric vehicle
SHE	standard hydrogen electrode

See also: **Recycling:** Nickel–Metal Hydride Batteries; **Secondary Batteries – Nickel Systems:** Electrodes: Nickel; Nickel–Cadmium: Overview; Nickel–Cadmium: Sealed; Nickel–Hydrogen.

Further Reading

Cui N, Luo JL, and Chuang KT (2000) Nickel–metal hydride (Ni–MH) battery using Mg_2Ni-type hydrogen storage alloy. *Journal of Alloys and Compounds* 302: 218–226.

Davolio G and Sorangi E (1998) The 'memory effect' on nickel oxide electrodes: Electrochemical and mechanical aspects. *Journal of Applied Electrochemistry* 28: 1313–1319.

Dhar SK, Ovshinsky SR, Gifford PR, Corrigan DA, Fetcenko MA, and Venkatesan S (1997) Nickel/metal hydride technology for consumer and electric vehicle batteries – a review and up-date. *Journal of Power Sources* 65: 1–7.

Fetcenko MA, Ovshinsky SR, Reichman B, et al. (2007) Recent advances in NiMH battery technology. *Journal of Power Sources* 165: 544–551.

Fukunaga H, Kishimi M, Matsumoto N, Ozaki T, Sakai T, Tanaka T, and Kishimoto N (2005) A nickel electrode with Ni-coated 3D steel sheet for hybrid electric vehicle applications. *Journal of the Electrochemical Society* 152: A905–A912.

Furukawa N (1994) Development and commercialization of nickel–metal hydride secondary batteries. *Journal of Power Sources* 51: 45–59.

Gifford P, Adams J, Corrigan D, and Venkatesan S (1999) Development of advanced nickel/metal hydride batteries for electric and hybrid vehicles. *Journal of Power Sources* 80: 157–163.

Ikoma M, Hoshina Y, Masumoto I, and Iwakura C (1996) Self-discharge mechanism of sealed-type nickel/metal–hydride battery. *Journal of the Electrochemical Society* 143: 1904–1907.

Kohler U, Antonius C, and Bauerlein P (2004) Advances in alkaline batteries. *Journal of Power Sources* 127: 45–52.

Kohno T, Yamamoto M, and Kanda M (1999) Electrochemical properties of mechanically ground Mg_2Ni alloy. *Journal of Alloys and Compounds* 293–295: 643–647.

Kritzer P (2004) Separators for nickel metal hydride and nickel cadmium batteries designed to reduce self-discharge rate. *Journal of Power Sources* 137: 317–321.

Kuriyama N, Sakai T, Miyamura H, and Ishikawa H (1992) Solid state metal hydride batteries using tetramethylammonium hydroxide pentahydrate. *Solid State Ionics* 53–56: 688–693.

Leblanc P, Blanchard P, and Senyarich S (1998) Self-discharge of sealed nickel–metal hydride batteries. *Mechanisms and Improvements. Journal of the Electrochemical Society* 145: 844–847.

Linden D and Reddy TB (2002) *Handbook of Batteries,* 3rd edn. New York: McGraw-Hill.

Morioka Y, Narukawa S, and Itou T (2001) State-of-the-art alkaline rechargeable batteries. *Journal of Power Sources* 100: 107–116.

Ohms D, Kohlhase M, Benczur-Urmossy G, and Schadlich G (2002) New developments on high power alkaline batteries for industrial applications. *Journal of Power Sources* 105: 127–133.

Ovshinsky SR, Fetcenko MA, and Ross J (1993) A nickel metal hydride battery for electric vehicle. *Science* 260: 176–181.

Pistoia G (2005) *Batteries for Portable Devices*. New York: Elsevier.

Potter BG, Duong TQ, and Bloom I (2006) Performance and cycle life test results of a PEVE first-generation prismatic nickel/metal-hydride battery pack. *Journal of Power Sources* 158: 760–764.

Rand DAJ, Woods R, and Dell RM (1998) *Batteries for Electric Vehicles*. England: Research Studies Press.

Shinyama K, Magari Y, Akita H, et al. (2005) Investigation into the deterioration in storage characteristcs of nickel–metal hydride batteries during cycling. *Journal of Power Sources* 143: 265–269.

Shukla AK, Venugopalan S, and Hariprakash B (2001) Nickel-based rechargeable batteries. *Journal of Power Sources* 100: 125–148.

Sun L, Liu HK, Bradhurst D, and Dou SX (1999) The electrode properties of $Mg_{1.9}Al_{0.1}Ni_{0.8}Co_{0.1}Mn_{0.1}$ alloy by mechanical grinding with Ni powders. *Electrochemical and Solid-State Letters* 2: 164–166.

Taniguchi A, Fujioka N, Ikoma M, and Ohta A (2001) Development of nickel/metal-hydride batteries for EVs and HEVs. *Journal of Power Sources* 100: 117–124.

Vincent CA and Scrosati B (1997) *Modern Batteries* 2nd edn. London: Arnold.

Weinstock IB (2002) Recent advances in the US Department of Energy's energy storage technology research and development programs for hybrid electric and electric vehicles. *Journal of Power Sources* 110: 471–474.

Yang C-C (2002) Polymer Ni–MH battery based on PEO-PVA-KOH polymer electrolyte. *Journal of Power Sources* 109: 22–31.

Yang X-G and Liaw BY (2004) Numerical simulation on fast charging nickel metal hydride traction batteries. *Journal of the Electrochemical Society* 151: A265–A272.

SECONDARY BATTERIES – NICKEL SYSTEMS

Contents

Electrodes: Nickel

AK Shukla, Indian Institute of Science, Bangalore, India
B Hariprakash, Indocel Technologies Private Limited, Bangalore, India

Introduction

Nickel electrodes constitute the positive plates of various nickel-based storage batteries, namely nickel–iron, nickel–cadmium, nickel–hydrogen, nickel–metal hydride, and nickel–zinc rechargeable batteries. The operating principles, crystal chemistry, and various stages of development of nickel electrodes are described in this article.

Electrochemistry of Nickel Electrode

In the battery technology, the nickel electrode is often referred to as a nickel oxide (NiO_2) electrode and the charge–discharge reactions on the nickel electrode are expressed as

$$NiO_2 + 2H_2O + 2e^- \underset{\text{charge}}{\overset{\text{discharge}}{\rightleftarrows}} Ni(OH)_2 + 2OH^-, \quad E^o = 0.49\ V \qquad [I]$$

Nickel oxide forms the active material of the positive plate with nickel hydroxide as the discharged product, which is retrieved as nickel oxide during recharge. In practice, however, β-$Ni(OH)_2$ is the discharge product and is converted to beta nickel oxyhydroxide (β-NiOOH) during recharge. Accordingly, eqn [I] becomes

$$\beta\text{-NiOOH} + H_2O + e^- \underset{\text{charge}}{\overset{\text{discharge}}{\rightleftarrows}} \beta\text{-}Ni(OH)_2 + OH^-, \quad E^o = 0.49\ V \qquad [II]$$

The standard electrode potential (E^o) for the nickel positive electrode is given by the Nernst relationship, namely

$$E^o = 0.49 - 0.059 \log \frac{a_{[Ni(OH)_2]}\, a_{[OH^-]}}{a_{[NiOOH]}\, a_{[H_2O]}} \qquad [1]$$

where a is the activity of the respective species. One can also write β-$Ni(OH)_2$ as H_2NiO_2 and β-NiOOH as $HNiO_2$, and both of these can be expressed by the general formula H_xNiO_2, where $x = 2$ refers to β-$Ni(OH)_2$ and $x = 1$ refers to β-NiOOH. The oxidation state of nickel is $+2$ in β-$Ni(OH)_2$ and $+3$ in β-NiOOH. On prolonged charging, β-NiOOH transforms irreversibly to γ-NiOOH, in which the oxidation state of nickel is $+3.7$ so that the compound may be expressed as $H_{0.3}NiO_2$. The mechanism of reaction [II] involves an equivalent diffusion of protons through the solid-state lattices of β-$Ni(OH)_2$ and β-NiOOH such that there is a continuous change in the composition of the active material between the fully charged β-NiOOH and the fully discharged β-$Ni(OH)_2$. Consequently, eqn [II] may also be written as

$$\beta\text{-NiOOH} + H^+ + e^- \underset{\text{charge}}{\overset{\text{discharge}}{\rightleftarrows}} \beta\text{-}Ni(OH)_2 \qquad [III]$$

Proton diffusion is the limiting mechanism in the oxidation of nickel hydroxide and nickel oxyhydroxide. Reported values for the diffusion coefficient of the protons range from 10^{-8} to $10^{-13}\,cm^2\,s^{-1}$. It has been found that

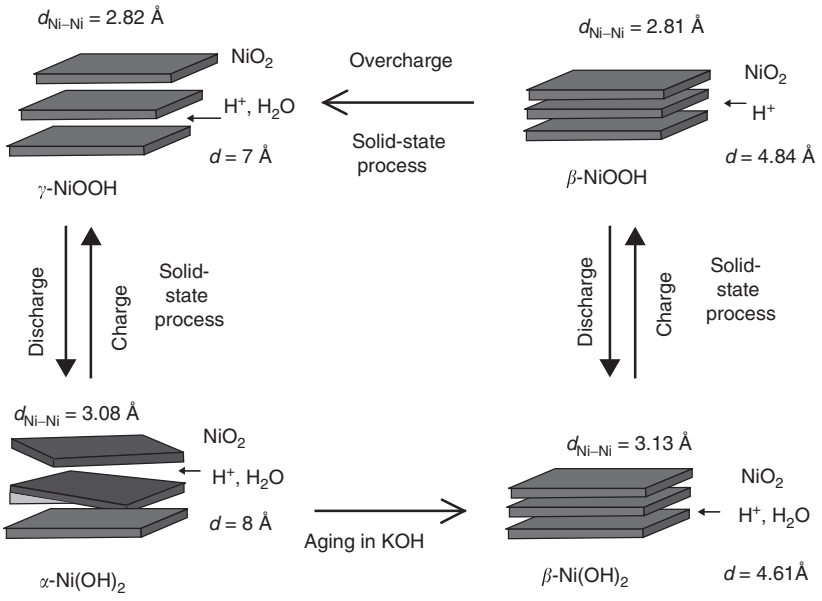

Figure 1 Bode diagram showing transformations among various phases of nickel positive electrode. Reproduced from Bode H, Dehmelt K, and Witte J (1966) Zur kenntnis der nickelhydroxidelektrode – I. Uber das nickel(II)-hydroxidhydrat. *Electrochimica Acta* 11: 1079–1087.

the proton diffusion coefficient is a strong function of the state-of-charge of the electrode and decreases from 4.4×10^{-8} to $6.4 \times 10^{-11}\,cm^2\,s^{-1}$ when the electrode is discharged from its fully charged state. Polarization losses due to diffusional limitations of protons are critical in determining the characteristics of the discharge curve. The electrochemical efficiency of β-$Ni(OH)_2$ is associated with the number of proton vacancies in the crystal lattice. These vacancies shift the oxidation potential of β-$Ni(OH)_2$ toward less positive values and thereby improve the chargeability, and hence the electrochemical efficiency, of nickel hydroxide.

As shown in the Bode diagram (Figure 1), γ-NiOOH is electrochemically reversible with α-$Ni(OH)_2$. As a larger number of electrons are exchanged per nickel atom during the $\alpha \rightleftarrows \gamma$ phase transition, a higher theoretical capacity is expected for a nickel positive electrode comprised of α-$Ni(OH)_2$ rather than β-$Ni(OH)_2$. In an alkaline medium, however, α-$Ni(OH)_2$ transforms to β-$Ni(OH)_2$ on aging. Efforts are therefore being expended to synthesize alkali-stable α-$Ni(OH)_2$, which has a turbostratic layered structure with an interlayer spacing of ~ 8 Å along its c-axis as against only 4.6 Å in the case of β-$Ni(OH)_2$ (see Figure 1).

Crystal Chemistry and Performance Characteristics of $Ni(OH)_2$

Nickel hydroxide has three crystalline modifications, all of which appear in the form of a lattice structure with alternate layers of nickel ions and hydroxide ions. These form interlamellar channels for the migration of protons, water, hydroxide, and foreign ions. The isomorphs differ in their stoichiometry. It is considered that the α-form is the starting material for the transformation of the alkaline electrode. On electrochemical preparation of nickel nitrate ($Ni(NO_3)_2$), the product α-$3Ni(OH)_2 \cdot 2H_2O$ is formed, in which the water of hydration is an integral part of the crystal structure. An interlayer of water increases the lattice distance between hydroxide layers in the α-hydroxide. On oxidation, this compound is converted to β-NiOOH, which is commonly found in battery plates that have been subjected to repeated cycling. The transformation is accompanied by a change of density from 2.50 to $3.85\,g\,cm^{-3}$. In concentrated potassium hydroxide, the γ-modification is obtained and potassium ions are incorporated in the lattice structure, for which the composition is given as $Ni_4O_4(OH)_4O_{1.5}(OH)_{0.5}K$. The K^+ ions in the lattice prevent complete reduction of γ-NiOOH to nickel hydroxide.

The volumetric capacity has been significantly improved by the development of spherical nickel hydroxide with high tap densities. Long-time stability and reversibility of spherical nickel hydroxide in an alkaline electrolyte are, however, still a cause of concern. This is particularly true for sealed cells, in which swelling of the nickel electrode after repeated overcharge dries out the electrolyte from the separator. The latter phenomenon is due to intercalation of water molecules into the nickel electrode and is mainly responsible for the degradation in the performance of both Ni–Cd and

Ni–MH batteries. Recently, stabilized α-$Ni(OH)_2$ has attracted much attention as active material for the positive plate in nickel-based batteries. Partial substitution of nickel cations with trivalent cations such as aluminum, cobalt, or iron (>20 wt%) stabilizes the α-form of the double-layered nickel hydroxide. Stabilized α-$Ni(OH)_2$ is prepared by electrochemical impregnation in a mixed metal nitrate bath. Aluminum-stabilized α-$Ni(OH)_2$ is the material of choice as it not only exhibits a higher specific electrochemical capacity, but also experiences a negligible change in electrode volume during cycling between the α- and γ-forms. The latter phenomenon is attributed to the low absorption of water molecules during cycling. For α- to γ-phase conversion, the average oxidation state of nickel in γ-NiOOH is reported to be 3.67. This corresponds to a theoretical specific capacity of 482 mAh g^{-1}, which is 66% higher than that observed for the conversion of β(III)-NiOOH to β(II)-$Ni(OH)_2$, namely 289 mAh g^{-1}. The theoretical specific capacity of the β-form is almost reached in practical batteries, and this leaves room for only marginal improvements. If the theoretical capacity of the α-phase could be more fully utilized, it would compensate for its lower tap density.

Thin films of nickel hydroxide are known to exchange 1.67 electrons per nickel atom. Nickel hydroxide doped with cobalt is reported to deliver a specific capacity of between 345 and 375 mAh g^{-1}, which corresponds to the transfer of 1.2–1.3 electrons per metal (nickel, cobalt) atom. A new hydrothermal synthetic route to produce aluminum-stabilized α-$Ni(OH)_2$ with extremely fine grain size but good crystallinity has recently been evaluated. The results show that nanosized α-$Ni(OH)_2$ with well-crystallized particles not only exhibits a high specific capacity of up to ~400 mAh g^{-1}, but also provides an excellent high-rate discharge capability with prolonged stability both during electrochemical cycling with up to 100% overcharge and during long-term float charge. By contrast, β-$Ni(OH)_2$ has lower specific capacity and poorer cycling stability under similar overcharge cycling. Despite a lower energy density than the β-phase (~500 mAh cm^{-3}), other features make the aluminum-stabilized α-$Ni(OH)_2$ a superior battery material. There is scope to increase the energy density of the α-phase by improving its tap density.

The low solubility product ($K_{sp} = 10^{-35}$) of nickel hydroxide makes it highly stable in alkaline medium. Although the solubility of nickel hydroxide active material in concentrated potassium hydroxide solutions is significantly low, it cannot be ignored. Recently, it has been shown that the charge efficiency of a nickel electrode stored in the discharged state can be considerably lowered owing to Oswald ripening of β-$Ni(OH)_2$ through a dissolution–precipitation reaction. The process is reversible and the material can be brought back to its original crystal form through repeated charge–discharge cycling.

Oxygen Evolution Reaction at Nickel Electrode

The oxidation state of nickel and its relative stability in its charge and overcharge states are of particular importance in battery operation, in conjunction with the oxygen evolution reaction. Under standard conditions, the nickel positive electrode reaction

$$Ni(OH)_2 + OH^- \rightleftarrows NiOOH + H_2O + e^- \qquad [IV]$$

has an $E^o = 0.41$ V versus Hg | HgO, OH^- (6 M potassium hydroxide) as compared with $E^o = 0.31$ V for the oxygen evolution reaction:

$$4OH^- \rightleftarrows O_2 + 2H_2O + 4e^- \qquad [V]$$

During the battery operation, however, oxygen evolution takes place at a much higher overpotential owing to the presence of impurities or additives.

A freshly charged positive electrode undergoes fairly fast self-discharge owing to the instability of the higher oxidation state of nickel (NiO_2) formed toward the end of charge. Charged positive active material is thermodynamically unstable and can spontaneously decompose with evolution of oxygen according to the reaction

$$2NiOOH + H_2O \rightarrow 2Ni(OH)_2 + \tfrac{1}{2}O_2 \qquad [VI]$$

After termination of charge, gas evolution continues with decomposition of the charged active material. The rates of decomposition of the charged active material at the nickel electrode and recombination of the oxygen gas at the negative electrode depend on the temperature, the structure of the active material, and other factors such as the interelectrode spacing and the presence of gas diffusion membranes, such as cellophane.

The mechanism of oxygen evolution in an alkaline medium at nickel electrodes includes a chemical association step between OH_{ads} and OH^-, and two electrochemical steps, one of discharge of OH^- and the other of discharge of O^-_{ads}, represented by

$$OH^- \rightleftarrows OH_{ads} + e^- \qquad [VII]$$

$$OH_{ads} + OH^- \rightleftarrows O^-_{ads} + H_2O \qquad [VIII]$$

$$O^-_{ads} \rightleftarrows O_{ads} + e^- \qquad [IX]$$

$$2O_{ads} \rightleftarrows O_2 \qquad [X]$$

Electrode Types and Their Properties

Nickel hydroxide is an amorphous colloid and is, at best, semiconducting. It must be supported and contained by a structural component that provides the electrode with a mechanical support, electrical conductivity, and a means

of current collection. Nickel electrodes can be classified depending on the type of substrate used and the method of preparation. These electrodes consist of two basic forms, namely sintered and nonsintered. Pasted nickel electrodes are most commonly used as nonsintered nickel electrodes. Each type has its own advantages and disadvantages, and may be selected according to the intended battery application. Other varieties of nickel electrodes, such as pocket plates, are generally not in common use.

Developmental work on the large-scale commercial applications of nickel electrodes was based on the pocket-plate technology initiated in Sweden, Germany, and the United States during 1897–1903. The active material is first pelletized with a conductive additive and a binder, and the pellets are then wrapped in a perforated nickel-plated steel sheet (pocket), which serves as both a current collector and a mechanical support. The tubular plate, the next major improvement in nickel electrode structure, was developed by Edison in 1908 to restrict the mechanical forces owing to swelling of the positive active mass and to extend the cycle life of the electrodes during deep-discharge duty. In tubular-plate construction, perforated nickel-plated mild-steel tubes were filled with alternating layers of nickel hydroxide and nickel flakes/graphite. The active material layers in the tube were compacted as and when they were introduced into the tube. The individual tubes had metal bands spaced at regular intervals along the length of the tube in order to control active material expansion during cycling. The tubes were then crimped at the ends. A number of tubes were arranged in parallel in a frame to form the tubular plate. Owing to the cumbersome manufacturing process and the high production cost, this technology is no longer used.

Sintered-plate technology, initiated in 1928, is considered as an important milestone in the development of nickel electrodes. Sintering is defined as a thermal process in which loose nickel particles are transformed into a coherent body at a temperature just below the melting point of nickel in a reducing atmosphere. Over 50% of the nickel-based batteries, which are currently being manufactured, use sintered electrodes for the positive plate. In sintered electrodes, a porous sintered plaque retains the positive active material within the pores and serves to conduct the electric current. Sintered plaques are produced by a wet-slurry or by a dry-powder (loose powder) process. In both procedures, the plaques are prepared by locating a pure nickel mesh or a perforated nickel-plated steel sheet centrally across the thickness of the carbonyl nickel powder (INCO 287) layer followed by sintering at temperatures between 800 and 1000 °C in a reducing atmosphere. The loose/dry powder sintering is exclusively used in the manufacture of hermetically sealed aerospace nickel–cadmium and nickel–hydrogen cells. The dry-powder process is labor intensive and hence expensive. For commercial applications, sintered plates are made from wet slurry that is pasted uniformly on both sides of a nickel-plated steel or nickel grid or another current-collecting material to a desired thickness. The viscous slurry comprises carbonyl nickel powder (INCO 255), a pore former/expander, a binder (polytetrafluoroethylene (PTFE) in general), and water. The plaque is dried to evaporate the water, and finally sintered between 800 and 1000 °C in a reducing atmosphere. The essential features of sintered plaques are high porosity, large surface area, and high electrical conductivity, in addition to good mechanical strength.

Sintered nickel electrodes are obtained by impregnating nickel plaques with nickel hydroxide active material by either a chemical or an electrochemical method. Chemical impregnation of the sintered nickel plaque involves filling the pores with aqueous $Ni(NO_3)_2$, polarizing the filled plaque in sodium hydroxide solution to convert it to nickel hydroxide rinsing, drying, and weighing. The weight pick-up is a measure of capacity and the process is repeated until the weight pick-up meets the required capacity criteria. The chemical impregnation process is time consuming and hence an alternative thermal decomposition method is used commercially. In this method, the plaques are immersed in molten nickel nitrate solution, heated to decompose the nitrate, soaked in potassium hydroxide solution, washed, and finally dried.

Electrochemical impregnation of sintered nickel plaque involves polarization of the plaque in a hot, aqueous or alcoholic solution of $Ni(NO_3)_2$ of pH 3 at a current density between 5 and 75 mA cm^{-2} to deposit nickel hydroxide active material, in a single step. An important advantage of electrochemical impregnation is that the electrodes are impregnated with active material from the inside out and this results in a uniform cross-sectional loading. The resultant electrodes display better active material utilization and high-rate capability in relation to other impregnation methods such as thermal decomposition of nickel salts. Electrochemical impregnation is typically used for space-grade nickel–cadmium and nickel–hydrogen cells. In the sintered-plate design, structural integrity is achieved without any binder in the active mass and continuity of the conductive path is accomplished without any particulate additive to the active mass. A typical example of the morphology of the sintered-type nickel substrates is illustrated in **Figure 2**.

A disadvantage of sintered nickel electrodes is that they contain a relatively low ratio of active to inactive materials compared with some types of nonsintered electrodes. Sintered electrodes typically contain as much as 60% inactive material, in the form of the porous electrode substrate and/or current collector. Practical sintered nickel electrodes yield about 100–120 mAh g^{-1},

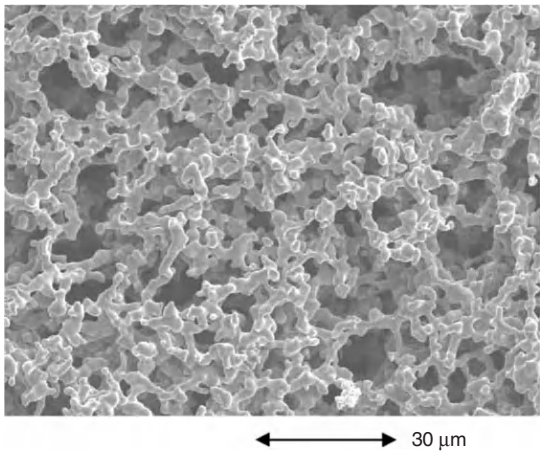

Figure 2 Morphology of sintered-type nickel substrate. Reproduced from Morioka Y, Narukawa S, and Itou T (2001) State-of-the-art alkaline rechargeable batteries. *Journal of Power Sources* 100: 107–116.

depending on the method of preparation and the degree of active material utilization; this is about 40% of the theoretical specific energy of the active material. Besides, the sintering process itself is relatively expensive and has to be carried out at high temperatures under a reducing atmosphere. The electrodes also utilize an excess amount of nickel per ampere hour, involve laborious processing, and require elaborate effluent treatment to mitigate environmental pollution.

In the pressed-plate design, nickel electrodes are fabricated either by pressing the active mass with a suitable binder (such as PTFE) and a conductive additive (such as nickel or graphite) onto a substrate of inert metal or by using a sintered (inert) metal substrate to contain the active mass in its pores. Pasted nickel electrodes consist of nickel hydroxide particles, preferably with high surface areas, in contact with a conductive network or substrate. There have been several variants of these electrodes, such as plastic-bonded nickel electrodes that utilize graphite as a conducting additive and foam-metal electrodes that employ high-porosity nickel foam as a substrate, which is loaded with spherical nickel hydroxide particles and with cobalt to enhance the conductivity. Indeed, pasted electrodes of the foam-metal type have penetrated the consumer market owing to their low cost and higher specific energy in relation to sintered nickel electrodes. It should be noted, however, that pasted electrodes suffer from relatively poor active material utilization, a tendency toward significant swelling during cycling and, consequently, relatively poor cycle life. The degree of utilization of nickel electrodes varies from 60% for the pocket/pressed plate to 90% for the sintered-plate electrodes. Conventional sintered electrodes normally have a volumetric capacity of about 500 $Ah\,L^{-1}$ as against 700 $Ah\,L^{-1}$ for foam-type nickel electrodes.

Roll-compacted, plastic-bonded nickel electrodes are preferred for large-scale applications given their economical and cost-effective production. For such electrodes to function effectively, a binder is added to provide sufficient structural integrity to the electrode while maintaining particle-to-particle contact. The commonly employed binder is PTFE and it is essential that electrolyte access to the active material is not restricted.

Plastic-bonded nickel electrodes also use a graphite composite structure that replaces the metallic nickel substrate. This modification results in electrodes with much lower metallic content and thus reduces both cost and weight. Corrosion of graphite in highly oxidizing environment of the cell is controlled by treating the carbon with nickel cobalt oxide ($NiCo_2O_4$). The increased impedance of the graphite composite electrode is partially offset by the increased surface area of carbon compared to that of the nickel powder or foam. The conductivity of carbon is also enhanced by cobalt treatment. The increased surface area provides greater interfacial contact between the active material and the carbon support and also between the active material composite structure and the electrolyte. The electrode is able to support current densities suitable for high-rate battery applications. As graphite has much lower density than nickel metal, the plastic-bonded electrode is much lighter in weight than the standard nickel counterpart for an equivalent energy storage capacity. Plastic-bonded graphite composite electrodes yield a capacity value of about 140–150 $mAh\,g^{-1}$. As graphite has a lower density, it occupies a larger volume for the same weight of metallic nickel; this results in a relatively lower energy density ($Wh\,L^{-1}$) for the electrodes.

Fiber nickel electrodes were introduced into the market in the late 1970s. These electrodes are manufactured by nickel plating a mat of synthetic fibers (graphite or plastic) by an electroless method followed by sintering under compression at 800 °C in a hydrogen atmosphere to form mats with 90% free volume. The metallized fibers form a three-dimensional structure (see **Figure 3**), which provides contact with the active material particles but remains elastic and thereby withstands volume changes during cycling. The metallized fiber substrates are mechanically impregnated with the active material, allowing production of electrodes with thicknesses between 0.6 and 10 mm without much variation in the ratio of current-conducting substrate to active mass. By virtue of their compactness and structural integrity, the electrodes offer significant improvement in specific energy, life, and cost over traditional sintered-plate cells.

Foam nickel electrodes, introduced in the mid-1980s, function in a similar manner to sintered-plate electrodes. A foam nickel substrate of high porosity and purity, known as INCOFOAM^{TM}, was developed by INCO

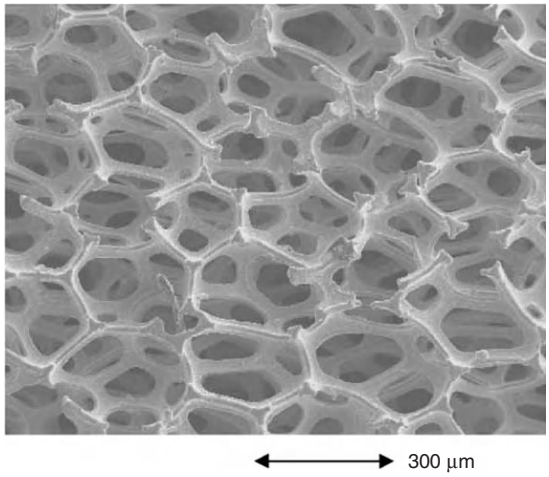

Figure 3 Fiber-electrode structure. Reproduced from Ohms D, Kohlhase M, Benczur-Urmossy G, and Schadlich G (2002) New developments on high power alkaline batteries for industrial applications. *Journal of Power Sources* 105: 127–133.

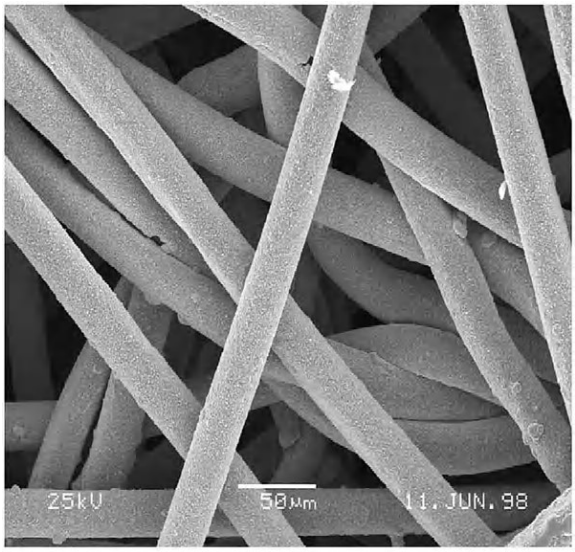

Figure 4 Morphology of foam-type nickel substrate. Reproduced from Morioka Y, Narukawa S, and Itou T (2001) State-of-the-art alkaline rechargeable batteries. *Journal of Power Sources* 100: 107–116.

(now called Vale Inco Limited). INCOFOAM is produced by nickel plating a porous synthetic material (polyurethane or acrylic fiber) followed by pyrolysis of the plastic material to obtain a nickel framework with approximately 95% free volume that facilitates the development of nickel foams of varying thicknesses and porosities to suit customer needs. The utilization of active material in these electrodes is inferior to that in sintered plates. Nevertheless, the higher pore volume and larger capacity for holding active material (which reduces the weight of the required conducting substrate) compensate for the loss in utilization efficiency and consequently improve the specific energy of the cell. The amount of active material to be incorporated into the pores of the nickel foam current collector is usually around 2.2 g cm^{-3}. The morphology typical of foam-type nickel substrates is shown in Figure 4.

Additives for Nickel Electrodes

Nickel oxide electrodes commonly employ cobalt hydroxide as a spacing agent, which is isomorphous with both β-NiOOH and β-$Ni(OH)_2$. There have been many investigations of the effect of foreign cations on the performance characteristics of nickel active material and its electrical conductivity. For instance, cobalt, lithium, cadmium, and zinc cations have all been found to be highly beneficial. Their functions are summarized in Table 1.

Nickel hydroxide active material can be formulated for specific applications. For operation at 65 °C, some manufacturers add calcium hydroxide, calcium fluoride, calcium sulfide, calcium oxide, or yttrium oxide to the paste to inhibit early oxygen evolution on charge. Calcium additives, however, may cause a loss in power and/or cycle life. For prolonged storage, it is common to increase the level of the cobalt additive to mitigate the breakdown of the conductive network and consequent isolation of the active material. For ultra-high-power discharge, metallic nickel fibers are added to the paste to enhance its conductivity. The addition of such fibers, however, lowers the amount of active material, with consequent reduction in capacity and specific energy.

Cobalt hydroxide is an ideal additive except for its increasing scarcity and high cost. Accordingly, some manufacturers have found it to be effective in reducing the cobalt content in nickel oxide electrodes. Zinc hydroxide with nickel hydroxide can provide a dimensionally stable electrode albeit with some loss in electrode utilization efficiency. Thus, nickel hydroxide active material is most commonly a triprecipitate of Ni–Co–Zn. The amount of cobalt and zinc, each usually about 1–5 wt%, can be adjusted for conductivity and oxygen overpotential with some trade-offs in terms of active material capacity and cost; the common composition is 94 wt% Ni, 3 wt% Co, and 3 wt% Zn.

Memory Effect in Nickel Electrodes

The available capacity of nickel electrodes apparently decreases under repeated partial discharge or overcharge. This phenomenon is known as the 'memory effect' and has been studied extensively. Unfortunately, no rational and consistent explanation has emerged from these

Table 1 Additives for nickel electrodes

S. No.	Function	Co	Cd	Zn	Li	As	Bi	$Cs(OH)_2$	$Rb(OH)_2$
1	Increase charge acceptance	✓	✓						
2	Inhibit self-discharge	✓				✓			
3	Prevent electrode swelling	✓	✓	✓					
4	Prevent formation of γ-NiOOH	✓	✓	✓					
5	Minimize formation cycles	✓							
6	Reduce oxidation potential of $Ni(OH)_2$	✓							
7	Reduce reduction potential of $Ni(OH)_2$	✓							
8	Increase overpotential for oxygen evolution	✓	✓	✓	✓				
9	Increase active material utilization	✓							
10	Enhance cycle life	✓						✓	✓
11	Eliminate poisoning effect of Fe (leached from substrate)				✓				
12	Stabilize α-$Ni(OH)_2$ structure						✓		

studies. For detailed discussion on this subject *see* **Secondary Batteries – Nickel Systems:** Memory Effect.

Concluding Remarks

The technology of nickel electrodes has undergone progressive improvement. Advanced nickel–metal hydride batteries for application in hybrid electric vehicles employ cost-effective, thin positive plates that are based on a nickel-coated steel-sheet substrate. The batteries exhibit a remarkable power density of $1055\,W\,kg^{-1}$ compared with $480\,W\,kg^{-1}$ achievable with conventional nickel batteries and can sustain 25 000 charge–discharge cycles during a projected hybrid electric vehicle service of 100 000 km. At present, nickel-based batteries – in particular, nickel–metal hydride batteries – are the prime choice for large-format batteries for both electric and hybrid electric vehicles.

Nomenclature

Symbols and Units

a	a thermodynamic function used in place of concentration in equilibrium constants for reactions that involve nonideal solutions and gases
d	distance
E^o	standard electrode potential (V)
K_{sp}	solubility product

Abbreviations and Units

PTFE	polytetrafluoroethylene

See also: **Secondary Batteries – Nickel Systems:** Memory Effect.

Further Reading

Arvia AJ and Posadas D (1975) Nickel. In: Bard AJ (ed.) *Encyclopedia of Electrochemistry of the Elements*, vol. III, pp. 211–421. New York: Marcel Dekker, Inc.

Bernard MC, Cortes R, Keddam M, Takenouti H, Bernard P, and Senyarich S (1996) Structural defects and electrochemical reactivity of β-$Ni(OH)_2$. *Journal of Power Sources* 63: 247–254.

Bode H, Dehmelt K, and Witte J (1966) Zur kenntnis der nickelhydroxidelektrode – I. Uber das nickel(II)-hydroxidhydrat. *Electrochimica Acta* 11: 1079–1087.

Bronoel G and Reby J (1980) Mechanism of oxygen evolution in the basic medium at a nickel electrode. *Electrochimica Acta* 25: 973–976.

Corrigan DA and Bendert RM (1989) Effect of coprecipitated metal ions on the electrochemistry of nickel hydroxide thin films: Cyclic voltammetry in 1 M KOH. *Journal of the Electrochemical Society* 136: 723–728.

Corrigan DA and Knight SL (1989) Electrochemical and spectroscopic evidence on the participation of quadrivalent nickel in the nickel hydroxide redox reaction. *Journal of the Electrochemical Society* 136: 613–619.

Davolio G and Sorangi E (1998) The 'memory effect' on nickel oxide electrodes: Electrochemical and mechanical aspects. *Journal of Applied Electrochemistry* 28: 1313–1319.

Dixit M, Jayashree RS, Kamath PV, Shukla AK, Kumat VG, and Munichandraiah N (1999) Electrochemically impregnated aluminium-stabilized α-nickel hydroxide electrodes. *Electrochemical and Solid-State Letters* 2: 170–171.

Falk SU and Salkind AJ (1969) *Alkaline Storage Batteries*. New York: John Wiley & Sons.

Faure C, Delmas C, and Willmann P (1991) Electrochemical behaviour of α-cobalted nickel hydroxide electrodes. *Journal of Power Sources* 36: 497–506.

Fritts DH (1982) The mechanics of electrochemically coprecipitated cobalt hydroxide in nickel hydroxide electrodes. *Journal of the Electrochemical Society* 129: 118–122.

Fukunaga H, Kishimi M, Matsumoto N, Ozaki T, Sakai T, Tanaka T, and Kishimoto T (2005) A nickel electrode with Ni-coated 3D steel sheet for hybrid electric vehicle applications. *Journal of the Electrochemical Society* 152: A905–A912.

Gunther RG and Gross S (eds.) *Proceedings of the Symposium on the Nickel Electrode*, vols. 82–84. New Jersey: The Electrochemical Society, Inc.

Halpert G (1984) Past developments and the future of nickel electrode cell technology. *Journal of Power Sources* 12: 177–192.

Harivel JP, Morignat B, Labat J, and Laurent JF (1967) Structure and electrochemical properties of nickel hydroxides. In: Collins DH (ed.) *Power Sources*, pp. 239–255. London: Pergamon Press.

Hu WK, Gao XP, Noreus D, Burchardt T, and Nakstad NK (2006) Evaluation of nano-crystal sized α-nickel hydroxide as an electrode material for alkaline rechargeable cells. *Journal of Power Sources* 160: 704–710.

Huggins RA (2007) Cause of the memory effect in 'nickel' electrodes. *Journal of Power Sources* 165: 640–645.

Kamnev AA (1996) The role of lithium in preventing the detrimental effect of iron on alkaline battery nickel hydroxide electrode: A mechanistic aspect. *Electrochimica Acta* 41: 267–275.

Kozawa A and Sato A (1996) Mechanism of the beneficial action of CaF_2 added to Ni–MH rechargeable EV batteries. *ITE Battery Newsletter* 1: 36.

McBreen J (1990) The nickel oxide electrode. In: White RE, Bockris JO'M, and Conway BE (eds.) *Modern Aspects of Electrochemistry*, vol. 21, pp. 29–63. New York: Plenum Press.

Micka K and Rousar I (1980) Theory of porous electrodes – XVI. The nickel hydroxide electrode. *Electrochimica Acta* 25: 1085–1090.

Morioka Y, Narukawa S, and Itou T (2001) State-of-the-art alkaline rechargeable batteries. *Journal of Power Sources* 100: 107–116.

Motupally S, Streinz CC, and Weidner JW (1998) Proton diffusion in nickel hydroxide. Prediction of active-material utilization. *Journal of the Electrochemical Society* 145: 29–34.

Ohms D, Kohlhase M, Benczur-Urmossy G, and Schadlich G (2002) New developments on high power alkaline batteries for industrial applications. *Journal of Power Sources* 105: 127–133.

Oliva P, Leonardi J, Laurent JF, et al. (1982) Review of the structure and the electrochemistry of nickel hydroxides and oxy-hydroxides. *Journal of Power Sources* 8: 229–255.

Oshitani M, Yufu H, Takashima K, Tsuji S, and Matsumaru Y (1989) Development of a pasted nickel electrode with high active-material utilization. *Journal of the Electrochemical Society* 136: 1590–1593.

Pralong V, Delahaye-Vidal A, Beaudoin B, and Tarascon J-M (2001) Bismuth contribution to the improvement of the positive electrode performances in Ni/Cd and Ni/MH batteries. *Materials Research Society Symposia Proceedings* 658: GG10.1.1–GG10.1.6.

Sato Y, Takeuchi S, and Kobayakawa K (2001) Cause of the memory effect observed in alkaline secondary batteries using nickel electrode. *Journal of Power Sources* 93: 20–24.

Shukla AK, Venugopalan S, and Hariprakash B (2001) Nickel-based rechargeable batteries. *Journal of Power Sources* 100: 125–148.

Song QS, Li YY, and Chan SLI (2005) Physical and electrochemical characteristics of nanostructured nickel hydroxide powder. *Journal of Applied Electrochemistry* 35: 157–162.

Srinivasan S, Weidner JW, and Newman J (2001) Hysteresis during cycling of nickel hydroxide active material. *Journal of the Electrochemical Society* 148: A969–A980.

Thaller LH and Zimmerman AH (2000) Selecting recharge protocols for deep-discharge nickel–hydrogen cells and batteries. *Proceedings of the 35th IECEC*, pp. 1073–1085.

Unates ME, Folquer ME, Vilche JR, and Arvia AJ (1992) The influence of foreign cations on the electrochemical behaviour of the nickel hydroxide electrode. *Journal of the Electrochemical Society* 139: 2697–2704.

Watanabe K, Kikuoka T, and Kumagai N (1995) Physical and electrochemical characteristics of nickel hydroxide as a positive material for rechargeable alkaline batteries. *Journal of Applied Electrochemistry* 25: 219–226.

Weast RC (1976/1977) *CRC Handbook of Chemistry and Physics* 57th edn., p. D-142. Florida: CRC Press.

Weininger JL (1982) The alkaline nickel hydroxide electrode. In: Gunther RG and Gross S (eds.) *Proceedings of the Symposium on the Nickel Electrode*, vols. 82–84, pp. 1–18. New Jersey: The Electrochemical Society, Inc.

Yohe D, Riga A, Greef R, and Yeager E (1968) Electrochemical properties of nickel oxide. *Electrochimica Acta* 13: 1351–1358.

Memory Effect

Y Sato, Kanagawa University, Yokohama, Japan

What Is the 'Memory Effect'?

When using electrical appliances such as shavers, stereo mobile audio player, and toothbrushes that are powered by alkaline rechargeable batteries, it is usually found that the batteries do not last as long as in the previous use of the respective devices. Accordingly, the batteries are said to suffer from a 'memory effect'. This phenomenon, which more accurately should be termed a voltage depression, has long been considered to be a major operational problem with rechargeable alkaline batteries that use nickel positive electrodes, namely, nickel–cadmium (Ni–Cd), nickel–hydrogen (Ni–H_2), nickel–metal hydride (Ni–MH), nickel–iron (Ni–Fe), and nickel–zinc (Ni–Zn) battery systems. The memory effect usually occurs during repeated recharging from a partially discharged state. When β-$Ni(OH)_2$ is used as the positive electrode in commercial batteries, the nominal capacity is limited by the amount of this active material loaded into the electrode. The following reaction occurs during the charge–discharge process:

$$\beta - Ni(OH)_2 + OH^- \underset{\text{discharge}}{\overset{\text{charge}}{\rightleftarrows}} \beta - NiOOH + H_2O + e^- \quad [I]$$

Thus the normal state is usually referred to the reaction between the β-$Ni(OH)_2$ and β-NiOOH. If, however, β-NiOOH is further oxidized to γ-NiOOH, that is, to a stage at which the batteries are usually said to be in an overcharged state, discharge voltage will decrease. Consequently, if the equipment powered by the battery is designed to shut down when the operating voltage reaches a certain level, the operation time may become shortened.

An example of the memory effect for an AAA-size Ni–Cd battery is illustrated in Figure 1. In this article, a battery prior to being subjected repeatedly to a shallow discharge followed by a full charge – hereafter referred to as 'shallow discharge, full charge (SDFC) cycle' – is called a normal battery and its discharge curve is defined as a normal discharge curve (curve A). Curve B is the discharge profile at 250 mA to 0.8 V after the battery has been subjected to 50 cycles, each comprising discharge at 50 mA to a 1.2 V cutoff voltage followed by recharge at 25 mA for 10 h. The discharge voltage of curve B is lower than that of curve A; in other words, the battery exhibits a memory effect. The battery can be returned to its normal state by repeated deep discharges to 0.8 V and recharges, as demonstrated by curves C and D both of which are closer to curve A for the normal state.

Unfortunately, the battery is generally embedded in a given consumer appliance, so that it is difficult to remove the battery and run deep discharge and charge operations to restore the normal state. Therefore, the devices are deemed to have failed and are discarded.

The memory effect was initially observed in a Ni–Cd cell and its origin was ascribed to the cadmium electrode. The Ni–Cd cell reaction is generally expressed as

$$\textit{Negative electrode}: \quad Cd(OH) + 2e^- \underset{\text{discharge}}{\overset{\text{charge}}{\rightleftarrows}} Cd + 2OH^- \quad [II]$$

$$\textit{Positive electrode}: \quad 2\beta - Ni(OH)_2 + 2e^- \underset{\text{discharge}}{\rightleftarrows} 2\beta - NiOOH + 2H_2O + 2e^- \quad [III]$$

At the negative electrode, cadmium hydroxide is reduced to cadmium metal during the charging process; the

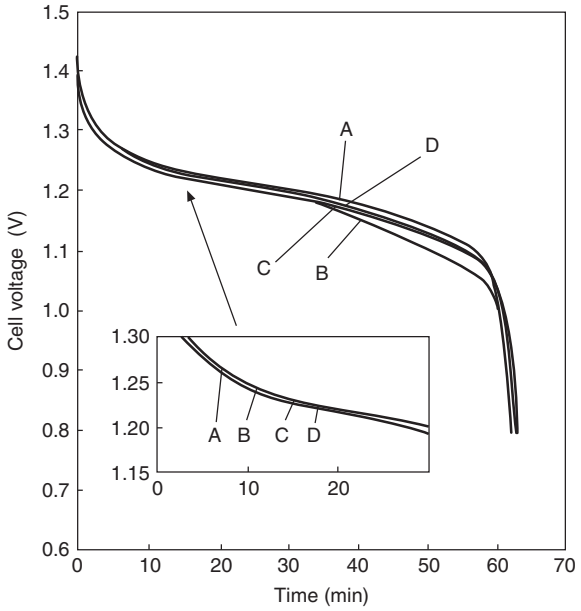

Figure 1 Discharge curves of AAA-size Ni–Cd battery at 250 mA and at 30 °C. A – discharge curve of normal-state cell; B – first discharge curve after 50 shallow discharge, full charge (SDFC) cycles; C – second discharge curve after 50 SDFC cycles; D – third discharge curve after 50 SDFC cycles. Charging performed at 25 mA for 16 h in curves A–D. Each SDFC cycle comprised discharge at 50 mA to 1.2 V and charge at 25 mA for 10 h. Reproduced with permission from Sato Y, Takeuchi S, Magaino S, and Kobayakawa K (2000) Cause of the memory effect observed in alkaline secondary batteries using nickel electrode. *Bulletin of the Chemical Society of Japan* 73: 1699–1713.

reverse reaction proceeds during discharging. On repeated charge–discharge cycling, the cadmium electrode is deformed and its protuberances press against the separator to cause semi-short-circuits with the positive electrode: thus, the voltage is lowered. It was claimed that the discharge voltage could be recovered to its normal state by dissolving the protuberances through a forced 'reconditioning' discharge. Another explanation associated the memory effect with the particle size of the cadmium hydroxide that is formed on discharge of the negative electrode. Whereas this particle size is usually quite fine in unused alkaline secondary batteries, some coarse cadmium hydroxide particles were observed after repeated cycling. These coarse particles were believed to increase both the discharge current density and the overpotential of the electrode and, therefore, the discharge voltage decreased. Other investigators have reported that the memory effect is closely related to the formation of inter-metallic compounds between the nickel current collector and the cadmium negative electrode after the repeated charge and discharge. It was found that formation of a Ni_5Cd_{21} alloy gave rise to a fall in the potential of the cadmium electrode during discharge. Therefore, it was argued that the memory effect would not occur in a Ni–MH cell, in which a hydrogen storage alloy instead of cadmium is used as the negative electrode. Subsequent studies have shown, however, that Ni–MH batteries are indeed subject to a memory effect. It was claimed that the cause was closely related to lowering of the potential of nickel electrode rather than that of the cadmium electrode, but a detailed mechanism was not presented.

The memory effect has also been observed in nickel–hydrogen (Ni–H_2) batteries used for space satellites. The discharge curves of an AAA-size Ni–MH battery are given in Figure 2. Curve A is the discharge curve of a normal cell, while curve B is the discharge curve after 300 SDFC cycles. The discharge voltage of curve B is lower than that of curve A and thus indicates a memory effect. It is noteworthy that if this battery is subjected to deep discharges to 0.8 V and then recharged for a few times, the shape of discharge curve approaches that of curve A.

In summary, the above findings suggest that the mechanism of the memory effect is related to the nickel positive electrode rather than to the negative electrode.

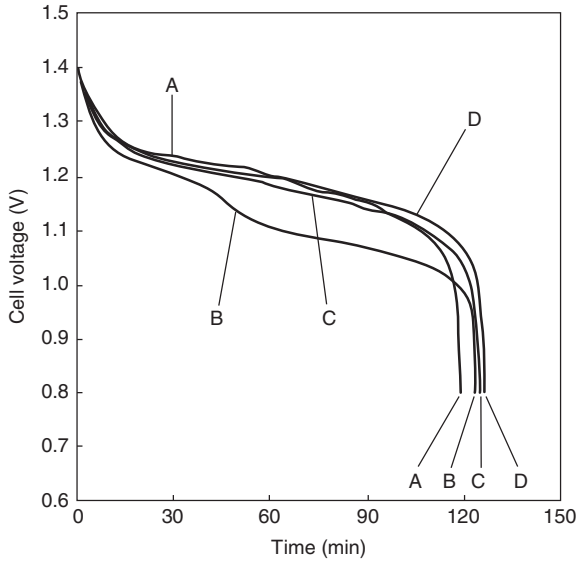

Figure 2 Discharge curves of AAA-size Ni–MH battery at 250 mA and at 30 °C. A – discharge curve of normal-state cell; B – first discharge curve after 300 shallow discharge, full charge (SDFC) cycles; C – second discharge curve after 300 SDFC cycles; D – third discharge curve after 300 SDFC cycles. Charging performed at 50 mA for 16 h in curves A to D. Each SDFC cycle comprised discharge at 50 mA to 1.2 V and charge at 50 mA for 16 h. Reproduced with permission from Sato Y, Takeuchi S, Magaino S, and Kobayakawa K (2000) Cause of the memory effect observed in alkaline secondary batteries using nickel electrode. *Bulletin of the Chemical Society of Japan* 73: 1699–1713.

Origin of the Memory Effect

Effect of Overcharge

For commercial batteries with high capacities, it would take a rather long time to charge and discharge them repeatedly until they show the memory effect. Thus, in the interest of expediency, tests were conducted on small cells of about 50 mAh that produce the memory effect more rapidly. Two different types of Ni–Cd cells were fabricated, namely, a cell limited by positive (nickel) electrode capacity and a cell limited by negative electrode (cadmium) capacity. The electrodes were taken from sintered-type, commercial batteries of AAA-size.

The discharge curves for the nickel-limited cell are given in Figure 3. Curve A is for the normal state, whereas curves B and C are the discharge profiles after SDFC cycling. Before obtaining curve B, the cadmium electrode was replaced by a new one in the charged state and with a capacity greater than that of the nickel electrode. This was because the cadmium electrode may have been affected by the preceding 50 SDFC cycles that were imposed to evaluate the memory effect. Therefore, only the behavior of the nickel electrode was observed. The discharge time is apparently longer, so there appears to be no capacity fading. On the contrary, a lowering of the voltage is observed, and it follows that the discharge time to the operating threshold voltage (1.2 V) is in fact shortened. After having measured the discharge curve B, the cell was charged and discharged to 0.8 V again, as represented by curve C. The voltage increases and the discharge performance approaches curve A, that is, the memory effect is virtually eliminated.

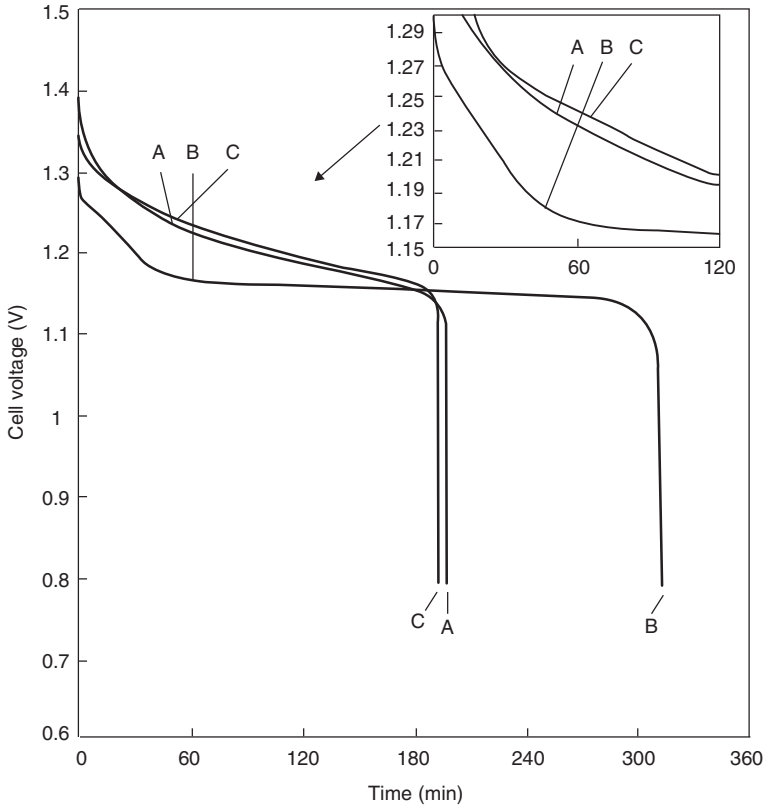

Figure 3 Discharge curves of Ni-limited Ni–Cd cell at 4.44 mA cm^{-2} and at 30 °C. A – discharge curve of normal-state cell; B – first discharge curve after 50 shallow discharge, full charge (SDFC) cycles; C – second discharge curve after 50 SDFC cycles. Charging performed at 2.22 mA cm^{-2} for 7 h in curves A to C. Before obtaining curve B, the cadmium electrode was replaced by a new one in the charged state; its capacity was greater than that of the nickel electrode. Each SDFC cycle comprised discharge at 2.22 mA cm^{-2} to 1.2 V and charge at 2.22 mA cm^{-2} for 7 h. Reproduced with permission from Sato Y, Ito K, Arakawa T, and Kobayakawa K (1996) Possible cause of the memory effect observed in nickel-cadmium secondary batteries. *Journal of the Electrochemical Society* 143: L225–L228.

A cadmium-limited Ni–Cd cell was assembled and subjected to similar cycling; the results are presented in Figure 4. For curve B, which was obtained after 50 SDFC cycles, the discharge voltage falls by about 0.04 V with respect to the normal discharge curve A. Clearly, this voltage drop is less than that for the nickel-limited cell (cf. curve B, Figure 3). Before measuring curve B, the nickel electrode was replaced with a new one in the charged state so that any influence of the cycle test would relate only to the cadmium electrode. After measuring curve B, the cell was charged and discharged to 0.8 V to obtain curve C. Further, discharge curve D was measured after obtaining curve C and recharging. Even after this treatment, the voltage was not restored to the normal curve A (cf. curves C and D, Figure 4). This behavior is contrary to that displayed by the nickel-limited cell (cf. curve C, Figure 3).

After 50 SDFC cycles of the cadmium-limited cell, the surface of the cadmium electrode in the charged state was examined with a scanning electron microscope. It was found that the particle size of the active material had significantly increased compared with that on the normal electrode surface. The enlarged particle size results in a decrease in the actual surface area, which, in turn, increases the current density during discharging, and consequently gives rise to an increased drop in voltage. In general, the enlarged particles of the cadmium-active material could not revert to their initial size after several deep discharges and charges, and therefore the discharge curve could not be immediately restored to its normal state, as demonstrated by curves C and D in Figure 4. From the data given in Figures 3 and 4, it is reasonable to conclude that the memory effect appears as a voltage depression and is due mainly to the performance of the nickel electrode. To provide further evidence in support of this conclusion, measurements were made of the potentials of the nickel positive and cadmium negative electrodes in the charged state. Each electrode was taken from the corresponding capacity-limited cell after 50 SDFC cycles; the results are shown in Figure 5. The potential of the nickel electrode is about 0.075 V below that of the normal electrode, but is restored after one deep discharge to 0.8 V followed by a charge. By contrast, the potential of the cadmium electrode is virtually

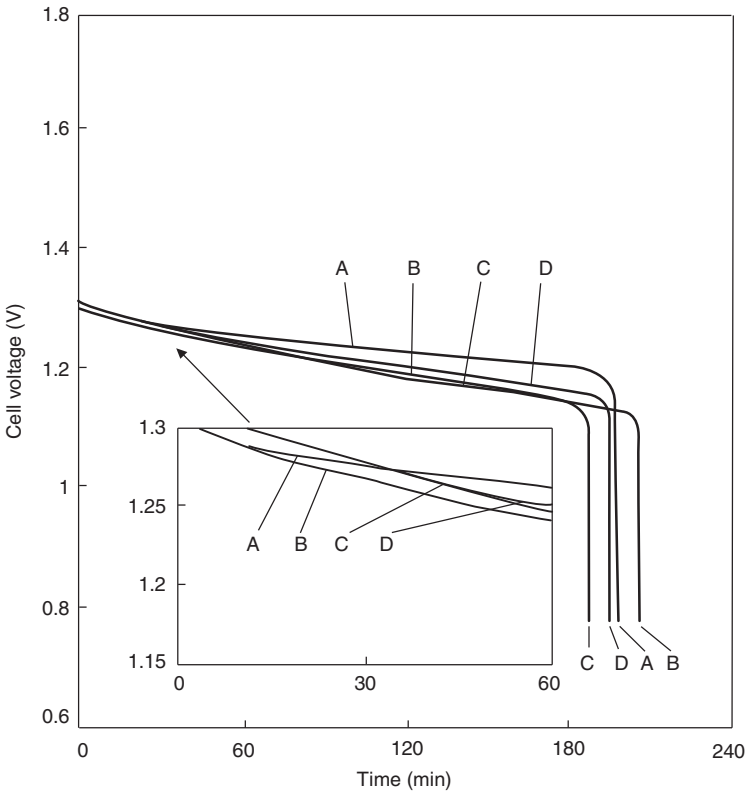

Figure 4 Discharge curves of Cd-limited Ni–Cd cell at 4.44 mA cm^{-2} and at 30 °C. A – Discharge curve of normal-state cell; B – first discharge curve after 50 shallow discharge, full charge (SDFC) cycles; C – second discharge curve after 50 SDFC cycles; D – third discharge curve after 50 SDFC cycles. Charging performed at 2.22 mA cm^{-2} for 7 h in curves A–D. Before obtaining curve B, the nickel electrode was replaced by a new one in the charged state; its capacity was greater than that of the cadmium electrode. Each SDFC cycle comprised discharge at 2.22 mA cm^{-2} to 1.2 V and charge at 2.22 mA cm^{-2} for 7 h. Reproduced with permission from Sato Y, Ito K, Arakawa T, and Kobayakawa K (1996) Possible cause of the memory effect observed in nickel–cadmium secondary batteries. *Journal of the Electrochemical Society* 143: L225–L228.

unaffected by SDFC cycling. These results clearly demonstrate that the nickel electrode is predominantly responsible for the voltage depression observed with SDFC cycling.

Nickel electrodes in the charged state were characterized by X-ray diffraction (XRD) analysis. Electrode A was taken from a nickel-limited cell operated under normal charge–discharge cycling, whereas electrode B was taken from a similar cell after five SDFC cycles. The XRD patterns are shown in **Figure 6**. Although electrode B had experienced a fall in voltage, its pattern is similar to that of the normal electrode A. Using sandpaper, material was removed from the surface of electrode B to successive depths of 0.11 and 0.17 mm. The resulting XRD patterns – B_s (slightly scraped), B_H (heavily scraped) – show the (003) and (006) diffraction peaks of γ-NiOOH near 13° and 26°, respectively. Moreover, the diffraction intensity of the γ-NiOOH becomes stronger with removal of the surface material. For a normal nickel electrode with 0.17 mm removed, only the diffraction peaks of β-NiOOH are detected and no γ-NiOOH diffraction is observed. For the AAA-size Ni–Cd and Ni–MH batteries (**Figures 1 (curve B)** and **2** (curve B)) that had suffered the memory effect, the presence of γ-NiOOH was also confirmed in the charged nickel electrodes. After several repeated deep charge–discharge cycles, the memory effect disappeared in both the Ni–Cd and Ni–MH batteries, and the diffraction peaks of γ-NiOOH became undetectable. These findings suggest that, with SDFC cycling, γ-NiOOH forms at the interface between the current collector and the nickel-active material and grows toward the surface of the electrode. This observation is in good agreement with the conventional view that, on overcharge, γ-NiOOH forms from β-$Ni(OH)_2$ through β-NiOOH, as illustrated in **Figure 7**. The β-$Ni(OH)_2$ in the discharged state transforms during the charge–discharge process as follows. During the charge process, hydroxide ions in the electrolyte initially combine with protons that diffuse into the active material to form water molecules and β-$Ni(OH)_2$ is oxidized to β-NiOOH; the reverse takes place on discharge. At the nickel electrode, charge and discharge ordinarily take place between β-$Ni(OH)_2$ and β-NiOOH. If, however, β-NiOOH is further charged, it

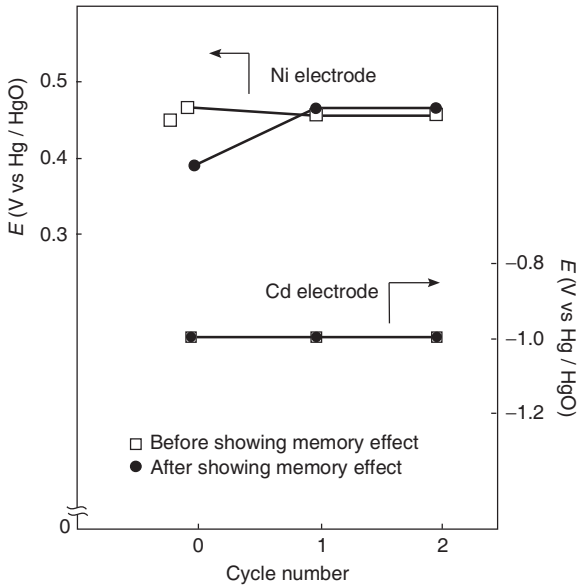

Figure 5 Potentials of nickel positive electrode and cadmium negative electrode in the charged state vs deep discharge cycle number before and after 50 shallow discharge, full charge (SDFC) cycles. □: electrode potential in normal state; ●: electrode potential after 50 SDFC cycles. Each SDFC cycle comprised discharge at 2.22 mA cm^{-2} to 1.2 V and charge at 2.22 mA cm^{-2} for 7 h. Nickel and cadmium electrodes are taken from Ni-limited Ni–Cd and Cd-limited Ni–Cd cells, respectively. Reproduced with permission from Sato Y, Takeuchi S, Magaino S, and Kobayakawa K (2000) Cause of the memory effect observed in alkaline secondary batteries using nickel electrode. *Bulletin of the Chemical Society of Japan* 73: 1699–1713.

transforms into γ-NiOOH. On discharge, the latter phase is converted into α-$Ni(OH)_2$, which, due to its instability in aqueous alkaline solution, immediately reverts to β-$Ni(OH)_2$.

Following SDFC cycling, the nickel electrode was subjected to cyclic voltammetric analysis. During the negative-going scan, the reduction peak for β-NiOOH appears and is followed by the peak for the reduction of γ-NiOOH. Because γ-NiOOH contains Ni^{4+}, its mean oxidation number is higher than 3, that is, about 3.6–3.67. The oxidation number of β-NiOOH is 2.8–3.2, and therefore the discharge capacity becomes higher if γ-NiOOH is present. This discharge behavior is demonstrated in Figure 3(curve B), that is, the discharge capacity of curve B is higher than that of curve A and thereby suggests that γ-NiOOH is present in the nickel electrode after 50 SDFC cycles. It is well known that γ-NiOOH formed by overcharge can degrade cell performance. The lattice volume of γ-NiOOH is about 30% greater than that of β-NiOOH and this results in expansion of the nickel electrode. The swelling leads to the formation of micro-cracks in the active material, which, in turn, lowers the conductivity of the electrode by breaking the conductive network or causing dry-out of the separator by extraction of the electrolyte solution into the electrode. Thus, formation of γ-NiOOH lowers both the capacity and the high rate discharge performance of the nickel electrode. Co-precipitation of cobalt hydroxide, cadmium hydroxide, zinc hydroxide with nickel hydroxide is now employed to minimize the development of γ-NiOOH. Remarkably, very few reports have identified γ-NiOOH as the cause of the memory effect.

Transformation of the α-$Ni(OH)_2$ phase to γ-NiOOH phase is reversible without the occurrence of mechanical deformation. In addition, because more than one electron is exchanged per nickel atom, a higher discharge capacity is to be expected. Thus, it is worth investigating the α-$Ni(OH)_2$–γ-NiOOH system as a possible approach to the development of new alkaline secondary batteries. The main problem is that α-$Ni(OH)_2$ is unstable in alkaline medium and easily transforms into β-$Ni(OH)_2$, as shown in Figure 7. Accordingly, much effort has been put on the preparation of a stabilized α-$Ni(OH)_2$ by partial substitution of cobalt, aluminum, iron, manganese, and zinc for nickel as a means of increasing the stability of the α-phase structure in strong alkaline medium.

Memory Effect Under Partial State-of-Charge Cycling

The progressive replacement of the conventional automobiles with hybrid electric vehicles (HEVs) is considered to be a promising approach to mitigate the present concern over energy sustainability in the transportation sector. The success of HEVs primarily depends on the performance of the Ni–MH batteries that provide the auxiliary power source. In order to facilitate charge acceptability, the batteries in HEVs are deliberately controlled to operate within a certain state-of-charge (SoC) window. In other words, they are subjected to a partial state-of-charge (PSoC) duty. As described in the previous section, if a Ni–Cd or Ni–MH battery undergoes SDFC cycling or an overcharge, γ-NiOOH forms in the nickel electrode and gives rise to the memory effect. By contrast, it is generally assumed that the memory effect will not occur in the batteries used in HEVs, because they never become fully charged or overcharged. Nevertheless, it has been found that γ-NiOOH is formed in the nickel electrode and gives rise to the memory effect that occurs in Ni–MH and Ni–Cd batteries when subjected to PSoC cycles between 50 and 70% SoC. The following discussion examines the cause of the memory effect during such duty.

The discharge curves of an AAA-size Ni–MH battery at 50% SoC before and after PSoC cycling between 50 and 70% SoC are given in Figure 8. Following the procedure employed above, a battery before PSoC operation is called the normal battery and its discharge curve (curve A) is defined as the normal discharge curve. The discharge curves B, C, and D after, respectively, 100, 200, and 300 PSoC cycles at 180 mA show a progressive lowering of the

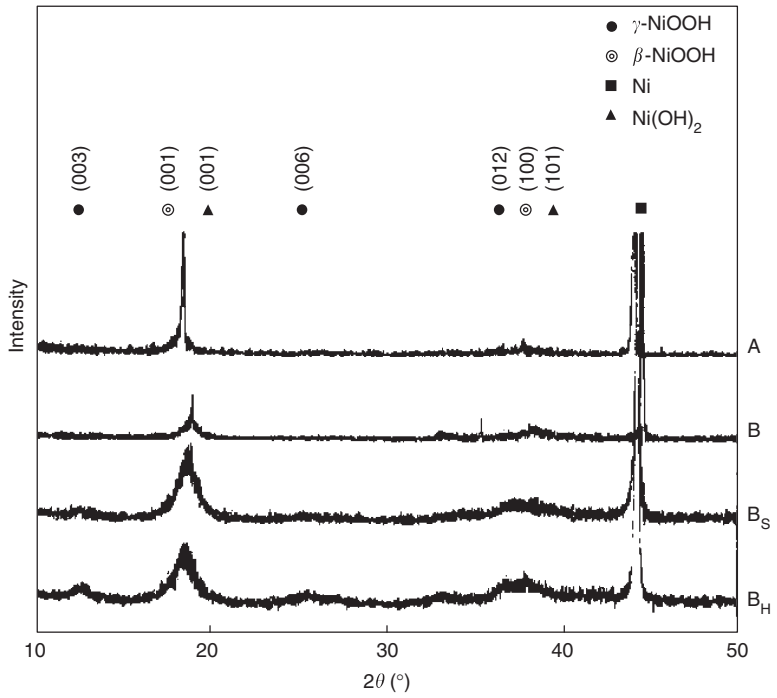

Figure 6 X-ray diffraction patterns for charged nickel electrode: A – normal electrode; B – electrode after five shallow discharge, full charge (SDFC) cycles; B_S – 0.11 mm shaved from electrode (electrode thickness: 0.12 mm) after five SDFC cycles; B_H – 0.17 mm shaved from electrode (electrode thickness: 0.06 mm) after five SDFC cycles. Each SDFC cycle comprised discharge at 2.22 mA cm^{-2} to 1.2 V and charge at 2.22 mA cm^{-2} for 7 h. Reproduced with permission from Sato Y, Takeuchi S, and Kobayakawa K (2001) Cause of the memory effect observed in alkaline secondary batteries using nickel electrode. *Journal of Power Sources* 93: 21.

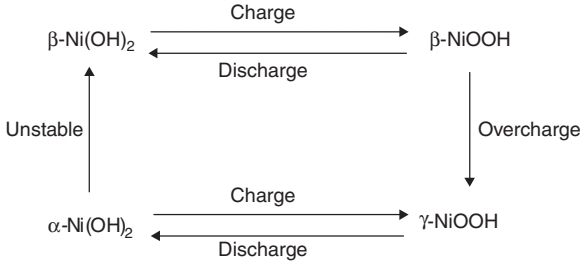

Figure 7 Bode representation of charge–discharge process of nickel positive electrode. Reproduced with permission from Bode H, Dehmelt K, and Witte J (1966) Nickel hydroxide electrodes. I. Nickel(II) hydroxide hydrate. *Electrochimica Acta* 11: 1079–1087.

working voltage. After 300 cycles, the battery was deeply discharged to 0.8 V for several times at 180 mA. This resulted in the voltage returning to its normal value. This behavior is obviously similar to the memory effect behavior. Thus, in the similar manner as discussed in the previous section, a small nickel-limited Ni–Cd cell was assembled to investigate the mechanism. Discharge curves after 100–500 PSoC cycles were recorded: curves B–E in Figure 9. Compared with the normal discharge curve A, the discharge curves B–E display a lowering of the working voltage. That is, the discharge behavior is similar

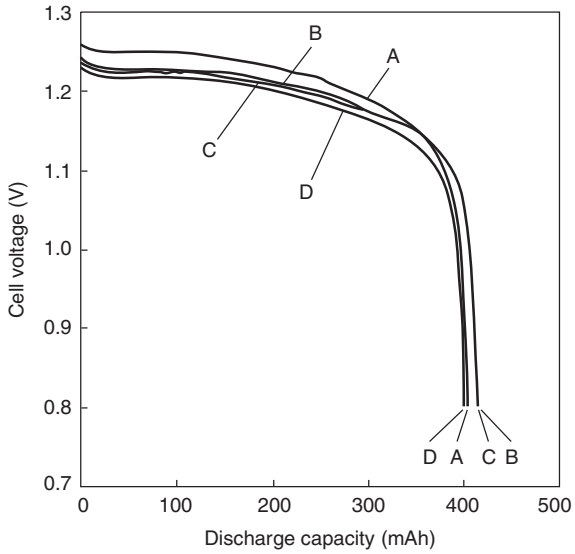

Figure 8 Discharge curves of AAA-size Ni–MH battery at 180 mA and at 30 °C. A – normal discharge curve at 50% state-of-charge (SoC). Discharge curves at 50% SoC after: B – 100, C – 200, and D – 300 partial state-of-charge (PSoC) cycles between 50% and 70% state-of-charge (SoC) at 180 mA. Reproduced with permission from Morishita M, Shikimori S, Shimizu Y, et al. (2006) The memory effect in the partial charge–discharge cycling of alkaline secondary batteries. *Electrochemistry* 74: 532–535.

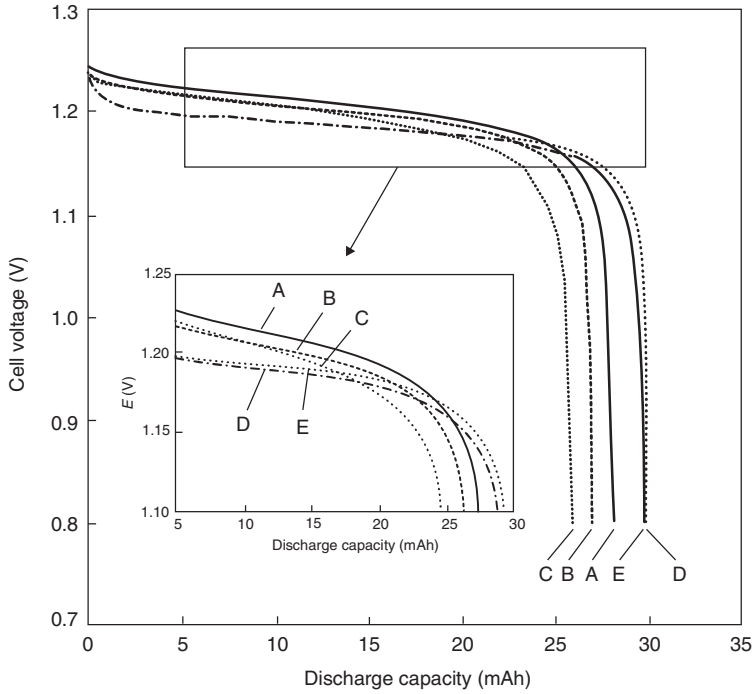

Figure 9 Discharge curves of Ni-limited Ni–Cd cell at 3.2 mA cm^{-2} and 30 °C. A – normal discharge curve at 50% state-of-charge (SoC). Discharge curves at 50% SoC after: B – 100, C – 300, D – 400, and E – 500 partial state-of-discharge (PSoC) cycles between 50% and 70% SoC at 3.2 mA cm^{-2}. Reproduced with permission from Morishita M, Shikimori S, Shimizu Y, et al. (2006) The memory effect in the partial charge–discharge cycling of alkaline secondary batteries. *Electrochemistry* 74: 532–535.

to that of a cell with a memory effect. Moreover, the decrease in discharge voltage increases with cycling. The voltage can be restored by subjecting the cell to repeated charge and deep discharge to 0.8 V at 3.2 mA cm^{-2}.

Nickel electrodes at 50% SoC were taken from the above Ni–MH battery and Ni–Cd cell and subjected to XRD phase analysis study; the results are given in Figure 10. Patterns A_{MH} and A_{Cd} are those for the normal nickel electrodes taken from the Ni–MH battery and the Ni–Cd cell, respectively. The diffraction peaks at 18°, 33°, and 38° can be ascribed to β-Ni(OH)$_2$ and β-NiOOH. After PSoC cycling, the diffraction peaks observed at about 13, 26, and 37° (patterns B_{MH} and B_{Cd}) can be ascribed to the γ-NiOOH phase. The data suggest that the memory effect occurs even if the nickel electrode is not overcharged. Following the occurrence of a memory effect, the Ni–Cd cell was subjected to three deep discharge and recharge cycles. The diffraction peaks for γ-NiOOH disappear (pattern C_{Cd}), whereas those assigned to β-Ni(OH)$_2$ and β-NiOOH reappear so that the diffraction pattern becomes similar to that for the normal electrode A_{Cd}, that is, the cadmium electrode C_{Cd} was revived.

The above results show that γ-NiOOH forms in the nickel electrode on PSoC cycling, even when the nickel electrode is not overcharged. Despite this observation, it is difficult to analyze where in the nickel electrode the γ-NiOOH begins to form and how it grows. Thus, the morphology of a cross-section of the nickel electrode at 50% SoC before and after 500 PSoC cycles was examined by scanning electron microscopy. Micrographs of the normal electrode, shown in Figure 11(a), reveal that the particle size of nickel hydroxide does not change from near the current collector to near the electrode surface and that there are no cracks. After PSoC cycling, however, cracks appear as seen in Figure 11(b). The difference appears to be the fact that the particles are both larger and more compact in Figure 11(b). In particular, the particles are larger close to the current collector. Thus, to search for causes of the particle growth, PSoC cycling was undertaken on a newly prepared cell, and then the nickel electrode in the charged state was subjected to XRD phase analysis. Although the memory effect occurred, no γ-NiOOH was detected at the nickel electrode surface; the diffraction peaks for only β-Ni(OH)$_2$ and β-NiOOH appeared near 18°, 33°, and 38° in the pattern. On the contrary, the (003) and (006) diffraction peaks due to γ-NiOOH appeared near 13° and 26° after 0.098 mm of the electrode was removed from the surface with sandpaper. The peaks intensified when 0.195 mm of material was scraped from the electrode surface. For each nickel electrode surface, the intensity ratio of the (003) diffraction peak of γ-NiOOH to the (001) diffraction peak of β-NiOOH increased toward the current collector. These findings indicate that, during the PSoC process, γ-NiOOH initially forms near the current collector and then grows toward the surface of the nickel electrode.

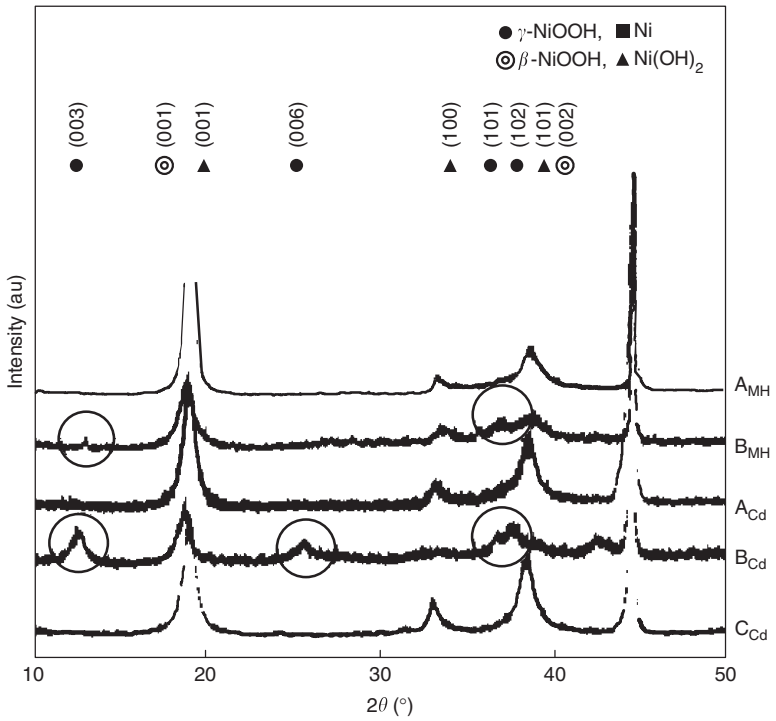

Figure 10 X-ray diffraction (XRD) patterns of 50% state-of-charge (SoC) Ni electrodes from AAA-size Ni–MH battery and Ni-limited Ni–Cd cell reported in **Figures 8** and **9**. A_{MH} and A_{Cd}: normal state electrodes from AAA-size Ni–MH battery and Ni-limited Ni–Cd cell, respectively. B_{MH}: 0.3 mm shaved from electrode from Ni–MH battery after 300 partial state-of-charge (PSoC) cycles between 50% and 70% SoC at 180 mA and 30 °C. B_{Cd}: electrode from Ni–Cd cell after 500 partial state-of-charge (PSoC) cycles between 50% and 70% SoC at 3.2 mA cm^{-2} and 30 °C. C_{Cd}: electrode after three deep discharge and recharge cycles of electrode B_{Cd}. Reproduced with permission from Morishita M, Shikimori S, Shimizu Y, et al. (2006) The memory effect in the partial charge–discharge cycling of alkaline secondary batteries. *Electrochemistry* 74: 532–535.

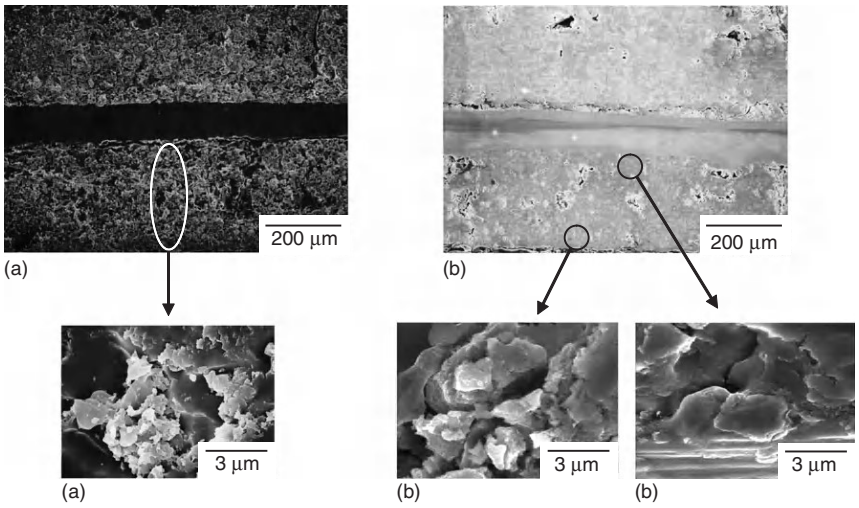

Figure 11 Scanning electron micrographs of a cross-sectional view of charged-state Ni electrodes: (a) normal state; (b) after 500 partial state-of-charge (PSoC) cycles between 50% and 70% state-of-charge (SoC) at 1.68 mA cm^{-2} and 30 °C. Reproduced with permission from Morishita M (2006) *A study on the memory effect observed in alkaline secondary batteries*. PhD Thesis, Graduate School of Kanagawa University, Japan. p. 41.

The mechanism shown schematically in Figure 12 was proposed for the formation of the γ-NiOOH during PSoC cycling without overcharge. Usually, cobalt hydroxide is added as a conducting material to the nickel electrode. If cobalt hydroxide is not homogeneously dispersed, however, some isolated clusters of nickel hydroxide particles may exist in the electrode without contacting the cobalt hydroxide particles, and thereby result in some domains

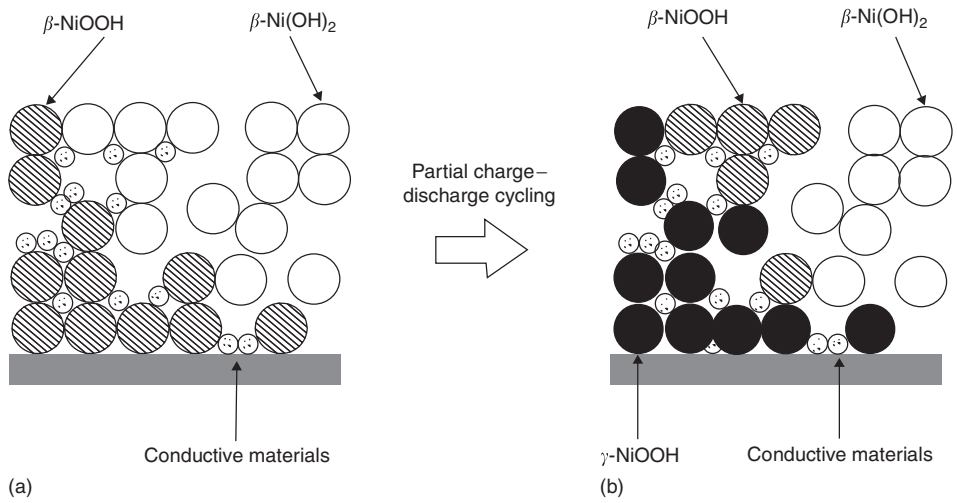

Figure 12 Mechanism of γ-NiOOH formation during partial state-of-charge (PSoC) cycling: (a) the charged-state Ni electrode; (b) the Ni electrode after partial charge–discharge cycling. Reproduced from Sato Y.

with high electro-conductivity and others with low electro-conductivity. The β-$Ni(OH)_2$ in the higher electro-conductive domain is first oxidized to β-NiOOH during the charging process and will favor the oxidation of the β-NiOOH to γ-NiOOH rather than the oxidation of the remaining β-$Ni(OH)_2$ in the lower electro-conductive domain to β-NiOOH. Therefore, although β-$Ni(OH)_2$ should be further oxidized to β-NiOOH during the PSoC cycling (e.g., between 50% and 70% SoC), the nickel electrode is locally overcharged in the high conductivity domains, where it is likely to form γ-NiOOH and thus give rise to the memory effect.

If the above assumption is correct, then it should be possible to suppress the memory effect during PSoC cycling through uniform dispersal of the conducting material in the active material. To verify this proposition, two different nickel electrodes were prepared. One contained micron-sized cobalt hydroxide and nano-sized cobalt(II) oxide, whereas the other contained nano-sized cobalt hydroxide and nano-sized cobalt(II) oxide; though the total content of the cobalt compounds was the same in both electrodes. Nickel–cadmium cells were assembled using these electrodes – cell A with the former and cell B with the latter electrode – and then subjected to PSoC cycling. The discharge curves are given in **Figure 13**. For each cell, curve a is the normal discharge curve before cycling and curve b is the discharge curve after 100 PSoC cycles. Despite the fact that the $Ni(OH)_2$ contents in the nickel electrodes are the same, the discharged capacity of cell B is higher than that of cell A, and thus indicates greater utilization of the active material. Moreover, close inspection of curve b in **Figures 13(a) and 13(b)** reveals the voltage depression of cell B to be smaller than that of cell A. Based on these two observations, it is expected that the nano-sized conducting material is dispersed more uniformly than the micro-sized conducting material and, accordingly, forms a better electro-conductive network in the electrode. Therefore, it is concluded that the higher utilization of active material in cell B than in cell A inhibits development of the memory effect. Energy-dispersive X-ray analysis showed

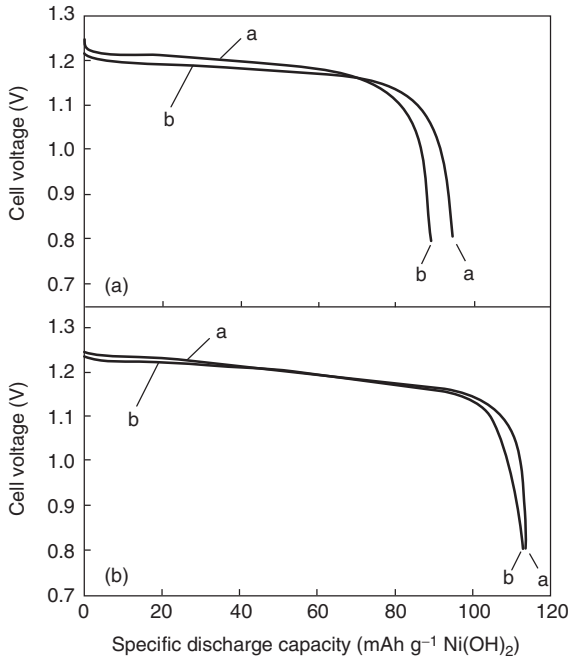

Figure 13 Discharge curves of Ni-limited Ni–Cd cell: curve a – normal state; curve b – after 100 partial state-of-charge (PSoC) cycles between 50% and 70% state-of-charge (SoC) at 3.2 mA cm^{-2} and 30 °C. Ni electrodes containing: (a) micron-sized $Co(OH)_2$ and 18 nm CoO; (b) about 15 nm $Co(OH)_2$, and 18 nm CoO. Reproduced with permission from Morishita M, Shikimori S, Shimizu Y, et al. (2006) The memory effect in the partial charge–discharge cycling of alkaline secondary batteries. *Electrochemistry* 74: 532–535.

that nano-sized cobalt hydroxide has a higher dispersion uniformity than that of micro-sized cobalt hydroxide, as shown in Figure 14. The data support the proposition that the use of a nano-sized conducting material restricts the occurrence of locally overcharged regions in the electrode, and consequently suppresses the formation of γ-NiOOH during PSoC cycling. Therefore, if it is possible to disperse a conducting material uniformly in the nickel electrode, it is indeed probable that the memory effect induced by PSoC cycling can be moderated. It should be noted, however, that this method is only effective for a cell operated in the PSoC mode. In an overcharged state, the memory effect cannot be suppressed, even if the dispersion uniformity of the conduction material is improved, because the β-NiOOH will transform to γ-NiOOH.

Second Low-Voltage Plateau

The second low-voltage plateau (called 'second plateau' in the following discussion) phenomenon, which is easily confused with the memory effect, is sometimes observed in alkaline secondary batteries using a nickel electrode. A typical discharge curve with a secondary low-voltage plateau is shown in Figure 15.

The portion of the discharge curve at the higher potential has been attributed to the reduction of β-NiOOH, whereas the second plateau usually appears at 0.03–0.4 V more negative. Many explanations have been advanced for the appearance of the second plateau and can be categorized as follows.

Reduction of Oxygen

In this hypothesis, the origin of the second plateau is ascribed to the reduction of oxygen present in the graphite, which is added to the nickel pocket electrode as a conducting material. On the contrary, it has been found that the second plateau appears even with a sintered positive electrode that does not contain graphite. This was attributed to oxygen adsorbed in the nickel hydroxide itself. A further explanation was that the second plateau originates from the reduction of oxygen dissolved in the electrolyte solution. This was supported by the claim that the second plateau did not appear when no oxygen was dissolved in the electrolytic solution. There were, however, many objections to the various proposed roles of oxygen. For example, no evidence of the oxygen adsorption was obtained from in-situ magnetic susceptibility measurements. Whereas another study showed that a second plateau was observed when discharging a porous nickel electrode, whether or not nitrogen had been injected into the electrolytic solution.

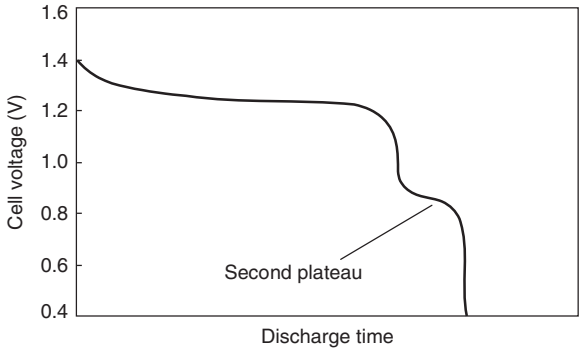

Figure 15 Typical example of the formation of the second plateau. Reproduced from Sato Y.

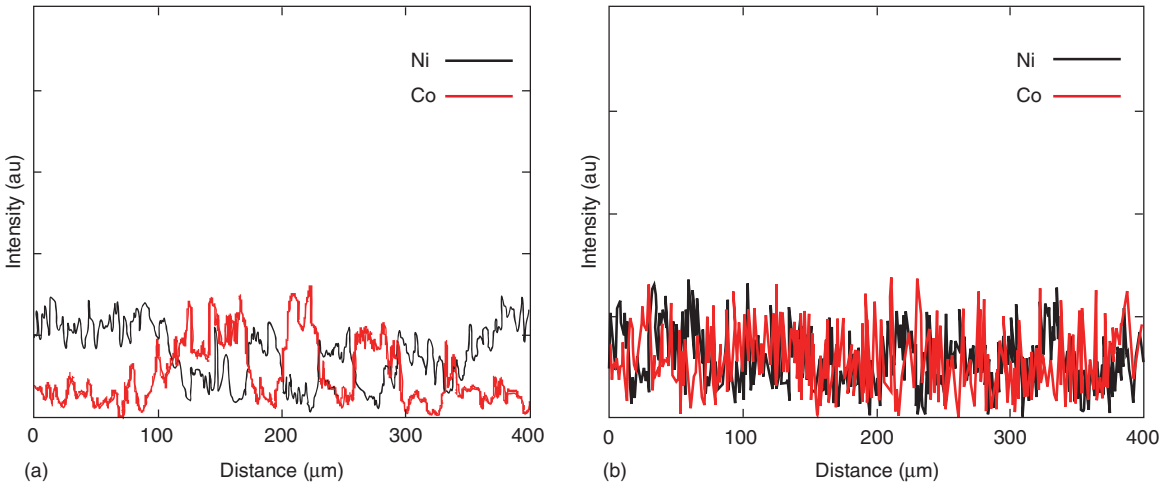

Figure 14 Energy-dispersive X-ray spectroscopic analysis of Ni electrodes containing: (a) micron-sized $Co(OH)_2$ and 18 nm CoO; (b) about 15 nm $Co(OH)_2$ and 18 nm CoO. Ni electrode after 150 partial state-of-charge (PSoC) cycles between 50% and 70% state-of-charge (SoC) at 3.2 mA cm^{-2} and 30 °C. Reproduced from Sato Y.

Electronic Behavior of Nickel Hydroxide

The second plateau has also been attributed to changes in the electronic behavior of the nickel hydroxide active material. In the charged state, the active material is a good electronic conductor; but as the depth-of-discharge increases, the conductivity gradually decreases due to a concomitant decrease in the number of charge carriers. If the charge carriers become markedly depleted, the active material exhibits a behavior similar to that of a semiconductor at the substrate/active-material interface. Accordingly, the remaining active material can no longer discharge at the potential of the first (main) plateau. This causes a loss of useful capacity and results in the development of a second plateau. Discharge at the second plateau ceases when all the charge carriers in the remaining active material have disappeared.

The above hypothesis was examined in terms of ohmic resistance effects and the semiconducting properties of the active material. It was found that the second discharge step of the nickel electrode could be suppressed in the presence of a Teflon binder or cobalt hydroxide, whereas the first step was enhanced. The effect of the binder can be attributed to an improvement in the contact between the electroactive particles. The existence of the second plateau was therefore attributed to difference in the ohmic contacts of the electroactive particles in the electrode (i.e., an ohmic resistance effect). The beneficial influence of cobalt can probably be explained by an increase in the hole conductivity of nickel hydroxide (i.e., an semiconducting effect). It was also reported that a second plateau appears when the internal resistance rises as a result of loss or swelling of the graphite additive. A mathematical model was presented to predict the two-step discharge behavior of a nickel electrode; the derivation was based on assumptions made for the proton diffusion and ohmic drop across the active material.

Less-Active Intermediate Products

The reduction of an intrinsically less-active material, which is formed as an intermediate during the reduction of β-NiOOH, has also been held responsible for the presence of the second plateau. The intermediate product was claimed to be $Ni_3O_2(OH)_4$ or $Ni_3O_4 \cdot xH_2O$ has been proposed, but it was also reported that the $Ni_3O_2(OH)_4$ represents a mixture of β-NiOOH and β-$Ni(OH)_2$. In another work, discharged active material was examined by XRD phase analysis and no such less-active nickel oxides were observed during cycling. Chemically and electrochemically impregnated porous nickel electrodes were investigated; only the electrodes containing a significant amount of γ-phase were found to display a second plateau. It was therefore concluded that the cause lies in the direct reduction of γ-NiOOH into β-$Ni(OH)_2$, for which a high overpotential (0.4 V) is required. On the contrary, the transformation from γ-NiOOH to α-$Ni(OH)_2$ is known to require an overpotential of only 0.05 V, that is, much lower than 0.4 V. Thus, the foregoing conclusion was questioned because the transformation from γ-NiOOH to β-$Ni(OH)_2$ is more energy intensive than that from γ-NiOOH to α-$Ni(OH)_2$, so that the transformation from γ-NiOOH to α-$Ni(OH)_2$ should easily occur compared with the transformation from γ-NiOOH to β-$Ni(OH)_2$.

In summary, none of the above three mechanisms for the second plateau has provided an unequivocal explanation for the appearance of the second plateau. Recently, a new hypothesis has been proposed, wherein the phenomenon was ascribed to the intercalation of the cations of the alkaline electrolytic solution into graphite. As discussed previously, the phenomenon usually appears in nickel positive electrodes with graphite added as a conducting material. It has also been shown that NiOOH contains K^+ ions that intercalate from the electrolyte solution during the charging process. The following series of experiments was conducted to examine the proposal that K^+ also intercalates into the graphite.

The discharge curves of Ni–Cd cells assembled using a nickel electrode composed of nickel hydroxide with various contents of graphite are shown as curves B–D in Figure 16. Curves A and E are the discharge curves of cells using, respectively, β-$Ni(OH)_2$ chemically synthesized γ-NiOOH

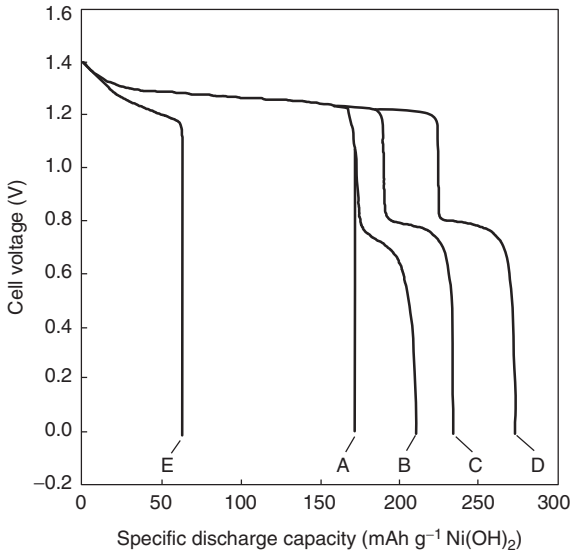

Figure 16 Fifth-cycle discharge curves of Ni-limited Ni–Cd cell obtained at 3.2 mA cm^{-2} in 8 mol L^{-1} KOH solution. $Ni(OH)_2$ electrode (6.28 cm^2): A – without graphite; B – with 4.72 wt% graphite; C – with 9.44 wt% graphite; D – with 14.16 wt% graphite; E – γ-NiOOH electrode without graphite. Reproduced with permission from Morishita M, Kobayakawa K, and Sato Y (2005) Alkaline cation intercalation into graphite used as a conducting material in nickel electrode of aqueous secondary batteries. *Electrochemical and Solid State Letters* 8: A539–A543.

as electrodes, both of which do not contain graphite; the second plateau is not observed in these latter two curves. By contrast, cells B, C, and D exhibit a second plateau near 0.8 V. Increasing graphite content extends both the discharge time in the 1.2-V region (which corresponds to the discharge of β-NiOOH) and the discharge time of the second plateau. Extension of the 1.2-V region may be due to improved conductivity, which consequently increases the utilization rate of NiOOH. The increase in the discharge time of the second plateau implies that the origin of the second plateau is related to the graphite additive. The maximum discharge capacity of the second plateau per unit weight of graphite is 200 mAh.

Cyclic voltammograms were obtained for three different nickel electrodes made of nickel hydroxide, nickel hydroxide containing graphite, and γ-NiOOH. The nickel hydroxide electrode (scan A, Figure 17) shows an anodic peak at 0.5 V that corresponds to oxidation to β-NiOOH , and a cathodic peak at 0.3 V that corresponds to the reduction from β-NiOOH to β-$Ni(OH)_2$. When graphite is in the nickel electrode (electrode B), the peak currents at 0.3 and 0.5 V increase because of the conductivity improvement over electrode A. Electrode B exhibits another cathodic peak at -0.2 V. This potential corresponds to the second plateau of the discharge curves B–D in Figure 16. An anodic peak complimentary to this cathodic peak is not observed and suggests that this cathodic process is irreversible. The potential of the cathodic peak of γ-NiOOH (electrode C) appears at a lower potential than that of β-NiOOH (electrodes A and B) and this is quite consistent with the understanding that γ-NiOOH is reduced at a lower potential than β-NiOOH. Because γ-NiOOH (electrode C) does not show a cathodic peak corresponding to the second plateau at -0.2 V, the proposal that γ-NiOOH is responsible for the second plateau is not convincing. Furthermore, the interpretation that the second plateau is related to the oxygen reduction seems to be equally unacceptable because: (1) there was no change in the shape of the voltammogram for electrode A when oxygen or nitrogen was injected into the solution prior to experiment; (2) the cell using the electrode B was unaffected by dissolving oxygen or nitrogen in the electrolytic solution.

To examine the possible influence of alkaline cations on the second plateau, the total concentration of the electrolyte was kept at 8 mol L^{-1} and some proportion of the potassium hydroxide was replaced with sodium hydroxide. An increase in the amount of sodium hydroxide resulted in an increase in the capacity of the second plateau. Furthermore, when sodium hydroxide was replaced with LiOH, the capacity noticeably increased with an increasing proportion of LiOH. The size of the Li^+ ion is smaller than that of K^+ and Na^+ ions. Therefore, it would appear that alkali cations with smaller ionic radii

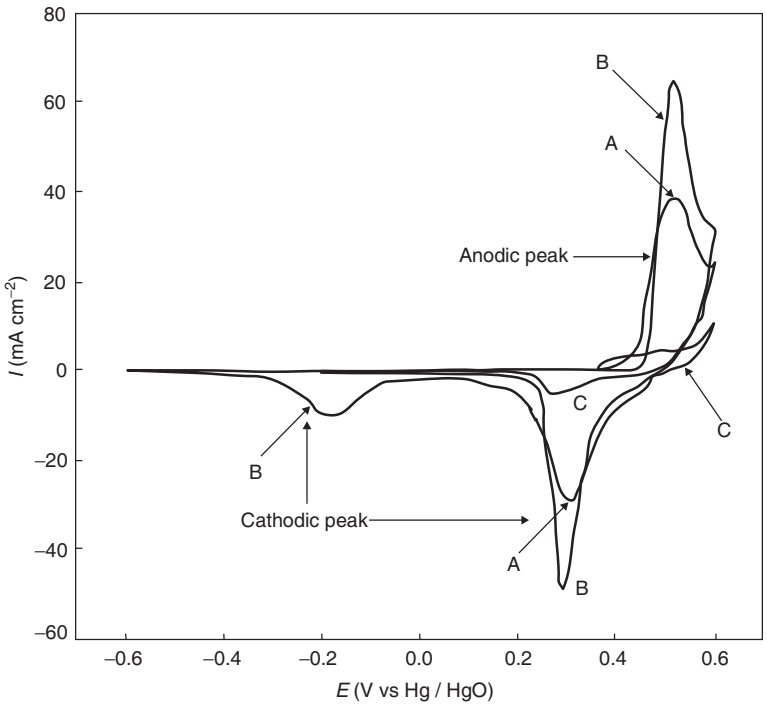

Figure 17 Cyclic voltammograms for A – $Ni(OH_2)$ electrode (1.57 cm^2); B – $Ni(OH)_2$ electrode (1.57 cm^2) containing 9.44 wt% graphite; C – γ-NiOOH electrode (1.57 cm^2). Experiments performed in 8 mol L^{-1} KOH solution at sweep rate of 10 mV min^{-1}. Reproduced with permission from Morishita M, Kobayakawa K, and Sato Y (2005) Alkaline cation intercalation into graphite used as a conducting material in nickel electrode of aqueous secondary batteries. *Electrochemical and Solid State Letters* 8: A539–A543.

are more prone to intercalate into the graphite layer and give rise to higher capacities at the second plateau.

On the basis of the above experimental studies, it may be concluded that the cause of the second plateau is the intercalation of alkaline cations into the graphite layer contained in the nickel electrode. According to this speculation, most of the results described above are understandable.

When the conducting material was changed from graphite to an active carbon with a turbostratic structure or Ketjenblack, both of which have a poor or random stacking order in terms of the graphene sheets, the second plateau again appeared, but its capacity was not as high as that with graphite. Moreover, the potential of the second plateau changed with the type of carbon used.

In summary, the second plateau is affected by both the type and amount of the added content, and is explained by differences in the ohmic contact of the electroactive particles. It could also be attributed to a difference in the intercalation mechanism provided that the various types of carbon have different micro-structures, for example, as regards the stacking of the graphene sheets. This, in turn, will influence the accommodation for the alkaline cations, and thereby affect the capacity and the potential of the second plateau.

A charge–discharge cycling test was conducted using a Ni–Cd cell with a graphite-containing nickel hydroxide, electrode. The discharge capacity to 1.2 V remained unchanged but the capacity of the second plateau gradually decreased. The latter behavior did not cause deterioration of the cell because the discharge capacity to 1.2 V was constant. If the second plateau phenomenon is an irreversible reaction, which is suggested by the cyclic voltammogram of electrode B in **Figure 17**, once a K^+ ion intercalates into the graphite layer, it is trapped there. Thus, the sites capable of accepting K^+ ions will progressively decrease and induce a decrease in the second plateau capacity.

To verify the existence of alkaline cations intercalated in the graphite layer, nickel electrodes with and without the graphite additive were put in a 7 mol L^{-1} potassium hydroxide solution containing 1 mol L^{-1} lithium hydroxide. After several full charge–discharge cycles, a nickel electrode with a graphite additive was analyzed by means of ^{7}Li nuclear magnetic resonance (^{7}Li-NMR) spectroscopy. The spectra for the charged and discharged electrode are presented in **Figures 18(a) and 18(b)**, respectively. For a solution containing K^+ and Li^+, the two ions are expected to exhibit similar NMR behavior. Therefore, if the ^{7}Li-NMR data indicate that the intercalation of Li^+ into the graphite layer is achieved, then it is reasonable to assume a similar interaction of K^+. When the nickel electrode is charged, the Li^+ ions deintercalate from the graphite, which corresponds to a discharge process for the graphite. Therefore, the spinning sidebands (SSBs) should not appear in the resulting NMR spectrum. This is contrary to the information given by the NMR spectrum for the charged electrode shown in **Figure 18(a)**. A main peak at a chemical shift δ of around 8 ppm and with accompanying SSBs is observed. This suggests that Li^+ ions are intercalated into the graphite layers. As mentioned above, the intercalation–deintercalation process is irreversible; thus, it is possible for Li^+ ions to remain in the graphite layer even in the charged state (electrode A). Usually, the main peak of Li^+ intercalated in graphite is accompanied by SSBs and appears at around 42 ppm. The fact that the chemical shift here is only about 8 ppm may be due to the effect of K^+ co-intercalated with Li^+. That is, the interaction of K^+ with the carbon atoms may weaken the corresponding interaction of Li^+ and may explain why a smaller chemical shift value is observed.

The electrode in the discharged state displays a main peak at around 0 ppm and several SSBs, as shown in **Figure 18(b)**. Compared with the spectrum in the charged state, the background is high and the peaks are broadened. This result means that the spin–spin relaxation time (T_2) of Li^+ has increased and the mobility of Li^+ may be strongly restricted, as predicted by the BPP theory postulated by Bloembergen, Purcell, and Pound. Given the presence of SSBs, it is certain that Li^+ is intercalated in graphite. A main peak should appear at around 8 ppm but it may be weakened by the strong SSBs and hidden by the large background. The effectively zero chemical shift of the main peak implies that the peak may be due to the formation of other ionic Li^+ compounds, such as lithium oxide (Li_2O) or lithium semi-carbonates, at the carbon/electrolyte interface, which is similar to the formation of solid electrolyte interface on the graphite negative electrode anode in the lithium-ion battery system.

A charged nickel electrode without graphite gives only one broad peak at $\delta \approx 7$ ppm, (**Figure 19(a)**). This appears to arise from intercalation of Li^+ into the nickel oxyhydroxide layer. In addition, the presence of paramagnetic Ni^{3+} may account for the broadening of this peak. The peak for the discharged electrode occurs at around 0 ppm and is due to Li^+ adsorbed on the electrode surface (**Figure 19(b)**).

The above ^{7}Li-NMR data suggest that Li^+ is intercalated into the graphite layer. Therefore, it is inferred that Na^+ and K^+ also will probably intercalate into the graphite layer. The theoretical specific capacity based on the intercalation of Li^+ in graphite is 372 mAh g^{-1}. The maximum specific capacity derived from the discharge time of the second plateau is about 200 mAh g^{-1}, which is not an unreasonable value. The weakness of the assumption that the second plateau is due to the intercalation of K^+ in graphite is that the intercalation potential of alkaline cations takes place at a highly positive

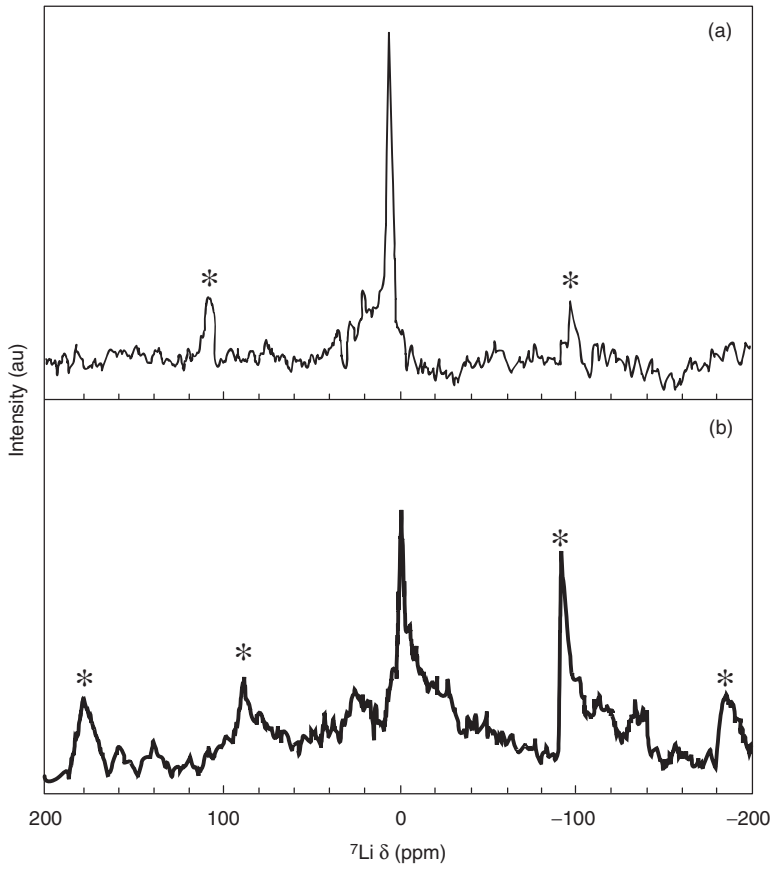

Figure 18 ^{7}Li-NMR spectra of nickel electrode containing graphite: (a) charged and (b) discharged electrode after five full-charge and full-discharge cycles at 3.2 mA cm^{-2}. Electrolyte: 7 mol L^{-1} KOH mixed with 1 mol L^{-1} LiOH. Reference: LiC1 ($\delta = 0.0$) and (*) spinning sidebands. Reproduced with permission from Morishita M, Kobayakawa K, and Sato Y (2005) Alkaline cation intercalation into graphite used as a conducting material in nickel electrode of aqueous secondary batteries. *Electrochemical and Solid State Letters* 8: A539–A543.

potential. It is generally concluded that the intercalation of alkaline cations into a graphite layer hardly proceeds in an aqueous solution because hydrogen evolution occurs. The situation here, however, is quite different. The intercalation of K^+ into β-NiOOH is well documented. Therefore, although it is difficult for K^+ in an aqueous solution to insert directly into graphite, it may be possible for K^+ contained in nickel oxyhydroxide to intercalate into graphite in contact with the nickel oxyhydroxide. This situation is similar to the process by which Li^+ dissolved in an organic electrolytic solution easily intercalates into a graphite, such as that which occurs during the charging of lithium-ion batteries.

During discharge of a nickel electrode, β-NiOOH will first be reduced near 1.2 V and then some K^+ ions will intercalate into the graphite in contact with that nickel hydroxide. This process cannot, however, explain why the second plateau is also observed in a cell that uses a sintered nickel electrode with no graphite or other carbon materials. Accordingly, the following mechanism is proposed. It is well known that some organic additives will be used during the preparation of a sintered nickel plate, such as water-soluble polymers. After sintering, some of the organics will transform to carbon and remain in the nickel plate as a residue. After impregnation of nickel hydroxide into the sintered nickel plate, cyclic voltammetric studies revealed that, whereas the peak current due to the $Ni(OH)_2$–NiOOH oxidation–reduction reaction did not depend on the carbon concentration, a reduction wave near -0.3 V tended to increase with increasing carbon content. The latter observation was ascribed to the reduction of oxygen. The behavior closely resembled that shown in **Figure 17(b)** for nickel hydroxide electrode containing graphite, and is therefore attributed to the intercalation of K^+ ions into carbon.

Conclusions

There have been many investigations of the memory effect shown by nickel-based alkaline secondary batteries when subjected repeatedly to a shallow discharge followed by a full charge (SDFC cycling). Among the several mechanisms put forward to explain this

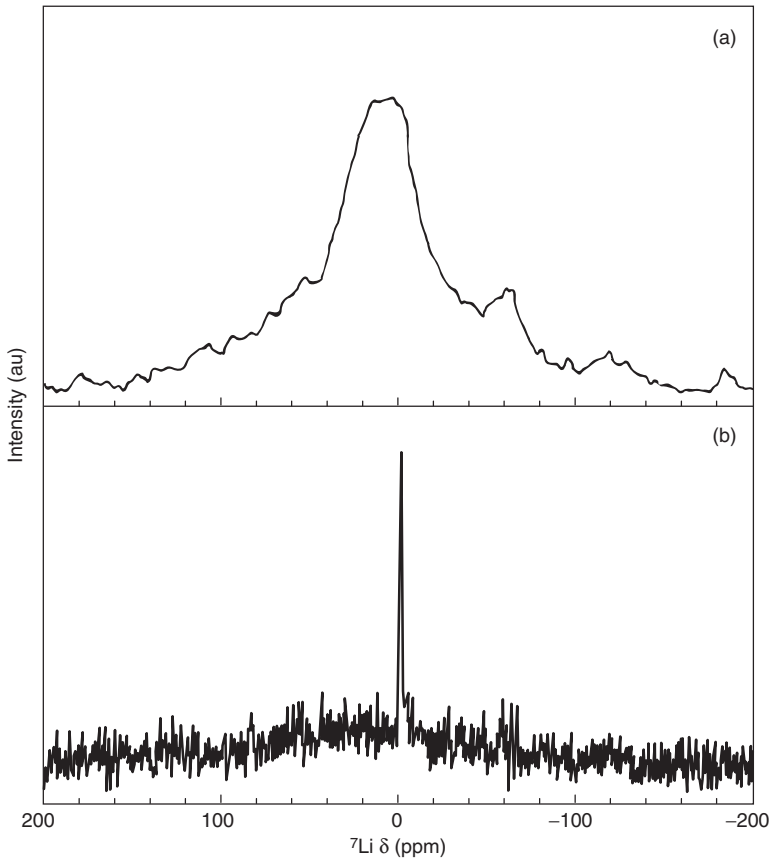

Figure 19 ^{7}Li-NMR spectra of nickel electrode without graphite: (a) charged and (b) discharged electrode after five full-charge and full-discharge cycles at 3.2 mA cm^{-2}. Electrolyte: 7 mol L^{-1} KOH mixed with 1 mol L^{-1} LiOH. Reference: LiC1 ($\delta = 0.0$). Reproduced with permission from Morishita M, Kobayakawa K, and Sato Y (2005) Alkaline cation intercalation into graphite used as a conducting material in nickel electrode of aqueous secondary batteries. *Electrochemical and Solid State Letters* 8: A539–A543.

phenomenon, the most reasonable is that the repeated SDFC process places the battery in an overcharged state and thereby results in the formation of γ-NiOOH in the nickel positive electrode – this γ-NiOOH causes the memory effect.

The second low-voltage plateau, which is sometimes observed during discharge of nickel-based alkaline secondary batteries, has been widely associated with the presence of graphite as a conductive agent in the nickel positive electrode. Specifically, the mechanism is attributed to the intercalation of K^+ ions, which co-exist with nickel oxyhydroxide in the charged positive electrode, into the adjacent graphite during the discharge process. It should be noted, however, that the presence/absence of the second plateau is not completely understood when graphite is not added as a conductive agent. Therefore, more research is necessary to elucidate the exact origin of the second plateau.

Recently, much effort has been focused on how to stabilize α-Ni(OH)$_2$ in strong alkaline media. To date, the partial substitution of nickel by cobalt, aluminum, iron, manganese, or zinc and the addition of organic materials into the α-Ni(OH)$_2$ have been attempted. The incentive for such work lies in the fact that the transformation between α-Ni(OH)$_2$ and γ-NiOOH takes place reversibly without any mechanical deformation. In addition, more than one electron is exchanged per nickel atom so that a higher discharge capacity is to be expected. Thus, it is worth investigating the α-Ni(OH)$_2$/γ–NiOOH system for the development of superior alkaline secondary batteries.

Nomenclature

Symbols and Units

T_2	spin–spin relaxation time
δ	chemical shift

Abbreviations and Acronyms

BPP	Bioembergen, Purcell, and Pound
HEV	hybrid electric vehicle
NMR	nuclear magnetic resonance
PSoC	partial state-of-charge
SDFC	shallow discharge, full charge

SoC	state-of-charge
SSB	spinning sideband
XRD	X-ray diffraction

See also: **Applications – Transportation:** Hybrid Electric Vehicles: Batteries; Hybrid Electric Vehicles: Overview; **Batteries:** Charge–Discharge Curves; **Chemistry, Electrochemistry, and Electrochemical Applications:** Nickel; **History:** Secondary Batteries; **Secondary Batteries:** Overview; **Secondary Batteries – Lithium Rechargeable Systems – Lithium-Ion:** Negative Electrodes: Carbon; Negative Electrodes: Graphite; Overview; Positive Electrode: Nanostructured Transition Metal Oxides; **Secondary Batteries – Nickel Systems:** Electrodes: Cadmium; Electrodes: Nickel; Nickel–Cadmium: Overview; Nickel–Cadmium: Sealed; Nickel–Hydrogen; Nickel–Iron; Nickel–Metal Hydride: Metal Hydrides; Nickel–Metal Hydride: Overview; Nickel–Zinc.

Further Reading

Ahlberg E, Palmqvist U, Simic N, and Sjovall R (2000) Capacity loss in Ni–Cd pocket plate batteries. The origin of the second voltage plateau. *Journal of Power Sources* 85: 245–253.

Barnard R, Crickmore GT, Lee JA, and Tye FL (1980) The cause of residual capacity in nickel oxyhydroxide electrodes. *Journal of Applied Electrochemistry* 10: 61–70.

Barnard R, Randell CF, and Tye FL (1981) Studies concerning charged nickel hydroxide electrodes. Part III. Reversible potentials at low states of charge. *Journal of Electroanalytical Chemistry* 119: 17–24.

Bloembergen N, Purcell EM, and Pound RV (1948) Relaxation effects in nuclear magnetic resonance absorption. *Physical Review* 73: 679–712.

Bode H, Dehmelt K, and Witte J (1966) Nickel hydroxide electrodes. I. Nickel(II) hydroxide hydrate. *Electrochimica Acta* 11: 1079–1087.

Crompton TR (1990) *Battery Reference Book*. Sect. 19.1.2. London, UK: Butterworths.

Dai Y, Wang Y, Eshkenazi V, Peled E, and Greenbaum SG (1998) Lithium-7 nuclear magnetic resonance investigation of lithium insertion in hard carbon. *Journal of the Electrochemical Society* 145: 1179–1183.

Davolio G and Soragni E (1998) The 'memory effect' on nickel oxide electrodes: Electrochemical and mechanical aspects. *Journal of Applied Electrochemistry* 28: 1313–1319.

De Vidts P, Delgado J, and White R E (1996) A multiphase mathematical model of a nickel/hydrogen cell. *Journal of the Electrochemical Society* 143: 3223–3238.

Endo M, Yasuda H, and Yamachi M (1984) Voltammetric behavior of $Ni(OH)_2$ electrode prepared from sintered nickel plaque containing carbon. *The 25th Battery Symposium in Japan*, Abstr., pp. 332–335. Nagoya, Japan.

Falk SU (1960) Investigations on the reaction mechanism of the nickel–cadmium cell. *Journal of the Electrochemical Society* 107: 661–667.

Ganapathy S, Rajamohanan PR, Ganguly P, Venkatraman TN, and Kumar A (2000) Two-dimensional solid state NMR and separation of ^{7}Li quadrupolar interactions in paramagnetic compounds. *Journal of Physical Chemistry A* 104: 2007–2012.

Huggins RA (2007) Cause of the memory effect in 'nickel' electrodes. *Journal of Power Sources* 165: 640–645.

Jones E and Wynne-Jones WFK (1956) Nickel oxide electrode. II. *Transactions of the Faraday Society* 52: 1260–1272.

Klapste B, Micka K, Mrha J, and Vondrak J (1982) Plastic-bonded electrodes for nickel – cadmium accumulators. X. The nature of the second discharge step of nickel oxide electrodes. *Journal of Power Sources* 8: 351–360.

Labat J (1964) Nickel hydroxides. *Annales de Chimie* 9: 399–427.

Laws DD, Bitter H-M L, and Jerschow A (2002) Solid-state NMR spectroscopic methods in chemistry. *Angewandte Chemie International Edition* 41: 3096–3129.

Lurie C (1980) Application of battery reconditioning techniques to achieve capacity restoration: A case history. *Proceedings of the 15th Intersociety Energy Conversion Engineering Conference*, pp. 1634–1637.

Mancier V, Willmann P, and Metrot A (2000) A semi theoretical approach of the second plateau appearing during the discharge of aged nickel oxyhydroxide electrodes. *Journal of Power Sources* 85: 181–185.

Morishita M, Kobayakawa K, and Sato Y (2005) Alkaline cation intercalation into graphite used as a conducting material in nickel electrode of aqueous secondary batteries. *Electrochemical and Solid State Letters* 8: A539–A543.

Morishita M (2006) *A study on the memory effect observed in alkaline secondary batteries*. PhD Thesis, Graduate School of Kanagawa University, Japan. p. 41.

Morishita M, Shikimori S, Shimizu Y, et al. (2006) The memory effect in the partial charge–discharge cycling of alkaline secondary batteries. *Electrochemistry* 74: 532–535.

Motupally S, Jain M, Srinivasan V, and Weidner JW (1998) The role of oxygen at the second discharge plateau of nickel hydroxide. *Journal of the Electrochemical Society* 145: 34–39.

Sac-Epee N, Palacin MR, Delahaye-Vidal A, Chabre Y, and Tarascon J-M (1998) Evidence for direct γ-NiOOH $\leftrightarrow$ β-$Ni(OH)_2$ transitions during electrochemical cycling of the nickel hydroxide electrode. *Journal of the Electrochemical Society* 145: 1434–1441.

Sato Y, Ito K, Arakawa T, and Kobayakawa K (1996) Possible cause of the memory effect observed in nickel–cadmium secondary batteries. *Journal of the Electrochemical Society* 143: L225–L228.

Sato Y, Takeuchi S, and Kobayakawa K (2001) Cause of the memory effect observed in alkaline secondary batteries using nickel electrode. *Journal of Power Sources* 93: 21.

Sato Y, Takeuchi S, Magaino S, and Kobayakawa K (2000) Cause of the memory effect observed in alkaline secondary batteries using nickel electrode. *Bulletin of the Chemical Society of Japan* 73: 1699–1713.

Takeno K, Ikeda K, Shiojima N, Hasebe H, and Sato Y (1990) Charge discharge behavior of nickel–metal hydride secondary cell. *The 31st Battery Symposium in Japan*, Abstr., pp. 157–158. Osaka, Japan.

Taniguchi A, Fujioka N, Ikoma M, and Ohta A (2001) Development of nickel/metal-hydride batteries for EVs and HEVs. *Journal of Power Sources* 100: 117–124.

Torresi SIC, Provasi K, Malta M, and Torresi RM (2001) Effect of additives in the stabilization of the α phase of $Ni(OH)_2$ electrode. *Journal of the Electrochemical Society* 148(10): A1179–A1184.

Van der Ven A, Morgan D, Meng YS, and Ceder G (2006) Phase stability of nickel hydroxides and oxyhydroxides. *Journal of the Electrochemical Society* 153: A210–A215.

Zaghib K, Tatsumi K, Sawada Y, Higuchi S, Abe H, and Ohsaki T (1999) ^{7}Li-NMR of well-graphitized vapor-grown carbon fibers and natural graphite negative electrodes of rechargeable lithium-ion batteries. *Journal of the Electrochemical Society* 146: 2784–2793.

Zimmerman AH and Effa PK (1984) Discharge kinetics of the nickel electrode. *Journal of the Electrochemical Society* 131: 709–713.

Hybrid Electric Vehicles: Batteries

U Köhler, Johnson Controls, Hannover, Germany

Introduction

The idea of combining electrical engines and internal combustion (IC) engines has a long history. In 1901 J. Lohner and F. Porsche had already presented a first hybrid electric vehicle (HEV). But this revolutionary concept did not reach full maturity because the electrical components were not developed. The main concern was the battery, a high-performing battery system with acceptable long-term endurance was not available at the time. The battery of the vehicle shown in **Figure 1** had a weight of not less than 1800 kg.

It was not until the end of the twentieth century that HEVs became a serious alternative to vehicles propelled by an internal combustion engine. The Toyota Prius appeared on the market in 1997 and was the first HEV series vehicle in history. A second version with improved performance came out in the year 2003 (**Figure 2**). Mainly its fuel-saving and extremely environmentally friendly technology were the drivers for the considerable market success since that time. Triggered by the technical opportunities for drastically reducing fuel consumption, other car manufacturers such as Honda and Ford developed their own products. Almost all car producers in the world are now working on HEVs with the clear goal of meeting the demand for fuel-saving and environmentally compatible vehicles.

There are several different vehicle concepts covered under the term hybrid vehicle. The following description is to explain the differences in the technologies that have consequences for the battery system used for them.

Full Hybrid Electric Vehicles

The most popular representative of a full hybrid electric vehicle (FHEV) (also called strong HEV) is the Toyota Prius (**Figure 2**). This type of vehicle uses the electrical storage system alone for relatively short periods in which the combustion engine would run with a lower energy efficiency. Regenerative braking, in which reclaimed energy is stored in batteries, is an important feature. Pure electric driving is possible for short distances, but playing only a minor role. It is regarded as an interesting feature for some special situations such as silent cruising in remote areas. For energy efficiency reasons, the electrical drive system operates at voltage levels above 200 V. The efficient combination of both, the combustion engine and the electrical drive system, enables a reduction of fuel consumption up to 40% in comparison to normal combustion engine-propelled vehicles.

Mild Hybrid Electric Vehicles

Mild hybrid electric vehicles (MHEVs) are a technical alternative to the FHEVs. In comparison to the FHEV, the MHEV needs a lower degree of electrical power performance. Electrical operation is mainly concerned with vehicle start and acceleration phases. Regenerative charging under deceleration and braking contributes to a reduction of fuel consumption. Pure electrical driving is not provided. The electrical drive system of MHEVs operates typically at voltages between 100 and 200 V. Earlier tendencies to realize MHEVs with 42 V systems

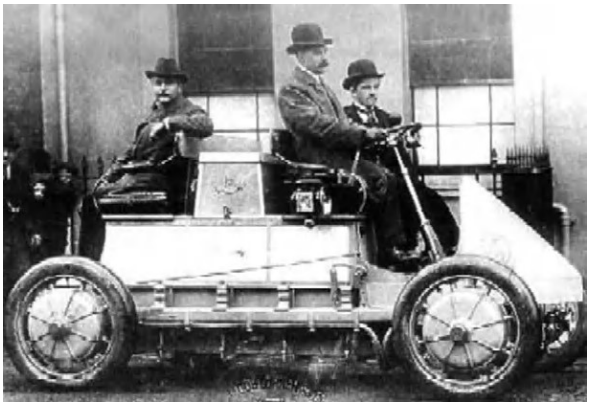

Figure 1 Porsche–Lohner hybrid electric vehicle (HEV) 1901. Source: Wikipedia.

Figure 2 Toyota Prius hybrid electric vehicle (HEV) 2003. Source: Toyota website.

were given up as the addressed energy efficiency goals could not be met. Typical fuel saving of vehicles using mild hybrid drive systems is in the range of 15–20%.

Microhybrid Vehicles

The term microhybrid has become popular for a class of vehicles that use an automatic start–stop system. Under vehicle braking and rest, the IC engine will automatically shut down. There is no electrically operated power assistance to the drive drain. Under urban driving, a reduction of fuel consumption up to 8% can be achieved.

Plug-In Hybrid Electric Vehicles

Plug-in hybrid electric vehicles (PHEVs) combine the advantages of an electrical vehicle with those of a vehicle that uses a combustion engine. The concerns about the action range limitation are faced with the additional employment of an internal combustion engine (ICE), which in the case of exhausting power from the battery system can take over the supply of the power train. Plug-in hybrids have been the subject of current political discussion facing the issue of drastically rising fuel costs. Preferred applications of PHEVs are delivery vans, which can be recharged periodically during their daily driving route, and also private cars, especially those used for daily commuting. Similar to a pure electric vehicle (EV), a PHEV may use power from the grid. The amount of carbon dioxide saving will depend on the power mix with its shares of fossil energy, nuclear energy, and energy from regenerative sources.

Hybrid Electric Buses and Delivery Trucks

Because of their continuous typical stop-and-go operation, city buses are considered as an ideal application for a hybrid drive system. Especially in European and Asian urban areas with relatively short distances between stops, energy recovery under braking and electrical acceleration can significantly improve the fuel efficiency. Fuel savings of more than 30% have been reported.

Technical Demands of Hybrid Electric Vehicle Battery Systems

General demand is for a high energy storage capability with high power performance, low weight, little volume, good long-term endurance, and low price. The actual battery is however always a compromise between these different properties. For hybrid vehicles, the power performance of the battery system is the most important property. Nonetheless, there are significant differences with respect to the requirements for the various vehicle concepts as described in the section 'Introduction'.

Full Hybrid Electric Vehicles

The general purpose of the battery is to efficiently absorb and release energy. This goes along with the demand for a low internal electrical resistance and high power performance. Energy losses because of high internal resistance and lack of charge efficiency could be detrimental to the intended fuel saving. Although not a major focus, the energy storage capability of the battery system plays an important role. Batteries have the general advantage of being capable of storing drastically higher amounts of energy than, for example, competing double-layer capacitors. This allows for more flexibility with the vehicle operation. A small pure electric driving range is a feature appreciated by many customers. The biggest challenge for the battery system is endurance in terms of capacity turnover and calendar life. A battery life covering the whole life period of the vehicle is the goal.

Typical technical data for an FHEV battery are as follows:

Voltage range	200–300 V
Discharge power	>35 kW
Recharge power	>30 kW
Recharge pulse power	>40 kW
Low-temperature (−28 °C) discharge power	>4 kW
Energy content	1.5–2 kWh
Capacity turnover (at <5% DoD)	>10 000
Calendar life	>10 years

DoD, depth-of-discharge.

Mild Hybrid Electric Vehicles

Batteries for mild hybrid vehicles are characterized by lower demands for power performance in contrast to those for FHEV batteries. A high energy efficiency is also essential. Because pure electric operation is not provided, the energy content may be small.

Typical technical data for an MHEV battery are as follows:

Voltage range	100–200 V
Discharge power	>15 kW
Recharge power	>15 kW
Recharge pulse power	>20 kW
Low-temperature (−28 °C) discharge power	>4 kW
Energy content	0.8–1 kWh
Capacity turnover (at <5% DoD)	>5000
Calendar life	>10 years

DoD, depth-of-discharge.

Microhybrid Vehicles

Battery systems for micro-HEVs have a similar function as batteries in a normal vehicle. They have to supply sufficient power to the electrical starter for cranking the IC engine over a very short period of time, and they have to supply much more frequently than in normal vehicles. The consequence is there is a demand for a drastically higher capacity turnover than for normal vehicles.

Voltage	12–14 V
Discharge power	>5 kW
Low-temperature (−28 °C) discharge power	>3 kW
Energy content	0.5–1 kWh
Capacity turnover (at <1% DoD)	>300
Calendar life	>3 years

DoD, depth-of-discharge.

Plug-In Hybrid Electric Vehicles

The energy storage capability mainly depends on the customer's expectations in terms of pure electric driving. A typical mid-class vehicle with a typical weight of 1.5 ton consumes around 200 Wh km^{-1} and, for a 50 km electrical range, will need a battery with ~10 kWh storage capacity. Restrictions to maximum weight and volume for the energy storing device are regarded as the biggest problems with PHEVs.

A typical specification of a PHEV battery may look as follows:

Voltage range	200–300 V
Energy content	>10 kWh
Discharge power	>40 kW
Recharge power pulse	>20 kW
Recharge time	<5 h
Low-temperature (−28 °C) discharge power	>6 kW
Capacity turnover (at 60% DoD)	>3000
Calendar life	>10 years

DoD, depth-of-discharge.

Hybrid Electric Buses and Trucks

Owing to the significantly higher vehicle mass in comparison to normal passenger vehicles, buses and trucks need much bigger battery systems. Because their specific functions with respect to engine start, power boost, and regenerative braking are very similar to those of an FHEV system, the batteries needed for this purpose represent more or less a scale-up of the FHEV battery systems. For improving the energy efficiency, bus and truck batteries are often operated at significantly higher voltages than FHEVs. These voltages may be as high as 700 V.

Voltage range	400–700 V
Discharge power	100–200 kW
Recharge power	50–100 kW
Recharge pulse power	100–200 kW
Low-temperature (−28 °C) discharge power	20 kW
Energy content	>10 kWh
Capacity turnover	>10 000
Calendar life	>5 years

The diagram in Figure 3 displays the typical energy and power demands for the different applications.

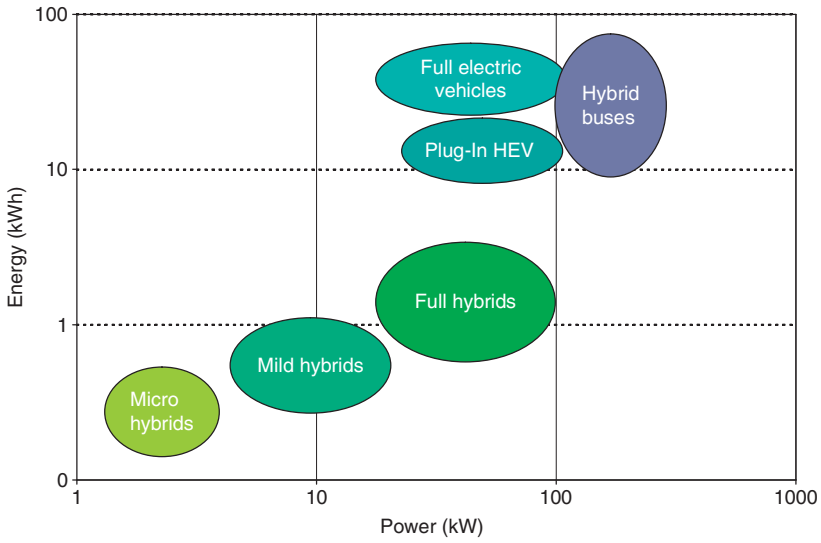

Figure 3 Energy and power requirements in various types of hybrid electric vehicles (HEVs).

Electrochemical Energy Storage Systems for Hybrid Vehicles – Characteristic Parameters

There are characteristic parameters that are used for describing and benchmarking the technical capabilities of electrochemical energy storing devices.

Specific and Volumetric Power

This parameter is regarded as the most important one for HEVs, because power is the most essential feature for an HEV battery. High power capability usually goes along with low energy losses because of low electrical resistances and low polarization effects. A high utilization of the employed electrode mass is a precondition for realizing a device with acceptable mass, volume, and cost. Discharge and recharge performances are generally determined by the electrochemical conversion kinetics at the electrodes, the conductivity of electrolyte, and the electrical collectors.

Specific Energy and Energy Density

Although there is more emphasis on power, energy is also an important parameter. It is especially the energy content that makes batteries the preferred choice compared to capacitors. Capacitors deliver power only for a short period of time and with a much steeper voltage characteristic. Materials with high specific energy and energy density are required. Weight and volume of the passive components have to be kept low.

Energy Efficiency

Energy efficiency of a battery system is defined as the ratio of dischargeable energy to charged energy. As this ratio is directly related to the energy-saving properties of the vehicle, the need for a high energy efficiency is evident. High energy efficiency directly translates into low waste heat generation in the batteries, which is beneficial for battery life suffering from thermal stress.

Capacity Turnover

A long service life is an important demand for an energy storage system as it is for other components in a vehicle. In order to avoid a battery change during the normal life period of a vehicle, materials and components have to be selected according to the demands. The small state-of-charge (SoC) window within which most HEV batteries are operated is very much in favor of a long-term endurance. Performance losses by capacity decrease and power fading are mostly related to stress and corrosion phenomena under charging and discharging reactions. High temperature significantly accelerates the altering processes.

Calendar Life

Calendar life refers to life period of a battery until failure with or without operation. A high capacity turnover is not directly related to a calendar life. There can be chemical processes inside the electrochemical storage systems that do not depend directly on the operation, but proceed continuously. Mostly these effects show a strong temperature dependence.

Electrochemical Storage Systems and Their Use for Hybrid Electric Vehicle Battery Systems

With respect to the general requirements and specifications described in the previous sections, the following four systems (operating at different voltage levels) out of the list of known electrochemical systems are of interest for an energy storage device to be used in HEVs:

- lead–acid (2 V),
- nickel–alkaline: Ni–MH (1.2 V), Ni–Cd (1.2 V), NiFe (1.2 V), NiZn (1.4 V),
- lithium ion: 3.6 V (carbon-based anode), 2.3 V (titanate-based anode), and
- sodium–nickel chloride (2.3 V).

Lead–Acid Batteries

The lead–acid battery system

Lead–acid batteries with a system voltage of 2 V per cell are the most widespread automotive battery systems. Almost all vehicles in the world use lead–acid batteries for starting, lighting, and ignition (SLI) applications. A large majority of these batteries are based on flooded cells in which liquid electrolyte fills the open pore volume in the electrodes and the separator.

Flooded batteries

These batteries are not designed for very high-capacity-throughput figures. The main purpose is to serve the cranking of the vehicle, which usually takes a couple of 100 ms at the maximum. Most critical demand is the cranking of the engine at low temperatures down to −30 °C. Normal SLI batteries have a life span of around 5–6 years.

The limitation to only short starting pulses with limited capacity turnover has allowed the development of batteries with a relatively low weight. This is in contrast to other lead–acid batteries that are used for example in industrial applications. The use of new corrosion-suppressing lead alloys for the grid and new active masses with a high degree of utilization has enabled a significant reduction of the amount of lead used in the battery.

Deep discharge cycling however is a general problem with normal lead–acid SLI batteries. Especially under deep discharge conditions that are not unusual for HEV applications, there is the risk of a reduced sulfuric acid concentration in the upper parts of the batteries. This phenomenon, called 'acid stratification', is hardly reversible. It may permanently reduce the function of the battery. Mainly the power performance is affected.

Absorbent glass mat batteries

Absorbent glass mat (AGM) batteries in general have a very similar battery design as normal liquid-based batteries. The main difference is in the function of the separator and the electrolyte. The separator consisting of a porous polypropylene (PP) foil is replaced with a separator consisting of a glass mat fiber sheet that absorbs the sulfuric acid electrolyte. By this electrolyte immobilization, the batteries can be operated independent of their orientation and they are protected from electrolyte leakage or spillage. The biggest advantage, however, is the avoidance of the 'acid stratification' effect during a more demanding battery operation. This is the reason why AGM batteries have been introduced in HEV-like applications.

Two different technologies may be used for AGM batteries. Besides the prismatic version (Figure 4), there is a battery type that uses cylindrical cells (Figure 5). The prismatic battery uses rectangular electrode plates that are very similar to those used in normal SLI lead–acid batteries with liquid electrolyte. The electrode stacks are contained in the prismatic compartments of a plastic housing and are interconnected through the plastic walls as in common lead–acid batteries. The cylindrical technology is based on spirally wound electrodes. Electrode strips, which are separated by a glass fiber sheet, are spirally wound into coils. These coils are inserted into the cylindrical compartments of a plastic housing. Mainly because of the specific electrode shape with a potentially higher surface area, there are some advantages with the round-type cells particularly with respect to low-temperature operation and long-term endurance.

Gel-type batteries

Employing a gel capable of absorbing sulfuric acid is another way of fixing the electrolyte. Lead–acid gel-type batteries are widely used for electric transportation, e.g., in electric bicycles, EVs, small electric buses, and for in-house transportation systems. The disadvantages of low-temperature discharge performance and a lower power performance are the reasons why gel-type batteries are not used for SLI applications.

ULTRA batteries

The battery system developed by CSIRO Energy Technology/Furukawa Battery Co. is a hybrid energy storage device that combines an asymmetric supercapacitor and a lead–acid battery in one unit. It is a combination of the advantages of both technologies without using extra electronic controls. The system has a greater power and a significantly improved service life in comparison to other lead–acid-based battery systems. Depending on the layout of the system, specific power may exceed 1000 W kg^{-1}. Under partial SoC, cycling

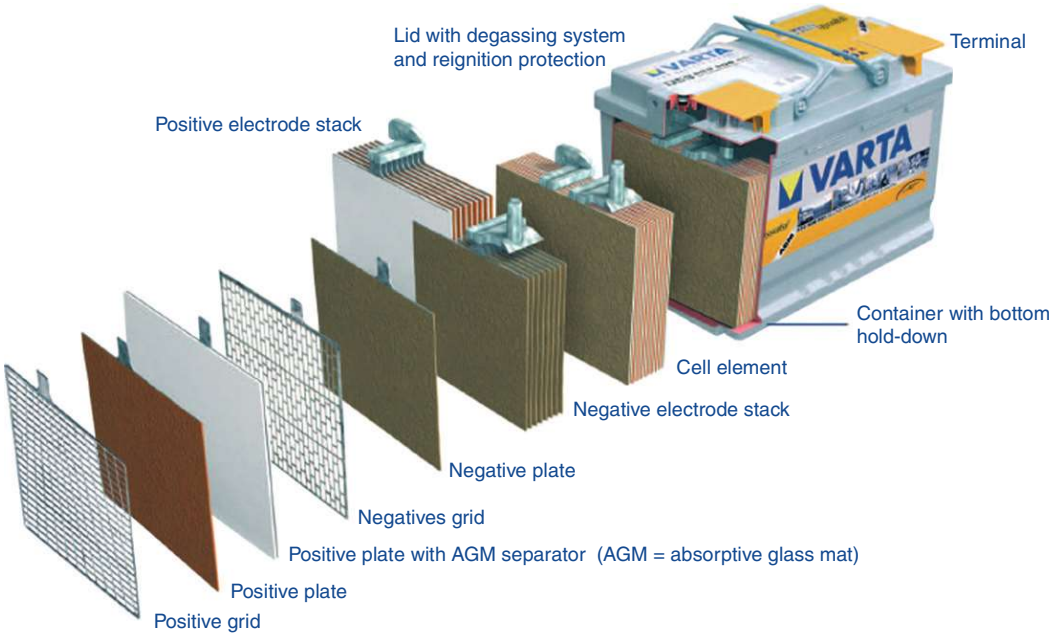

Figure 4 12 V lead–acid battery (Johnson Controls – VARTA) based on absorptive glass mat technology.

Figure 5 12 V lead–acid battery (Johnson Controls – OPTIMA) with spirally wound cells based on absorbent glass mat (AGM) technology.

operation up to 10 000 capacity turnovers could be demonstrated.

Nickel–Metal Hydride Batteries

Alkaline rechargeable batteries based on nickel hydroxide as the active cathode material have a history of more than 100 years. Four electrochemical couples have been under development:

- nickel–iron (Ni–Fe),
- nickel–cadmium (Ni–Cd),
- nickel–zinc (Ni–Zn), and
- nickel–metal hydride (Ni–MH).

In spite of tremendous efforts, the Ni–Fe system (system voltage: 1.2 V per cell) and the Ni–Zn system (system voltage: 1.4 V per cell) have never achieved a technical stage that would have allowed them to be considered for a wider use in automotive applications. Also in other areas (industrial batteries and portable applications) they have not succeeded mainly because of technical reasons. The Ni–Cd system (voltage: 1.2 V) however has been a big technical and market success for more than 100 years. Since the 1990s, Ni–Cd batteries in the portable markets have been displaced more and more by the new battery system – Ni–MH. The reason was the higher energy storage capability achievable with Ni–MH and the general concern about cadmium as an environmentally hazardous material. Although nickel–iron, nickel–cadmium, and nickel–zinc batteries do not play an essential role in HEVs, they are briefly described here.

Nickel–iron batteries were invented by Thomas Alva Edison in 1901, and they are the first rechargeable alkaline battery system for practical usage. They played a certain role in the early years of the electrical vehicle. Despite many efforts, Ni–Fe batteries never succeeded in winning a major market share for a couple of reasons. Spontaneous discharge of the negative iron electrode is the reason for a poor charge stability. The related hydrogen generation and the water loss do not allow for a maintenance-free operation. Furthermore, iron contamination from the negative counterelectrode causes a poisoning of the positive electrode, negatively affecting performance and life endurance.

Nickel–cadmium batteries invented by Waldemar Jungner almost in parallel, have overcome the technical problems described above. Key was the replacement of iron as the active material at the negative polarity with cadmium. Nickel–cadmium batteries thus became a serious competitor to lead–acid batteries in many fields. There are three general significant advantages with these batteries. Their weight is some ~20–30% lower, they have a drastically better life endurance especially under deep discharge cycling, and their low-temperature discharge performance is superior.

Nickel–cadmium cells have been manufactured as a maintenance-free sealed battery system since the 1950s. The introduction of new plastic fiber-based separator materials and the application of some other important inventions have enabled a hermetically sealed cell that could be operated in any position. This was a crucial step for making the system absolutely maintenance-free and hence usable for portable applications. Similar efforts were made also for big cells and batteries (**Figure 6**). But difficulties with a homogeneous distribution of the electrolyte and an efficient waste heat dissipation turned out to result in limitations with respect to larger cell formats. Finally, it has been an open cell version (developed to a technical status requiring only very low maintenance and service), which has become the most suitable technical solution for traction systems. Moreover, as the Ni–Cd battery system became a subject of environmentally related discussions, the step to the more environmentally compatible Ni–MH system was the better choice for automotive applications. Cadmium is a hazardous heavy metal and has been banned from many applications.

The higher system voltage (1.4 V) as well as the lower specific weight of zinc versus cadmium make the Ni–Zn system an attractive candidate for automotive battery systems. This is the reason why there have been so many efforts over a more than 70 year period with regard to this electrochemical system. A real technical breakthrough in this technology making it competitive with the established systems is still not in sight. There are two main obstacles to practical usage of this system. The cycling endurance is not satisfactory and is far away from

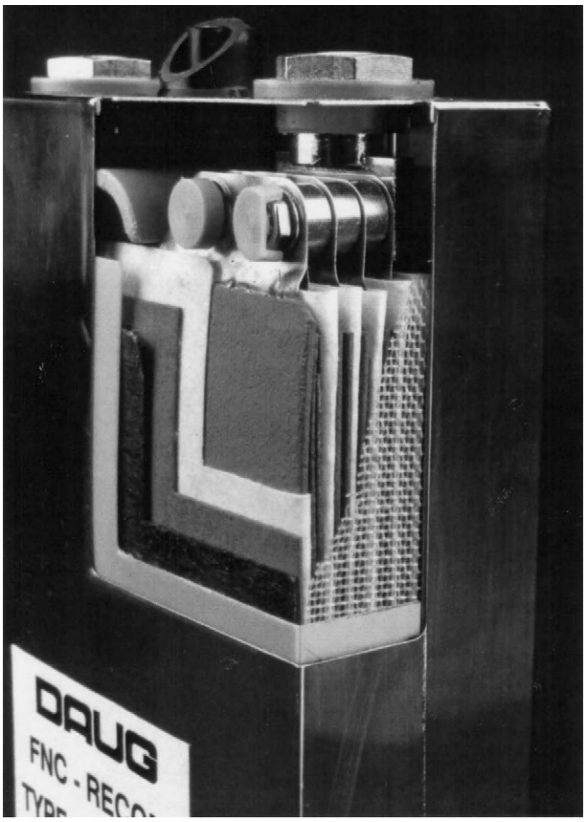

Figure 6 Sealed prismatic Ni–Cd cell (DAUG 1992).

what is possible with other electrochemical systems. The most severe problem is the tendency to form zinc dendrites. High solubility of zinc in the caustic electrolyte and its replating during charging lead to the generation of soft shorts over a long period of time. Furthermore, there is the general problem to realize a gastight, sealed system that would enable a maintenance-free operation as is required for automotive applications. Although the earlier problem of spontaneous gassing with hydrogen evolution could be overcome to a certain degree, there is still the risk of hydrogen generation under high-rate charging. The thus-generated hydrogen cannot be reconverted to water inside the cell in a reasonable period of time.

The industrial progress achieved with Ni–Cd battery systems over a period of almost 100 years was the basis for the fast implementation of Ni–MH as the follower system. The basic technologies for the electrodes as well as for other components used in Ni–MH cells are very similar to what has been developed for Ni–Cd cells in a variety of applications.

The nickel–metal hydride system

The Ni–MH system was developed in the 1980s for energy-hungry new electronic devices. It had its best period on the market for portable batteries in the 1990s with a volume of more than 1 billion cells per year. With the appearance of the lithium-ion battery system in the mid-1990s, a rapid displacement process started. The reasons for this were the evident technical advantages of the lithium-ion system, drastically lower weight, and a lower volume. However, the Ni–MH system had an exciting comeback with the market penetration by HEVs at the beginning of the twenty-first century.

There are some significant differences between the Ni–MH battery technology employed for cells and batteries in portable applications and that used for automotive batteries. Specific power performance demands of automotive systems are typically one order of magnitude higher. The requirements to longevity are oriented at the life endurance of the vehicle, as a replacement may undermine the economical benefit of the HEV concept. High power performance was achieved by various measures. The most important were changes in the electrode geometry and the implementation of a current collector system capable of carrying high currents. High power performance requires a high electrode surface area and a low electrode thickness. Active storage materials with high discharge capability, good electrical conductivity, and long endurance properties are the key components required for the high-power Ni–MH cells.

Positive electrode

There are two types of electrodes that are usually being employed in Ni–MH cells – the sinter-type and the foam-type electrode. The sinter electrode is based on the use of a highly porous electrode body manufactured by a nickel powder-based sinter process on a nickel-coated steel strip. The pore volume of the thus generated sinter body is filled with nickel hydroxide as the main constituent and with hydroxides of additives in a couple of subsequently performed precipitation procedures. The general advantage of the sinter-type electrode is its high internal surface area and its fine pore structure. This and the relatively high amount of conductive material give the sinter electrode a high discharge and recharge performance characteristic. Sinter-type electrodes are very stable over an extremely high number of cycles and under deep discharge storage conditions.

Nickel foam-type electrodes employ a nickel metal foam material with a high initial pore volume in which the active mass is filled by a special coating process. The nickel foam itself with a skeleton-like structure is produced from a plastic foam that is electroplated with nickel from a liquid solution. In a subsequent pyrolysis, the polymer is burned out leaving a porous metal foam. The open pore system is filled with the active electrode mass. It consists of a mixture of beta-type nickel hydroxide with spherical particles as the main component and additives for improving the electrical conductivity and the charge absorption capability. The advantage of

the nickel foam electrode in comparison to the sinter-type electrode is a 10–15% higher energy storage capability. Moreover, the manufacturing process is less complicated and less environmentally sensitive than is the production process of the sinter-type electrode.

Negative electrode

A standard negative electrode manufacturing technology for automotive Ni–MH cells is the slurry coating process. The paste consists of an alloy powder capable of reversibly storing hydrogen, binder materials, and carbon powders as the main constituents. The slurry is used for coating thin layers to both surfaces of a perforated nickel-coated steel strip. After drying, the layer is compacted to its final thickness. The thickness of the layer and the particle size of the alloy powder are essential for the high power performance.

Power performance and long-term endurance of the negative electrode are also highly determined by the composition of the alloy powder. The potential tendency to corrosion makes the hydrogen storing alloy the most sensitive component in the cell. Almost all hydrogen storing alloys used in automotive applications at present have an AB_5-type crystalline structure. The A-part consists of a misch metal (MM) with a special combination of rare earth elements. In the B-part, nickel is the main constituent. The degree of its substitution with other metals such as cobalt, manganese, and aluminum or other metal elements has a major influence on electrode and cell performance properties. A certain amount of cobalt is indispensible for a long cell life endurance by suppressing the corrosion processes at the alloy particles. A typical alloy composition for an automotive cell is as follows: $MM_1Ni_{3.9}Co_{0.4}Mn_{0.3}Al_{0.4}$. Generally, the application of a slight over-stoichiometry (AB_{5+x}) is helpful for a better long-term stability. Also, the material composition of the A(MM)-part may have a significant influence on performance properties. This is valid for the composition of the rare earth fractions (lanthanum, cerium, neodymium, etc.) in MM in general. However, a small degree of MM substitution with other metal components, e.g., zirconium, may favor stabilization of the power performance over long-time operation.

Cell design

In contrast to cells used for portable applications, cells for automotive systems have some special design features.

Cell match: In all sealed Ni–MH cells, the negative electrode capacity (N) is oversized to the capacity of the positive electrode (P). An N/P match significantly greater than 1 is the precondition for manufacturing sealed and maintenance-free cells. For meeting the high power demands of automotive applications with respect to high charge and discharge rates, the negative electrode capacity in automotive cells however exceeds the capacity of the positive electrode by a much higher extent than in portable battery cells. The negative excess capacity is also important for compensating the negative capacity losses caused by corrosion over battery service life.

Electrode geometry: As high power is the focus of HEV batteries, the surface area of the electrodes is drastically higher and the thickness significantly lower. Also, because of the high currents, the application of a multicontact collector design at the electrode edges is essential. A tab design, which is generally used for portable batteries, would not be sufficient for carrying the high currents.

Separator and electrolyte: For meeting the long-term life expectations and the required high-capacity-throughput figures, special separator materials have to be used. The first goal is to reliably prevent the cells from short-circuiting. The second goal is to hold a sufficient amount of electrolyte over the entire life span for a stable power performance. Modern Ni–MH battery systems employ PP/polyethylene (PE) fiber sheet materials with specially treated surfaces. Besides their function of maintaining the hydrophilic properties, the specially treated surfaces of the fibers also act as a trap for ammonia molecules (originating from impurities of nickel hydroxide manufacturing process) that are responsible for undesired self-discharge reactions. As with portable cells, the electrolyte is a strong caustic solution mainly based on potassium hydroxide with a concentration of around $7\,mol\,L^{-1}$(30 wt%). Special demands for charge acceptance and discharge capability at high and low temperatures may require necessary variations of the composition involving the addition of lithium and sodium hydroxides to the potassium hydroxide.

Cell types

Two different cell types are currently being used for automotive batteries: cylindrical cells and prismatic cells.

Cylindrical cells

Cylindrical cell manufacturing is the more conventional way of cell manufacturing. This type of cell is widespread in the portable battery business. Two polarities separated by the fiber sheet are spirally wound on a mandrel. The thus-formed electrode coil is provided with electrical collectors and inserted into the cell can. Winding has been a proven technology for many years. It was the basis for the mass manufacturing of Ni–Cd cells in the beginning of sealed alkaline rechargeable cells for portable systems. It is a reliable and very cost-effective manufacturing method. Especially, the high power demanding applications made some changes necessary. The negative polarity is usually electrically connected to the cell case forming the negative terminal. The positive electrode is electrically connected to the cell lid. For safety reasons, a resealable vent is integrated in the cell lid. In the case of

Figure 7 Nickel–metal hydride module based on cylindrical cells (Johnson Controls – Saft).

Figure 9 Prismatic Ni–MH module (Panasonic EV).

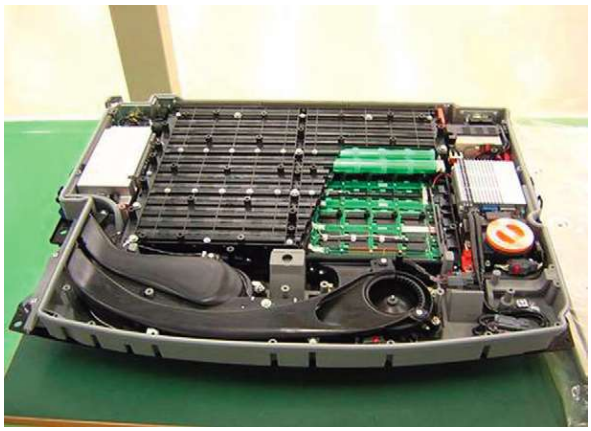

Figure 8 Battery for full hybrid electric vehicle (HEV) (Ford Escape) with cylindrical Ni–MH cells.

accidental situations such as overcharging, over-discharging, short circuit, and overheating, it has to be ensured that no safety-critical pressure build-up occurs inside the cell.

Mainly, cells with relatively low capacity (up to 10 Ah) are manufactured as cylindrical cells. Technical limitations for using cylindrical cells of bigger size are a consequence of the limitations in heat transfer. Too high diameters pose problems with waste heat dissipation from the interior of the cells. Currently, the most popular type is a D-size cell, a derivative of a corresponding cell used for portable battery applications. The cylindrical cells are usually assembled into cell rods (Figure 7). These cell rods are used as the basic components for the final battery assembly (Figure 8).

Prismatic cells and modules

In prismatic cells, electrode stacks are built with single rectangular positive and negative electrode plates separated by a fiber sheet. Often, one of both polarities is enveloped in a bag of fiber sheet material. This facilitates the automatic stack assembly in the production process. For the cell housing, steel and plastic materials are used. Steel has a certain advantage with respect to long-term endurance as it is not permeable to water and hydrogen.

A prismatic cell design is the preferred way for realizing high cell capacities. Low thickness and high surface area are in favor of a good heat exchange with air or liquid as coolants. Moreover, prismatic cells offer advantages with respect to an easier and more volume-efficient packaging. Available prismatic cells have a relatively wide range of capacities ranging from ~ 5 Ah to more than 100 Ah.

Full HEV applications require relatively small, but highly performing cells connected in series. As handling a high cell count is a general problem, there has been the idea of a module, which comprises a certain number of cells in one subunit. The Japanese company Panasonic EV was the first to generate such a module (Figure 9). Nickel–metal hydride electrode stacks are housed in separate compartments of a plastic case. The cells in the neighboring compartments are interconnected through the separating plastic walls in between the single cell compartments. The modules usually have a common head space. This allows a significant simplification of the design in comparison to a corresponding single cell arrangement. The number of safety vents and terminals can be drastically reduced. By their high surface area the modules enable a good heat transfer and an efficient cooling. The advantage of the prismatic format is that it enables an efficient packaging of the battery (Figure 10).

Technical data of nickel–metal hydride cells

The Ni–MH battery system can serve a wide range of energy and power demands as indicated in the following table:

	High energy	*High power*
Specific energy (Wh kg^{-1})	70	43
Specific power (W kg^{-1})	140	1600

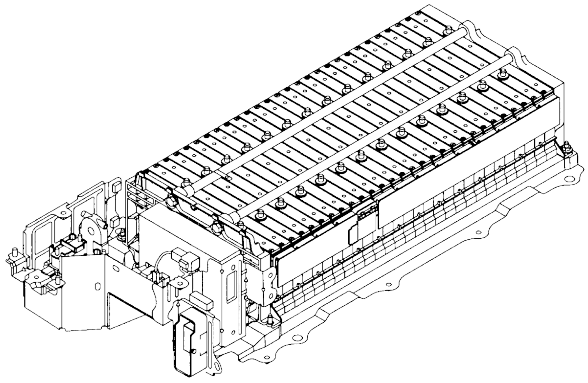

Figure 10 Full hybrid electric vehicle battery with prismatic NiMH modules (Panasonic EV-Toyota).

Energy density ($Wh\,L^{-1}$)	200	90
Power density ($W\,L^{-1}$)	400	3300
Capacity turnover		
– DoD = 80%	2000	>4000
– DoD = 5%	8000	>20 000

DoD, depth-of-discharge.

Especially, the high power achievable with the Ni–MH battery design is the greatest attraction for automotive applications. Specific power performance at a cell level may be up to $1600\,W\,kg^{-1}$. Capacity turnover figures of more than 20 000 times the nominal capacity (at 5% depth-of-discharge (DoD), 25 °C) have made the Ni–MH battery the enabling energy storage technology for the first generation of HEV. As an aqueous-based system, it has intrinsic safety properties similar to lead–acid batteries. In contrast to the high-power system, the high-energy version originally planned to be used for EVs has not achieved significant commercial relevance. Even in its energy-optimized version, a Ni–MH battery is too heavy for becoming an enabler for the EV.

A certain disadvantage of the Ni–MH system is the irreversible energy loss caused by the hysteresis character of the nickel hydroxide electrode under charge and discharge. This behavior generally limits the energy efficiency in terms of the ratio of dischargeable energy to charged energy to a value of about 92% at the maximum (at room temperature). Electrical resistance–related losses further decrease the energy efficiency.

Nickel–metal hydride battery management

Batteries comprise a multitude of single cells in a series. A parallel arrangement of cells is unpopular as it needs extra efforts in the battery management. As indicated in Technical Demands of Hybrid Electric Vehicle Battery Systems, modern hybrid vehicles work with relatively high voltages. Taking into account that one single Ni–MH cell has a voltage of only 1.2 V, this means that a relatively high cell count is required. Besides the general need for managing the risks of high voltage, there is the task of managing the cells in such arrangement for an optimum function. The adjustment of an optimum and well-balanced SoC over all cells is compulsory for an efficient operation.

Ni–MH batteries offer a relatively wide SoC range with a stable energy efficiency. The voltage characteristics as well as the internal resistance are relatively independent of SoC. This results in a stable power performance even with a small battery. It opens chances of using a small battery system even for some short-range electrical driving. The typical battery operation range for HEV operation usually lies between 50% and 60% SoC. At these SoC levels, the battery on the one hand provides sufficient discharge power capability for serving the discharge power needs. On the other hand, it has the ability of reabsorbing energy even at high rates as may occur particularly under regenerative braking.

Keeping the whole cell ensemble at a balanced SoC level is also a necessity for making the system reliably work over a long life period. Ni–MH cells with a high and uniform charge retention over time do not need a single cell monitoring. Some charge balancing has to be done from time to time by a controlled low-rate overcharging and an SoC readjustment later. The control of the electrical operation is organized on a module or battery segment base.

Figure 11 illustrates how the monitoring and control system of a Ni–MH battery operates. Module/segment voltages and temperatures are monitored by module control units, which transmit their data to the battery management system (BMS). The BMS controls the consistency of the voltages and the temperatures in the battery pack. From these data, the SoC value and the state-of-function (SoF) are determined. The SoC determination is usually done in two different ways in parallel. The characteristics of module voltages versus SoC allow for a direct determination of the SoC. In parallel, the SoC is controlled by a balancing of charge input to charge output (bookkeeping method). In case the module voltages indicate an unacceptable SoC imbalance, the BMS automatically initiates an equilibration charging procedure.

Lithium-Ion Batteries

The lithium-ion system

There is a strong tendency these days to make the lithium-ion system available for automotive applications also. First car manufacturers have announced the introduction of HEVs with lithium-ion batteries in the year 2009.

The lithium-ion battery system was developed in the 1980s and came to the portable battery market in larger volumes by the mid-1990s. Japanese companies such as

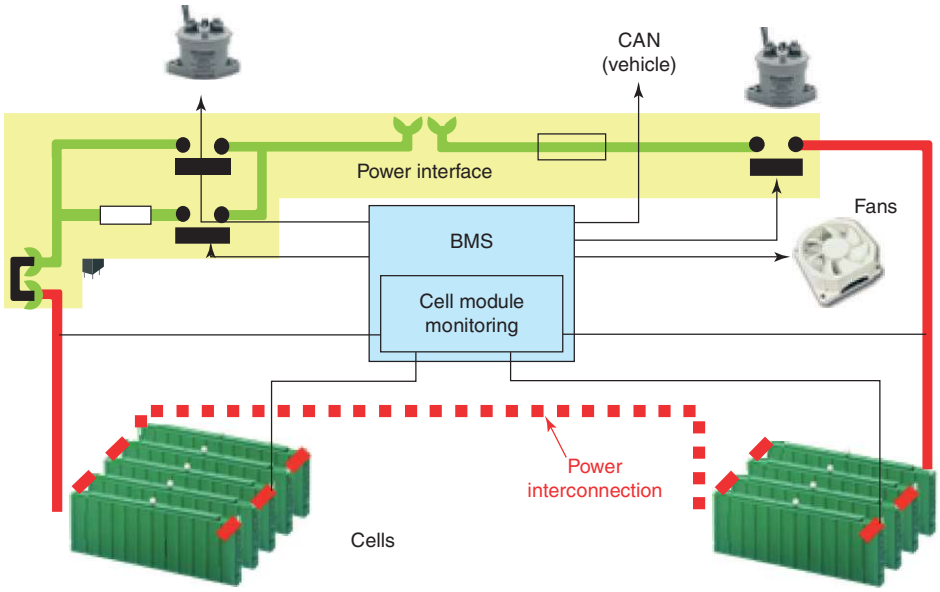

Figure 11 Battery management system (BMS) for Ni–MH batteries (schematic).

SONY and ASAHI were the pioneers in this development. The first portable battery cells used lithium cobalt oxide ($LiCoO_2$) cathode material exclusively. Motivation for the fast introduction of the lithium-ion batteries was electronic devices with high energy consumption. The tendency to smaller and lighter devices has pushed the development of lithium-ion batteries tremendously over the past decade. Application of new materials and components enabled an almost tripling of the energy density of lithium-ion cells.

The lithium-ion polymer system is a special form of a lithium-ion battery system. In this cell type, the liquid electrolyte is fixed by a porous polymer material. Because of the lower amount of liquid electrolyte, the internal electrical resistance is significantly higher. Lithium-ion polymer batteries are generally not used for high-power applications. They are mainly used for high-energy applications with medium power performance. Lithium-ion batteries require a more sophisticated operation control in comparison to Ni–MH and lead–acid batteries. Voltage limitations have to be carefully considered for avoiding cell damage and also for safety reasons.

In contrast to portable batteries, automotive batteries have to meet much stronger demands. For applications in FHEVs and MHEVs, a specific power performance beyond the $2500\,W\,kg^{-1}$ (at cell level) is required. But lithium-ion batteries are also a candidate for EV and PHEV batteries. Cells with a high-energy design may achieve specific energy values of more than $150\,Wh\,kg^{-1}$. Besides power performance and energy, there is the demand for a long life endurance. Portable lithium-ion batteries have a typical life in the range of 3–4 years. For automotive applications, a life period of more than 10 years is required.

Similar to what was true for the Ni–MH battery systems, Li-ion automotive batteries have also benefited from what has been achieved for portable batteries. Particularly, active storage materials, organic solvent–based electrolytes, conductive salts, and separator materials have been the subject of many successful innovations.

Positive electrode

The cathode powder is the most crucial material not only with respect to power and energy performance, but also with respect to life, abuse tolerance, and cost. Lithium cobalt oxide ($LiCoO_2$) is the still-preferred basis material for portable batteries but not for automotive batteries. One reason is the limitation of calendar life and the achievable capacity turnover figures under the dramatically more aggressive conditions in vehicles. In addition, there could be a severe raw material availability problem. Cobalt is not an abundant element, only produced in relatively low volumes as an allied product to nickel and copper from mining. If being used for automotive products in larger volumes, a shortage and a price increase would be the consequence. This fact and its already high price level make cobalt-based materials prohibitive for this special use. Best-suited materials for an overall performance in automotive applications are currently nickel-based oxides. Lithium–nickel oxides with a certain degree of substitution with other elements (e.g., $LiNi_xCo_yAl_zO_2$), $LiNi_{1/3}Co_{1/3}Mn_{1/3}O_2$, are currently regarded as the best-suited materials. At present, they are the only materials that have shown evidence of exceeding the 10-year-life threshold.

Besides the nickel-based oxides mentioned above, a couple of alternative cathode materials have been under

investigation for a long time for their employment as cathode materials in lithium-ion battery system. Despite many efforts, the manganese spinel-based materials could not fully overcome life problems when used for a lithium-ion 4 V system (in combination with a carbon negative electrode). Lithium iron phosphate ($LiFePO_4$) is a new candidate for an advanced positive cathode material that is getting more and more attention. Earlier problems with high electrical resistance because of the lack of electrical conductivity could be overcome meanwhile. The high thermal decomposition temperature of $LiFePO_4$ makes this material particularly interesting with respect to abuse tolerance.

A standard manufacturing method for the positive electrode is thin film coating of a slurry to an aluminum metal foil. The slurry containing the active powder, conductive carbon, and a binder as the main constituents is processed with an organic liquid. Owing to the very thin layers and the required high accuracy of the area-related mass loading, a highly sophisticated coating equipment has to be employed.

Negative electrode

For the negative electrode, usually a carbonaceous material capable of reversibly intercalating lithium ions is used. Depending on the technical and process demands, several different carbon materials and configurations (e.g., graphite, hard carbon) may be used. The quality of the carbon material has a significant influence on the later cell performance. For enabling a good fast charge and high discharge capability, the carbon material must be capable of easily absorbing lithium ions from the electrolyte. On the contrary, a long-term performance stability has to be ensured. Crucial for this is the generation of a stable so-called solid electrolyte interphase (SEI) protecting the electrolyte from being dissociated at the surface of the negative electrode.

An alternative anode material to the carbon-based material is lithium titanate ($Li_4Ti_5O_{12}$). A disadvantage of cells using this material is the lower cell voltage. It is about 1.3 V (~30%) lower in comparison to cells using carbon-based materials. For an equivalent battery pack voltage, a higher count of cells and voltage and temperature sensors are needed. The higher weight of the titanate anode material significantly reduces the energy density. Besides these serious disadvantages, cells with $Li_4Ti_5O_{12}$ anodes have several remarkable features that may be of interest for future car applications. Charge efficiency is very good even at medium and low temperatures. There are further advantages under abuse conditions due to the oxide character of the anode material. Very good cycle life data have been reported and also calendar life is said to exceed the 10-year period significantly.

The manufacturing of negative electrodes for lithium-ion cells is similar to what has been described for the positive electrode. Anode powder and binder materials are mixed with an organic liquid to form a slurry, which is used to coat a thin metal foil. For the negative polarity, a thin copper foil serves as substrate and collector material. The loading has to be controlled very carefully because an insufficient homogeneity of the area loading may have detrimental effects on the later cycling performance.

Cell design

The high surface area of electrodes in lithium-ion cells to be used in automotive applications makes an assembly technique based on a winding operation the preferred method. Separators used in lithium-ion cells are thin rectified PE and PP foils with special coating for safety reasons (shutdown behavior under short circuit). In general, a high open pore volume is beneficial with respect to good ion conductivity. By generating this pore volume with a very fine structure, a sufficient ion conductivity and a reliable protection against the penetration of mass particles generating soft shorts can be managed at the same time.

The electrolyte used in lithium-ion automotive cells is optimized to an optimum conductivity. At present, a typical solution of 1 mol L^{-1} $LiPF_6$ in a mixture of organic solvents such as propylene carbonate (PC), dimethyl carbonate (DMC), ethylene carbonate (EC), and ethyl methyl carbonate (EMC) is used. Depending on the special needs and preferences, there may also be alternative conductive salts. Lithium bis(oxalato)borate (LiBOB), for example, is said to have some advantages especially in cells with manganese oxide-based cathodes and in cells operating at high temperatures. There are also some additives in use whose main purpose is the improvement of cell life endurance. The most popular additive is vinylene carbonate (VC) because of its positive effect on the formation of stable SEI layers at the negative electrode surface.

Lithium-ion cells use a cell match with a significant negative excess capacity. This is considered especially important under charging to high SoC values and at low temperatures. It has to be made sure that the lithium ions are intercalated with sufficient kinetics even under quick charge conditions in order to prevent lithium metal plating at the electrode surface.

Cell types

Lithium-ion cell depends on a reliable and long-term stable sealing technique. Even small water contaminants migrating into the cell could be very detrimental to their life endurance. Lithium-ion cells are available in two different geometric cell shapes.

Cylindrical cells

This cell type (Figure 12) is the most widespread cell type. Winding of a spiral coil is the easiest way of manufacturing and has been proven in the manufacturing of billions of lithium-ion portable cells. As already mentioned above, the winding of electrodes, which are by factors longer and thinner than what is used for portable cells, is a very sensitive subject. Cylindrical cells typically employ an aluminum can. Sealing of cells for automotive use is mostly done by laser welding.

Prismatic cells

Most of the prismatic cells use electrodes wound to form an oblong-shaped bobbin. These electrode coils are inserted into a prismatic metal housing. Closing and final sealing is done by high-precision laser welding at the cell lid as a standard method. The technology is more sophisticated than the cylindrical technology with regard to coil winding as well as the final assembly and sealing.

Pouch-type cells (the so-called coffee bag design) are a special sort of prismatic cells. Two aluminum-coated plastic foils are welded to each other to form a 'bag' in which the cell stack is inserted. The aluminum coating of the foils is crucial for preventing water permeation into the cell. Collectors and terminals are integrated into the interface structure between both foils. Long-term endurance of pouch-type cells is highly dependent on the quality of the embedding of the feedthrough system.

Maintaining a high mechanical pressure over time is an essential point for keeping the high power performance capability at a high level over the entire battery life. It is evident that cylindrical cells have an intrinsic advantage with respect to this demand. On the contrary, a prismatic design allows for higher surface areas even with larger format cells. This gives them a certain advantage with respect to cooling by heat dissipation.

Technical data of lithium-ion cells

Independent of the special cell shape, lithium-ion batteries can cover a wide range of energy and power. The range characteristic for automotive applications is given in the following table:

	High energy	*High power*
Specific energy ($Wh\,kg^{-1}$)	150	70
Specific power ($W\,kg^{-1}$)	600	>2200
Energy density ($Wh\,L^{-1}$)	320	150
Power density ($W\,L^{-1}$)	1300	>4600
Capacity turnover		
DoD = 80%	>2000	>2500
DoD = 5%	n.d.	>25 000

DoD, depth-of-discharge.

Besides the weight-saving aspects, it is the long service life that has made this battery system so especially attractive for automotive batteries. As with all other battery systems, there is a reduction in power performance with lower temperatures, which has to be considered in the system layout. Cell temperatures have to be given special attention, particularly for the recharging process in order to avoid lithium plating at the negative electrode as mentioned earlier.

Lithium-ion battery management

Lithium-ion batteries (Figure 13) need a more exact BMS than other battery systems as each single cell in the battery has to be monitored separately. For optimum functioning, a reliable SoC determination is required. The significant slope in the voltage characteristics over SoC for most lithium-ion systems facilitates this task. Voltage limits of the cell have to be strictly considered; exceeding the limits may cause damage to the cells by detrimental electrochemical reactions. Misbalancing in the SoC of the cells has to be managed by special devices in the electrical system.

Figure 12 Cylindrical Li-ion cells and a Li-ion module for automotive applications (Johnson Controls – Saft).

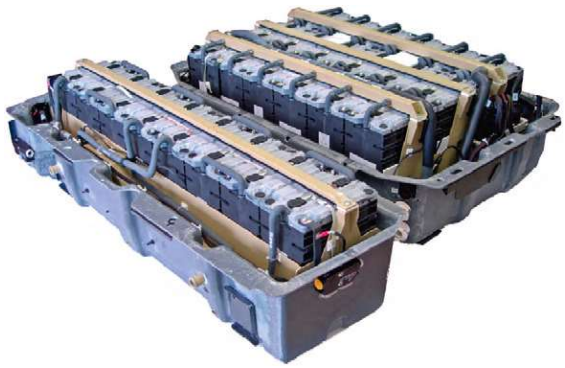

Figure 13 Lithium-ion battery for electric vehicle (EV) (Johnson Controls – Saft).

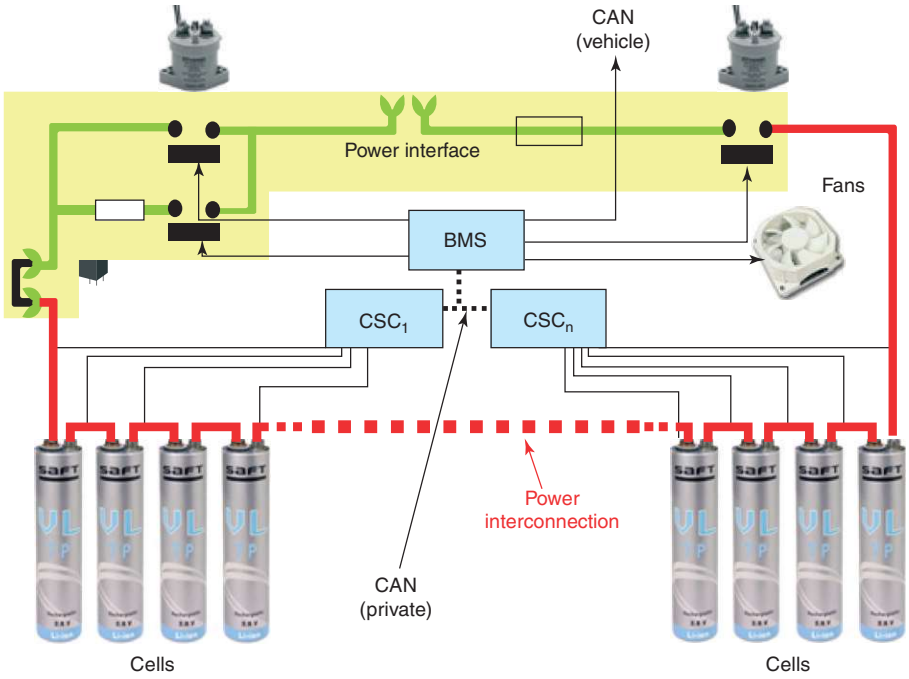

Figure 14 Battery management system (BMS) for Li-ion batteries (schematic). CSC, cell supervisory circuit.

Most battery control systems used these days employ the so-called master–slave architecture. As illustrated in Figure 14, the controlling of the single cells is managed on the basis of a module comprising a certain number of cells. The so-called cell supervisory circuits (CSCs) monitor the voltages of the cells and the temperature at characteristic sites inside the module. The CSCs communicate with the BMS, which processes the incoming information for determining the status of the battery (SoC, SoF, state-of-health (SoH), etc.). The SoC may be controlled redundantly by the amount of incoming and outgoing charge. In the case of SoC imbalance, an equilibration of the single cells in the arrangement is usually managed by devices on the CSC boards.

Although the energy efficiency of lithium-ion batteries is higher than that of other battery systems, they need an efficient thermal control system that is capable of dissipating the waste heat generated under battery operation. Lithium-ion batteries are more sensitive to heat generation because of their lower heat capacity in comparison to Ni–MH and lead–acid batteries. The thermal control concepts that are currently used, are based on air ventilation as well as on liquid cooling.

Sodium–Nickel Chloride High-Temperature Batteries

High-temperature systems

Two high-temperature battery systems that are candidates for automotive applications are the sodium–sulfur system (Na–S) developed by ABB and the sodium–nickel chloride ($NaNiCl_2$) system. The battery is also known under the term ZEBRA, which stands for the original project name: Zeolite Battery Research Africa. Out of these two, the $NaNiCl_2$ system turned out to be the superior one at least for traction purposes. Sodium–sulfur batteries could not overcome life problems, especially under operation conditions, whereas the $NaNiCl_2$ system has been showing a much more robust behavior. The use of $NaNiCl_2$ batteries (Figure 15) however will be limited to applications where pure electrical autonomy is the essential feature, as specific high power performance is limited. At present, it is mainly pure EVs that are employing this type of battery. However, plug-in HEVs or special hybrid vehicles with a significant electric action range (by internal recharging) may become a field of application.

Electrodes

The sodium–nickel chloride battery system works at a temperature level of more than 270 °C. The high temperature is necessary for enabling sufficient mobility of the sodium ions, which are the charge carriers in this electrochemical system. Active material at the cathode is nickel chloride. The negative electrode consists of liquid sodium absorbed in a matrix-like system.

Cell technology

The outer steel case serves as the negative polarity. It has a direct contact with the liquid sodium electrode. The positive electrode consisting of nickel chloride and nickel

Figure 15 Sodium–nickel chloride high-temperature battery ZEBRA (MES-DEA).

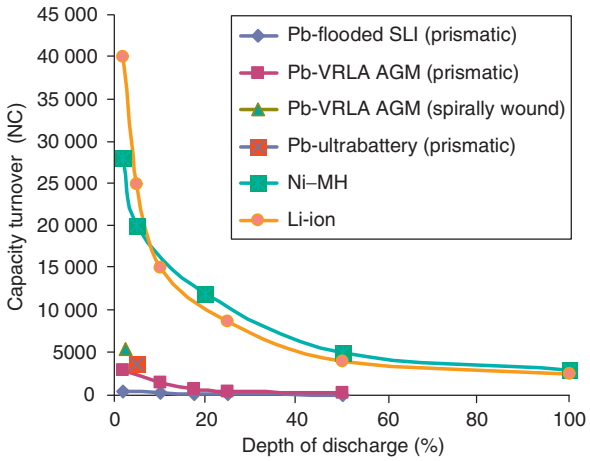

Figure 16 Achievable capacity turnover figures of various HEV battery systems under cycling with different depth-of-discharge DoD. Data from VB Autobatterie (Pb-flooded SLI, Pb-VLRA AGM, prismatic), Exide (Pb-VRLA AGM, spirally wound), CSIRO Energy Technology (Pb-ultrabattery), Johnson Controls – Saft (Ni–MH and Li-ion). VRLA, valve-regulated lead–acid; AGM, absorbent glass mat; SLI, starting, lighting, and ignition.

(for electrical conductivity) is located in the middle of the cylindrically shaped cell. It is surrounded by a molten sodium chloroaluminate ($NaAlCl_4$) medium, which serves as an ion conductive electrolyte. Separation of both electrodes is done by a ceramic material based on β-alumina. The ion conductivity of the ceramic material serving as the separator and of the molten electrolyte is crucial for the power performance of the battery cells.

Battery system

Basic technical reasons cause a limitation of the maximum cell capacity to about 10 Ah. For meeting the energy demand of different automotive applications, a parallel arrangement of cells is applied. Because of the high operation temperature, the battery design has to take into account the strong demands for thermal insulation as well as mechanical stability and safety. Modern insulation technologies allow the heat losses to be minimized. Typical losses of a 20 kWh battery can thus be reduced to less than 200 W. In the case of vehicle rest without being plugged to the grid, the heat losses have to be compensated by the internally stored energy. In order to have the battery always in a stage of full operation capability, the system has to be equipped with an efficient thermal control system. It should be capable of controlling the temperature during the rest periods as well as dissipate waste heat generated under battery operation.

Because of the permanent heat losses, sodium–nickel chloride batteries are not seen as a viable solution for passenger vehicles for private use. They are an acceptable solution for pure EVs and HEVs used for fleets with a relatively high degree of daily utilization. Hybrid buses and delivery vans with a high share of electrical driving range and with the chance to recharge the batteries in the internal combustion engine-operated phases are typical examples for this application. According to announcements made by the manufacturers, $NaNiCl_2$ batteries may have a life of up to 10 years.

Technical data

The main technical data of a complete $NaNiCl_2$ battery system may be summarized as follows:

Specific energy ($Wh\,kg^{-1}$)	120
Specific power ($W\,kg^{-1}$)	180
Energy density ($Wh\,L^{-1}$)	190
Power density ($W\,L^{-1}$)	270
Capacity turnover	
DoD = 80%	>1500
DoD = 5%	n.d.

DoD, depth-of-discharge.

Summary and Perspectives

The life span of the battery system – calendar or as capacity turnover – is of crucial importance for the operating efficiency in automotive applications. The feasible capacity throughput is largely determined by the charging and discharging conditions. Figure 16 shows the dominating influence of the discharge depth on the feasible capacity throughputs of different battery systems, which have been operated under different cycling conditions.

Microhybrid applications, such as start–stop systems, will continue to be served by lead–acid batteries, owing to reasons of economy. Absorbent glass mat lead–acid batteries are relatively favorably priced owing to the

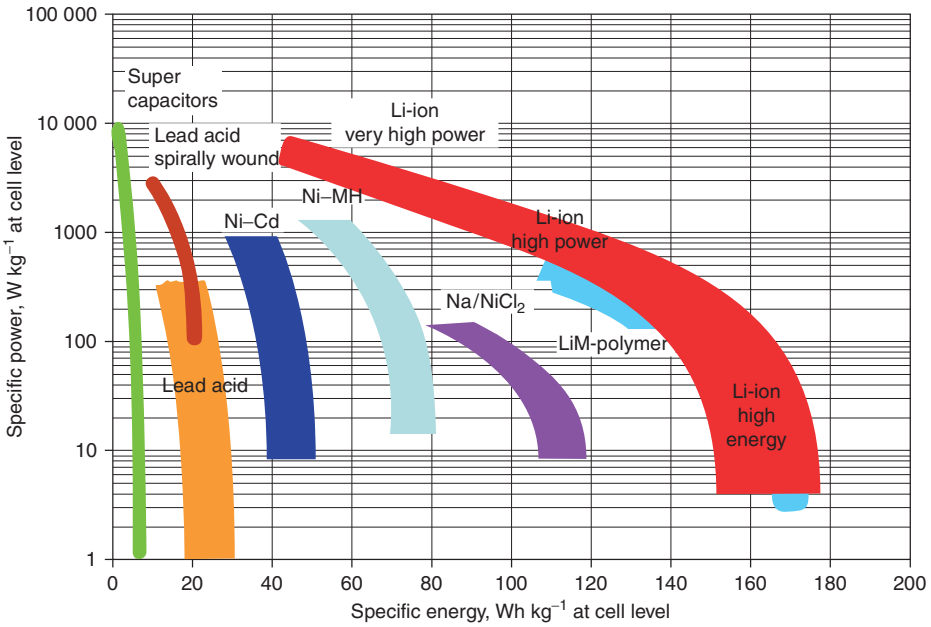

Figure 17 Specific energy versus specific power plot for different electrochemical systems.

relatively low price of the raw materials, which makes them the preferred solution for standard automotive applications, where no great expectations concerning range and life span apply.

For FHEVs, MHEVs, as well as for hybrid electric buses and trucks, the Ni–MH system provides a battery technology that has been proven over years of service. But the system is considered largely exhausted from a technical point of view. It is expected that lithium-ion will take over more and more of the battery market for FHEVs and MHEVs. In contrast to Ni–MH, the lithium-ion system still has a considerable potential concerning better performance. Whereas for the Ni–MH system today an upper technical limit of the specific power of $\sim 1700\,\mathrm{W\,kg^{-1}}$ is foreseeable, the lithium-ion system still has room for significant growth, e.g., the specific power will increase to values clearly above $3000\,\mathrm{W\,kg^{-1}}$ (Figure 17).

Because of the increased energy demand, plug-in hybrid vehicles will very much depend on lithium-ion battery systems. They will be a key component for their market success. Ni–MH and lead–acid batteries are no solution because of simple weight reasons, at least not for vehicles with a medium or long driving range. Current discussions about the electric autonomy of a PHEV place the driving range between 10 and 60 km.

Nomenclature

Abbreviations and Acronyms

AGM	absorbent glass mat
BMS	battery management system
CSC	cell supervisory circuit
DMC	dimethyl carbonate
DoD	depth-of-discharge
EC	ethylene carbonate
EMC	ethyl methyl carbonate
EV	electric vehicle
FHEV	full hybrid electric vehicle
HEV	hybrid electric vehicle
IC	internal combustion
ICE	internal combsustion engine
LiBOB	lithium bis(oxalato)borate
MHEV	mild hybrid electric vehicle
PC	propylene carbonate
PE	polyethylene
PHEV	plug-in hybrid electric vehicle
PP	polypropylene
SEI	solid electrolyte interphase
SLI	starting, lighting, and ignition
SoC	state-of-charge
SoF	state-of-function
SoH	state-of-health
VC	vinylene carbonate
VRLA	valve-regulated lead–acid
ZEBRA	Zeolite Battery Research Africa

See also: **Applications – Transportation:** Electric Vehicle: Batteries; Hybrid Electric Vehicle: Plug-In Hybrids; **Batteries:** Fast Charging; Modeling; **Batteries and Fuel Cells:** Efficiency; **Capacitors:** Electrochemical Metal Oxides Capacitors; Overview; **Safety:** Cell Reversal; High Voltage; Thermal Runaway; **Secondary**

Batteries – High Temperature Systems: Sodium–Nickel Chloride; **Secondary Batteries – Lead–Acid Systems:** Automotive Batteries: New Developments; Overview; Valve-Regulated Batteries: Absorptive Glass Mat; **Secondary Batteries – Lithium Rechargeable Systems:** Hazards and Protection Circuits; Lithium Polymer Batteries; Overview; **Secondary Batteries – Lithium Rechargeable Systems – Lithium-Ion:** Aging Mechanisms; Lifetime Prediction; Lithium-Ion Polymer Batteries; **Secondary Batteries – Nickel Systems:** Nickel–Metal Hydride: Overview.

Further Reading

Bosch R (2003) *Motor Vehicle Batteries and Electrical Systems*. Stuttgart: Robert-Bosch Aftermarket.

(2007) *Hybrid Vehicles and Energy Management, 4th Symposium*. Gesamtzentrum für Verkehr Braunschweig (gzvb).

Aurbach D (ed.) (1999) *Nonaqueous Electrochemistry*. New York: Marcel Dekker.

Bagotzky V and Skudin AM (1980) *Chemical Power Sources*. London: Academic Press.

Bergveld HJ, Kruijt WS, and Notten PHL (2002) *Battery Management Systems*. Dordrecht (The Netherlands): Kluwer Academic Publishers.

Berndt D (1986) *Bleiakkumulatoren*. Düsseldorf: VDI Verlag GmbH.

Berndt D (1997) *Maintenance-Free Batteries*. Taunton, England: Research Studies Press Ltd.

Besenhard JO (ed.) (1998) *Handbook of Battery Materials*. Weinheim: Wiley-VCH.

Conway BE (1999) *Electrochemical Supercapacitors*. New York: Kluwer Academics, Plenum Publishers.

Kinzelbach R (1974) *Stahlakkumulatoren*. (Hannover: Varta Batterie AG). Düsseldorf: VDI Verlag.

Lam LT and Louey R (2006) Development of ultra-battery for hybrid-electric vehicle applications. *Journal of Power Sources* 158: 1140–1148.

Lam LT, Louey R, Haing NP, et al. (2007) VRLA ultrabattery for high-rate partial-state-of-charge operation. *Journal of Power Sources* 174: 16–29.

Linden D and Reddy TB (2001) *Handbook of Batteries*, 3rd edn. New York: McGraw-Hill.

Naunin D (ed.) (2004) *Hybrid-, Batterie- und Brennstoffzellen-Elektrofahrzeuge*. Renningen: Expert-Verlag.

van Schalkwijk WA and Bruno S (2002) *Advances in Lithium-Ion Batteries*. New York: Kluwer Academic, Plenum Publisher.

Soria ML, Trinidad F, Lacadena JM, Valenciano J, and Arce G (2007) *Journal of Power Sources* 174: 41–48.

Tuck CDS (ed.) (1991) *Modern Battery Technology*. Chichester, UK: Ellis Horwood Ltd.

Varta Batterie AG (1982) *Sealed Nickel Cadmium Batteries*. Düsseldorf: VDI Verlag.

Wakihara M and Yamamoto O (eds.) (1998) *Lithium-Ion Batteries – Fundamentals and Performance*. Weinheim: Wiley-VCH.

Westbrook MH (2001) *The Electric Car, IEE Power and Energy Series No. 38*. London, UK: The Institution of Electrical Engineers.

Willems JJG (1984) Metal hydride electrodes – stability of $LaNi_5$-related compounds. *Philips Journal of Research* 39(supplement 1): 54–70.

Charging Methods

E Lemaire-Potteau, M Perrin, and S Genies, INES/CEA, Laboratory for Solar Systems, Le Bourget du Lac, France

Introduction

Electrochemical power sources can be of primary nature, in which case they are either discarded or refilled (e.g., fuel cell) after discharge. Secondary power sources have the ability to be recharged in order to deliver power again. In the charging process, direct current (DC) electric power is used to reform the active materials of the cell or battery to restore them to their high energy state. This means that during charge, a battery is led back to a high state-of-charge (SoC). The amount of power and energy a secondary power source will be able to deliver after recharge depends to a large extent on the method of recharge. In the similar manner, the number of cycles a secondary cell or battery will be able to perform, or in other words its state-of-health (SoH), will also be largely influenced by the charging methodology. Therefore, charging methods are crucial to the performance and life of secondary batteries.

The parameters that determine charging and influence both the final SoC and SoH of a secondary battery after recharge are

- time elapsed between the last discharge and the recharge,
- charging time,
- charging rate or charging current,
- charging voltage, and
- charging temperature.

Depending on the battery technology and the battery use, these different parameters will have more or less influence on the performance or life, so that the optimum charging method for a given technology will always be a trade-off between the impact on the electrical performance in the next discharge, the impact on the life, and the efficiency of the charge. Therefore, the following sections will present generalities about power sources charging, then give some information on the relation between the application or use of the battery and the charging method, before they detail the specificity of the charging methods for different secondary power sources technologies and provide some hints of 'the optimum charging method' for a given technology and its use.

Common Issues for All Secondary Power Sources

The nature of the reactions taking place in rechargeable power sources has been described earlier in **Capacitors:** Overview; **Secondary Batteries:** Overview; **Secondary Batteries – Flow Systems:** Overview; **Secondary Batteries – High Temperature Systems:** Sodium–Nickel Chloride; Sodium–Sulfur; **Secondary Batteries – Lead-Acid Systems:** Overview; **Secondary Batteries – Lithium Rechargeable Systems:** Overview; **Secondary Batteries – Nickel Systems:** Nickel–Cadmium: Overview; Nickel–Iron; Nickel–Metal Hydride: Overview; Nickel–Zinc. During recharge, the current flow is reversed compared to that during discharge, and oxidation takes place at the positive electrode and reduction at the negative electrode.

Typical Charge Strategies

Most of the charge strategies are based on control of the current and/or power source voltage, which are not independent. Indeed, the reactions occurring at each electrode obey the laws of both thermodynamics and kinetics and when no current is flowing, the potential of each electrode is governed by the Nernst equation, with the difference between the two electrode potentials giving the cell's electromotive force (EMF). Compared to this value, the cell voltage decreases during discharge and increases during charge when current is flowing, electrode polarization appears, in relation with charge transfer, mass transport, and ohmic losses mainly via the electrolyte.

The main basic charge methods are

- constant current (I charge, variant: trickle charging),
- constant voltage (U charge, variant: float charging),
- constant current, then constant voltage (IU charge), and
- IU charge with additional charge phase (IUI or IU0 U charge).

Pulse charging can also be used, especially at the end of charge. This designation involves in fact a family of methods that have been designed mainly for aqueous systems (lead–acid, nickel–cadmium (Ni–Cd), nickel–metal hydride (Ni–MH)).

Many manufacturers also recommend specific charge methods for applications in which the time available for charging is limited to few hours. These fast-charging methods are specific for each battery technology and will be described in the corresponding sections, if appropriate.

Finally, more complex methods can be based on controlling, for instance, the power or the temperature.

They are rather seldom used and will not be detailed here.

Constant current (I charge)

This is one of the simplest charging methods, suitable for most of the batteries, provided the charging current is adapted to the battery capacity and to its technology. I charge will generally cause an increase in the battery voltage (Figure 1), with a different variation profile depending on the battery type, as shown for instance by D. Linden. For some battery types such as lead–acid or lithium-ion batteries, in order to mitigate this voltage increase and to optimize the coulomb efficiency, one can use several successive constant-current periods, with different current values. This accounts for the variation of the battery charge acceptance, which can be lower at low or high SoC. In general, a smaller current will result in an increase of the coulomb efficiency.

Trickle charging

A trickle charge is a continuous I charge at a low rate (around $C/100$), used to maintain the battery in a fully charged state. It aims at compensating permanently the losses owing to self-discharge. However, the determination of the current to be applied is quite difficult, because the required value will vary during the life of the battery. This method is not suitable for some power sources that can be damaged from overcharging, such as lithium-ion batteries.

Constant voltage (U charge)

In this method, the battery voltage is imposed by the charger and the current is regulated in relation with the internal resistance of the battery. For several types of batteries, the current will be very high at the beginning and will then decrease (Figure 2). This method is thus seldom used alone, because it requires a high charging power, and moreover in many cases the energy efficiency will be poor. In practice, modified constant-voltage methods are used.

Float charging

Float charging is in fact a permanent U charge, whose voltage is most often specified by the battery manufacturer. For lead–acid batteries, it is the most widely used method to keep the battery in a fully charged condition at any time and compensate only the self-discharge.

Constant current, then constant voltage (IU charge)

In this method (Figure 3), the battery is first charged at a constant current, until the voltage reaches the regulation voltage, the value of which is often recommended by the battery manufacturer. Charge then switches to constant-voltage mode, and the current is regulated as explained above.

IU charge is one of the most popular charge strategies, easy to implement and commercially available at low cost. It offers a good compromise between I and U charges, taking over the advantages of both methods while compensating their drawbacks. The I phase at the beginning allows limiting the charging power and then the U phase limits the voltage increase of the battery and optimizes the energy efficiency.

Constant current, constant voltage with additional charge (IUI/IU0 U charge)

The IU charge can be followed by an additional charging phase at constant current (IUI) or constant voltage (IU0 U). It is specific to certain battery technologies, in particular those that require a controlled amount of overcharging. Its implementation requires supplementary hardware (sensors, etc.).

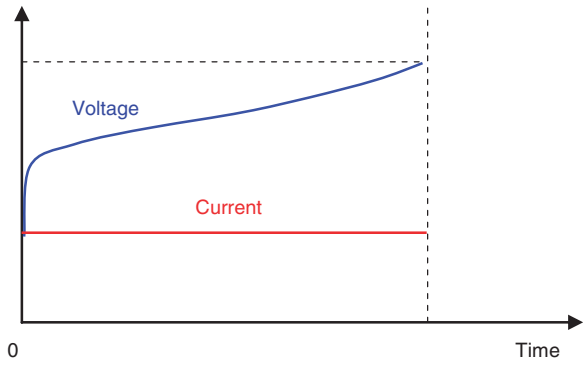

Figure 1 Schematic evolution of the current and voltage during I charge.

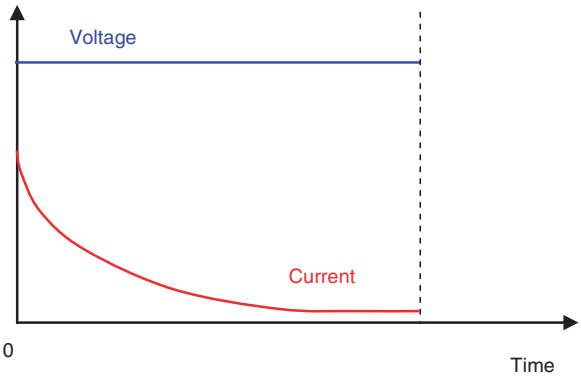

Figure 2 Schematic evolution of the current and voltage during U charge.

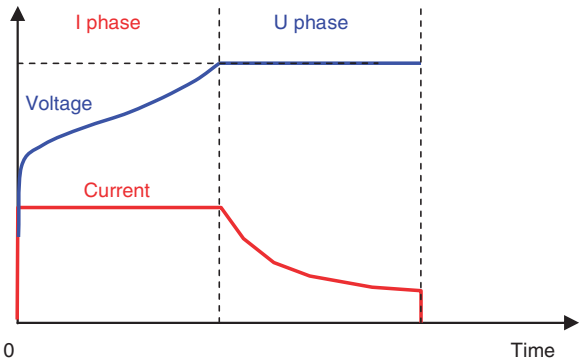

Figure 3 Schematic evolution of the current and voltage during IU charge.

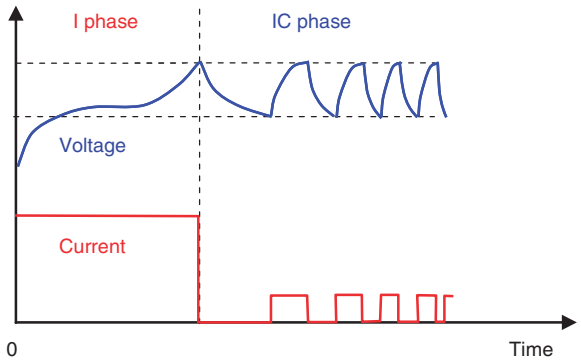

Figure 4 Schematic evolution of the current and voltage during intermittent charging (IC).

Pulse charging and variants

In this method, the current is fed to the battery in pulses: short rest periods between pulses allow the chemical reactions in the battery to stabilize by equalizing throughout the bulk of the electrode. It is also claimed that this method can reduce unwanted chemical reactions at the electrode surface such as gas formation, crystal growth, and passivation. The optimum current profile and parameters depend on the cell chemistry and design.

Reflex or negative pulse charging

Reflex or negative pulse charging, also called 'burp charging', is a method in which a very short discharge pulse, typically 2–3 times the charging current for 5 ms, is applied during a charging rest period to depolarize the cell. These pulses are supposed to dislodge any gas bubbles that have built up on the electrodes during fast charging, speeding up the stabilization process and hence the overall charging process. The release and diffusion of the gas bubbles is known as 'burping'. Controversial claims have been made for the improvements in both the charge rate and the battery lifetime as well as for the removal of dendrites made possible by this technique.

Intermittent or 'on–off' charging

The intermittent charging (IC) method, also called 'on–off' charging, was developed to avoid the continuous overcharging of the U or I charge, and is especially useful for the end of charge or self-discharge compensation. After charging the battery (usually with I charge), its voltage is maintained between two threshold values as shown in Figure 4. The battery is charged for a short period of time and then kept in open circuit until the voltage drops and triggers the lower regulation voltage. At this point, it is recharged over a short period of time with a constant current. The recharge process repeats intermittently, and end of charge is identified when the duty cycle of the IC current reaches steady-state value. The IC regime reduces the degree of overcharging of the battery and leads to longer battery life.

Interrupted charge control and pulse width modulation

Interrupted charge control (ICC) and pulse width modulation (PWM) are two variants of the IC method. ICC has rest periods and a fixed duty cycle; and in PWM, the two voltage thresholds are very close to each other, tending toward float charging.

Influence of the Temperature

Among all environmental factors, temperature is the most influential factor governing the power sources behavior (charge, discharge, self-discharge, lifetime), in relation with the temperature dependence of the electrochemical processes.

On the contrary, the so-called 'high-temperature batteries' such as sodium sulfur (NaS) or Zebra batteries must be operated at higher temperatures than the ambient temperature. These are a rather special case and will not be considered in this section.

Influence on the voltage

As detailed above, the battery voltage is the sum of the EMF, given by Nernst's law, and the overvoltages of the two electrodes. In Nernst's law, the potential depends on the species concentration as well as on the temperature. The different components of the overvoltages are also temperature dependent: the ohmic part, the charge transfer rates, and mass transport rates. Figure 5 illustrates the effect of temperature on the voltage during I charge at $C/10$ for a sealed Ni–MH battery.

For this reason, the end-of-charge (as well as end-of-discharge) voltages need to be temperature compensated; this is especially true for power sources that can be damaged by overcharge. For example, for lead–acid batteries, the charge voltage must be decreased by 3–4 mV per cell and per 1 °C rise in temperature.

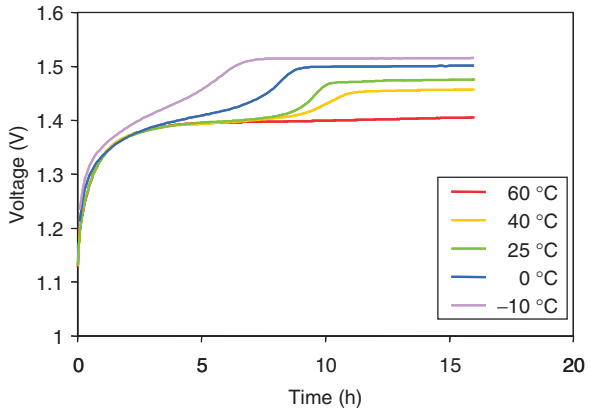

Figure 5 Influence of temperature on the voltage evolution of a sealed nickel–metal hydride (Ni–MH) cell during I charge.

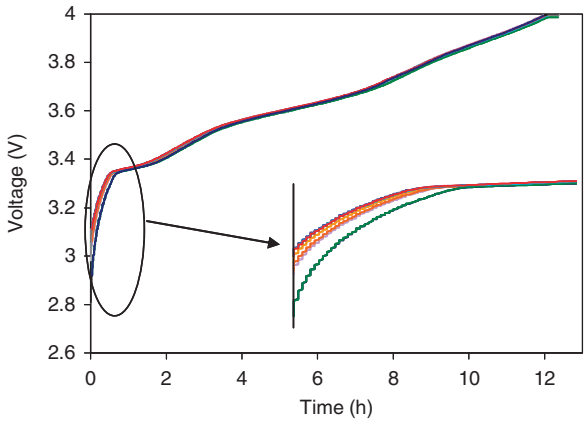

Figure 6 Observation of the equalization process for a Li-ion battery consisting of eight cells in series.

Influence on the capacity and self-discharge

When the temperature increases, the diffusion of ions toward the reaction sites and the electrodes polarization are improved, and the discharge capacity is then higher. However, the self-discharge rate is also increased and more energy is required to keep the power source in the 'fully charged' state.

Influence on the lifetime

Increasing temperature also accelerates other phenomena such as secondary reactions decomposing the electrolyte, active material aging, and corrosion. This alters the power source performances, and this is also the reason why accelerated aging tests are in many cases performed above the normal operation temperature.

For the specific case of batteries under float voltage, the Arrhenius law describes the battery life duration at different temperatures; thus, increasing the battery temperature by 10 °C halves the battery life, provided the float voltage is not compensated.

Case of Cells Association: Equalization Charge

In order to reach the required voltage and capacity for the power source, individual cells are frequently associated in series and/or in parallel, which gives what is often named a 'battery pack'. The charging method needs to be adapted to this specific type of configuration. Depending on the power source type and its manufacturing, there can be an initial dispersion between cells. Moreover, after a certain time of operation, a high-voltage battery having many cells in a series string can become unbalanced, with certain cells limiting charge and discharge because of their different internal resistance. Limiting cells receive more overcharge than other cells in the string, which will in turn accelerate their aging.

For balancing the cells and leading them all to the fully charged state, an equalization charge is performed, either periodically or at each recharge. Equalization protocols are defined for each type of power source, depending especially on its tolerance to overcharge.

Power sources with nonaqueous electrolyte

Power sources with nonaqueous electrolyte do not accept any overcharge, because of the risk of electrolyte decomposition, irreversible degradation, and even safety problems. This is the case for instance of lithium-ion batteries. Charging of a battery pack then requires monitoring each cell, and equalization is in fact performed during each charge. 'Passive' equalization consists basically in discharging the highest voltage cells into a resistor until they reach the voltage of the lower cells. In 'active' equalization, electronic components are used to manage the energy exchanges between the cells. Figure 6 illustrates this process for a lithium-ion battery consisting of eight cells in series.

Power sources with aqueous electrolyte

The equalization here is simpler and can be performed globally: the cells that reach full charge first will be slightly overcharged while the others complete their charge. This is often done at the end of the normal charging, with a U or I charge with a current around $C/20$. Equalization is considered complete when the cell voltages and in some cases electrolyte densities rise to a constant and acceptable value. The frequency of this equalization charge depends on the battery operation profile, especially the depth of discharge (DoD). It is normally specified by the battery manufacturer.

End-of-Charge Control and Criteria

All charge methods require control, to stop the charge or reduce the charging rate before an excessive rise in

gassing, pressure, or temperature occurs (depending on the type of battery), affecting the performance, lifetime, or safety of the battery.

However, only general considerations can be given here, because the charge termination criteria are highly dependent on the battery technology. They will be addressed more precisely in the next sections.

End-of-charge control can be based on SoC measurement, which can be performed by direct measurement of one battery variable (voltage, impedance, and so on) or 'Ah-counting' method, based on current integration (*see* for instance **Secondary Batteries – Lead-Acid Systems:** State-of-Charge/Health for lead–acid batteries). In this case, the end of charge would simply occur when SoC reaches 100%. However, it is often not so simple: several types of batteries require a certain amount of overcharge to reach the 'fully charged' state (e.g., for Ni–MH batteries, up to 60% overcharge is needed).

Another approach consists in using specific signals from the battery that indicate its full charge, e.g., by analyzing its U versus I curve. This can be the value, or the variation, of I when U is controlled, or of U when I is controlled. A typical end-of-charge criterion is when the current goes down to a given value under constant-voltage charging. Other examples of this approach use the 'coup de fouet' phenomenon for lead–acid batteries (*see* **Secondary Batteries – Lead-Acid Systems:** Coup de Fouet) or the voltage decrease for Ni–Cd and Ni–MH batteries.

In some cases, the end-of-charge control can also rely on temperature measurements, for the technologies that show exothermic overcharge processes. Resistance or impedance changes may also be used as criteria.

Typical Applications and Specific Methods

Automotive application

In this application, batteries are almost always in floating mode: they undergo a high-current discharge peak at starting, then a very little current to power the additional devices in the car, as illustrated in **Figure 7(a)**. However, the latter tends to increase owing to the larger number of onboard electrical equipment, and the battery cycling is a little stronger. The battery is usually recharged by an onboard generator or alternator powered by the car engine, using IU charge.

Traction

In this case, charging is done separately from the system using the battery. Minimizing the charging time is important in this application, and charge is usually performed right after the discharge. **Figure 7(b)** illustrates the type of cycling profile.

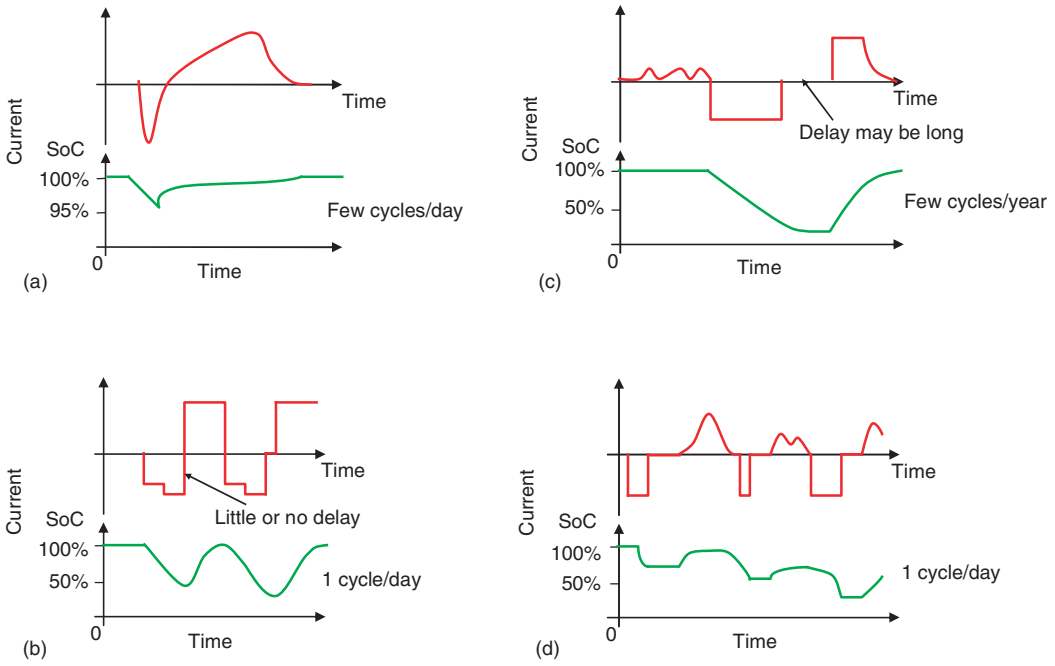

Figure 7 Illustration of the evolution of current and state-of-charge (SoC) for four main types of applications of rechargeable power sources: (a) automotive; (b) traction; (c) uninterruptible power supply (UPS); and (d) renewable energies.

Uninterruptible power supply

The batteries must be able to power the installation immediately in case of necessity, and are thus generally kept under permanent float charge. In some cases, and especially when they are used in large installations for safety power backup, a control discharge is performed periodically, often yearly, as illustrated in Figure 7(c).

'Unpredictable' charging: EV, HEV, renewable energies

All of the above applications involve controlled charge of the battery; however, there are many applications where the energy to charge the battery is only available, or is delivered, in some uncontrolled way. This applies to electric vehicle (EV) and hybrid electric vehicle (HEV) applications, especially with the use of regenerative braking: this generates large power spikes during braking, which the battery must absorb. In renewable energy systems, the power level is generally lower, but the specificity of these applications is that the recharge is dependent on the availability of resource, i.e., of the weather (sun, wind, and so on). The batteries will typically perform one cycle per day, and Figure 7(d) shows the example of solar photovoltaic (PV).

The charge strategy consists in accepting all current from the DC source as long as the battery voltage remains under a certain limit. Then the battery management system (BMS) operates according to its charging strategy (an example is given in Figure 8 for PV).

Specificities of the Different Battery Technologies

The applicability of the different charging methods to different types of rechargeable power sources is discussed here. In many cases, the reader will find it useful to refer to the other articles in this encyclopedia specific to each power source technology (*see* **Capacitors:** Overview; **Secondary Batteries:** Overview; **Secondary Batteries – Flow Systems:** Overview; **Secondary Batteries – High Temperature Systems:** Sodium–Nickel Chloride; Sodium–Sulfur; **Secondary Batteries – Lead-Acid Systems:** Overview; **Secondary Batteries – Lithium Rechargeable Systems:** Overview; **Secondary Batteries – Nickel Systems:** Nickel–Cadmium: Overview; Nickel–Iron; Nickel–Metal Hydride: Overview; Nickel–Zinc.

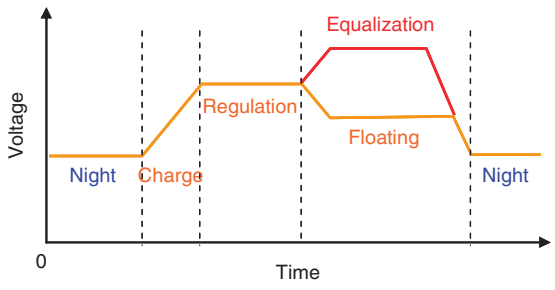

Figure 8 Example of a battery management system (BMS) charging strategy (PV application).

First, the systems with aqueous electrolyte will be dealt with: flooded or sealed lead–acid, Ni–Cd, and Ni–MH batteries. Then, for the nonaqueous systems, the main different types of lithium-ion batteries followed by the more 'exotic' technologies will be addressed: supercapacitors, NaS, Zebra, and redox-flow batteries.

Flooded and Valve-Regulated Lead–Acid Batteries

The charge of this type of batteries is the subject of a dedicated article (**Secondary Batteries – Lead-Acid Systems:** Charging), and only the main indications will be given here.

Main characteristics

In the case of the lead–acid battery, the charge processes involve the conversion of $PbSO_4$ into PbO_2 at the positive electrodes, that of $PbSO_4$ into metallic lead at the negative electrodes, and the increase of concentration of the sulfuric acid electrolyte. These charge processes involve dissolution and reprecipitation of materials of different conductivity and specific volume. Moreover, like in all electrochemical systems with aqueous electrolyte, active material charging reactions are in concurrence with the overcharge reactions, resulting in the production of hydrogen and oxygen (the so-called 'gassing') and in loss of water. Proper charging is required to minimize physical degradation owing to these phenomena.

The selection of the appropriate charging method will depend on several parameters, such as the type and design of the lead–acid battery, service conditions, time available for charging, number of cells or batteries to be charged, and of course charging facilities. A fully discharged lead–acid battery can absorb high currents with the charging voltage remaining relatively low. However, as the battery becomes charged, the voltage increases, leading to overcharge and gassing. The charge current must then be reduced to reasonable values.

In valve-regulated lead–acid (VRLA) batteries, the gas recombination principle allows O_2 generated at normal overcharge rates to be reduced at the negative plate, eliminating oxygen outgassing. Hydrogen generation can be substantially reduced by the use of appropriate grid material (antimony-free). However, if the charge current is very high, gassing can become faster than the recombination process, and O_2 and H_2 will be released from the cell as the cell vents, and the water that is lost, unlike in flooded batteries, cannot be refilled. If the drying of the separator becomes critical, this can cause

thermal runaway of the battery. The heat produced by the gassing is not evacuated through the electrolyte and by the recombination reaction, leading to an increase of the battery temperature. In turn, this temperature increase causes an increase of the gassing current, and this phenomenon amplifies itself until the thermal runaway of the battery. Finally, it can go up to an explosion by inflammation of the gas produced.

Preferred charging methods

Constant-current charging, at one or more current rates, is not widely used for lead–acid batteries. This is because of the need for current adjustment, especially at the end of the charge, or to keep the current at a low level throughout the charge, which will result in long charge times of 12 h or more.

The IU charge is the conventional method for flooded lead–acid batteries and is also preferred for VRLA batteries. The optimum value of the two parameters of this charge (maximum current and voltage) will often be specified by the battery manufacturer. These limits depend on the battery's internal design, and especially the nature of the positive grid alloy. Voltage limits are usually in the range of 2.35–2.45 V cell^{-1} for lead–antimony alloys, and up to 2.5 V cell^{-1} for alloys with higher hydrogen overvoltage, such as lead–calcium.

The IUI charge is common for deep-cycling batteries, with a final current around $C/10$, until reaching 110–120% charge factor (relative to the previous discharge).

For batteries used in applications where recharge is partly unpredictable (typically in renewable energy systems), the charge controller uses specific strategies to optimize the battery charging (see the section entitled 'Common Issues for All Secondary Power Sources').

End-of-charge control

End-of-charge control can be based on SoC measurement, as described in **Secondary Batteries – Lead-Acid Systems:** State-of-Charge/Health. For lead–acid batteries, SoC measurement is a difficult issue, and especially for the end of charge, owing to overcharge reactions. Another approach consists in using specific signals from the battery that indicate its full charge. For lead–acid batteries, a good example is the 'coup de fouet' phenomenon (*see* **Secondary Batteries – Lead-Acid Systems:** Coup de Fouet). A simpler method consists, for U charge, in stopping the charge when the current reaches a sufficiently low value or a constant value. The current value depends on the regulation voltage and the temperature, but is usually below $C/50$.

Flooded and Sealed Nickel–Cadmium Batteries

Main characteristics

For Ni–Cd batteries, the charge processes involve the conversion of nickel hydroxide into nickel oxyhydroxide at the positive electrode, and that of cadmium hydroxide into metallic cadmium at the negative electrode. The composition or density of the potassium hydroxide electrolyte is not significantly changed during this process, in contrast to the sulfuric acid in lead–acid batteries. Charging always occurs in competition with water electrolysis, resulting in the production of H_2 and O_2 toward the end of the charge. In sealed cells, the gases are recombined internally, whereas in an open cell, the gases are allowed to vent, and periodical water addition is required.

During overcharge of a sealed cell, the only result is that electricity is converted into heat, the overcharge reaction being exothermic, particularly the chemical recombination of oxygen. The overcharge reaction on the positive plate starts before the cell is fully charged, so that some oxygen evolution on charging is unavoidable. At higher temperatures, the oxygen evolution starts at a lower voltage, and the charging efficiency is lower.

Preferred charging methods

Vented Ni–Cd batteries may be charged with I, U, or IU methods. U charging is not recommended for sealed Ni–Cd batteries because it can lead to thermal runaway. In this case, the recommended method is I charge, with a rather low current. $C/10$ charge up to 140% charge factor is typical: at this rate, the battery can be safely charged without being damaged by overcharging. At higher charge rates (up to C or 2 C), care must be taken to avoid excessive overcharge or temperature increase. **Figure 9** shows typical voltage variation during an I charge for open and sealed Ni–Cd batteries. The voltage increases less for sealed batteries: the negative electrode SoC remains lower owing to the oxygen recombination reaction.

End-of-charge control

At the end of charge, several phenomena can be observed simultaneously (**Figure 10**): the temperature rises, and for sealed batteries, the voltage increases and then decreases,

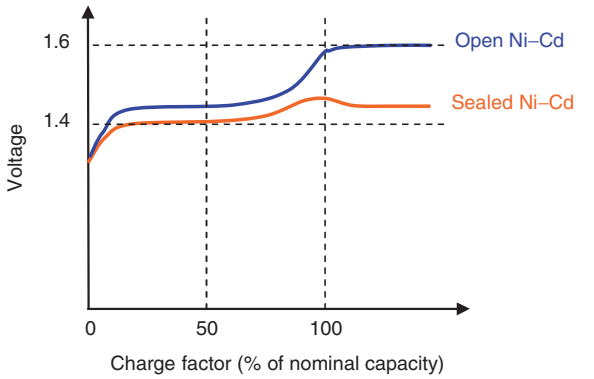

Figure 9 Typical voltage variation during I charge for open and sealed nickel–cadmium (Ni–Cd) batteries.

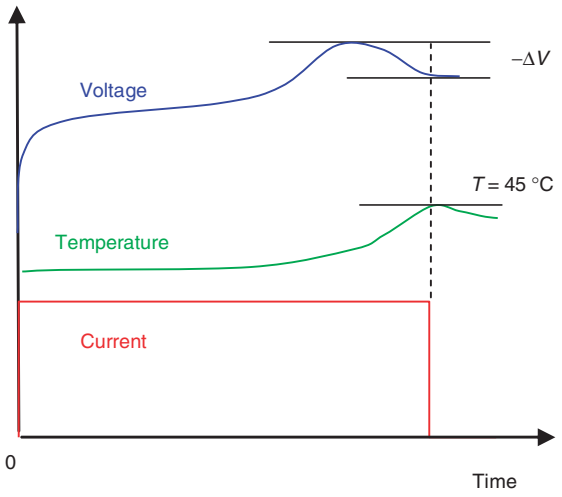

Figure 10 End-of-charge phenomena in nickel–cadmium (Ni–Cd) batteries during I charge.

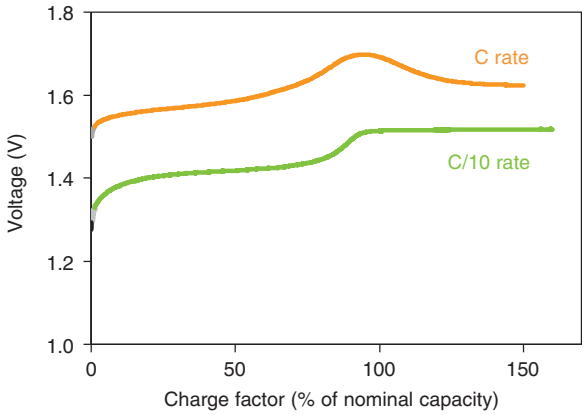

Figure 11 Voltage variation of a sealed nickel–metal hydroxide (Ni–MH) battery during I charge at *C*/10 and *C* rates.

in relation with the internal resistance drop owing to higher temperature. End of charge can be triggered by a high temperature threshold, typically 45 °C. In the 'negative delta V' method, the voltage decrease by 10–20 mV is used as an end-of-charge criterion. At low charge rates, below $C/2$, the voltage variation is smaller, and the end of charge is more difficult to detect. However, overcharge will be limited due to the low current.

Flooded and Sealed Nickel–Metal Hydride Batteries

Main characteristics

For Ni–MH batteries, the chemistry at the positive electrode is the same as in the Ni–Cd battery. The negative active material, in the charged state, is hydrogen in the form of a metal hydride. As the battery is charged and discharged, a reversible hydrogen absorption–desorption reaction occurs. The electrolyte is aqueous potassium hydroxide, with lithium hydroxide additive to improve the charging efficiency of the positive electrode, by reducing oxygen evolution. Almost all Ni–MH batteries are of the sealed type.

As for all types of batteries with aqueous electrolyte, the charge current must be controlled at the end of the charge and during overcharge, to limit the generation of oxygen and remain below the rate of recombination. In Ni–MH batteries, the negative electrode has excess capacity compared with the positive, to handle both overcharge and overdischarge.

Preferred charging methods

Nickel–metal hydride batteries are flexible and accept diverse charge methods. Their recharging characteristics are generally similar to those of sealed Ni–Cd batteries, but with stronger requirements for charge control. The most common charging method is I charge, but with the current limited. The main issue is to limit overcharge, in order to avoid excessive heating and electrolyte losses by venting. Typical charging regimes are between $C/10$ and C.

In the EV application, an interesting charge method consists in I charge with several steps triggered by a temperature-compensated voltage limit. During the first step, Ni–MH batteries can accept from 60 to 80% charge within 15 min. Then, after the first voltage threshold is reached, the current is reduced and charging continues until the next voltage threshold. Moreover, in EV and HEV applications, large Ni–MH batteries have demonstrated their ability to accept efficiently regenerative braking energy over a wide SoC and temperature range. This means accepting high-power recharge pulses.

End-of-charge control

Figure 11 shows the voltage variation during charge at $C/10$ and C rates. At $C/10$ rate, the generated oxygen can be recombined as and when it is produced. A simple time limit is then sufficient, and the charge is complete after around 150% charge input. This ensures maximum capacity, but at the expense of the cycle life. The longest cycle life is obtained with 120% charge input, but the capacity is then lower.

There are numerous methods for detecting the end of charge, as the time when overcharge becomes very strong. All these methods are based on the heat produced by the oxygen evolution/recombination mechanism. It is possible to measure absolute temperature, temperature variation (ΔT) or increase rate ($\Delta T/\Delta t$), the voltage plateau ($0\Delta V$) or drop ($-\Delta V$), or pressure rise.

Lithium-Ion Batteries

Main characteristics

Rechargeable lithium batteries can be of very different chemistries and design. Negative electrodes can be based

on lithium metal, lithium alloys, or lithiated carbon. For the positive electrode, one finds intercalation solid compounds, soluble inorganic cathodes, and polymeric materials. Liquid aprotic organic and inorganic electrolytes are used in many cells, as well as solid polymer electrolytes, which provide a safer design because of their lower reactivity with lithium. Among these possibilities, the lithium-ion cell has a safety advantage as it does not contain lithium in a metallic form. As a result, it holds a dominant position in the market. In Li-ion batteries, both positive and negative electrodes are made of lithium intercalation compounds. As a battery is cycled, exchange of Li^+ ions takes place between the two electrodes. Unlike the aqueous systems, there is practically no parasitic reaction in concurrence with the main charging process. For this reason, overcharge is not required, but on the contrary, it causes irreversible damage and safety problems. In this context, lithium-ion batteries generally come with a protection circuit, especially when they are supplied as a battery pack.

Preferred charging methods

The charge of Li-ion batteries is normally done using IU method. Because of the absence of parasitic reactions, such as the water decomposition reactions in aqueous systems, more complex charge methodologies, such as pulse charging, are unnecessary.

The maximum charging voltage depends on the nature of the electrochemical couples used in the battery. Lithium-ion batteries with lithium cobalt oxide or lithium manganese dioxide as a cathode material are generally charged at a voltage between 4.0 and 4.2 V. Mixed oxides $LiNi_{1-x}Co_xO_2$ are more sensitive to the charge voltage and a very high value, even if it gives higher discharge capacities, can affect cycle life and stability. A charge voltage of 4.0–4.1 V is then preferable. For $LiFePO_4$/C batteries, the charging voltage is 3.7 V.

During the I phase, the voltage variation is different for lithium cobalt oxide and lithium ion phosphate ($LiFePo_4$) chemistries (Figure 12). For the lithium cobalt oxide cells, the voltage increases linearly, whereas for the $LiFePO_4$ cells, the voltage shows little variation from 20 to 80% SoC.

To compensate the very small self-discharge and the self-consumption of the protection circuits, a short complementary U charge can be done periodically (typically every 500 h), or when the open-circuit voltage (OCV) falls below a threshold value.

End–of-charge control

Because of the absence of required overcharge, and of reactions concurrent to the main charge reactions, the end-of-charge control is easier than for aqueous systems. The first possibility is to stop the I charge when a threshold voltage value is reached, but this is not very reliable for high charge rates. It is also rather easy to sum up the charge input into the battery and stop charging when the balance with discharged capacity is reached. Correspondence tables between the battery voltage and the SoC can also be used, but this is not applicable for lithium ion phosphate cells, as shown in Figure 12.

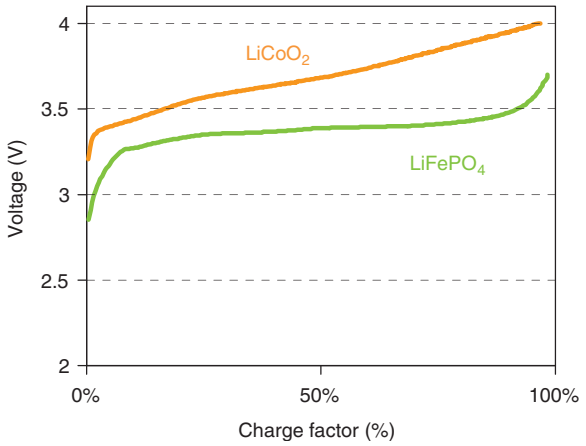

Figure 12 Voltage variation during the I phase for two types of Li-ion batteries ($LiCoO_2$ and $LiFePO_4$ chemistries).

Supercapacitors

In supercapacitors, also called electrochemical double-layer capacitors, energy is stored electrostatically by polarizing an electrolytic solution, and no chemical reactions are involved. This mechanism is highly reversible, and allows the supercapacitors to be charged and discharged at a very high rate, during a large number of cycles.

The minimum charge time of a supercapacitor is about 10 s, but the charge rate is often mainly limited by the capabilities of the charger. Because of this ability to rapidly charge, the use of large supercapacitors is proposed, for example, for regenerative braking on vehicles.

The voltage of the supercapacitor varies linearly with SoC, and charge must be stopped when a maximum voltage, specified by the manufacturer, is reached.

Sodium–Sulfur Batteries

In NaS batteries, the active materials are sulfur at the positive electrode and sodium at the negative electrode. At the operating temperature (300–350 °C), both sulfur and sodium are liquid. A solid β-Al_2O_3 ceramic serves as the electrolyte by conducting sodium ions. During discharge, the sodium is oxidized at the sodium/β-Al_2O_3 interface, forming Na^+ ions. These ions migrate through the electrolyte and combine with the sulfur that is being reduced in the positive electrode compartment to form sodium pentasulfide (Na_2S_5). The sodium pentasulfide is immiscible with the remaining sulfur, thus forming a

two-phase liquid mixture. After all of the free sulfur phase is consumed, the sodium penta sulfide is progressively converted into single-phase sodium polysulfides with progressively lower sulfur content (Na_2S_{5-x}). During charge, these chemical reactions are reversed. There are no secondary reactions in these types of batteries.

Sodium–sulfur batteries are commercially produced and used in stationary applications for power quality and peak/load shaving. Cells are assembled into modules in various series/parallel configurations within a thermal enclosure. The battery itself is then constructed by connecting these modules again in a series/parallel arrangement to obtain the desired voltage, energy, and power. The resultant battery is combined with a power conditioning system (PCS) to form an integrated device that can be connected to an electrical network.

In charging NaS batteries, special attention has to be paid to the end of charge: at high SoC, the internal resistance, and thus voltage, increases strongly because pure sulfur is not conductive. Pulse charging at half the maximum charge rate is often recommended. Anyway, the NaS battery normally comes with the PCS and its preprogrammed charge strategy.

Sodium–Nickel Chloride Batteries (Zebra)

Sodium–nickel chloride (Na–$NiCl_2$) batteries are another member of the 'high-temperature' family. They are currently produced by one single manufacturer under the commercial name Zebra. They operate at 270–350 °C and share two common features with NaS batteries: liquid sodium and β-Al_2O_3 ceramic. In the charged state, a Zebra cell consists of a negative liquid sodium electrode and a solid positive electrode containing NiCl and nickel. A β-Al_2O_3 ceramic tube physically separates the electrodes and ensures the transport of sodium ions. To ensure contact between the solid positive electrode and the ceramic electrolyte, the positive electrode is flooded with molten chloroaluminate ($NaAlCl_4$), which is an equimolar eutectic mixture of sodium chloride and aluminium tri chloride. During discharge, sodium is oxidized into Na^+ ions, forming sodium chloride, and NiCl is reduced to metallic Ni.

There are no secondary reactions in Zebra batteries. In case of overcharge, when all the sodium chloride has been consumed, excess nickel in the positive electrode reacts with sodium chloroaluminate, which occurs at a higher potential than the cell reaction. In doing so, the current flow through the cell is stopped and this constitutes an intrinsic protection mechanism.

The typical charging method for Zebra cells is an IU charge at $C/6$ rate for normal charge and C rate for fast charge. The voltage limitation is 2.67 V cell^{-1} for normal charge and 2.85 V cell^{-1} for fast charge. Regenerative braking is also possible, limited to 3.1 V cell^{-1}.

As for NaS batteries, the Zebra cells are connected in series/parallel to obtain the required voltage and capacity. A battery management interface (BMI) ensures thermal management, controls the main circuit breaker, supervises all electrical parameters, and controls the charger by a dedicated PWM signal.

Redox-Flow Batteries

In this type of power source, the electrolyte contains one or more dissolved electroactive species and flows through a reactor where the electrochemical reactions take place. The electrolyte is stored externally, generally in tanks, and is pumped through the cells of the reactor. The main difference with conventional batteries is that the energy and power of the redox-flow battery are fully independent: the energy is related to the electrolyte volume (tank size) and the power to the reactor size. The notion of charge/discharge rate is then not really meaningful, because power and energy are not linked. However, maximum allowed current is specified, from the maximum acceptable current density.

The main examples of redox-flow batteries at the present time are the vanadium redox-flow battery (VRB), polysulfide bromide battery (PSB), and zinc–bromine battery (ZBB).

- VRB: The positive and negative half-cell electrolytes are vanadium ions at different oxidation states in sulfuric acid.
- PSB (also called Regenesys system): The redox couples are sulfide/polysulfide and bromine/bromide in the negative and positive half cells, respectively.
- ZBB: During charge, metallic zinc is plated from the electrolyte solution onto the negative electrode surfaces, whereas bromide is converted to bromine at the positive electrode. In the electrolyte tank, bromine is under a chemically complexed organic form.

Redox-flow batteries normally use a PCS, which manages the charge and discharge. The charging and discharging currents are more or less equal. The charge factor needs to be adapted to the losses level (typically 25–35% for VRB, for instance). Additionally, VRB could also be recharged by replacing the discharged electrolyte by a fresh solution, in a sort of 'refueling station'.

Nomenclature

Symbols and Units

Δt	change in time
ΔT	change in temperature
ΔV	change in voltage

Abbreviations and Acronyms

BMI	battery management interface
BMS	battery management system
DC	direct current
DoD	depth of discharge
EMF	electromotive force
EV	electric vehicle
HEV	hybrid electric vehicle
IC	intermittent charging
ICC	interrupted charge control
OCV	open-circuit voltage
PCS	power conditioning system
PSB	polysulfide redox battery
PV	photovoltaic
PWM	pulse width modulation
SoC	state-of-charge
SoH	state-of-health
UPS	uninterruptible power supply
ZBB	zinc–bromine battery
VRB	vanadium redox-flow battery
VRLA	valve-regulated lead–acid

See also: **Batteries:** Charge–Discharge Curves; Fast Charging; **Capacitors:** Electrochemical Double-Layer Capacitors; **Secondary Batteries – Flow Systems:** Overview; **Secondary Batteries – High Temperature Systems:** Sodium–Nickel Chloride; **Secondary Batteries – Lead-Acid Systems:** Coup de Fouet; Charging; Overview; State-of-Charge/Health; **Secondary Batteries – Lithium Rechargeable Systems – Lithium-Ion:** Overview; **Secondary Batteries – Lithium Rechargeable Systems:** Overview; **Secondary Batteries – Nickel Systems:** Nickel–Cadmium: Overview; Nickel–Cadmium: Sealed; Nickel–Metal Hydride: Overview.

Further Reading

Bergveld HJ, Kruijt WS, and Notten PHL (2002) *Battery Management Systems*. Dordrecht, The Netherlands: Kluwer Academic Publishers.

Crompton TR (2000) Constant-current charging. *Battery Reference Book*, 3rd edn., pp. 1–24. Oxford: Reed Elsevier group, Newnes.

Dhameja S (2002) Electric vehicle battery charging. *Electric Vehicle Battery Systems*, pp. 69–94. Oxford: Reed Elsevier group, Newnes.

Linden D and Reddy TB (2002) *Handbook of Batteries,* 3rd edn. New York: McGraw-Hill.

Muneret X, Gobé V, and Lemoine C (2005) Influence of float and charge voltage adjustment on the service life of AGM VRLA batteries depending on the conditions of use. *Journal of Power Sources* 144: 322–328.

Nelson RF (1998) Valve-regulated lead/acid battery designs and charging strategies – are they linked? *Journal of Power Sources* 73: 104–109.

Wagner R and Sauer D-U (2001) Charge strategies for valve-regulated lead/acid batteries in solar power applications. *Journal of Power Sources* 95: 141–152.

Wong YS, Hurley WG, and Wölfle WH (2008) Charge regimes for valve-regulated lead–acid batteries: Performance overview inclusive of temperature compensation. *Journal of Power Sources* 183: 783–791.

Fast Charging

V Svoboda, Huntsville, AL, USA

Introduction

Increased environmental concerns and fuel costs have made a significant impact on transportation technology, as a result of which advanced vehicles with enhanced fuel economy and less emission have started to penetrate the market and have gained popularity. The current market offers hybrid electric vehicles (HEVs), which combine internal combustion motor with electric drive train and battery energy storage. Electric vehicles (EVs) with only electric drive train and battery energy storage have never grown over the prototyping and testing phases. Although the state-of-the-art HEVs provide enhanced fuel economy, in order for them to significantly influence global fuel consumption and the environmental situation they need to be developed further. One of the approaches is moving from micro-HEVs to plug-in HEVs, which have increased utilization ratio of the electric drive train. Technically, besides other advancements the main development tasks should focus on high-capacity batteries with fast charging abilities and fast charging techniques. Such development might also trigger utilization of EVs in the future.

There is no single definition of fast charging. Generally, any technique that provides charge duration of less than 1 h at charge rate $>1\,C$ is considered to be fast charging. The importance and difficulty of fast charging may be represented by comparing with conventional gasoline tank filling in which about 90 kWh of energy is stored in a vehicle in a couple of minutes. A conventional, single-phase household charger delivers about 30 kWh in 10 h.

This article focuses mainly on fast charging of advanced lead–acid and nickel–metal hydride (Ni–MH) batteries. Lead–acid batteries have very low internal resistance, which makes them favorable for high charge and discharge rates. Nickel–metal hydride batteries have higher capacity density and cycle life than lead–acid batteries. Although the capacity density and cycle life of lead–acid and Ni–MH batteries are not as high as that of rechargeable lithium batteries, they are still favored because of their cost, safety, endurance, and recyclability. Rechargeable lithium batteries are considered especially for new generation EVs and plug-in HEVs. Lithium batteries are a relatively young technology and are undergoing a fast development. A short overview of their charging and specific requirements is provided in the end of the article based on current experience and limited data available.

Battery Technology

Lead–Acid Battery Chemistry

The principle of a lead–acid battery is a double sulfate chemical reaction. Both lead active mass on the negative electrode and lead dioxide active mass on the positive electrode form lead sulfate during discharge. At discharge, sulfate ions are consumed at both the electrodes and water is formed resulting in a decrease in the specific gravity of the electrolyte. The negative lead electrode has a high overpotential for hydrogen evolution in comparison with other metals, allowing high cell voltage in aqueous electrolytes. Its surface area measured by Brunauer–Emmet–Teller (BET) equation ranges from 0.3 to 0.6 $m^2\,g^{-1}$. Typical lead–acid accumulators have a relatively simple design and simple manufacturing, with a nominal cell voltage of 2 V, 80% energy storage efficiency, and 90% coulombic (Ah) efficiency. The high molecular weight of lead limits specific energy of the cell; theoretical coulombic capacity of lead is 259 Ah kg^{-1}. Utilization of active mass (AM) in a lead–acid cell is however limited by the maximum AM conversion rate, which is dependent on acid diffusion into AM pores and recrystallization, and it significantly depends on the discharge rate. Both electrodes are solid electrode reactants of the same chemistry, and their products maintain porous structure; thus, a reverse polarization is not fully destructive for the cell. In addition, any mutual contamination of the positive and the negative electrode is not risky, which lowers the need for a separator. A high variation of the cell's internal resistance with the state of charge (SoC) is a drawback. The lead metal, sulfuric acid electrolyte, and other components of a lead–acid battery are relatively inexpensive. Lead exists in considerable abundance in nature, and the recycling process of old batteries is very efficient.

There is no need to control individual cells voltage either during charge or discharge, and their SoC can be rebalanced by a slight overcharge. Flooded cells are refillable with deionized water to compensate water loss that might have resulted from an extensive overcharge. Individual cell components have a low specific resistance, which leads to high-power capabilities. The cells operate under a wide range of temperature, i.e., from -30 to $+70\,^{\circ}C$. Lead–acid batteries may work without any additional expensive peripheral system like a special battery management system (BMS), temperature monitoring, and cooling/heating system.

Lead–Acid Battery Components

Negative electrodes with sponge lead AM are most typically pasted plates on a grid, which mechanically supports the AM and functions as a current collector. The negative plates' as well as positive plates' grids are still optimized and further developed. Grid modifications usually focus on the grid segment's shape, mesh density along the plate surface, and the grid's thickness. Optimized grids, despite higher cost, facilitate better electrode conductivity, more homogeneous current distribution, and enhanced mechanical resistance to AM swelling. Thinner grids are convenient for batteries with more high-powered abilities.

Positive electrodes, for traction applications, are thin pasted grid plates, thin tubular plates, or special electrodes. Lead dioxide (PbO_2) active mass of theoretical capacity 224 Ah kg^{-1} and BET surface area 4–6 $m^2\ g^{-1}$ is applied on positive electrodes.

Tubular plates consist of three main components: a grid system made of vertical lead rods called spines, woven or nonwoven textile tubes resistant to sulfuric acid called gauntlets, and PbO_2 active mass. Spines work as current collectors whereas gauntlets hold and provide mechanical integrity to positive active mass (PAM), preventing PAM shedding and internal short circuit. Tubular electrodes are usually about 10–12 mm in thickness. Special 3.5-mm-thick tubular plates are already designed and demonstrated by CMP Batteries Ltd. in order to increase power performance and specific energy of tubular plate valve-regulated lead–acid (VRLA) batteries for EV applications. Batteries with tubular positive plates have higher mechanical endurance against vibrations and shocks, which makes them preferable for traction applications, particularly as HEV or EV batteries. The expected cycle life of tubular electrodes is 1500 cycles in a full charge–discharge cycling and 15–20 years lifetime in a float charge operation.

Spiral electrodes are special electrodes used, e.g., in OPTIMA (JCI), Cyclon (Hawker), and Orbital (Exide) VRLA batteries. Both positive and negative spiral electrodes are actually of thin grid design, and they are spirally rolled together with a separator. The advantage of these thin electrodes is a low electrical resistance and self-mechanical suspension to AM. Batteries with spirally wound electrodes are commercially available on the market. Other special electrodes include bipolar electrodes, e.g., Effpower, Pulsar, and Horizon batteries, and thin metal film (TMF®) electrodes (0.25 mm thick) used in, e.g., Bolder and Inspira (JCI) batteries. As mentioned, thin electrodes are lightweight and have a large surface area; they are suited for high-power applications. As a trade-off, the lifetime of such thin electrodes is expected to be lower owing to corrosion and lower mechanical durability. The latest example is the UltraBattery developed for HEV by CSIRO and manufactured by East Penn and Furukawa; it combines thin electrodes with asymmetric supercapacitor, improving the power performance of the negative electrode.

Grids or spines of grid or tubular plates, respectively, are made of lead alloy, which has a unique corrosion-resistant property in a diluted sulfuric acid electrolyte and positive polarization. The corrosion resistance is due to the formation of a dense lead dioxide layer on the grid surface, which reduces further fast corrosion. Unfortunately, the lead dioxide layer has 1.26 times larger volume than lead metal, which tends to crack and allow further corrosion. Charge–discharge reaction of PAM includes a dissolved state. It means that, during discharge, dissolved bivalent lead ions are formed, which then precipitate as less soluble lead sulfate. Positive active mass particles chemically change during the charge transfer reaction within a very close distance; their dissolution and solidification occur within micrometer range. Charge–discharge cycling causes gradual recrystallization and disintegration of the PAM. This is usually observed as an increase in the thickness of PAM, i.e., positive electrodes swell and PAM becomes mechanically softer. This process is called positive electrode softening.

Nickel–Metal Hydride Battery Chemistry

Charge transfer reaction in Ni–MH batteries is based on reversible shuttling of hydrogen proton between positive and negative electrodes. The reactions at charge (left to right) and reversible discharge are as follows:

$$\textit{Positive electrode}: \mathrm{Ni(OH)_2} + \mathrm{OH^-} \rightleftarrows \mathrm{NiOOH} + \mathrm{H_2O} + \mathrm{e^-}$$
$$\textit{Negative electrode}: \mathrm{M} + \mathrm{H_2O} + \mathrm{e^-} \rightleftarrows \mathrm{MH} + \mathrm{OH^-}$$
$$\textit{The overall reaction}: \mathrm{Ni(OH)_2} + \mathrm{M} \rightleftarrows \mathrm{NiOOH} + \mathrm{MH}$$

where M represents a metal hydride (MH) alloy that is capable of reversibly absorbing and desorbing hydrogen atoms. Nickel hydroxide active mass in the positive electrode undergoes a redox charge transfer reaction at charge and discharge. The alkaline electrolyte is an aqueous solution of potassium hydroxide. The Ni–MH cell nominal voltage is 1.2 V.

In contrast to lead–acid batteries, there is no change in electrolyte concentration or volume during charge and discharge. This allows battery operation and design with a minimal amount of electrolyte (lower battery mass and volume); the electrolyte needs to provide good ionic conductivity at low internal resistance. The charge reaction is exothermic, and contributes to heating up of the battery during charging.

Charge capacity of positive and negative electrodes and their SoC balance are crucial for long lifetime and overcharge capability. The positive electrode in a Ni–MH

battery is designed and produced with lower charge capacity compared to the negative electrode forming charge reserve in the negative electrode. This means that close to 100% SoC and during overcharge, the excess of charging energy is mainly consumed in electrochemical decomposition of electrolyte. Practically, on the positive electrode, oxygen gas is produced while the negative electrode can still accept charge. Gaseous oxygen from the positive electrode diffuses through gas channels in the separator to the negative electrode where it efficiently recombines with hydrogen to form water. Such charge reserve and higher efficiency oxygen recombination cycle are very effective mechanisms against overcharging. During discharge, the oversized negative electrode has an overdischarge reserve. The reserve compensates overdischarging to some degree and reduces corrosion of the MH alloy.

Nickel–Metal Hydride Battery Components

The positive electrode is commonly fabricated by pasting nickel hydroxide slurry in a nickel current collector. A nickel current collector is either a perforated nickel sheet or nickel foam (see **Figure 1**). Various additives might be used in the PAM; cadmium is typical for improved electronic conductivity. Nickel oxide hydroxide, in the active mass of the positive electrode, undergoes redox reaction, which is an intercalation process between β-nickel hydroxide and β-nickel oxide hydroxide. Protons need to pass in and out from the crystal center to the surface to react with the electrolyte. The surface of the AM particles needs to be conductive, and the electronic transfer to the electrode current collector must be available for the charge transfer reaction to proceed. As with lead–acid batteries, PAM loses electronic conductivity with discharge; thus, fabrication and preservation of the original PAM properties (e.g., particle-to-particle interconnection) during cycling is essential.

The negative active mass (NAM) is metal alloy (MH), which is also commonly applied by pasting it on a nickel current collector. A nickel current collector is either a perforated nickel plate or nickel foam. The alloy is capable of absorbing hydrogen during charging and desorbing during discharging. During charging, hydrogen atoms are catalytically reduced on the MH surface and adsorbed into voids in the metal lattice via diffusion. The AB_5 type MH alloy, sometimes called 'misch metal', is typically used; a representative is lanthanum penta nickel ($LaNi_5$), which provides theoretical specific charge capacity of 372 Ah kg^{-1}. Some metal additives in the alloy provide corrosion protection and long lifetime, whereas others provide increased charge storage capacity. Usually, those properties are a trade-off, and a balanced optimum is desired. This is also valid for other alloys including AB_2 type (represented by $Zr(MnVCrNi)_2$) and other types developed and demonstrated till today.

The negative electrode in the Ni–MH battery is usually designed with higher capacity than the positive electrode, which guarantees oxygen evolution before the negative electrode is fully charged and hydrogen gas starts to form. Oxygen gas, formed on the positive electrode, can pass through open pores in the separator to the negative electrode, where it recombines with hydrogen protons to form water. This provides an effective oxygen recombination cycle allowing certain overcharge with a continuous low-rate charging. Safety of the Ni–MH battery is high, but a fully charged negative electrode, when exposed to humid atmosphere, starts high-rate oxidation with atmospheric oxygen, which might cause a fire.

As mentioned before, an alkaline electrolyte is an aqueous solution of potassium hydroxide and in total it does not change concentration or volume during charging or discharging. Therefore, electrolyte volume in the battery can be minimized for lower battery mass and volume. Certain electrolyte volume is, however, required for good ionic conductivity. Often, the electrolyte is only soaked in a separator, without a free electrolyte in the battery.

The main function of the separator is to separate positive and negative electrodes from an internal short circuit. The separator also works as a substrate in which an electrolyte is soaked and which then maintains open pores for gas transport.

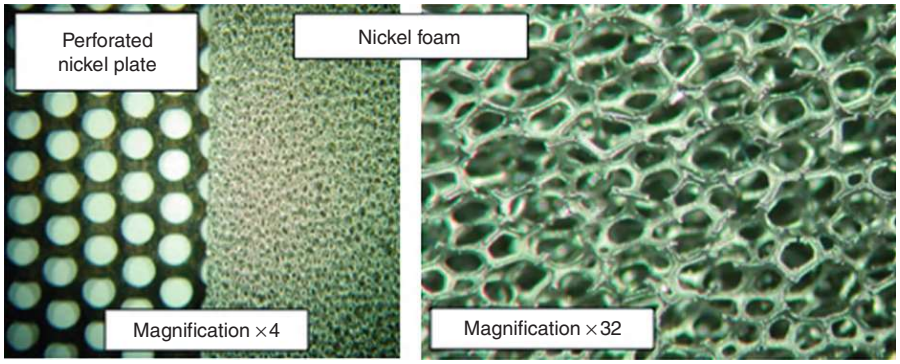

Figure 1 Current collectors of nickel–metal hydride (Ni–MH) battery, perforated Ni plate, and Ni foam.

Conventional and Fast Charging Method

Conventional and fast charging algorithms vary for lead–acid and Ni–MH batteries. The charging technique of these batteries is provided below.

Conventional Charging of Lead–Acid Batteries

The very basic charge methods are constant current (CC) and constant voltage (CV) charges. Usual current rates are $C/5$ or lower, and chargers are of very simple design and control.

The CC charge method can involve just one or more charge steps. In this method, Ah counting is a linear function of time. Current step(s) are usually terminated by voltage and/or time. The problem with this charging method, for VRLA batteries, may be insufficient charge leading to undercharge resulting in irreversible sulfation. This might, for instance, happen when aged batteries start higher efficiency oxygen recombination cycle, which depolarizes negative electrode and consumes charge. On the contrary, if the final CC charging step is of a higher rate, then there is an extensive gassing at the initial phase of cycle life and later a risk of drying out and thermal runaway as the oxygen cycle starts to dominate the end of the charging.

In CV charging, the initial stage is limited by the maximal current of the charger or maximal charge acceptance of the battery. Usual rates are around $C/5$ or lower while battery voltage is monitored. As soon as the battery reaches a given voltage, the charger unit maintains the voltage and controls – reduces charge current. The charge process is completed when charge current decreases below a specified value, which is usually a low rate in the range of $C/50$ to $C/100$. Some advanced CV chargers might continue with a permanent float charge after the main charge is completed. A disadvantage of this charge method is a very long end of the charge phase, in which the current is controlled down to the limit. A faulty charging may occur with aged VRLA batteries, owing to higher efficiency oxygen recombination cycle and depolarized negative electrode. Then the charger applies a higher current, which increases positive electrode polarization, which acts as a positive feedback and increases oxygen evolution rate. Such positive feedback fault charging causes drying out and increases the risk of thermal runaway.

Another conventional charging method is a combination of CC and CV methods, called CC-CV-CC_{a1}-CC_{a2}. Time duration of this charge type is usually 4–12 h; the initial CC charge of $C/5$ rate is limited by voltage, followed by CV charge, in which voltage is kept constant until the charge current drops to a given value in the range of $C/50$ to $C/100$. The following step is CC_{a1} charging of lower rate compared to previous step current termination limit; this step is limited by voltage. The following and the final step of the charge process is a lower rate CC_{a2} charging, which is voltage and time limited. An example of this charging method is shown in Figure 2.

Manufacturers recommend end of the charge by 100% charge return of the previous discharge (it supposes that the previous Ah discharge is measured through a BMS and the information is available in the charging control) plus additional charge of 3–5% of the nominal capacity for a new battery and 7–8% for aged battery. The charge factor is the ratio of 'charged Ah' to previously 'discharged Ah'; thus, the usual charge factor is in the range of 1.03–1.05. Charge factor accounts for empirically estimated charge consumed with gassing and oxygen recombination cycle and with certain overcharge that is necessary for rebalancing individual cells' SoC in the battery.

Conventional Charging of Nickel–Metal Hydride Batteries

Conventional charging of lead–acid batteries cannot be used for Ni–MH batteries because end of charge voltage

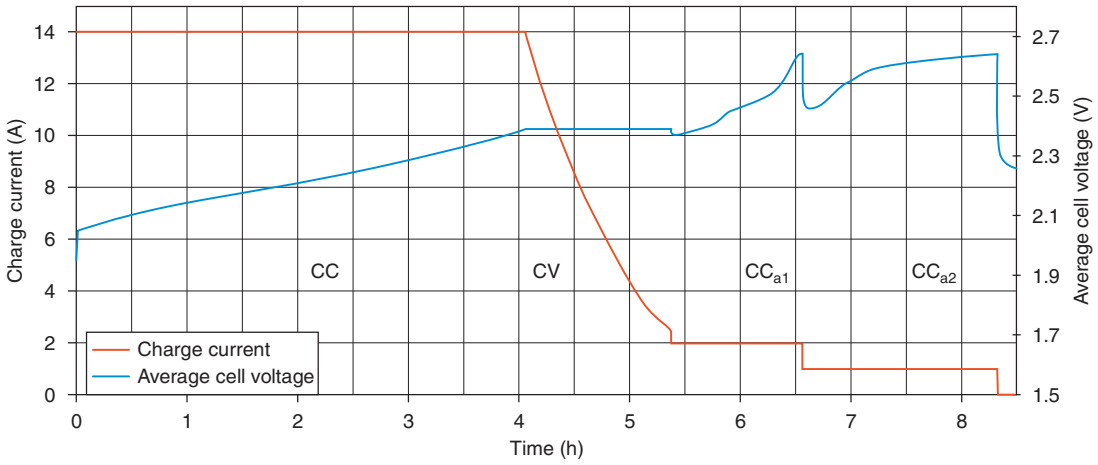

Figure 2 An example of CC-CV-CC_{a1}-CC_{a2} charging method.

varies significantly throughout the cycle life because of variation in internal resistance (see an example in Figure 3). These mechanisms are discussed later.

The inability to use end of charge voltage with a low-rate conventional charging leaves the charge limitation to time or charge and relying on a low current rate, which may be completely consumed in the oxygen recombination cycle with a fully charged battery. Thus, the simplest Ni–MH charger is a low-rate CC charger that is controlled by a timer or by switching the charging off by the user who measures the charging time. The charge factor (charged Ah/discharged Ah) determines the charge duration; it is typically in the range of 1.3–1.6. The charging time of the simplest charging method is set to fully recharge a completely discharged battery. It cannot be avoided that the batteries are not fully discharged before charging, or the user forgets to terminate the charging process. This defines the requirement that the charge current rate must be lower compared to oxygen recombination cycle. For instance, the standard IEC 61436 requires 16 h charging for a full charge with 0.1 *C* CC. Permanent overcharging of 0.1 *C* can be usually consumed by oxygen recombination cycle. See capacity development under such overcharge in Figure 4; also notice increase of internal resistance, which represents the progression of a degradation mechanism, which is discussed later.

Smart conventional chargers may utilize $-\Delta V$ and/or $\mathrm{d}T/\mathrm{d}t$ charge termination; both methods however

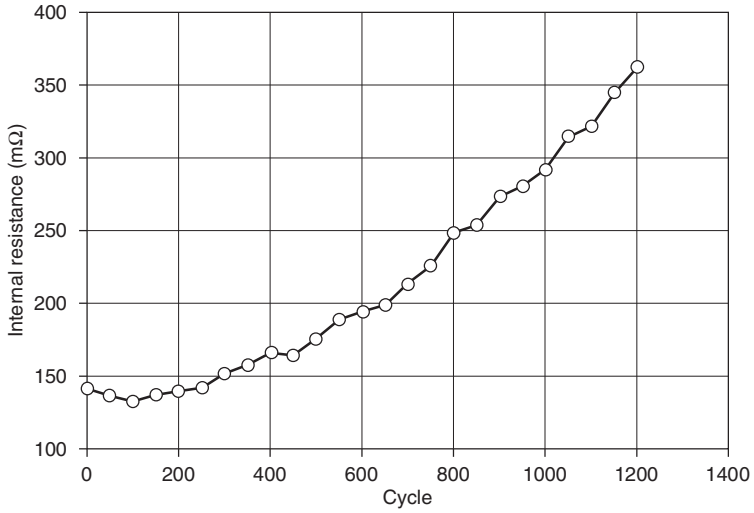

Figure 3 An example of internal resistance development in nickel–metal hydride (Ni–MH) battery during cycling.

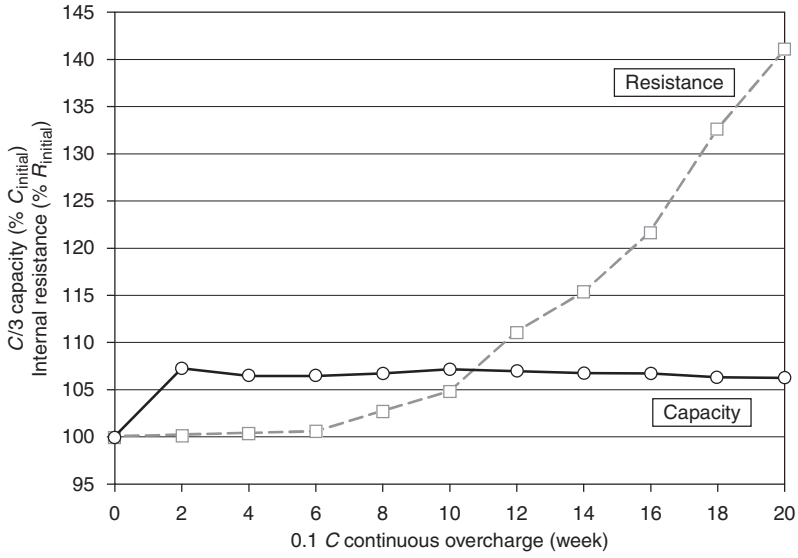

Figure 4 An example of discharge capacity and internal resistance development during 0.1 *C* continuous overcharge of nickel–metal hydride (Ni–MH) battery.

require a higher charge rate. The methods are described in the section entitled 'Fast Charging of Nickel–Metal Hydride Batteries'.

Trickle charging is basically a pulse charging method. A high-rate pulse charging is discussed later. Trickle charging of a low charge rate allows continuous charging and compensates self-discharge during storage. Most common trickle charging can bring a battery to 100% SOC, while temperature and gassing remain low. Continuous trickle charging compensates charge loss, due to self-discharge, but also reduces battery life due to slightly elevated temperature and electrode polarization accelerating corrosion and electrolyte loss. Attempts were made to apply a short reverse polarization pulse prior to each charging pulse to depolarize electrodes and lower gassing. The technique is sometimes called 'negative pulse charging'; however, its benefits are still discussed against increased charge duration and requirements and cost of the charger hardware.

Fast Charging of Lead–Acid Batteries

The main requirement for fast charging is minimal charging time without abuse to the battery for the duration of the battery life. Advanced high-power chargers for traction battery provide recharge in 5–30 min. Such chargers must be connected to a high-power grid, for example, recharging 200 V, 50 kWh battery in 20 min requires the charger to supply more than 150 kW power and 750 A current.

In the charger hardware, two main units may be distinguished: (1) a high-power switching rectifier, which delivers direct current (DC) power to the battery, and (2) a microprocessor charge control unit. The design strategies are different, including a favorite concept, where the charge control unit specific to a battery is onboard the vehicle. Also important are standardized power and communication connectors and communication protocols to the vehicle, user and billing interface, grid power connection, etc. An inductive charging avoids any galvanic contact between the charger and the battery onboard a vehicle, and thus makes the charging simpler and safer for the user. Energy from charger to battery is transmitted via electromagnetic field by means of two inductors. The first is stationary by the charger, and the second onboard the vehicle. Power transfer range via the inductive charging is 1–150 kW, which allows fast as well as conventional low-power charger coupling.

In power systems with a large difference in consumption between peak time and off-peak time, EV and plug-in hybrid vehicle might balance the consumption with conventional overnight charging. A fast charging, rather provided in centralized charging stations, enables a quick recharge in a couple of minutes for immediate use whenever required. Scheduling with respect to power consumption profile balancing is, therefore, impractical, although such consumption may be predictable for a typical user profile. The method of indirect control is an electricity price variation for recharging in peak and off-peak time.

With respect to charge duration, the charger must continuously control charging to the maximal charge acceptance of the battery. Figure 5 depicts a three-dimensional chart clearly showing and distinguishing the area of dominating charge acceptance versus overcharging of VRLA battery. The pale curve indicates development of maximal current during charging to follow the maximal charge acceptance of the battery and avoid extensive gassing, temperature rise, and other overcharge effects. Thus, a prerequisite for fast charging is detailed information about the battery for a fast charger provided in the charger–battery communication.

With respect to battery design, batteries suitable for fast charging must have high charge acceptance and low internal resistance for minimal joule losses. In order to achieve minimal charge duration, fast charging does not need to provide full recharge to 100% SoC. Recharging of the last few percents of SoC requires low charge rate and a much longer charge time. Practically, a battery can provide typical service in its application without recharge to 100% SoC. A full recharge must be, however, regularly performed to prevent irreversible sulfation (promoted by undercharge operation) and to equalize SoC of individual cells in the battery. Usually, a full equalization charge once every 20 cycles is recommended; however, for some batteries, this frequency is insufficient. Checking the frequency with the battery manufacturer is desirable. For plug-in hybrid vehicle or EV, a user is required to regularly perform an overnight full equalization charge. In hybrid vehicles, this might be a feature implemented in the BMS.

Battery voltage is the central parameter for controlling the charge process. However, the battery voltage consists of more voltage contributors, and the effective voltage (responsible for the charge transfer reaction) is only a fraction of the measured battery voltage during charging. The advanced fast charging approach is to recognize the voltage contributors and compensate the controlled battery voltage for the inactive fractions. Differences in the voltage fractions' time constant can be used for the recognition. Practically, the constants play a role during voltage relaxation after a current interruption.

Inductance of lead–acid batteries usually varies in the range of 10^{-9}–100^{-9} H, and thus the influence of inductance on battery voltage curve is practically negligible. On the contrary, the overpotential caused by the ohmic resistance is very significant; it has a time constant in the range of 10^{-7} s. Direct current ohmic resistance can be analyzed from the voltage relaxation curve after a current interruption or measured through alternating

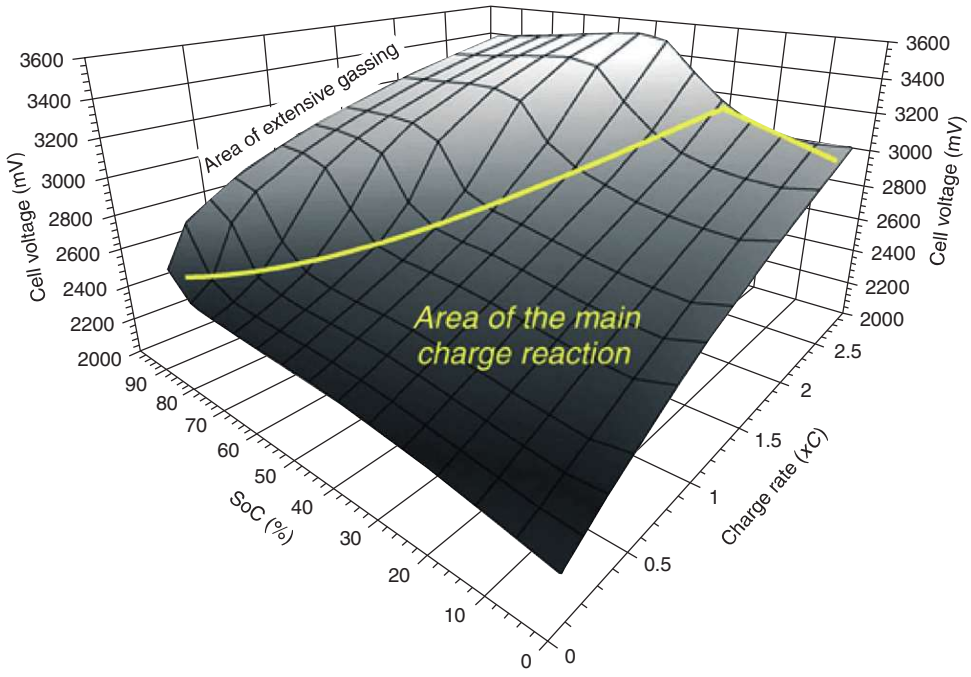

Figure 5 Voltage–current–state-of-charge (SoC) three-dimensional chart defining maximal charge acceptance of value-regulated lead–acid (VRLA) battery.

current impedance. Therefore, the compensation of ohmic resistance is the most popular technique for fast charge. The concept was originally introduced by K. V. Kordesch in 1960, and used in a charge control in 1972. Compensation of other voltage losses, such as diffusion overpotential, would be beneficial; however, this voltage relaxation requires measurement for several tens of seconds after the current interruption, which is impractical for any fast charge application. The time constants (τ) of the major processes during voltage relaxation at charge current interruption are shown in **Figure 6**.

Charging voltage (V_{ch}) may be simplified by the equation

$$V_{ch} = V^{\circ} + \mathrm{IR} + \eta$$

where V° is the open-circuit voltage, IR represents internal resistance contribution, and overpotential η denotes polarization. Only polarization is directly linked to the electrode processes. In fact, charge voltage compensated for the internal resistance part (IR), which is the so-called resistance-free charge voltage (V^{*}_{ch}), is a better charge control parameter. The resistance-free voltage might be expressed as

$$V^{*}_{ch} = V_{ch} - \mathrm{IR} = V^{\circ} + \eta$$

The beneficial effect of the internal ohmic resistance compensation increases with charging current and provides a much more effective means of controlling charging. Pulse-like interruptions of battery charging current allow monitoring of internal resistance during the charge, which might be integrated with voltage step-down CV-controlled pulses. A patent for resistance-free charge control was granted to F. H. Mullersman in 1970, R. F. Chase in 1971, and later in many other patents. Commercial fast chargers providing IR compensation were, for instance, MinitCharger originally manufactured by Norvik. An example showing how significantly IR of a VRLA battery develops during the initial 50% SoC recharge after a full discharge is presented in **Figure 7**.

Subsequent theories and discussions showed that a fast charging prolongs battery cycle life owing to numerous effects; some that are presented in this article are generally accepted, others are still being discussed.

Pulse charging

As mentioned earlier, pulse charging is convenient for IR free charging. Other benefits of pulse charging were claimed; some are supported by experimental measurements, some are rather vague and disputable. During a pulse switch on current, voltage increases, reflecting the same voltage fractions as at the current interruption with nearly the same time constants. Battery voltage during the pulse is monitored. Once it reaches gassing voltage, the pulse current is interrupted. Thus, such pulse charging might reduce gassing. On the contrary, in comparison with equivalent average CC, pulse current generates higher joule losses and longer charging time at

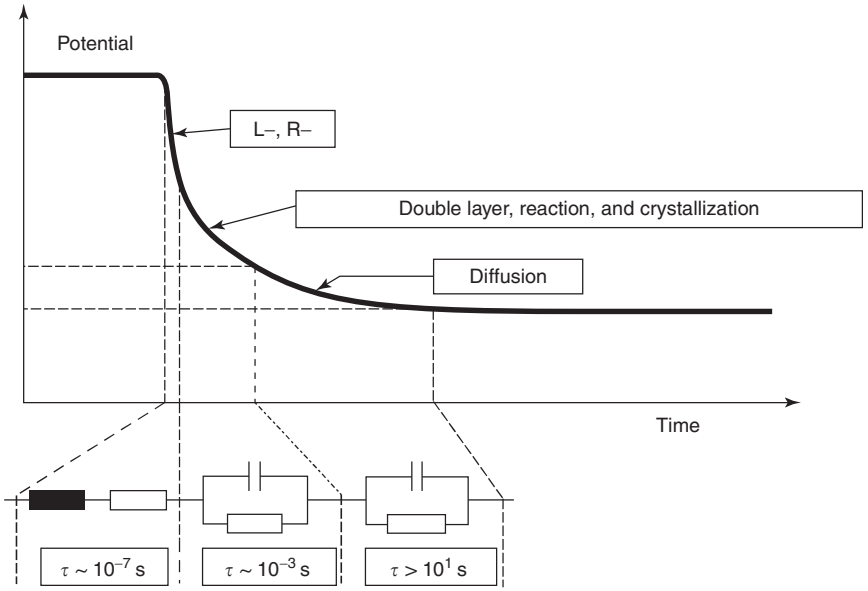

Figure 6 Voltage relaxation at charge current interruption in a lead–acid battery.

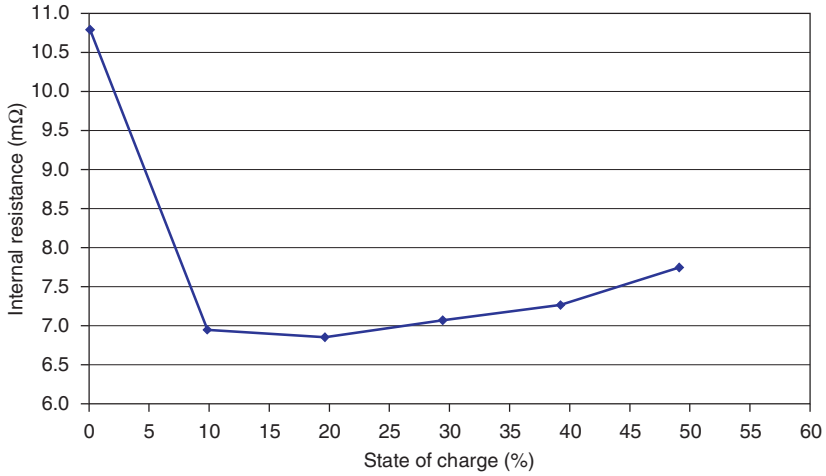

Figure 7 Direct current (DC) internal resistance measurement of a valve-regulated lead–acid (VRLA) battery during charging.

the same maximal current rate. Pulse charging has no influence on diffusion; however, it leads to lower gassing and higher negative electrode polarization at the end of charging. For better control of pulse charging, individual electrodes' potential control would be desirable; however, this is technically challenging. Installation of durable and reliable reference electrode would increase the battery cost significantly.

The pulse charging with a short reverse polarization pulse prior to each charging pulse is called 'negative pulse charging'. It is supposed to lower electrode polarization during charging and reduce gassing. Some reports claim dislodging gas bubbles from the porous electrodes active mass. Application of this technique with the same maximal charge rate results in longer charge duration. With the same average current, it causes higher joule losses and battery temperature. Most of the benefits are disputable and have not been generally accepted by the scientific community.

In summary, pulse charging is technically challenging. It requires much more sophisticated charger hardware, which reflects its cost, and the practical benefits are questionable.

Voltage-controlled current step-down fast charging

To control the charge process to follow the maximal charge acceptance, the battery's maximal charge acceptance as a function of SoC must be known. The principle of the step-down fast charge uses voltage-controlled CC

steps. An example of current and voltage time development in the step-down fast charge is shown in Figure 8. In the figure, it is noticeable that the first low-power steps and the following high-power steps are not voltage controlled – they are time controlled and voltage drops during the very initial charging phase after a previous full discharge. The initial two steps are time limited (30 s) and recharge about 8% SoC. In the third step, the voltage control is already activated; the voltage control delay is introduced owing to IR development. During the initial recharge 'activation' phase following a full discharge, IR drops significantly (see Figure 8), and before it stabilizes it causes battery voltage to drop.

In a simplified control mechanism, a battery's internal resistance versus SoC might be measured as a part of the battery characterized and integrated in the charging algorithm. In the step-down fast charging, it can be measured 'on-line' with each CC step change and integrated with the step voltage control. As explained before, diffusion overpotential is empirically compensated, to any means of its 'on-line' measurement is impractical. During high-power charging, temperature control is an essential function not only for safety and battery protection reasons, but also as a temperature compensation function in the voltage control algorithm. Temperature compensation voltage control coefficient of -4 mV K^{-1} per cell was found effective against temperature abuse in the step-down fast charging.

The mentioned full (100% SoC) recharge is difficult for fast charging; the current step-down procedure can be set to reach approximately 95% SoC. For lead–acid battery technology, it is a problem when a partial recharge is realized permanently causing irreversible hard sulfation and battery capacity loss. Therefore, a regular full recharge is necessary to prevent undercharge degradation and to equalize the SoC of individual cells.

A particular problem is the negative electrode undercharge during fast charging. Application of the mentioned pulse charge research in the step-down fast charging led to the introduction of current pulses in the final charging phase. Using a reference electrode, it was proven that the relatively low rate and time-limited current pulses (0.2 *C* for 30 s followed by 15 s rest time) at the end of charge increased the negative electrode polarization whereas the positive remained unchanged and gassing remained at minimum level (Figure 9). Thus, the risk of the negative electrode undercharging was lowered. Experimentally measured, the step-down fast charging performed on 70 Ah fully discharged thin tubular plate VRLA batteries recharges the battery to 80% SoC in approximately 30 min and to 95% SoC in approximately 60 min. Such charge duration results are reasonable and acceptable for automotive VRLA batteries.

Fast charging and temperature effect

During fast charging, battery temperature must be directly involved in the charge control. Heat is produced during charging and discharging from (1) reversible thermodynamic contribution, which is entropy change related to temperature dependence on free energy of the charge ($-T\,\Delta S$); (2) contribution of the charge transfer reaction irreversibility (practically the overpotential); and (3) particularly joule losses on battery IR are dominating in fast charging and high rate discharge. During fast charging, high-concentration sulfuric acid diffuses

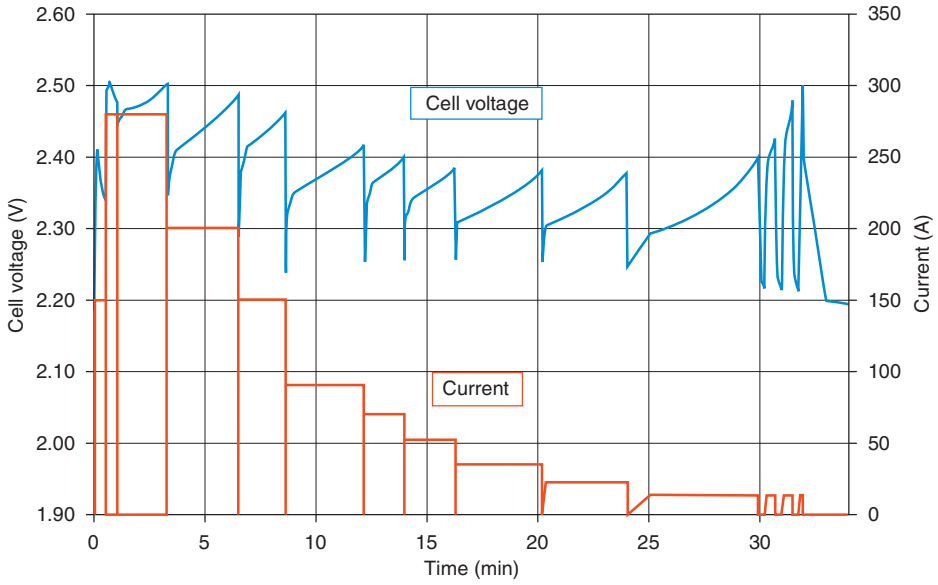

Figure 8 Current step-down fast charging procedure.

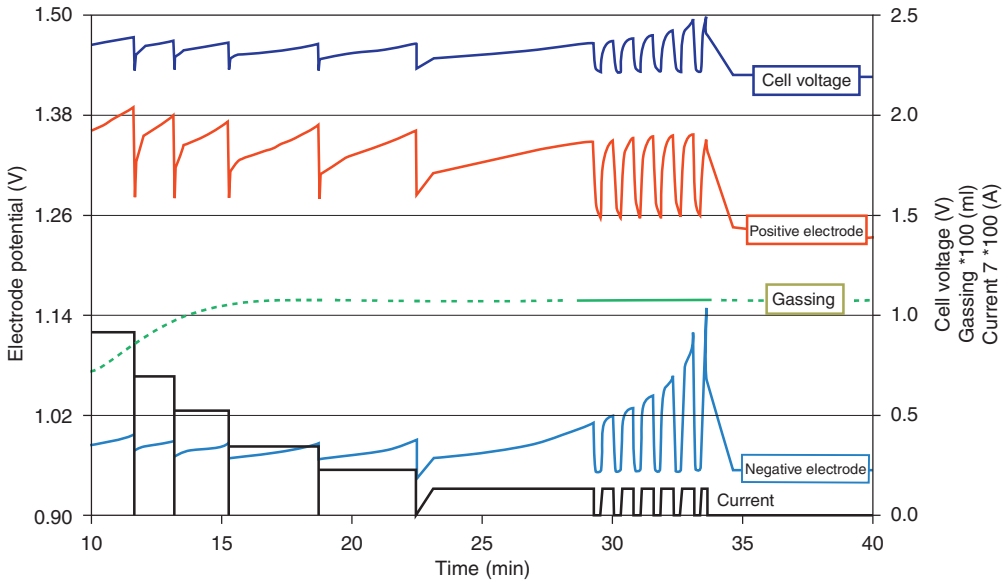

Figure 9 An example of final pulses of the step-down fast charging of valve-regulated lead–acid (VRLA) battery (negative electrode potential inverted).

from AM pores and significant energy is released from the acid dilution in low-concentration bulk electrolyte.

Battery temperature is an important parameter for almost all internal processes including side reactions. Charge transfer reaction kinetics strongly varies with battery temperature. This translates into increasing battery capacity with battery temperature and vice versa in a narrow temperature range around the standard room temperature ($T_o = 298\,\mathrm{K}$); the variation can be approximated as

$$\Delta C = 0.01\,C_n(T - T_o)$$

The approximated capacity dependence on temperature also reflects electrolyte conductivity, electrolyte diffusion, recrystallization, and other processes varying with temperature. Temperature variation has very limited influence on the equilibrium battery voltage at the standard conditions; it is defined by the approximated equation

$$\frac{\mathrm{d}V^0}{\mathrm{d}T} = 0.23\,\mathrm{mV}\cdot\mathrm{K}^{-1}$$

The dependence of the kinetic constant of the reactions (k) (including side reactions) on variation in battery temperature (ΔT) is defined by Arrhenius equation. The kinetic rate is about double when the temperature is increased by 10 K:

$$\frac{k(T+\Delta T)}{k(T)} = 2^{\Delta T/10}$$

Besides the charge transfer reaction kinetics and capacity, the following major side reactions and mechanisms are observed:

- higher corrosion (particularly of the positive electrode),
- irreversible sulfation is promoted by accelerated recrystallization,
- irreversible sulfation is hindered with higher solubility and recharge of lead sulfate ($PbSO_4$) particles,
- higher gassing,
- destruction of an expander/crystal modifier in the NAM,
- 'leading' process in the negative electrode resulting in lower active surface area, and
- risk of thermal runaway.

When a battery is cycled at a low temperature, the following main effects should be considered:

- lower power performance,
- lower discharge capacity,
- lower ion mobility in the electrolyte,
- lower kinetics of the charge–discharge reaction,
- lower solution of lead sulfate,
- lower self-discharge,
- lower rate of the corrosion process, and
- risk of electrolyte to freeze.

At a low temperature, battery capacity utilization may be reduced and it may get overcharged owing to decreased charge acceptance.

An optimal operation temperature for the battery may slightly vary with the battery type and design and it is within a temperature range of 25–45 °C. Accelerated and

enhanced lead sulfate dissolution at higher battery temperature promotes recharging of some irreversibly sulfated AM and recovers some lost capacity. A certain increase in battery temperature in combination with a certain cycling profile may result in cycle life prolongation. Battery life prolongation with a certain increase in temperature is reported in the literature.

Standard ANSI/IEE Std 535-1986 defines accelerated cycle life test with increased temperature. Temperature-based acceleration factor F_a is defined in the following equation, in which T_E (K) is the increased temperature of the test and $T_o = 298$ K is the standard room temperature. A chart of relative cycle life dependence on battery temperature is shown in Figure 10, in which coefficient $\alpha = 0.03$.

$$\log F_a = \alpha * (T_E - T_o)$$
$$F_a = \left(\frac{\text{CycleLife}(T_o)}{\text{CycleLife}(T_E)}\right)$$

Localized temperature development in a single VRLA cell was measured during fast charge with an infrared camera. The snaps after 4, 8, and 13 min are shown in Figure 11. The pale rectangle represents the border of the cell's plastic case; the view is perpendicular to the electrode's plate. The cell stands in a typical vertical position with both electrodes lugs and terminals on the top (visible on the most left snapshot). Heat generation in the cell during fast charging is not homogeneous over the electrode plates. The explanation is provided later in this article.

Besides integration of battery temperature control with the charging algorithm, battery temperature may be directly controlled with an active battery air- or water-heating/cooling system. Battery temperature might be finally the most limiting factor for fast charging in particular for larger batteries.

Fast Charging of Nickel–Metal Hydride Batteries

As discussed in the section entitled 'Conventional Charging of Ni–MH Batteries', any absolute voltage value cannot be used for charge control of Ni–MH batteries owing to a significant variation of internal resistance with cycle number. Fast charging using higher rate charge

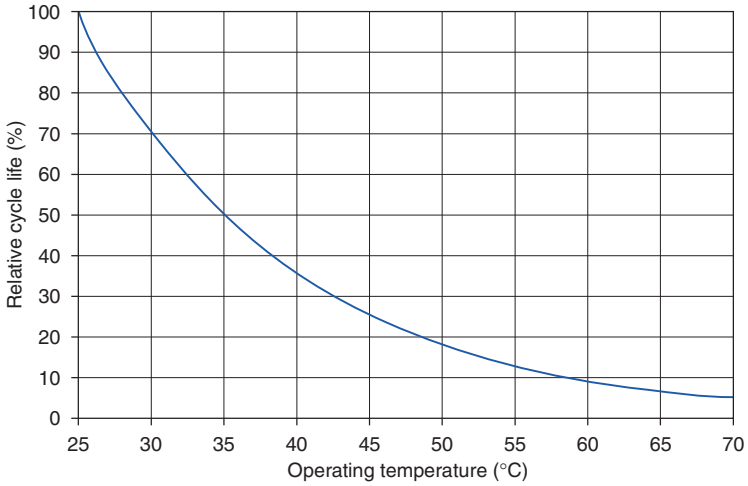

Figure 10 The influence of temperature on cycle life according to ANSI/IEE Std 535-1986 standard.

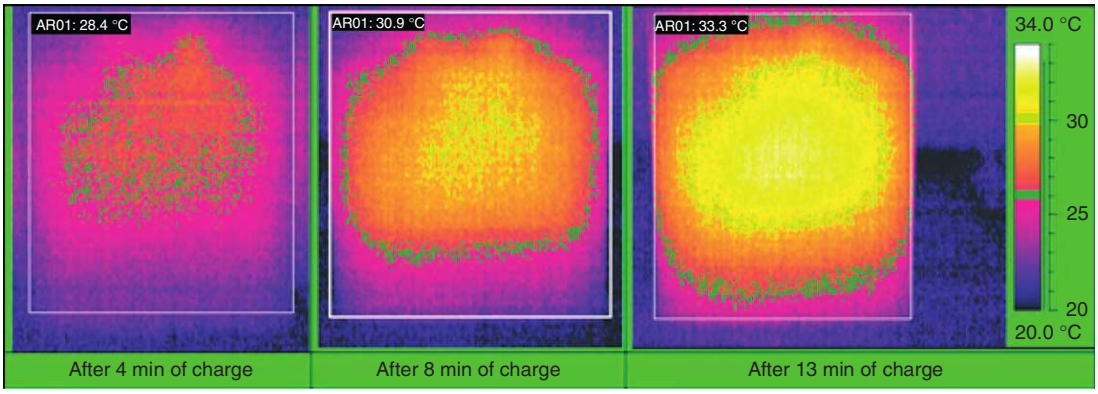

Figure 11 Infrared pictures development of a single valve-regulated lead–acid battery (VRLA) cell during fast charge.

cannot rely on overcharge protection provided through the oxygen recombination cycle. Usual charge termination methods with higher charge rates are $-\Delta V$ and battery temperature increase rate $\mathrm{d}T/\mathrm{d}t$.

The $-\Delta V$ charge control is practically constant current charge termination when the battery voltage drops by a defined value. The battery voltage drop during CC charge is caused by a start-up of intensive rate of oxygen recombination cycle. Once the positive electrode, which is by design capacity limiting, gets fully charged or charging rate exceeds charge acceptance, the overcharge energy is consumed in electrochemical water splitting. Oxygen gas is produced on the positive electrode and transported through separator gas channels to the negative electrode, where it recombines with hydrogen atoms stored in the MH alloy to form water; this is called oxygen recombination cycle in the Ni–MH battery. The oxygen recombination depolarizes the negative electrode causing the battery voltage to drop, which is detected as $-\Delta V$. A modification of this method is $\mathrm{d}V/\mathrm{d}t = 0$ in which the end of charge voltage curve plateau is detected rather than voltage drop ($-\Delta V$). Chargers using $-\Delta V$ charge termination method often apply a timer to delay the voltage drop detection. This is for a similar reason as discussed in 'Fast Charging of Lead–Acid Batteries'. After a deep discharge or a long storage, a thin oxide layer may be formed on the electrode's surface; at the beginning of charging, it might be reduced and broken resulting in a fast internal resistance and voltage drop, which might be wrongly detected as $-\Delta V$.

Another parameter that is used for detection of charge termination is the temperature increase rate $\mathrm{d}T/\mathrm{d}t$. With the start of intensive rate of exothermic oxygen recombination reaction, the battery temperature rises rapidly. The end of charge can be defined and detected by $\mathrm{d}T/\mathrm{d}t$ value. Both $-\Delta V$ and $\mathrm{d}T/\mathrm{d}t$ detection methods are graphically depicted in **Figure 12**.

Another parameter, which is less commonly used for charge control, is internal pressure of the battery. It has a similar increasing profile at the end of charge as temperature owing to oxygen evolution in the cell. Internal pressure can be monitored only after battery modification with a reliable and well-sealed pressure sensor, which results in significant cost increase. Another method might be external measurement of a battery case expansion, which is not as sensitive and precise over the battery life. An internal pressure sensing method was applied in the so-called 'I-C3 15 minute' AA and AAA Ni–MH batteries manufactured by Rayovac. A pressure-sensitive switch was developed and built into the batteries to detect internal pressure increase without any electronic pressure sensor. The batteries, however, require a special charger and a conductive strip in the label for the charger to detect this particular battery type. The batteries have not been very successful in the real business world because of their higher price. This practically demonstrates the importance of battery production costs.

All the fast charging methods require a high charge rate. For instance, typical $-\Delta V$ value per cell is 0.005 V; a Ni–MH battery represented in **Figure 13** needs a charging rate of at least 0.3 C for reliable $-\Delta V$ detection and charge control.

Another method for charge control, or rather a measure for increased safety, is hydrogen gas detection in the vicinity of batteries. It benefits from the advantage of external installation of hydrogen sensor in the battery.

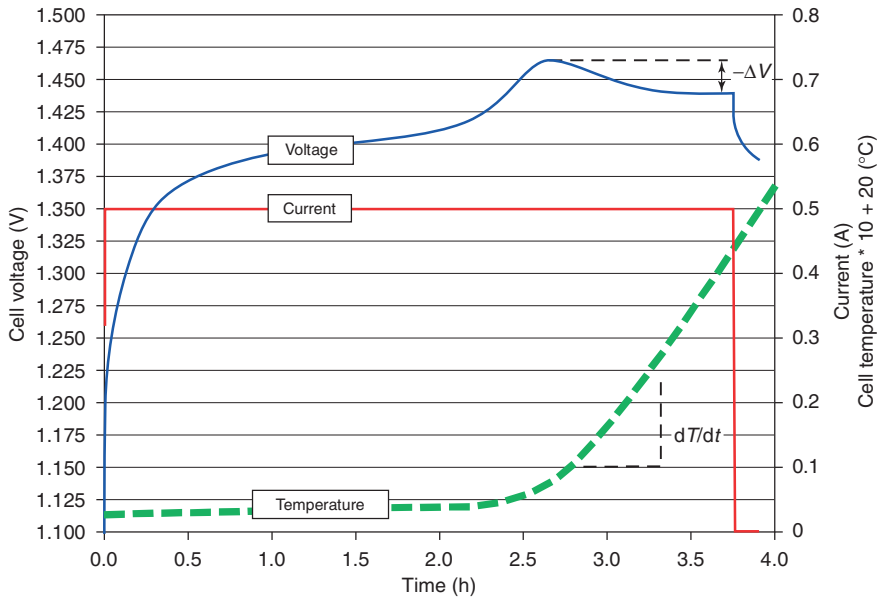

Figure 12 Explanation of $-\Delta V$ and $\mathrm{d}T/\mathrm{d}t$ charge control.

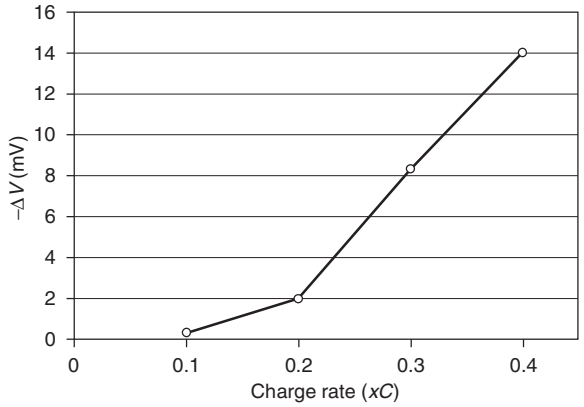

Figure 13 $-\Delta V$ dependence on charge rate.

Detection of hydrogen outside the battery is of great significance for safety control, but remains questionable as a reliable charging control. Hydrogen leakage from the battery varies depending on design parameters including material of the battery case and sealing. Hydrogen leaking varies over the battery life with variation of oxygen recombination efficiency, separator electrolyte saturation, rate of internal aging processes, and degradation of battery casing and seals. Furthermore, the detection is influenced by external parameters such as close or open battery compartment, placement and distribution of batteries in the compartment, and venting design.

If a battery remains connected to a charger after fast charging is completed, then a trickle charging might be applied. Trickle charging may slowly complete a full recharge at reduced temperature and internal pressure.

Lifetime and Degradation Mechanisms at Fast Charging

Degradation Mechanisms at Fast Charging of Lead–Acid Batteries

Current distribution and irreversible sulfation

Experimental measurement of current distribution over electrode plates proved that higher currents lead to a less homogeneous current distribution and lower relative current density at the bottom of the electrode plates. The effect of current rate on the current distribution is stronger at charging in comparison with discharging. A complete recharge of the bottom parts of the electrodes occurs only close to 100% SoC. In concert with the experimental results, later reports confirmed simulation results of the current distribution. Current distribution on electrodes' plates is governed by the plates' resistance distribution together with Butler–Volmer current dependence on the charge transfer overpotential. The undercharge of bottom parts of electrode plates at fast charge in turn promotes localized irreversible sulfation.

Water loss – gassing

Fast charging lowers gassing and water loss in comparison with conventional charging. Conventionally charged batteries had 65% higher water loss and gassing in comparison with the average value of step-down fast charged batteries (average of the sequence: four fast charging cycles followed by one conventional charging cycle). The step-down fast charged batteries have higher charge coulombic efficiency and lower charge factor. Despite this, in fast charged batteries, the temperature rises in a controlled manner; owing to advanced charge control, shorter duration at charge polarization, recharge to less than 100% SoC, and favorable kinetic factors, the cumulative gassing is lower. Extensive gassing in VRLA batteries generates significant heat and increases battery temperature; oxygen bubbles cover AM and lower surface area and block access to the AM pores. Extensive gassing directly promotes other degradation mechanisms such as AM shedding from the positive electrode plates and indirectly accelerates all the degradation mechanisms via increase in temperature. Extensive gassing provides electrolyte mixing and reduces electrolyte stratification.

Thermal runaway

The thermal runaway is a faulty process that may appear under certain conditions in a VRLA battery when a battery charger does not have any temperature control or does not function properly. Thermal runaway is a positive temperature feedback effect of a system with higher heat generation than effective cooling through the battery walls.

Thermal runaway appears during charging while oxygen cycle is running for a long time at a high rate. The oxygen recombination cycle is a complete transformation of electric charge energy into thermal energy via electrochemical oxygen evolution and reduction. During charging, temperature rise has a positive feedback on oxygen evolution rate on positive plates, and oxygen recombination on negative plates is an exothermic reaction, which further increases the battery temperature. Temperature-dependent gassing kinetic is also described by the Arrhenius equation. Thermal runaway in a faulty charging without functional temperature control is further accelerated as the excessive oxygen recombination depolarizes the negative electrode. In that case, if a charger controls the battery to cv, it provides the battery a higher charging current, which increases positive electrode polarization and thus the oxygen evolution rate. This positive feedback loop is the thermal runaway process, and is well demonstrated in Figure 14, which shows current and temperature development during CV charging without any temperature control. Thermal runaway is eliminated when a battery is in a good state of

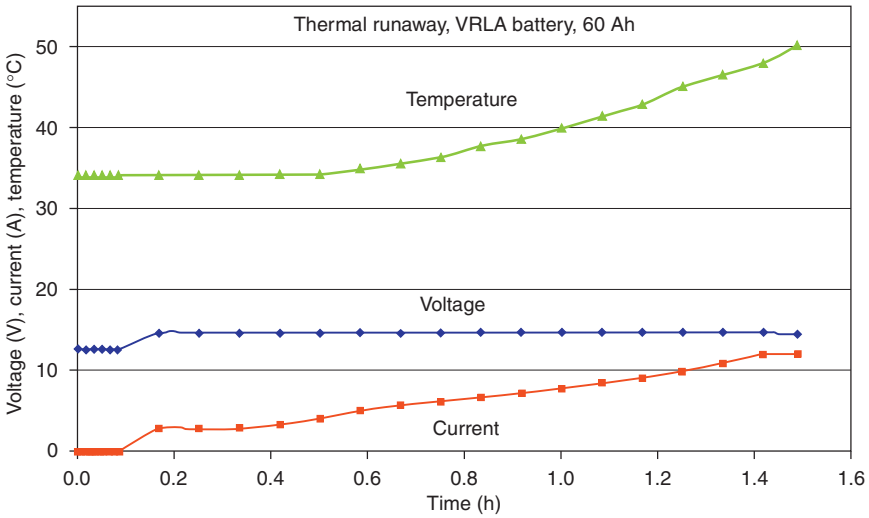

Figure 14 An example of thermal runaway in a valve-regulated lead–acid (VRLA) battery.

health and a charge control with effective temperature compensation works well.

Electrolyte stratification

Electrolyte stratification describes vertical distribution of the electrolyte density. Electrolyte stratification differs significantly between flooded and VRLA type batteries. At fast charging, the electrolyte stratification might be expected to be worse than conventional charging for two main reasons: (1) as explained, gassing, which mixes electrolyte and reduces stratification, is lower because of limited SoC recharge and better charge control; and (2) higher inhomogeneous current at the top portion of the electrodes generates higher acid density, which forced by gravity results in higher electrolyte stratification.

Once electrolyte stratification builds up, higher density electrolyte at the bottom locally increases electrochemical potential, which further prevents recharge of the bottom part of the electrodes. Self-potential equalization may even discharge the bottom part of the electrodes while recharging the top parts, which makes the inhomogeneous charge distribution over the electrodes worse and promotes irreversible sulfation on the bottom.

Positive electrode current collector corrosion

Although not expected, lower corrosion of positive plates cycled with step-down fast charging regime in comparison with conventionally charged batteries was reported. There are two main reasons for the phenomenon: (1) charging is controlled to the maximal charge acceptance right from the beginning; it means that electrodes get highly polarized compared to a conventional charge. Considering the dependence of anodic corrosion of lead on potential, the potential region of highest corrosion rate is quickly passed over with higher polarization of fast charging. (2) Fast charging polarizes the electrode for a shorter time duration in comparison with a conventional charge.

Active mass particle size and porosity

Theories and reports have been published about particle size and AM porosity. It is known from crystallization theories that electrochemically grown crystals are smaller with increasing current because of the increasing nucleation rate. This means that fast charging promotes and maintains the initial small AM particles that have high surface-to-volume ratio, better particle-to-particle interconnection and thus better electronic conductivity, and provides easier conversion in the charge transfer reaction in comparison with recrystallized larger AM particles.

Smaller particle size was experimentally analyzed and reported. In concert with previous discussion, a different situation was analyzed on the bottom parts of the electrodes. Lower porosity and higher stiffness of PAM of the fast charged battery were reported. The porosity of PAM agglomerates tends to increase and stiffness decreases with cycling owing to PAM expansion forced by recrystallization and irreversible sulfation. The problem of lower electronic conductivity and gradual irreversible sulfation of expanded PAM is due to smaller conductive 'necks' between larger particles; the process is described by 'Kugelhaufen model'.

Summary of lead–acid degradation mechanisms under fast charging

Different degradation effects dominate in conventionally and fast charged batteries. In conventionally charged batteries, the dominating degradation effects are expected

to be corrosion of the positive electrode current collector, which causes degradation changes of the PAM–current collector interface, the degradation of structural properties of PAM, and the drying out process. The dominating degradation effects in the fast charged batteries are hard/irreversible sulfation particularly on the bottom of the electrodes, less homogeneous current distribution causing undercharging and severe degradation at the bottom of the electrodes, and the tendency to higher electrolyte stratification.

Impact of fast charging on lead–acid battery lifetime

The inhomogeneous current distribution on electrode plates prevents any substantial cycle life prolongation of fast charged batteries. Particularly, the bottom parts of the electrodes are undercharged and suffer from associated degradation processes. Advanced batteries for fast charge should consider this problem and their design might address and minimize the described effect. This might involve grid design and modified electrode plates connection (i.e., alternative top–bottom connection, or both top and bottom connection). The positive influence of the redesigned electrode plates connection was simulated and reported.

It was reported that with higher cycle number the negative electrode of VRLA batteries may become capacity limiting and for a low-rate discharge ($C/2$), the cycle life of the fast charged battery may exceed the cycle life of the conventionally charged battery. It was reported that fast charging may preserve the performance of the negative electrode. The mechanism may involve AM smaller particles and preserved AM initial porosity (slowing the negative electrode 'leading' process). The structure and properties of the AM in the positive electrode's top parts in the fast charged battery may also be preserved to a greater extent compared to conventionally charged electrodes. The PAM of the fast charged battery was reported to be more compact and stiff, and in conclusion, fast charging reduced PAM softening. Current collector of the positive electrode suffers less from corrosion in the fast charged battery. On the contrary, the tendency to higher electrolyte stratification measured in the fast charged batteries together with higher sulfation on the bottom of the electrodes limited the performance of the fast charged battery at a high-power discharge. At a high-power dynamic discharge such as ECE15, the cycle life prolongation of the fast charged battery is practically not significant.

Degradation Mechanisms at Fast Charging of Nickel–Metal Hydride Batteries

As described earlier, the positive electrode of Ni–MH batteries is capacity limiting, and thus any degradation of the positive electrode directly reduces the battery capacity. Degradation of the negative electrode in the first phase reduces the capacity reserve, which promotes further degradation mechanisms explained in this section.

Positive electrode particle electronic conductivity

Nickel hydroxide particles do not have good electronic conductivity, and particle-to-particle interconnection in the positive electrode and a connection pathway to the current collector are critical parameters. The main degradation processes of the positive electrode affect these parameters. One reason for using additives (e.g., cobalt) is to provide electronic conductive network, and thus facilitate particles interconnection. Additives, however, suffer particularly from deep discharge in which the conductive network gets distorted and that increases internal resistance and 'disconnects' the active mass particles.

In general, recrystallization and other effects leading to disintegration of the PAM must be minimized under a wide temperature and polarization range associated with fast charge.

Positive active mass overcharging

The standard charge transfer redox reaction in the PAM proceeds between β phases of β-$Ni(OH)_2$ and β-NiOOH. At overcharge and accelerated with high charge rate and temperature, a transition to γ-NiOOH might occur. The γ-phase change is accompanied by water and electrolyte ions uptake and volumetric increase (1.44 times compared to β phase) of the PAM particles. This results in mechanical stress and disintegration of PAM. Another effect is the drying out process because of uptake of water, and reduction of the negative electrode charge reserve because of the higher oxidation state of the γ phase. Although formation of the γ phase is reversible, discharge, which proceeds to α phase, occurs only at lower potential, i.e., at full or deep discharge. This might be only rarely available in transportation battery applications. Various additives might be added to PAM and electrolyte (e.g., lithium hydroxide (LiOH) to reduce the process.

Impact of temperature on positive electrode

The efficiency of the positive electrode charge reaction depends strongly on temperature, as shown in the example in Figure 15. Despite lower potential, the charge transfer reaction competes with side reactions, the major one being oxygen evolution. The rate of oxygen evolution reaction increases with temperature and reduces charge efficiency at elevated temperature, which is unavoidable with fast charging. Therefore, with fast charging, temperature control and homogeneous temperature distribution among cells in Ni–MH battery are more important than in lead–acid batteries. Oxygen evolution overpotential can be increased with additives to PAM.

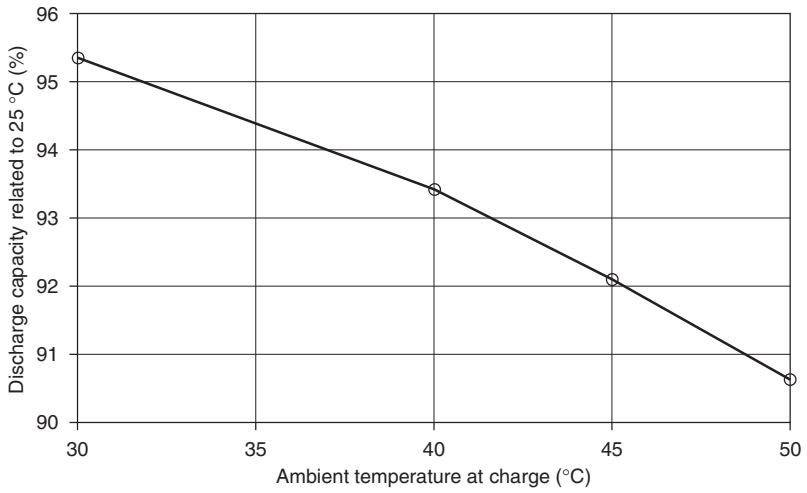

Figure 15 Effect of temperature on the charge efficiency of nickel–metal hydride (Ni–MH) battery; discharge was performed always at 25 °C.

Negative electrode corrosion

Corrosion of MH alloy in an alkaline electrode does not proceed homogeneously on various metal particles of the alloy. Obviously, a bare metallic surface oxidizes easily compared to a metal surface with a thick and dense oxide layer. There might be various reaction mechanisms of corrosion, but in each of them, the MH active mass storage capacity reduces for the corroded mass. Parallel with the corrosion process, MH alloy gets charged with hydrogen atoms. Thus, corrosion leads to (1) loss of MH active mass, (2) reduction of the negative electrode charge reserve, and (3) loss of electrolyte and increase of internal resistance. Corrosion products dissolved in the electrolyte might decrease the charge efficiency of the positive electrode and increase the rate of oxygen evolution. The corrosion process is accelerated with increasing battery temperature; therefore, batteries with improved corrosion resistance are convenient for fast charging.

Pulverization of metal hydride alloy

With repeated adsorption and desorption of hydrogen atoms into MH alloy particles, the particles crack and disintegrate into smaller particles. This process is often called 'pulverization'; it is induced by mechanical stress in the MH particles. The metal lattice expands and contracts with adsorption and desorption of hydrogen atoms at charging and discharging. The process is more pronounced at fast charging owing to adsorption and desorption rate and temperature effect. Similarly, as in the positive electrode, pulverized MH particles suffer from electronic contact, and freshly exposed particles' surface is prone to corrosion with all the associated degradation mechanisms.

Electrolyte loss – drying out

Loss of electrolyte called 'drying out' is a very critical process in Ni–MH batteries. The separator of Ni–MH batteries is only soaked with electrolyte to provide open gas channels for oxygen gas transport and thus effective oxygen recombination cycle. Not any free electrolyte reserve is commonly available in the batteries, and the delicate balance in electrolyte amount in the cell can be easily broken. The drying out process is induced mainly by corrosion, formation of γ-NiOOH, and high-rate overcharge causing defective venting.

Loss of electrolyte significantly increases internal resistance, reduces power performance and charge acceptance (fast charge ability), and increases heat generation at charge and discharge via joule losses. Fast charging is particularly critical for inducing drying out through increased battery temperature and higher charge rate, which may cause overcharge and defective venting. Drying out is a very common and dominating degradation mechanism of Ni–MH batteries that leads to fast end of life.

Loss of overcharge reserve

The capacity oversize of the negative electrode and the SoC of individual electrodes form the negative electrode overcharge reserve at the fully charged battery. This reserve is used to prevent hydrogen gas evolution at overcharge. Hydrogen gas in the cell is practically hard to oxidize back to water without a special catalyst, which is not used in Ni–MH batteries. Hydrogen gas formed in the cell builds up internal pressure. At a certain overpressure, the cell's safety valve opens, which is called 'defective venting', preventing explosion and reducing internal pressure. The defective venting causes very intense and fast drying out. The overcharge reserve is

reduced and minimized mainly by corrosion and overcharging formation of γ-NiOOH; other side reactions involving additives and separator may also promote the loss of overcharge reserve.

Impact of temperature on degradation mechanisms

Higher battery temperature induced by fast charging accelerates all the above-listed degradation mechanisms. Lower positive electrode charge efficiency at higher temperature results in higher rate of oxygen recombination cycle and increases internal pressure with additional heat generation.

Higher temperature increases hydrogen equilibrium pressure with the hydrogen stored in the MH active mass. The storage capacity is reduced with temperature, which determines the maximal operating temperature for Ni–MH battery to around 50 °C.

Increased internal pressure might result in defective venting causing fast drying out.

Corrosion and other side reactions are also accelerated with increased temperature.

High charge rate

Higher charge rate of fast charging accelerates the degradation mechanisms through elevated temperature, which results directly from higher joule losses. Furthermore, reduced charge acceptance during the lifetime leads to overcharging and increased temperature through oxygen cycle. Higher charge rate increases internal pressure and the risk of defective venting.

Depth of discharge

The cycle life dependence on the depth-of-discharge (DoD) cycling of Ni–MH batteries is stronger than lead–acid batteries. The main problem of preserving long cycle life with high DoD cycling is the pulverization process and corrosion of the MH alloy. These are induced through maximal volume changes and associated mechanical stresses of maximal hydrogen throughput in each cycle. With fast charging, lower DoD cycling is recommended with operation in favorable DoD and SoC range, particularly avoiding the end of charge (close to 100% SoC) region. Thus, temperature increase and pressure might be reduced as well as the risk of overcharge.

Summary of Nickel–Metal Hydride batteries degradation mechanisms under fast charging

Critical parameter at fast charging of Ni–MH batteries is temperature and its even distribution across all cells in a battery. High internal resistance of Ni–MH batteries and its increase with cycling cause significant joule losses, which increase as square of the current. Thus, without a proper fast charging and temperature control, battery temperature may increase significantly with increasing charge rate. High battery temperature lowers charge acceptance and charge efficiency and increases the rate of competitive oxygen recombination cycle. This further increases the battery temperature, prevents efficient recharging, accelerates critical degradation mechanisms such as drying out and loss of overcharge reserve, and all this in turn shortens the battery life. A reliable fast charging of Ni–MH batteries combines a couple of control techniques described with emphasis on the control of battery temperature.

Charging of Lithium Batteries

In the terminology used in this section, lithium battery represents rechargeable lithium battery chemistry. During charging and discharging of a lithium battery, lithium cations are reversibly transferred between the electrodes in a nonaqueous electrolyte. At charging, lithium cations pass from the positive to the negative electrode. The intercalation process represents electrochemical alloying of metal with lithium cations; it may be described with the following reactions where charging is shown in the right to left direction:

$$\textit{Negative electrode}:\ \mathrm{Li}_{x+\Delta x}\mathrm{M} \rightleftarrows \Delta x\mathrm{Li}^{+} + \Delta x e^{-} + \mathrm{Li}_{x}\mathrm{M}$$

$$\textit{Positive electrode}:\ \Delta x\mathrm{Li}^{+} + \Delta x e^{-} + \mathrm{Li}_{x}\mathrm{MO} \rightleftarrows \mathrm{Li}_{x+\Delta x}\mathrm{MO}$$

A fast and continuous development of lithium batteries has led to new anode and cathode materials, which in turn have provided a wide range of cell voltages, capacities, charging and discharging rate capability, cycle life, temperature characteristics, safety, and other parameters. Therefore, a standardized charge protocol and typical charging performance has not been established yet. Practically, for each type of lithium battery, the manufacturers define specific charge parameters and a provider-specific charger and power management.

Currently, there is only one practical charge regime for lithium batteries, i.e., a CC charging followed by a CV charging (CC-CV). The charge process is terminated when the charge current in the CV phase drops below a defined limit. To minimize the charging time, the CV phase may be eliminated, in which case only a partial recharge is provided by the CC phase. Despite the continuous development of the technology, there are some specific characteristics with charging lithium batteries that are different from lead–acid and Ni–MH batteries. In distinction from other chemistries, rebalancing the individual cells' SoC in a battery cannot be done with a simple controlled overcharge. A charge control is very critical owing to lithium batteries' high sensitivity to overcharge and high temperature, which leads to irreversible side reactions and significant safety

issues including fire and explosion. Therefore, all series-connected cells in the battery must be controlled individually to avoid any overcharge through a BMS, which is an essential component of the battery. The BMS must also avoid overdischarge, which may oversaturate cathode with lithium cations followed by irreversible formation of lithium oxide and other side reactions. Typically, the battery design includes some features to increase safety. Some of these features are not reversible. The features include special shut down separator activated by excessive temperature, tearaway tab contactors activated by high internal pressure, safety vent releasing excessive internal pressure, and external current and thermal fuse preventing excessive current and temperature.

Lithium batteries might have lower internal resistance compared to Ni–MH and lead–acid batteries, which makes them favorable for fast charging and high-rate performance. Commercially available high-rate lithium batteries, e.g., Toshiba super charge Ion Battery (SCiB) lithium-ion battery, can be recharged to 90% SoC in 5 min. The maximal charging rate acceptance is however strictly limited and any excess leads to serious irreversible processes that decay the performance and may permanently damage the battery and cause serious safety issues. The charge rate limitation is controlled by solid-state diffusion of Li^+ ions into the bulk of the active mass particles. The diffusion coefficient varies with the material composition and structure. Therefore, the cell design and fabrication process play a role in the battery charge rate capability. In general, high surface-to-volume ratio materials favor high-rate capability; on the contrary, materials with porous small particles have increased tortuosity of mass transport and decreased percolation threshold. Cyclic insertion and extraction of Li^+ cations in the active mass particles induce mechanical stress, which promotes further pulverization of the particles with cycling. This leads to a loss of interparticle electronic connection, electrode conductivity, and capacity. During high charge or discharge rate, Li^+ concentration gradient builds up from the particle surface to its bulk causing concentration polarization with the active mass. Mass transport through the tortuous architecture of the electrode active mass also contributes to polarization losses. In addition, polarization losses and reduced charge transfer kinetic rate may arise from Li^+ diffusion through a device oxide layer, which might build up on the surface of the active mass particles promoted by impurities and abusive operation.

With respect to the operating conditions, the diffusion coefficient is strongly dependent on temperature. At a low temperature, the solid-state Li^+ ions diffusion is lower, which reduces the charge acceptance significantly. A typical degradation process of an excessive high-rate charging at a low temperature is irreversible electroplating of anode with metallic lithium, which decays the performance and causes serious safety issues. Therefore, at charging, lithium battery must be monitored for low temperature and charge process controlled accordingly. Excessive battery temperature particularly with cobalt- or nickel-based cathode might trigger spontaneous thermal runaway. Therefore, battery temperature must be monitored and controlled.

Conclusions

Properly designed fast charging algorithm and fast charger hardware provide battery recharge in 10–30 min without abusing the battery. With time constrain, fast charging does not recharge batteries to 100% SoC. Close to full recharge, charge acceptance drops and significantly prolongs the charge duration. The battery life prolongation processes provided with fast charging are however compensated by other accelerated degradation mechanisms. Therefore, a real prolongation of a battery life with fast charging at a high-power dynamic operation cannot be generally expected.

Nomenclature

Symbols and Units

C	battery charge capacity (Ah)
C_n	battery nominal charge capacity (Ah)
dT/dt	battery temperature increase rate
F_a	battery cycle life acceleration factor
I	current (A)
k	kinetic constant of the reactions
R	resistance (Ω)
T	temperature (K)
T_E	increased temperature of the test
T_o	standard room temperature
V	voltage (V)
V^*_{ch}	resistance-free charge voltage (V)
V°	open-circuit voltage (V)
V_{ch}	charging voltage (V)
α	coefficient
ΔC	change in capacitance
ΔS	change in entropy (J K^{-1} mol^{-1})
ΔT	change in temperature
ΔV	change in voltage
η	overpotential (V)
τ	time constant

Abbreviations and Acronyms

AM	active mass
BET	Brunauer–Emmet–Teller
BMS	battery management system
CC	constant current
CV	constant voltage

DC	direct current
DoD	depth of discharge
EV	electric vehicle
HEV	hybrid electric vehicle
IR	internal resistance
MH	metal hydride
NAM	negative active mass
Ni–MH	nickel–metal hydride
PAM	positive active mass
SCiB	Super Charge Ion Battery
SoC	state of charge
TMF®	thin metal film
VRLA	valve-regulated lead–acid

See also: **Secondary Batteries – Lead–Acid Systems:** Automotive Batteries: Conventional; Automotive Batteries: New Developments; Charging; Overview; Performance; State-of-Charge/Health; Valve-Regulated Batteries: Oxygen Cycle; **Secondary Batteries – Lithium Rechargeable Systems – Lithium-Ion:** Overview; Positive Electrode: Lithium Nickel Oxide; **Secondary Batteries – Lithium Rechargeable Systems:** Overview; **Secondary Batteries – Nickel Systems:** Nickel–Cadmium: Overview; Nickel–Metal Hydride: Overview.

Further Reading

Berndt D (1993) *Maintenance-Free Batteries*. Taunton, Somerset, England: Research Studies Press Ltd.

Besenhard JO (1999) *Handbook of Battery Materials*. Weinheim, Germany: Wiley–VCH.

Bode H (1977) *Lead–Acid Batteries*. New York: John Wiley & Sons, The Electrochemical Society Series.

Calasanzio D, Maja M, and Spinelli P (1993) Fast charging of lead/acid batteries. *Journal of Power Sources* 46: 375–381.

Chreitzberg AM and Kelley JJ (1986) Accelerated life cycle test. Advanced lead–acid cells at elevated temperature. *Journal of Power Sources* 17: 183–187.

Constable DC, Gardner JR, Harris K, Hill RJ, Rand DAJ, and Zalcman LB (1984) Effect of elevated and variable temperature on the performance of lead/acid batteries operated under simulated electric-vehicle service. *Journal of Electroanalytical Chemistry* 168: 395–414.

Dhameja S (2001) *Electric Vehicle Battery Systems,* p. 252. Newnes, Boston, USA: Elsevier.

Fleming FA, Shumard P, and Dickinson B (1999) Rapid recharge of valve-regulated lead–acid batteries for electric vehicle applications. *Journal of Power Sources* 78: 237–243.

Groiss R (2000) *Schnellladung und Pulsladung von Bleibatterien*. PhD Thesis, University of Ulm.

Guo Y, Groiss R, Doering H, and Garche J (1999) Rate-determining step investigations of oxidation processes at the positive plate during pulse charge of valve-regulated lead–acid batteries. *Journal of the Electrochemical Society* 146(11): 3949–3957.

Kanda M, Yamamoto M, Kanno K, Satoh Y, Hayashida H, and Suzuki M (1991) Cyclic behavior of metal hydride electrodes and the cell characteristics of nickel–metal hydride batteries. *Journal of the Less-Common Metals* 174(1–2): 1227–1235.

Koehler U, Kuempers J, and Ullrich M (2002) High performance nickel–metal hydride and lithium-ion batteries. *Journal of Power Sources* 105: 139–144.

Kordesch KV (1960) Sine wave current tester for batteries. *Journal of Electrochemical Society* 107(6): 480–483.

Kordesch KV (1972) Charging method for batteries, using the resistance free voltage as endpoint indication. *Journal of the Electrochemical Society* 119(8): 1053–1055.

Kral P, Krivak P, Baca P, Calabek M, and Micka K (2002) Current distribution over the electrode surface in a lead–acid cell during discharge. *Journal of Power Sources* 105: 35–44.

Krivak P, Baca P, Calabek M, Micka K, and Kral P (2006) Current distribution over the electrode surface in a cylindrical VRLA cell during discharge. *Journal of Power Sources* 154: 518–522.

Lam LT, Ozgun H, Lim OV, et al. (1995) Pulsed-current charging of lead/acid batteries – a possible means for overcoming premature capacity loss? *Journal of Power Sources* 53(2): 215–228.

Lander JJ (1956) Further studies on the anodic corrosion of lead in H_2SO_4 solutions. *Journal of the Electrochemical Society* 103: 1–8.

Le Guenne L and Bernard P (2002) Life duration of Ni–MH cells for high power applications. *Journal of Power Sources* 105(2): 134–138.

Morioka Y, Narukawa S, and Itou T (2001) State-of-the-art of alkaline rechargeable batteries. *Journal of Power Sources* 100(1–2): 107–116.

Micka K and Koudelka V (1981) The influence of temperature on the discharge capacity of positive lead–acid battery plate, theory and experiments. *Journal of Power Sources* 6: 319–325.

Sastry AM, Choi SB, and Cheng X (1998) Damage in composite NiMH positive electrodes. *Journal of Engineering Materials and Technology* 120(4): 280–283.

Schleuter W (1982) *Ein Beitrag zur Beschreibung des Elektrischen Verhaltens von Blei-, Nickel–Cadmium und Nickel-Eisen-Akkumulatoren*. PhD Thesis, Rheinisch-Westfaelischen Technischen Hochschule Aachen.

Soria ML, Chacon J, Hernandez JC, Moreno D, and Ojeda A (2001) Nickel–metal hydride batteries for high power applications. *Journal of Power Sources* 96(1): 68–75.

Svoboda V (2002) *The Influence of Fast Charging on the Performance of VRLA Batteries*. PhD Dissertation Thesis, Brno University of Technology; PhD Thesis, Brno University of Technology.

Svoboda V, Doering H, and Garche J (2005) The influence of fast charging on the performance of VRLA batteries. *Journal of Power Sources* 144(1): 244–254.

Winsel A, Voss E, and Hullmeine U (1990) The aggregate-of-spheres ('Kugelhaufen') model of the PbO_2/PbO_4 electrode. *Journal of Power Sources* 30(1–4): 209–226.

Yang XG and Liaw BY (2001) Charge performance of a commercial nickel–metal hydride traction battery system. *Journal of the Electrochemical Society* 148(9): A1023–A1028.

Lifetime Prediction

DU Sauer, RWTH Aachen University, Aachen, Germany
H Wenzl, Clausthal University of Technology and Beratung für Batterien und Energietechnik, Osterode, Germany

Introduction

Lifetime prediction of electrochemical systems obviously requires a detailed understanding of aging processes and their causes. However, lifetime prediction on the basis of such detailed understanding is only possible in the few applications where one aging process dominates and where test procedures and methods are available, which allow investigation of this dominant aging process without the influence of other aging processes. A typical application where this is true is uninterruptible power supply systems, which are operated at float charge conditions. For lead–acid batteries, corrosion and dry-out are the major aging effects in this traditional application.

However, where a number of aging processes take place in parallel due to complex operation conditions (for batteries, e.g., a combination of cycling, partial state-of-charge (PSoC) cycling, rest periods at different states of charge (SoC), incomplete or rare full charging, and for fuel cells, e.g., start–stop operation, high mass utilization, and low-power operation at high voltage) or operation in a wide range of temperatures, the complex interaction between the various aging processes and the operating conditions must be analyzed. For mobile applications, additional requirements and combinations of stress factors such as vibration may occur. Again, it is necessary to understand if different aging processes can be analyzed in experiments one by one followed by a superpositioning of the effects, or if aging effects interact with each other in a nonlinear way. This would, e.g., require vibration tests and electrical cycling of thermal stress test in parallel. This increases the number of parameter combinations dramatically. In any case, it is very difficult to develop appropriate laboratory aging tests to analyze the interaction between the aging processes and link them to lifetime expectation. For lead–acid batteries, different authors have tried to define test procedures that accentuate individual aging effects. Their work shows that this is possible only up to a certain point. These difficulties become obvious when looking at the following examples:

1. Small currents or even rest periods have a significant impact on lead–acid battery lifetime or fuel cells, but to measure their effect in laboratory tests costs a lot of time, which is typically either not available or too expensive due to the large number of test benches required. Accelerated tests to investigate small currents and rest periods are a contradiction in terms. Also, the effect will depend on SoC and electrolyte stratification (lead–acid batteries) or gas pressures and oxygen to hydrogen ratios (fuel cells) and may depend on the microstructure of the active material, which in turn depends on the conditions under investigation.
2. High temperature accelerates certain aging effects like drying out and corrosion. On the other hand, beneficial effects like dissolution of sulfate crystals (lead–acid batteries) are also supported by high temperatures. Therefore, desulfation is better at higher temperatures and the aging effect of sulfation will be significantly smaller at high-temperature operation compared with lower temperatures. To show the complexity even more pronounced: the statement made in the last sentence is true, if the battery is cycled. If the battery is at rest or in open-circuit conditions, high temperatures accelerate sulfation by enhancing the recrystallization process of lead sulfate crystals (Ostwald ripening) resulting in larger crystals with reduced active surface.

To achieve a credible lifetime prediction, it is necessary to take these effects and their interactions into account properly.

A clear distinction must be made between 'onboard' diagnosis of the remaining lifetime of an individual product and lifetime prediction for planning purposes, which requires a comparison between different, well-characterized products, system designs, or operating strategies.

Here, lifetime prediction for planning purposes as a tool for estimating the effect of changes in operating conditions and battery characteristics on the expected lifetime and for detecting optimum operating conditions is the focus. All of the models discussed below can be used for this purpose. However, it is necessary to state that the precision of all lifetime prediction models is limited with respect to a precise prediction of the lifetime in years. This does not reduce their usefulness in any way. The models are intended to determine the impact of operating conditions and strategies, system sizing, or the choice of competing products on the lifetime and to provide a ranking between the different options. A precise lifetime prediction is difficult, because typically not all factors can be taken into account, such as high frequency ripples, and the exact operating conditions cannot be predicted accurately. Lifetime prediction can be made in a first-order approach only for a well-defined product with mean properties. Statistical variations in the product quality also result in statistical variations of the lifetime.

Nevertheless, quantitative lifetime models are a necessary tool for the design of systems taking into account lifetime cost and reliability issues (Figure 1).

The purpose and precision of lifetime prediction can be defined by three levels:

1. Correct ranking of products, operating conditions or operating strategies in tests, or field installation is predicted by models.
2. Determining correctly the relative difference in lifetime between different options.
3. Determining the absolute lifetime of different options correctly.

It is necessary to note that models or algorithms for achieving level 3 are not yet available or published for secondary batteries or fuel cells.

For a stringent discussion the following definitions will be used throughout this article:

- *Operating strategy*. Parameters and settings of the management system affecting the operation of the electrical systems.
- *State variables*. Describe the global (cell level) or the local condition of the electrochemical device by means of potentials, current densities, temperature, SoC, electrolyte, or fuel concentration.
- *Operating conditions*. Time series of all state variables of the battery.
- *Stress factors*. Parameters that can be calculated from the time series of the state variable and describe the severity of the operating conditions and the rate with which aging processes proceed; if a certain condition considered to be a stress factor depends on the battery type and technology.
- *Aging processes*. Processes that lead to irreversible changes of the structure of components and materials.
- *Effect of aging processes*. Impact of aging processes on the performance of the battery such as capacity loss, internal resistance, high-rate power capability, charge acceptance, etc.

It is not within the scope of this chapter to describe models in technical details, but to discuss the general concept of the different concepts to model and to predict the lifetime, their advantages and disadvantages, means to verify them, their limitations, the necessary input data and parameters, and the possibility to transfer the models to different battery technologies and fuel cells.

Three Different Lifetime Modeling Concepts

Three different approaches will be discussed and compared within this article:

1. *Physicochemical aging model*: A detailed electrical, physical, and chemical model of the aging processes of the electrochemical system for time step simulation is used. It provides detailed information on local conditions with spatial and time resolution of all state variables, which result from the operating conditions. Each single aging effect is examined according to its

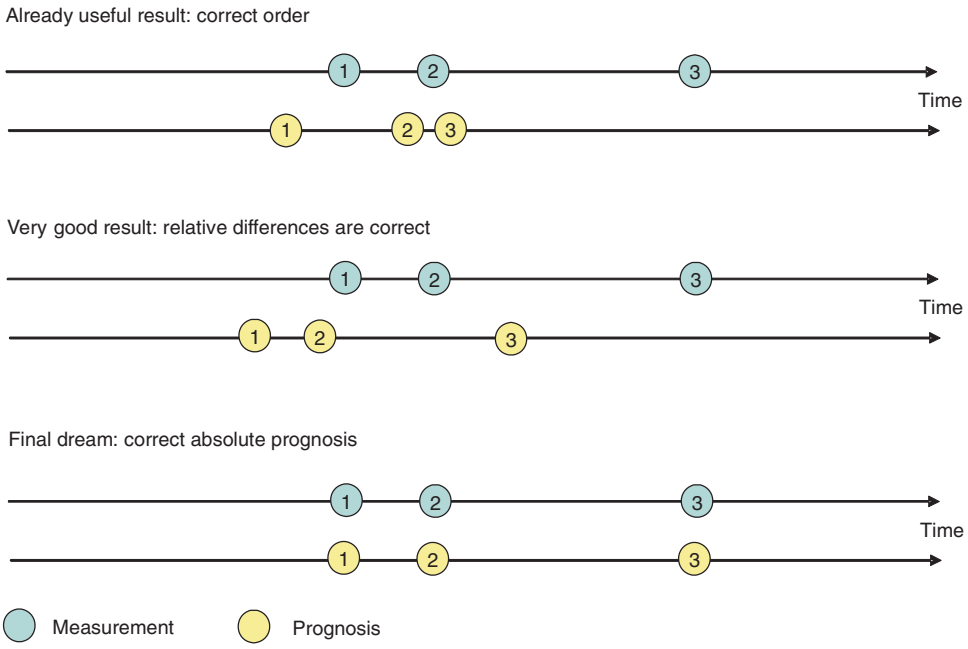

Figure 1 Diagram showing schematically possible results of lifetime prediction models. A correct ranking (order of lifetime actually achieved corresponds to order of lifetime predicted by models) is already a useful result.

dependency on the state variables and quantifies, e.g., loss of active mass surface due to recrystallization processes or loss of grid conductivity due to corrosion. Based on the knowledge of the correlation between aging effects and state variables, the rate of the aging processes at any place in the system can be evaluated. The resulting changes in the performance are used directly for the modification of model parameters. Therefore state variables may change even if the use of the system remains unchanged, e.g., as a consequence of increasing grid resistance, local loss of active mass surface or blocking of pores by insoluble crystals and therefore a change in the local fuel or electrolyte concentration. Current distributions along the electrodes may change as well. This type of model is typically complex, requires a lot of parameterization efforts, and is particularly suitable for understanding aging processes and optimizing cell designs and operation strategies (off-line).

2. *Weighted Ah aging model*: A weighted Ah aging model is based on the assumption that the impact of a given Ah throughput on the lifetime depends on the details of the conditions during the Ah throughput. It is assumed that, under standard conditions, a battery can achieve an overall Ah throughput until the end of the lifetime is reached. Deviations from the standard conditions result in a virtual increase (or decrease) of the physical Ah throughput, e.g., cycling at low SoC is known to be detrimental in lead–acid batteries resulting in lifetime reduction. Depending on the lifetime that has already been spent, the electrical parameters of the model can be adapted continuously. This type of model can be used for rapid comparison of system designs and operating strategies, but it is also suitable for online use. By comparing the actually measured performance with the predicted performance of the continuously updated model, a self-learning algorithm can be implemented.
3. *Event-oriented aging model*: Adding up the incremental loss of lifetime caused by different events is a standard approach for lifetime prediction in many areas of engineering and is referred to as Wöhler or SN curve. This approach is frequently used for planning purposes and for designing and estimating the lifetime of components. For electrochemical systems this approach can also be used provided that several conditions are fulfilled. 'Events' must be identified whose impact on lifetime can either be determined experimentally or can be evaluated based on expert knowledge and/or an analysis of field data. Events must be described clearly and must be distinguishable from all other events. The order of occurrence of the events, if properly defined, does not have to be of relevance, which simplifies the analysis. The approach is mainly suitable for the rapid comparison of system designs and operating strategies and can also be used for online changes of operating strategies.

The weighted Ah aging model and the event-oriented aging model share a number of similarities, in particular the concept of incremental loss of lifetime as a result of the operating conditions. However, there are important differences concerning the parameterization of the two models and limitations of their use. Under certain operating conditions, for instance, it will be difficult to define the end of an event.

Lifetime prediction models must provide credible results to be useful. Credibility is achieved by comparing predictions of a model with lifetime tests where the test conditions differ from those used for extracting parameters for the model. There are significant differences among the three models. The three concepts will be discussed in more detail elsewhere in this encyclopedia. As all models have been realized at least for lead–acid batteries, this technology will serve as an example for the implementation of the concept. Nevertheless, it will be pointed out where the approaches are technology specific and where they are of general nature.

It is necessary to note that the described concepts deal with single cells and assume that all cells age in the same way. Deviations in the aging of cell in series-connected strings occur due to inhomogeneous temperatures, variations in the production process, or due to self-accelerating processes. They are not addressed by the presented concepts. This would require statistical approaches.

Physicochemical Aging Model

The physicochemical aging model is based on a two-step approach (**Figure 2**). In the first step a battery model based on the fundamental equations of the chemical and electrochemical reactions, Ohm's law, and the diffusion processes of reactants and ions in the battery is developed and applied. This model provides all relevant state variables for any point in the battery at any time, such as local potential, local current density, local SoC, local microstructure of active material (porosity, size of active mass crystals (electrochemical active surface)), local acid concentration and local Pb^{2+} ion concentration, local temperature, local gassing current rates, local recombination current rates, local corrosion current, gas pressure in the battery cell, or in the case of fuel cells local fuel concentrations.

In the second step the information is used to quantify aging processes and their impact on the performance of the battery. All boundary conditions are well known, and therefore information from laboratory experiments on the aging effects can be used. Aging effects are typically quantified as a function of state variables as mentioned above. The changes of material and component

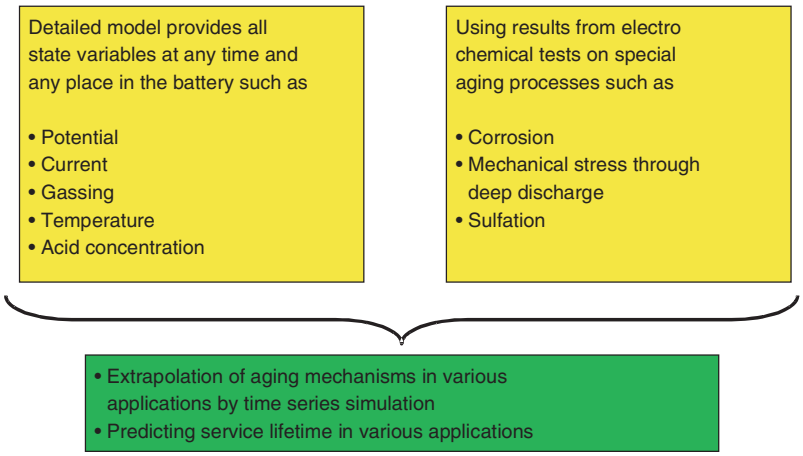

Figure 2 General approach for the physicochemical aging model.

properties as a function of aging and their dependencies on state variables are incorporated in the model, which is capable of calculating the future state variables at every point in the cell at every point in time. Running the model as part of an overall system simulation, which also takes into account the interaction among performance, system requirements, and operation strategies allows following the changes in performance over time and therefore a lifetime prediction becomes a reality.

Modeling of State Variables

The simulation model can be implemented based on a set of coupled, nonlinear differential equations representing all relevant physical and chemical laws that are of relevance for the determination of the state variables. The differential equations are solved on a predefined or dynamic adaptable simulation grid representing the geometry and the different elements of electrodes, electrolytes, separators, and cells for any point in time depending on the boundary conditions defined by the ambient temperature, the currents required by the application, and the interactions with the management strategies.

In reality it turned out that these differential equation systems are highly nonlinear and unstable. Therefore equivalent electrical circuit models are used instead and have proved to be equivalent to the differential equations if the elements of the electrical circuit represent all processes accordingly including all nonlinearities. Such an equivalent electrical circuit model for the positive electrode of a lead–acid battery is shown in Figure 3. In this case the model has a spatial resolution of 3×3 elements and is based on a two-dimensional representation of the electrode. More elements are possible; however, compromises between spatial resolution and calculation speed must be made.

The circuit is solved in every time step by applying Kirchhoff's laws and a Newton algorithm to solve the nonlinear model. Voltage sources and resistors are calculated in each time step according to the actual local conditions from the local state variables for the different processes that are represented by the model. The equilibrium voltages of the voltage sources are calculated from the local fuel or electrolyte concentrations, or from SoC of the active materials. For the resistors of the main charging/discharging reaction, the full Butler–Volmer equation is used. This also includes a calculation of the available inner surface for the reactions, which depends on SoC, the coverage of surfaces with inactive discharge products (e.g., lead sulfate crystals in the lead–acid batteries), or gases. Hence, the overvoltage of reactions and current pathways depend on the current that flows through them. As the electrochemical processes are highly nonlinear (described by the Butler–Volmer equation), the resistance value of the resistor that represents this process must be calculated in an iterative manner until the error is below defined limits.

The first-order outcome is a spatial distribution of currents and potentials. Second-order effects such as changes in local electrolyte or fuel concentrations, temperature, SoC, or local cycle depth are calculated accordingly. For temperature distribution, diffusion, and transport models of fuels and electrolytes, an additional model layer is used, which is coupled with the same spatial resolution in any time step. For the lead–acid battery, the electrolyte concentration is calculated on the basis of Fick's law of diffusion, generation and use of sulfate ions during charging and discharging, gravity effects, and electrolyte mixing by gassing in a separate model. The acid concentration at any point in the battery is returned to the main model to calculate the resistance of the electrolyte, the rates for the charge/discharge reaction, the electrochemical equilibrium voltage, and the equilibrium concentration of Pb^{2+} ions in the electrolyte. Therefore there

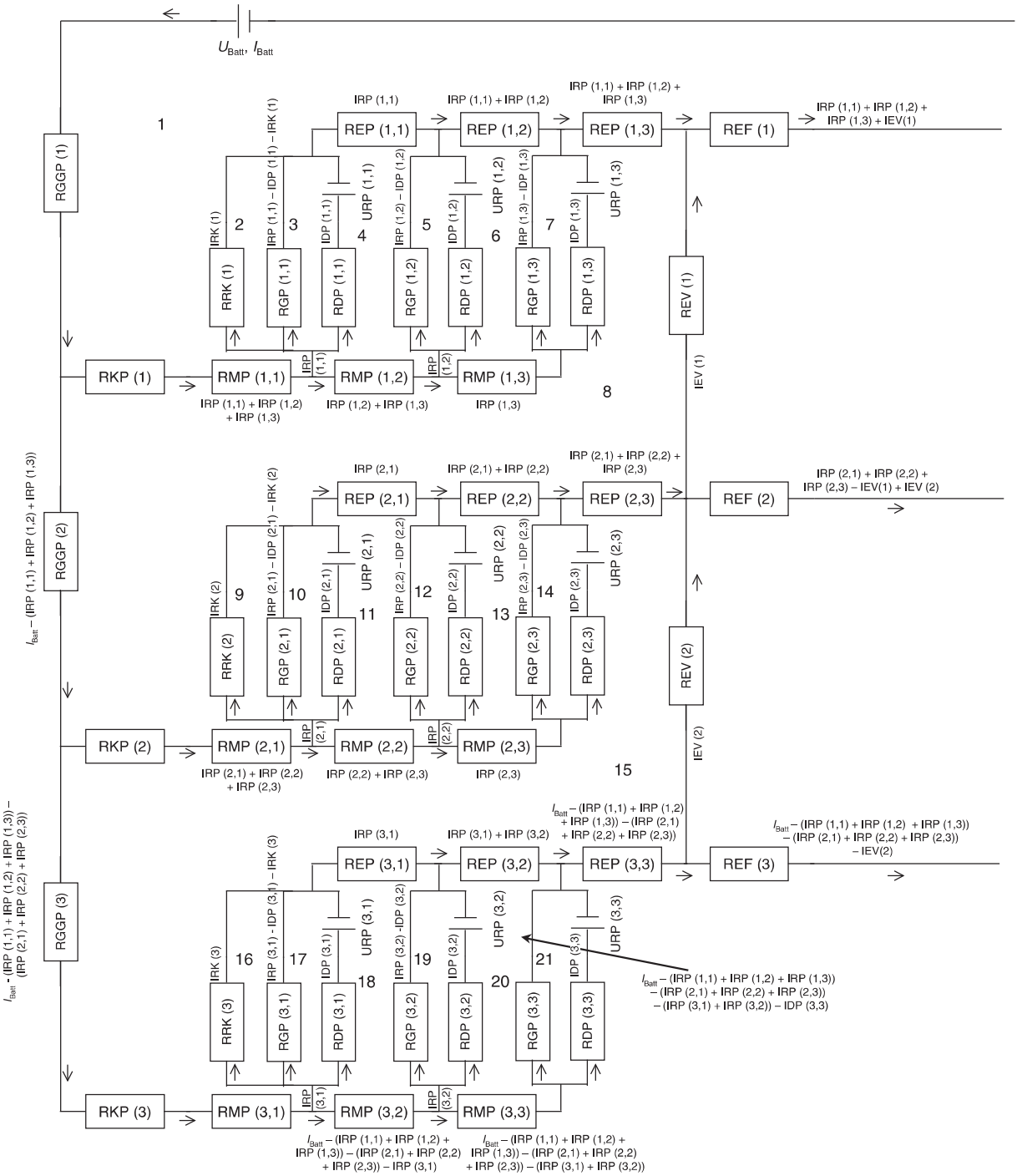

Figure 3 Equivalent circuit diagram of the positive electrode of a lead-acid battery in a two-dimensional model with a spatial resolution of 3 × 3 elements (left-hand side of the figure: grid, right-hand side: electrical pathway through the electrolyte to the negative electrode). Explanation of elements: I_{Batt}, Battery terminal current; RDP, pathway for main reaction current at positive electrode, leading to a charge or discharge of the electrode, resistance calculated from the Butler–Volmer equation (depending on potential, temperature, active surface, and acid and Pb^{2+} concentration); REF, resistance of the electrolyte in the free electrolyte volume between the positive and the negative electrode (depending on acid concentration and temperature); REP, resistance of the electrolyte within the porous positive electrode (depending on porosity, acid concentration and temperature); RES, resistance of the electrolyte in the separator between the positive and the negative electrode (depending on acid concentration, porosity of the separator, and temperature); REV, vertical resistance of the electrolyte in the free electrolyte volume between the electrodes (depending on acid concentration and temperature); RGP, pathway for gassing current at the positive electrode, resistance calculated according to gassing reaction (depending on local electrode potential, temperature, active surface, and acid concentration); RKP, resistance of the corrosion layer of the positive electrode (depending on the corrosion process); RMP, resistance of active material of the positive active mass (depending on porosity, state of charge, and temperature); RRK, pathway for corrosion current, resistance calculated accordingly; URP, electrochemical voltage source of positive electrode, depending on acid concentration, and temperature; U_{Batt}, battery terminal voltage.

is continuous and direct interaction between the electrical model and the acid concentration distribution.

All parameters that can be affected by aging processes are changed continuously according to the output of the aging models. This could affect, e.g., internal surfaces, size distribution of crystals, thickness of passivation layers, loss of catalysts, and loss of conductivity due to corrosion or porosities of the active masses.

Typically, a reduction of the dimensions is made by symmetry assumptions to reduce the number of nodes in the spatial resolution and therefore to save computational time. The example presented above is in fact a two-dimensional model and the geometry of the cell is reduced to one single pair of positive and negative plates facing each other. It is assumed that all other pairs of electrodes have similar conditions due to symmetry reasons. Furthermore it is assumed that the current distribution is homogenous along the width of the electrodes, which is true in first-order approximation. In reality there might be inhomogeneities along the electrode due to asymmetrical grids and the position of the current collector. However, it is assumed that these effects are only of secondary importance due to the very good conductivity of the grids. Capacitors that are required to model changes of voltage and current correctly are omitted here as they would increase the complexity of the model considerably and are not relevant when simulating the behavior of a battery using long time steps with constant current conditions during each time step. However, dynamic effects are taken into account by a detailed simulation of the concentrations of the relevant ions in the electrolyte.

Aging Processes

With the above-described model, the conditions at each point of time and every point in the electrodes and the electrolyte are well known. Therefore it is relatively simple to analyze quantitatively the impact of different aging effects.

In the laboratory, the analysis of aging effects is always done under well-controlled conditions. The earlier described model now provides information on the local conditions. The transfer of knowledge of the local conditions in the battery to a quantified impact on the aging processes and battery performance is carried out in a two-step approach.

First, from the literature the general dependencies of most aging mechanisms on the state variables are known or, if not, need to be investigated. Corrosion in lead–acid batteries is used here as an example. Corrosion depends on temperature, potential, and electrolyte concentration. The general dependencies have already been described by J. J. Lander 50 years ago. As a result of the experimental investigations, look-up tables for corrosion rate as a function of temperature, potential, and acid concentration are generated. Effects of compression or corrosion layers or the impact of cycling can be taken into account additionally, provided that there are quantitative data available. However, the speed of corrosion also depends very much on the alloy, the active mass coverage, or even the casting conditions. It is impossible to calculate the corrosion rate from first principles. In a second step therefore, specific corrosion tests on grids are performed under well-defined conditions in the laboratory. This information is used to scale the look-up table with the already implemented dependencies on state variables. Finally, it is possible to calculate the local degree of corrosion of a grid under the given operating conditions. Obviously, a number of assumptions are made, e.g., that the general shape of the Lander curve is independent of alloy composition and production processes.

Based on the same general concept, the impact of all major aging effects can be analyzed. As the aging effects change the performance of the battery locally or of the complete cell, their interactions are taken into account directly, e.g., by adapting the resistance of the grid, the inner surface of the active masses, etc. To be able to do this requires knowledge of some of the design parameters of the battery, e.g., thickness of the grid.

Consequently, the degree of aging of a battery or fuel cell and the impact on their performance can be analyzed at any point in time. 'Measurements' of the inner resistance or 'capacity tests' can be made regularly with the model to determine the current state of health and therefore the end of lifetime.

Advantages, Disadvantages, and Limitations of Physicochemical Aging Models

Compared with the other two concepts described in the following sections, the physicochemical aging model is the most complex and most sophisticated approach. This model approach not only provides an aging model, but also a model for the electrical and thermal performance. This is an additional feature of the model as it addresses the increase of stress factors when an aged battery is subjected to the same power and performance requirements as a new battery.

However, the model approach requires several input information. There are on the one hand geometric data for the battery cell including the porosity of the active materials and on the other hand data of laboratory experiments on the major aging effects. The model for the state variables requires mainly detailed geometrical data on the size, thickness, and porosity of the electrodes; the battery case; and the electrolyte volume and concentration. These are typically nonconfidential data and can be measured by many laboratories very simply. The tests concerning aging effects are more complex. The duration

of the tests is typically in the range of several weeks to few months and several tests must be performed in parallel. This is already out of the scope of what a 'normal' end user of batteries can do. In addition, the design of the experiments to limit the interaction between parallel aging effects must be carried out with great care. Because of the complexity of the model the computational speed of simulation is significantly lower compared with the other models. The limited resolution of the model is a compromise between computing speed (increases more than linear with number of simulation points) and resolution of the model. Currently, the calculation is 200 times faster than real time, e.g., runs $\sim$40 h for 1 year of operation.

An advantage of this approach is its self-check feature. The model has to be parameterized in such a way that the model output is consistent with the measured data. Measured current and temperature data are used as input to the model and, if the voltage calculated from the model is similar to the measured voltage values throughout prolonged aging, the model is verified.

The approach is generally generic and can be transferred to any other battery or fuel cell technology. This requires on the one hand the representation of the technology-specific processes affecting the state variables and on the other hand the identification of the relevant aging processes and appropriate laboratory tests to characterize the specific material or technology.

As major advantages of the model the following aspects need to be recognized. Once the parameters are determined for a certain battery or fuel cell, the model allows for an analysis of a wide variety of operating conditions and control strategies. There are no limitations because the model approach does not use simplifications that limit the validity of the model. The second advantage is that the model provides a very detailed understanding of the effect of aging processes and the interactions between operating strategies and battery aging. This can be used by manufacturers for improving the design and meeting the requirements of certain operating conditions better.

The concept is appropriate for an off-line analysis but it is not suitable for online use in applications such as vehicles.

Weighted Ah Aging Model

Lifetime data given by manufacturers are based on well-defined test conditions. Cycle lifetime of batteries is simply determined by discharging the battery with a constant current to a certain depth of discharge (DoD) and a subsequent full charge with a given charging regime. Lifetime of fuel cells is typically defined as operating hours at a certain power level. From these standard conditions the overall Ah or energy throughput until the capacity or power has fallen below a preset level is measured. For lifetime prediction purposes, the lifetime of a battery is simply given as the time until the total Ah throughput is identical to the Ah throughput measured under such constant conditions.

However, in real application the operating conditions typically deviate from these standard operating conditions and the Ah throughput of the battery may be more or less severe with regard to aging than during the standard operating conditions. The weighted Ah aging model takes these deviations into account and makes the assumption that the battery is at the end of its lifetime once the weighted Ah throughput has exceeded the expected unweighted Ah throughput that has been measured under nominal operating conditions. The challenge of the model is finding the appropriate weighting factors f_i at any time during the lifetime simulation.

Mathematically, the end of lifetime is reached if the following relation becomes true where L_{standard} is the number of cycles under standard cycling conditions until end of lifetime conditions.

$$\frac{\int_t \prod_i f_i \cdot i_{\text{batt}} \cdot \mathrm{d}t}{C_{\text{nominal}}} > L_{\text{standard}} \qquad [1]$$

where C_{nominal} is the nominal capacity throughtput.

As per the definition, the end of lifetime is reached once the capacity of the battery under standard test conditions (e.g., 10 h discharge current, 25 °C) is below 80% of the nominal capacity or the internal resistance may have increased by, e.g., a factor of 2.

The following example shows the general idea of the approach for lead–acid batteries:

1. Cycling a lead–acid battery at low SoC stresses the battery more than cycling at high SoC. Therefore, any Ah that is charged or discharged to the battery needs to be weighted with a factor which increases with decreasing SoC.
2. Cycling of a battery while acid stratification is present is known to result in inhomogeneous current distribution along the electrode. As a result, parts of the electrodes are stressed very much. Again, the Ah throughput needs to be weighted with a factor that depends on the degree of acid stratification.
3. Long periods without a full charge of the battery are known to be detrimental as well because the sulfate crystals grow. This finally results in sulfation (active mass that cannot be reconverted under normal charging conditions) and capacity loss. Therefore the Ah throughput also needs to be weighted with a factor depending on the time since the last full charge.
4. Operation at high temperatures leads beside others to increased corrosion processes and therefore the Ah

throughput is weighted accordingly. This is also an example for a stress factor that acts more as a function of time rather than as a function of Ah throughput. This needs to be taken into account in the model.

For lead–acid batteries a very detailed Ah throughput model has been developed. Various versions have been published and can be found in the literature. The model takes into account acid stratification, voltage, temperature, SoC, time, and the quality of a full charge, i.e., the degree to which homogeneity of the state variables in the cell has been achieved. In this advanced model weighting factors for acid stratification, bad full charges, microcycles, and current rates are taken into account.

Figure 4 shows an operation profile, which has been taken from a laboratory bench test for the characterization of lead–acid batteries with special respect to operation in photovoltaic power supply systems. Figure 4 shows the SoC of a flat plate battery with liquid electrolyte. The SoC is scaled to nominal capacity ($C_{10} = 54\,\text{Ah}$), the initial C_{10} capacity of the battery was $\sim 160\%$ of the nominal capacity. In addition the figure shows the voltage and the battery current. Together with the calculated SoC the capacity measured during capacity tests is shown (stars) and the capacity curve calculated by the model. For the calculation of the capacity curve, a standard curve of capacity against Ah throughput is used so that the effect of the current profile on voltage can be modeled properly.

Figure 5 shows more details of the model calculated from the data shown in Figure 4. The upper graph shows the accumulated Ah throughput as it occurs (unweighted Ah throughput) and the weighted Ah throughput according to the model. While the real Ah throughput is ~ 320 times the nominal capacity until the capacity dropped below its set value after a test period of 210 days, the weighted Ah throughput is by a factor of 5 higher. The short calendar lifetime results from the fact that the data come from an accelerated lifetime test. The middle graph and the lower graph show selected weighting factors. The lower graph shows

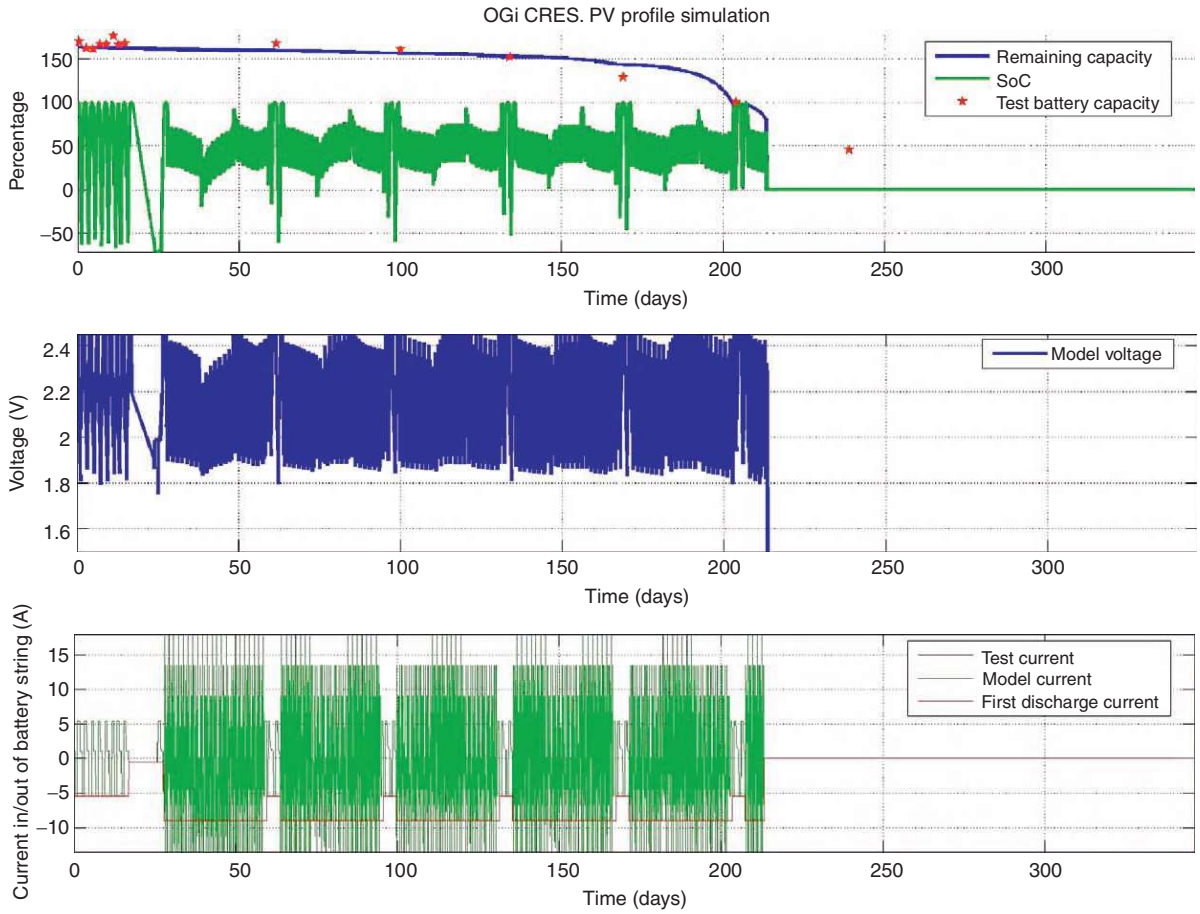

Figure 4 Remaining capacity calculated by the model, measured capacity and state of charge (SoC) (upper graph), voltage (middle graph), and current (lower graph) for an OGi (flat plate) lead–acid battery with flooded electrolyte during a laboratory test with test profile representing typical operating conditions in photovoltaic power supply systems.

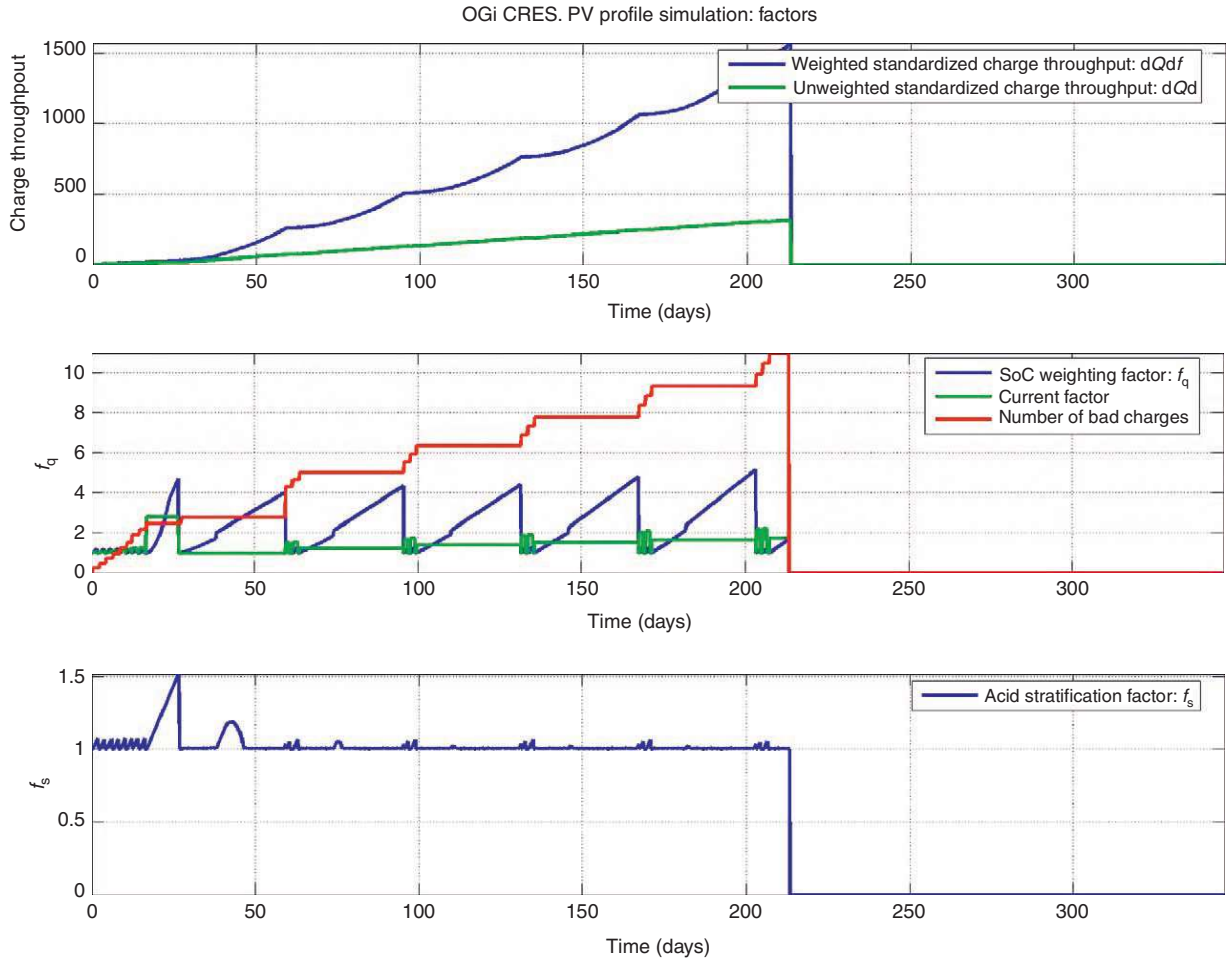

Figure 5 As an example, details from the weighted Ah aging model for a lead–acid battery for the operating conditions is shown in Figure 4. The upper graph shows the unweighted charge throughput (lower straight line) and the weighted Ah throughout (upper line). In the middle graph weighting factors for the current and the factor 'SoC and time since last full charge' are shown. The lower graph shows the weighting factor for acid stratification. After 210 days the test is finished, therefore all curves are set to zero after 210 days.

the acid stratification factor, which, in this example, is mostly close to 1 (i.e., no additional stress). The reason is that the battery is frequently at a voltage of 2.4 V, resulting in gassing and therefore a natural mixing of the electrolyte. Therefore, acid stratification is assumed to be small. The middle graph shows the weighting factor for the current rate (green). This factor is 1 if the current is I_{10} (current for which the lifetime has been defined). Filter functions are used to calculate the average current. The blue curve shows the weighting factor taking into account the SoC and the time since the last full charge of the battery. It increases between two full charges and is reset to 1 once the battery has been fully charged and all inhomogeneities are removed. In addition a counter for the number of incomplete full charges (red curve) is shown. Incomplete charging has an impact on the distribution of the size of the sulfate crystals and therefore the charge efficiency.

For the weighted Ah throughput the current is multiplied with the weighting factor in any time step (without feedback loops) and integrated over time.

For the parameterization of the model first of all standard lifetime data provided by the manufacturers are necessary. In addition, the parameters for the weighting factors are needed. There are two different approaches to determine the parameters: expert estimates or parameter identification from measured data. If measured data are available as those that have been presented in **Figure 4**, the parameter identification is an efficient and appropriate way. The benefit of the model is that the parameters need to be identified only once. Afterward any other operating conditions can then be analyzed with the model without further modifications. The same set of parameters can be used for high-rate or low-rate cycling regimes or for different applications. This allows analyzing and comparing of system designs (sizing of components) and operation strategies efficiently.

The advantage of the model is a very high computational speed and therefore it is very useful for system design tools where a large number of systems must be analyzed in a short time. Furthermore the basic structure of the model is easy to understand and therefore it can be adapted to different battery or fuel cell technologies by taking into account the relevant stress factors and their quantitative impact on aging for each technology.

However, the model is a heuristic approach. The model does not represent aging effects on a physical or chemical basis. Therefore the model does not provide direct feedback to the manufacturers of the batteries to improve the technology. This would require a link between the weighting factors and the specific design features.

Event-Oriented Aging Model

General Concept

In many fields of mechanical engineering an event-oriented aging model is used, which is often referred to as SN or Wöhler curve. The lifetime of a component – in mechanical engineering simply the lifetime before breaking in a catastrophic failure mode – is estimated by assigning the incremental loss of lifetime associated with well-defined events and adding up the loss of lifetime per event. Usually, each event is described by one scalar value, e.g., the force of bending or the amplitude of vibration. We will refer to this scalar value as 'stress factor'. When varying the magnitude of the stress factor, the number of events before breaking changes in a characteristic fashion: the greater the damage induced in the component by a certain value of the stress factor, the fewer events can take place. Figure 6 shows the cycle lifetime of a nickel–metal hydride (Ni–MH) battery as a function of the DoD during the cycling regime. This relationship represents a Wöhler curve. The higher the lifetime the smaller the change of DoD. It is well known that this is mainly due to the mechanical stress caused by the volume expansion and reduction, which occurs during charging and discharging of the active materials. Small changes of DoD cause only a little stress whereas high DoD stresses the active materials dramatically.

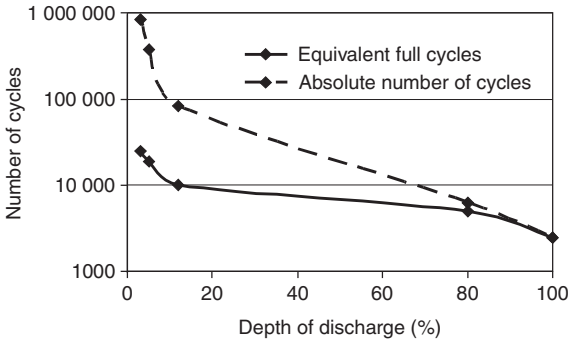

Figure 6 Example of a Wöhler curve for batteries. Cycle lifetime for a nickel–metal hydride (Ni–MH) battery is shown as a function of the depth of discharge of each cycle. Number of cycles is shown in absolute values and as equivalent full cycles.

Two types of Wöhler curves are used today to estimate the battery lifetime:

1. The curve showing the number of cycles of a battery as a function of DoD until the end of lifetime. This curve is given by most battery manufacturers in data sheets (see Figure 6).
2. The curve showing the lifetime of a battery in days or years as a function of its float charging voltage or temperature.

However, both of these Wöhler curves as well as a lot of Wöhler curves in mechanical engineering are one-dimensional curves using only one stress factor as a parameter and leaving all other parameters of the operating conditions constant. For batteries and fuel cells, such one-dimensional curves do not provide a realistic description of the operating conditions because there is a complex combination of stress factors in real applications.

The mathematics of event-oriented aging models is simple: if NE_i^{max} is the number of events i that can occur during the lifetime of a battery until the failure occurs (under the assumptions that only events of type i occur) and NE_i is the number of events that have occurred during the period of observation, then the loss of lifetime associated with event i is

$$LL_i = \frac{NE_i}{NE_i^{max}} \quad [2]$$

With regard to the example in Figure 6, NE_i^{max} is the number of cycles shown on the y-axis and the event of type i is a cycle with a certain DoD as displayed on the x-axis.

The portion of lifetime lost during a period of observation is then the sum over all types of events during this period:

$$LL = \sum_i LL_i \quad [3]$$

The end of lifetime is reached when LL is equal to one. As every event is associated with a length of time, the lifetime is the sum over the duration of all events i that have taken place. Figure 7 shows an example where assumed cycles during the lifetime of an electric vehicle sum up in a way that the lifetime of the battery is at its end (LL = 1). Cycles with higher DoD are due to electric driving between two recharges. Cycles with low DoD occur due to regenerative braking during driving.

Obviously the use of this model is based on a number of assumptions:

1. The loss of lifetime per event is very small.

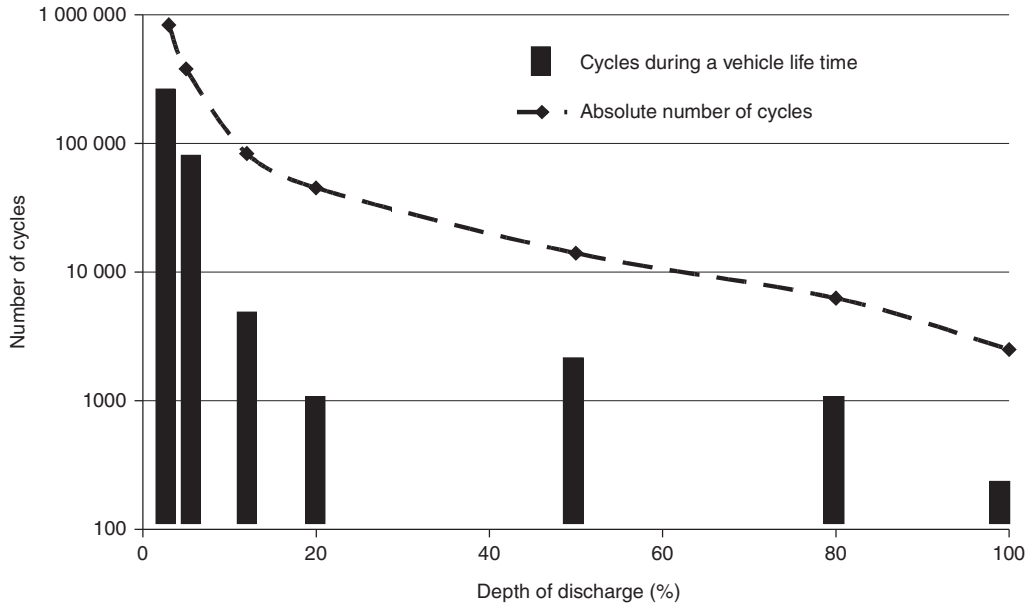

Figure 7 Wöhler curve for a nickel–metal hydride (Ni–MH) battery according to **Figure 6** with an example for the number of cycles at different DoD as it could occur in an electric vehicle.

2. The loss of lifetime for a given event does not depend on the order of events, i.e., it is independent of the events that took place previously.
3. The loss of lifetime associated with an event does not depend on the accumulated loss of lifetime. The incremental loss of lifetime caused by a particular event for a new battery or fuel cell is assumed to be identical to the loss of lifetime for an old one at the very end of its life.
4. Every point in time must be assigned to exactly one event for which data from a Wöhler curve exist. The simultaneous assignment to several types of events is not allowed.

The first assumption is true for batteries and fuel cells under normal operation. It does not hold for severe operating conditions capable of destroying a battery or fuel cell after a few repetitions (e.g., discharging or operation at 0 V, or overheating of the system beyond specified temperature limits).

The second assumption is fulfilled only in battery practice, if the battery at the end of the event has returned to an appropriate condition. For lead–acid batteries this requirement means being fully charged with conversion of all discharged active material and removal of acid stratification. An event therefore must start with a fully charged battery and finish with a fully charged battery. In applications where this is not assured, it is necessary to analyze whether the approach is appropriate and can be used at all. However, this assumption is fulfilled in many applications. The assumption as formulated here also means that different events must be statistically distributed. Otherwise, it would be necessary to discuss whether a battery that will be subjected to float operation for the first half of its life and cycling operation for the second half will have a different life expectancy than a battery with a statistical mixture of these two types of events.

The third assumption is the most difficult one. When defining an event using parameters that already incorporate aging (e.g., DoD based on the actual capacity of the battery during the event), aging effects are at least partially incorporated. However, such definitions may not always be possible.

Regarding the last assumption, **Figure 8** shows an example of the voltage, current, and temperature of a battery in a railway application. It is immediately obvious that a simple one-dimensional Wöhler curve cannot be used and the definition of an event must be made carefully so that every point in time will be assigned to only one type of event.

Definition of Events

Batteries in many applications can be considered to be subject to a combination of three different types of events: float operation, cyclic operation, and cycling at a PSoC. The exact definition of 'event' is application and technology specific and, as an example, is given here for lead–acid batteries for railway applications. The main classes of events are listed below. Each main class is subdivided into several subclasses of events, which are discussed in more detail after the definition of the main classes.

Float operation: Batteries in railway applications may remain at a full SoC for a long time; however,

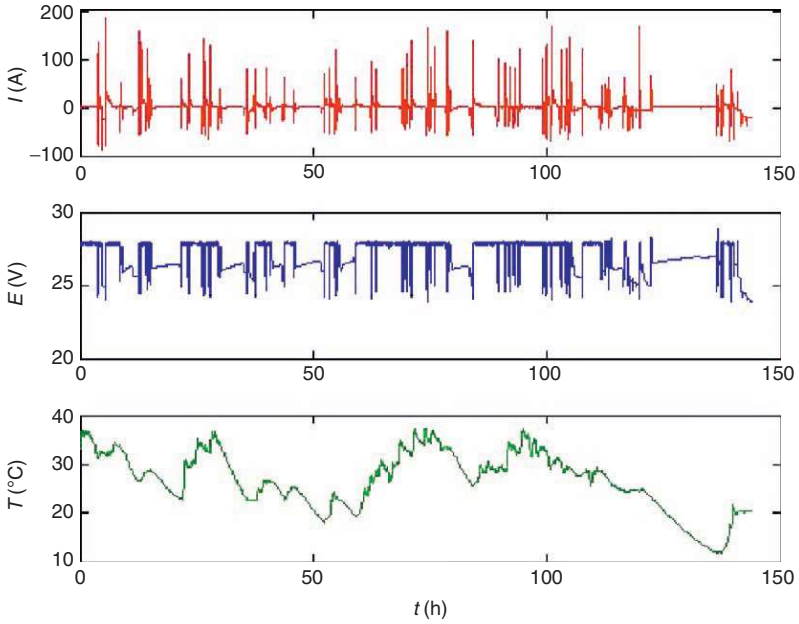

Figure 8 Measured data of current, voltage, and temperature for a period of 150 h from a battery system in railway (24-V system) applications.

during that time they may undergo severe temperature changes and changes in the charging voltage as the availability of electrical power on board a train changes. Float operation may also be interrupted by short low-rate discharge periods. In addition, the batteries may have to provide high-rate discharge currents for starting the internal combustion engine of a train. Approximately 0.25% of the capacity is removed and float voltage is reached immediately after starting the motor. Neither of these occurrences is considered to be a discharge cycle.

Cyclic operation: Train batteries are occasionally discharged as part of their normal operation, e.g., shunting operations. For safety reasons, certain consumers are never switched off even if this leads to a damaging deep discharge of the battery and the battery may remain at a very low SoC for a few hours. Recharging the battery always occurs via a constant current/constant voltage charging regime with I_5 and usually up to a voltage of 2.35–2.4 V per cell. During discharging the battery current will tend to fluctuate as loads will be switched on and off, and during charging the charging current may sometimes fall below the set value as the availability of electrical power on board a train is limited.

Cycling at partial state of charge: Occasionally, a battery does not reach its full SoC before another discharge starts. Damaging conditions like sulfation and acid stratification are then allowed to exercise their effect longer than in a normal discharge followed by a full charge. The duration of such an event, starting and ending with a fully charged battery may last up to a week and the total Ah throughput and the lowest DoD that is reached during this time may vary within a wide range.

The distinction between a cyclic operation and cycling at PSoC is conceptually simple. In a cyclic operation there is a continuous discharge followed by a continuous charging process, which is finished when the battery has reached its full SoC. Interruptions of the discharge or charge ($I_{\text{Battery}} = 0$) are permitted. If the discharging process is interrupted by charging currents, even if the charging process takes only a very short time, or the recharging process is interrupted by a period of discharging before the battery is fully charged, then cycling at PSoC exists. When analyzing data in detail, a more differentiated definition has to be used, e.g., one where regenerative braking is still considered to be a cyclic operation and opportunity charging is cycling at PSoC.

Based on these considerations, events were accurately defined and battery experts asked to provide estimates by how much the total number of events during the lifetime of a battery would change if well-defined stress factors would change.

For float operation, the stress factors to be considered were voltage (eight groups of float voltages between 2.23 and 2.4 V per cell) and number of short, high-rate discharges (no discharges, 1–5 discharges per 24 h, 6–11 discharges per 24 h, 12–24 discharges per 24 h).

For cycling operation, the stress factors were DoD and amplitude of discharge current. The stress factor 'DoD' was grouped in categories according to Table 1. The percentage values given here are for an average discharge current in the range of I_2–I_5 for flooded tubular batteries.

It is necessary to take into consideration that the identification of the events is the result of a detailed analysis of typical events that occur in this specific application. Currents of approximately I_{200} correspond to the current requirement of some safety features of railway systems that are never switched off and very deep discharges with waiting times before recharging starts may therefore occur. Concepts used in pattern recognition or expert systems may be used for identifying events that may occur in an application of interest.

Table 1 Example for the rating of stress factors for current rates between I_2 and I_5

Maximum DoD 0–10% followed immediately by a full recharge	887%
Maximum DoD 0–20% followed immediately by a full recharge	452%
Maximum DoD 20–40% followed immediately by a full recharge	247%
Maximum DoD 40–60% followed immediately by a full recharge	157%
Maximum DoD 60–80% followed immediately by a full recharge	100%
Maximum DoD 80–100% followed immediately by a full recharge	68%
DoD 100% followed by a waiting period of up to 24 h before a full recharge is started	58%
DoD 100% followed by a further discharge with approximately I_{200} for up to 24 h followed by a full recharge	37%

Lifetime defined for cycling with 80% depth of discharge (DoD).

In all cases, the recharge was assumed to be a constant current/constant voltage charging regime. The discharge currents were grouped into currents above I_2, I_2–I_5, I_5–I_{10}, I_{10}–I_{20}, I_{20}–I_{100}, and less than I_{100}. This is a second dimension of Table 1.

The stress factors in cycling at PSoC are (1) length of time before reaching full SoC again and (2) Ah throughput during this time. The stress factor 'length of time' was grouped into duration of up to 1 day, 1–2 days, 2–3 days, 3–4 days, and up to 7 days, and the stress factor 'Ah throughput' into duration up to 0.5 nominal capacity throughput (C_N), 0.5–1 C_N, 1–1.5 C_N, 1.5–2 C_N, 2–4 C_N, and 4–6 C_N.

Figure 9 shows Wöhler curves as an example for the above-discussed case of cyclic operation. The data should be taken as a general example.

For the parameterization of the model first of all standard lifetime data provided by the manufacturers are necessary. The data of all Wöhler curves are given as a percentage so that the transfer to other battery systems is straightforward. For each event, an increase of 10 K above 20 °C was assumed to half the number of events.

The task of estimating lifetime is then reduced to a computational program, which identifies events from measured or simulated current, voltage, and temperature curves. The program identifies the events defined above from the current and voltage profile of measured data or data from simulations and assigns the loss of lifetime per event taking the effect of temperature into account. Computational speed is very high.

Data as shown in Figure 5 were used to analyze the stress events and to predict the lifetime. The analysis of a 7-day period from which the data in Figure 5 were taken showed a loss of battery lifetime of 1%, i.e., the battery

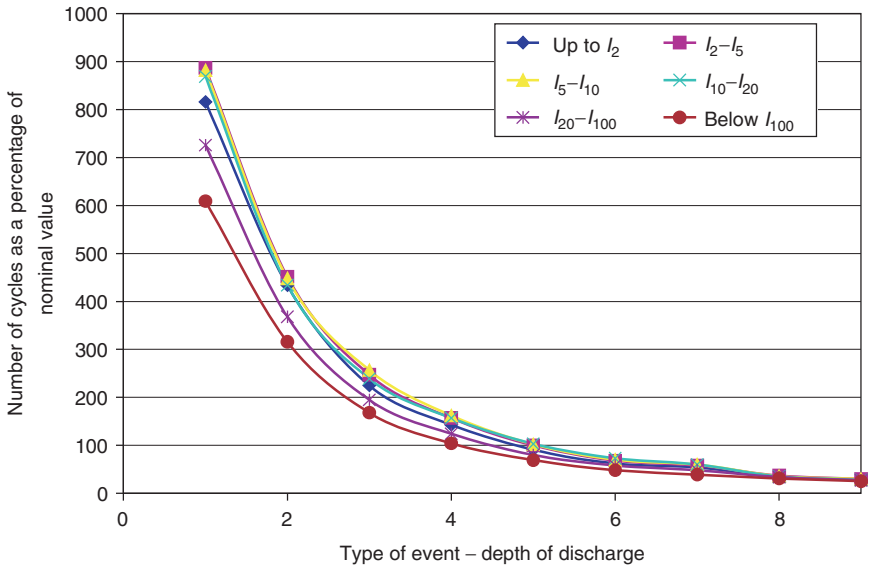

Figure 9 Example for Wöhler curves for different events (compare **Table 1**) for different current rates.

under these conditions would have had a lifetime of about 2 years.

Application of the Model for Different Batteries and Fuel Cell Technologies

Three concepts for modeling lifetime have been presented using the lead–acid batteries as an in-depth example. However, they clearly apply to other electrochemical systems as well, including fuel cells.

To adapt the models to other electrochemical technologies, the specific aging conditions and their stress factors must be identified. As an example, the following effects, among others, should be taken into account for lithium batteries:

- Cycle depth – owing to breathing of the active mass during cycling the lifetime depends significantly on the cycle depth;
- Operational SoC (some materials show better lifetimes if the batteries are cycled at medium or low SoCs rather than at high SoC due to increased side reactions at high SoC or high potentials) and its impact on cycle lifetime;
- Charging voltage – the electrolyte will be irreversibly decomposed at too high charging voltages;
- Formation of solid electrolyte interface;
- Temperature (typical lifetime reduction as for all electrochemical systems); and
- Lithium plating in case of too high current rates (depending on the temperature).

It is necessary to take into account that lithium-based batteries are a class of batteries with a very wide range of different technologies. Therefore, the weighting factors, stress factors, or events are different for different materials. For lead–acid batteries or nickel–metal hydride batteries the situation is simpler because the materials used are always the same and vary only little (alloys, additives in the lattice material). This definitely changes the performance of the cells as well and therefore adaptation of the model parameters is necessary here as well.

If interactions between the various stress factors and aging effects are described in principle and the knowledge of what causes loss of lifetime has been quantified, each of the three modeling approaches can be applied depending on the application for the lifetime prediction.

Experimental investigation on the current and temperature distribution within a fuel cell have proven that the approach with the physicochemical aging model can be transferred to fuel cells as well. State variables within a cell can deviate significantly from what is expected from the mean values measured from the outside of the cell. Therefore, corrosion processes or any other detrimental effects that depend on potential, current rates, temperature, and concentration of fuels can be modeled and linked to aging effects.

But the event-oriented model can also be applied. Different operating temperatures, start and shutdown of the cells, power decrease or increase rates, or normal operation at different current levels are different events with unequal impact on the overall lifetime.

Comparison of the Different Approaches

The information requirement for the three concepts discussed above and the methods to verify them differ greatly. Verification of lifetime prediction models is difficult and time consuming because models can only be verified for a battery or fuel cell that is well characterized when it is new and for which the complete data sets of voltage, current, and temperature are available from installation to decommissioning including a capacity or performance test and possibly other tests at the time of decommissioning. Furthermore, real verification would require non-accelerated operation of the battery or fuel cell and this takes years. There are hardly any such data sets available. If lifetime prediction models need to be parameterized, then the validity of the model cannot be checked by using the same data set that has been used for the parameterization. Additional data sets are required for verification.

The physicochemical model requires knowledge of the interaction between electrochemical and physical measurements (state variables: resistance and voltages as a function of SoC, temperature, and microstructure of the active material) and aging processes that are usually not accessible to non-destructive measurements. Only the loss of performance as a result of the combination of aging processes that have taken place can be measured when testing the complete cell. But the detailed modeling approach allows separating the aging effects and this is unique within the different approaches presented in this chapter. The calibration of the models for the different aging effects can be done most efficiently if parts of the cell are subjected to aging tests, e.g., grids or bipolar plates only to corrosion tests. Once this has been accomplished for all components and aging processes and the model describes correctly the changes of performance during the lifetime of a battery or fuel cell and thus correctly predicts the lifetime of the battery, the model has achieved a considerable step toward verification. A single lifetime test in the laboratory, which confirms the lifetime prediction model will be sufficient. The model can then be considered to predict lifetime sufficiently well even if changes of operating strategies and materials lead to a different combination of aging effects. When analyzing measured data, the current, voltage, and temperature values have to be created by the model first. Good agreement between measurements and model will immediately qualify the model and provide credibility to the lifetime prediction.

Table 2 Comparison of the different model approaches with regard to parameter identification, model complexity, and transfer to other applications, designs, and technologies (electrochemical systems)

	Parameter identification	*Preciseness and quality of information*	*Model complexity and calculation speed*	*Transfer of model to other applications and battery designs*	*Transfer of model to other electrochemical systems*
Physicochemical aging model	Through laboratory experiments and literature study	High, can give very detailed information	High/slow	Only battery design parameters needed	Same structure, but new models required
Weighted Ah aging model	Expert expertise and data from lifetime tests (field or laboratory)	Medium, allows optimization of operating conditions	Medium/medium	Deviating aging effects must be identified and included	Same structure, but new weighting factors needed
Event-oriented aging model	Expert expertise	Low, does not allow extrapolations to applications with other types of events	Low/high	New expert expertise needed if other stress events occur	Same structure, new expert expertise needed

The transfer to other types of batteries or fuel cells of similar technology is quite easy and requires mainly adequate knowledge of design parameters and results from specific aging tests of cell components. The mathematical algorithms remain the same, but the description of the specific electrochemical reactions and knowledge concerning the dependence of aging effects on the state variables must be obtained newly.

The situation is different for the weighted Ah model: the weighting factors cannot be derived from first principles and need to be obtained differently. Expert expertise or parameters fitting are two options to predict the lifetime correctly. Support from physicochemical models or a first principle approach is possible and helpful. When analyzing measured data, the current, voltage, and temperature values have to be created by the model first. Good agreement between measurement and model will not in itself qualify the model and provide credibility to the lifetime prediction because the electrical performance model is typically a black box model. High credibility of the model is achieved only if good agreement of the electrical performance between reality and model is achieved throughout the whole lifetime.

The use of this approach requires the availability of measurements to fit the parameters or to verify that the combination of expert estimates does in fact lead to the lifetime, which has been measured. Subsequently, another set of measurements is required, sufficiently different not to be a repeat of the parameterization process but sufficiently close to remain within the model constraints. An extension beyond 'similar' data sets offers increasingly less credibility, as does the transfer of the model to other battery types.

The event-oriented concept is the approach used today for lifetime prediction but is extended to variations in the operating conditions that are at present not accounted for properly. It requires an application-oriented definition and classification of events and information concerning the number of these events until the end of lifetime is reached. For some events, measurements are available, e.g., number of cycles at a certain temperature and DoD or days at float charging. In principle, of course, it is possible to determine all the required data in the laboratory correctly without any doubts concerning their validity, but this process takes very long and is exceedingly expensive. However, interpolation by expert opinion can be used as long as measurements for a few types of events exist. This approach therefore is simple and depends on the assumption that the loss of lifetime caused by an event does not depend on the previous event or on the age of the battery. Verification of the model is therefore simply a question of analyzing one single set of measurements, which extends over the lifetime of the battery. A detailed characterization of the battery at the beginning is not necessary but the end of lifetime criteria need to be chosen suitably.

In contrast to the other models, measured data can be taken as they are and need not be recalculated before applying the lifetime prediction models.

A transfer of results to other batteries or fuel cells is straightforward as the model is independent of technology or design but requires the adjustment of the input matrices accordingly.

Table 2 sums up advantages and disadvantages of the different models.

All approaches allow an optimization of the operating strategy of an application. However, only the weighted Ah throughput model and the event-oriented model are applicable for an online optimization of the operating strategy. The physicoelectrochemical model typically is too complex for online applications. However, if sufficient computing power and data storage is available it could become an online tool as well.

If the online models show an increase of the various weighting factors or the battery is classified to be in an event, which uses up a significant portion of the lifetime, then a cost–benefit analysis can be made concerning changes in the operating strategy. In renewable energy systems, for instance, the cost of providing a full charge can be easily compared to the cost of operating the battery in a mode that reduces lifetime significantly. For fuel cells, e.g., the flow rates of gases or the moisture inside the cell and therefore the water content of the membrane could be adjusted to avoid critical situations.

Summary

Lifetime prediction of electrochemical power sources is still a wide field for innovations with regard to algorithms, parameter identification, and verification of the results.

Three different concepts have been discussed:

1. Physicochemical modeling approaches are based on a detailed model for the state variables such as potential, current density, fuel concentration, pH, or temperature with time and spatial resolution inside the cell. Aging processes are analyzed in the laboratory in depth as a function of state variables. The detailed model and the models for different aging models are combined and allow for lifecycle simulations. The parameterization is time consuming and complex and must be repeated each time new materials are used in the cell. Once the model is parameterized, it allows a detailed insight into the device, to identify weak points and to analyze the impact of operating strategies and load profiles on the lifetime.
2. The weighted Ah aging model assumes a standard aging profile and assigns to all operating conditions stress levels above or below the standard aging profile. This is done by multiplying a factor higher or lower than 1 to the Ah throughput. The parameterization can be done

by expert knowledge or comparison of appropriate experimental data. Such models help to analyze the impact of changing operating conditions and load profiles but do not allow any conclusion with regard to the weak parts of cell, etc. The model is calculating aging continuously and can be coupled directly with an electric performance model. Therefore, such models are suited for use in simulation tools.

3. The event-oriented aging model separates the operation profile in a certain number of characteristic events. Based on a model the operating conditions are split into these events and according to expert knowledge or experimental verification the stress and therefore a certain amount of lifetime consumption is added up for each such event. This model is relatively simple to install. It is parameterized by rating the lifetime effect of the different events. Such models help to analyze the impact of changing operating conditions and load profiles, but do not allow any conclusion with regard to the weak parts of cell, etc. Once the model is parameterized computation time is very fast.

If lifetime prediction is needed, it is necessary to ask first for the purpose of the predicition. This results in the selection of the appropriate model. Identification of appropriate parameters is difficult and time consuming in any case.

In the long run it is necessary to identify a general acceptable aging model for the different electrochemical systems and to obligate the manufacturers to deliver the parameters for the model. This would allow users to identify the lifetime expectation in their specific applications.

Nomenclature

Symbols

C_N; $C_{nominal}$	nominal capacity throughput
E	electrode potential (V)
f_i	weighting factor
f_q	SoC weighting factor
f_s	acid stratification factor
I	current
$I_{Batt\ or}$ $I_{Battery}$	battery terminal current
LL_i	Loss of lifetime
$L_{standard}$	number of cycles under standard cycling conditions
NE_i	number of events that have occurred during the period of observation
NE_i^{max}	number of events i that can occur during the lifetime of a battery until the failure occurs
t	time
T	temperature
U_{Batt}	battery terminal voltage

Abbreviations and Acronyms

DoD	depth of discharge
PSoC	partial state of charge
SoC	state of charge

See also: **Batteries and Fuel Cells:** Lifetime; **Fuel Cells – Overview:** Lifetime Prediction.

Further Reading

Buch A (1988) *Fatigue Strength Calculation*. Aedermannsdorf, Schweiz: Trans Tech Publications.

Ellyin F (1997) *Fatigue, Damage, Crack Growth and Life Prediction*. London: Chapman & Hall.

Kulikovsky AA, Schmitz H, Wippermann K, et al. (2006) DMFC: Galvanic or electrolytic cell? *Electrochemical Communications* 8: 754–760.

Kulikovsky AA, Schmitz H, Wippermann K, et al. (2007) Bifunctional activation of a direct methanol fuel cell. *Journal of Power Sources* 173: 420–423.

Lander JJ (1956) Further studies on the anodic corrosion of lead in H_2SO_4 solutions. *Journal of the Electrochemical Society* 103: 1–8.

Meissner E and Richter G (2003) Battery monitoring and electrical energy management: Precondition for future vehicle electric power systems. *Journal of Power Sources* 116: 79–98.

Sauer DU (1997) Modelling of local conditions in flooded lead–acid batteries in PV-systems. *Journal of Power Sources* 64: 181–187.

Sauer DU (2003) Optimierung des Einsatzes von Blei-Säure-Akkumulatoren in Photovoltaik-Hybrid-Systemen unter spezieller Berücksichtigung der Batteriealterung. PhD Thesis, Universität Ulm.

Sauer DU, Sanders T, Fricke B, et al. (2008) Measurement of the current distribution in a direct methanol fuel cell – Confirmation of parallel galvanic and electrolytic operation within one cell. *Journal of Power Sources* 176: 477–483.

Seidel K (1978) *Eine Theorie der Wöhlerkurve, Fortschr.-Berichte VDI-Z. Reihe* 5, Nr. 39. Düsseldorf: VDI-Verlag, ISBN 3-18-143905-3.

Wenzl H, Baring-Gould I, Kaiser R, et al. (2005) Life prediction of batteries for selecting the technically most suitable and cost effective battery. *Journal of Power Sources* 144: 373–384.

Modeling

Chee Burm Shin, Ajou University, Suwon, Republic of Korea

Introduction

The 'ideal' rechargeable battery is obviously the one that has high power and energy density, high discharge rate, flat discharge curves, good low-temperature performance, and long service and shelf life as well as safety. However, the mentioned preferable characteristics of rechargeable batteries conflict with one another and require trade-offs. The objective of advanced battery research and development should be to obtain a compromise among the battery requirements. Mathematical modeling of batteries plays an important role in battery development, as nearly limitless design iterations can be performed using computer simulations.

There are a wide variety of battery models with varying degrees of complexity. They may be classified into analytical models, electrical models, and electrochemical models. Analytical models have been developed where analytical expressions are formulated to calculate actual battery capacity and lifetime. One of the earliest analytical models is Peukert's equation, which expresses the nonlinear relationship between the battery capacity and the discharge rate. More sophisticated analytical models have been proposed, where the capacity and lifetime are expressed in terms of discharge current, temperature, and additional operating parameters. Analytical battery models can include both constant load and variable load. All these models capture rate-capacity effects and some capture thermal effects, but none addresses the effects of phenomena such as storage and aging. These models are flexible and can be easily configured for specific batteries. They are computationally efficient, because they require only simple evaluation of analytical expressions. Electrical models are based on constructing equivalent electrical circuits comprised of voltage sources, resistors, and capacitors. The charge stored in the battery is modeled by using a capacitor, whereas the voltage across the capacitor is used to represent the output voltage of the battery. The discharge process is modeled by continuously applying corrections to both the charge stored in the capacitor and the output voltage. Further corrections accommodate the cycle life of the battery, the change of internal resistance during charge and discharge, and thermal characteristics. For electrical engineers, electrical models may be more intuitive, useful, and easy to handle. Because they use parameters derived from typical electrochemical characterizations, such as charge and discharge curves, they can be very versatile to simulate any type of batteries, but they have minimal details in the cell chemistry. Electrochemical models describe the mass, energy, momentum, and charge conservation for each phase and component of the cell. The kinetics and thermodynamics of the chemical and electrochemical reactions are also included. Electrochemical models typically solve the electrolyte potential, electrolyte concentration, solid-phase potential, and solid-phase potential in the porous electrodes, and the electrolyte potential and electrolyte concentration in the separator. These models are usually complex because of the nonlinear coupling of the dependent variables in the governing equations and the nonconstant kinetic and transport parameters. They are able to predict not only macroscopic quantities such as the cell voltage and current, but also the local distribution of concentration, potential, current density, and temperature inside the cell on a microscopic scale. They can readily accommodate the capacity loss during storage and the capacity fade owing to aging. They have been used by various researchers to optimize the cell design and to study the effect of system parameters and thermal behavior. Electrochemical models are more detailed than the other models and hence the most accurate among the models mentioned in this article. However, they are the most computationally intensive.

In this article, the analytical and electrical models are briefly reviewed. The electrochemical model is reviewed in detail to demonstrate its usefulness in predicting the effect of cell design on the performance and thermal behavior of a battery with case studies of a lead–acid battery and a lithium-ion polymer battery.

Performance Modeling

Analytical Model

Peukert's equation states that the discharge current of a battery decreases with increasing 'constant current' discharge time, and it is expressed as follows:

$$I^n t = \text{constant} \qquad [1]$$

where I is the discharge current, t is the maximum discharge time, and n is the 'Peukert coefficient' unique to a battery of a certain make and model. A Peukert coefficient of $n = 1$, for example, means that the accessible total capacity of that battery does not depend on the discharge rate, which is not true for real batteries, which usually have a Peukert coefficient >1. More sophisticated

analytical models can accommodate the effects of variable current load, temperature, and additional operating parameters on the battery capacity and lifetime.

Electrical Model

There have been many electrical models for batteries. One of these is the Thevenin equivalent circuit model. It contains an open-circuit voltage source in series with a resistor (internal resistance) and a parallel combination of a capacitor and resistor (overvoltage model). This model is not very accurate, because the values of its elements are not constants but functions of various battery conditions such as state of charge (SoC), rate of charge/discharge, and temperature. An improvement upon the Thevenin model is a linear electrical model. It uses series and parallel networks of resistors and capacitors to account for self-discharge and various overvoltages. A nonlinear electrical model is a modification of the linear electrical model. This model incorporates the nonlinear elements, which are the functions of the SoC and temperature, to represent the nonlinear dependence of the battery performance on the battery conditions.

Electrochemical Model

Electrochemical models can be used to predict battery performance under various conditions of charge and discharge. A two-dimensional modeling of a 12-V automotive lead–acid battery is shown to demonstrate the capabilities of the electrochemical model. A schematic representation of the lead–acid cell is shown in Figure 1. The cell is composed of a current-collecting grid at the center of the negative electrode, a negative lead electrode, a reservoir of electrolyte, a porous separator, a positive lead oxide electrode, and a current-collecting grid at the center of the positive electrode. In this work, the model considers the variations of the electrical potentials of the solid matrix of electrodes and the electrolyte, the acid concentration, the electrochemical kinetics, the SoC of electrodes, and the electrode porosity. The governing equations expressing the above phenomena are listed below:

Conservation of charge in the solid phase of electrode:

$$\nabla \cdot \left(\sigma^{\text{eff}} \nabla \phi_s\right) - Aj = 0 \qquad [2]$$

Conservation of charge in the liquid phase of electrode:

$$\nabla \cdot \left(\kappa^{\text{eff}} \nabla \phi_l\right) + \nabla \cdot \left[\kappa_D^{\text{eff}} \nabla (\ln c)\right] + Aj = 0 \qquad [3]$$

Ionic species conservation:

$$\frac{\partial(\varepsilon c)}{\partial t} = \nabla \cdot \left(D^{\text{eff}} \nabla c\right) + a_2 \frac{Aj}{2F} \qquad [4]$$

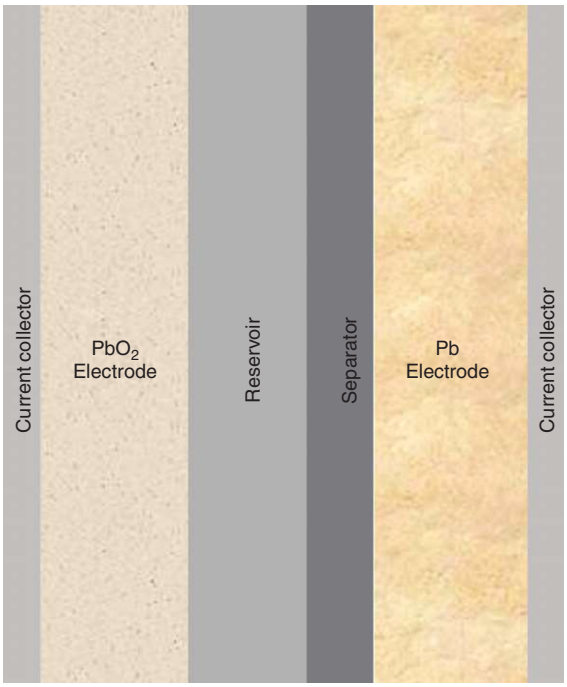

Figure 1 Schematic illustration of a lead–acid cell.

Butler–Volmer equation for an electrochemical reaction:

$$j = i_0 \left(\frac{c}{c_{\text{ref}}}\right) \left[\exp\left(\frac{\alpha_a F}{RT}\eta\right) - \exp\left(-\frac{\alpha_c F}{RT}\eta\right)\right] \qquad [5]$$

Variation of SoC:

$$\frac{\partial(\text{SoC})}{\partial t} = \pm \frac{\nabla \cdot i_l}{Q_{\text{MAX}}} \qquad [6]$$

Variation of porosity:

$$\frac{\partial \varepsilon}{\partial t} - a_1 \frac{Aj}{2F} = 0 \qquad [7]$$

where ϕ_s is the potential of solid phase, ϕ_l is the potential of liquid phase, σ^{eff} is the effective conductivity of the solid matrix, A is the specific electroactive area, j is the transfer current density, κ^{eff} is the effective conductivity of the liquid phase, κ_D^{eff} is the effective conductivity of the liquid phase owing to diffusion, c is the acid concentration, ε is the porosity, t is the time, D^{eff} is the effective diffusivity, a_2 is the coefficient accounting for volumetric ion production or consumption, F is Faraday's constant, i_0 is the exchange current density, c_{ref} is the reference concentration, α_a is the anodic transfer coefficient, α_c is the cathodic transfer coefficient, R is the universal gas constant, T is the absolute temperature, η is the electrode overpotential, SoC is the state of charge of electrodes, Q_{MAX} is the theoretical electrode capacity, and a_1 is the volumetric change per mole of the material converted.

The solutions of the governing equations were obtained by using the finite element method. In order to validate the modeling, the modeling results were compared with the measurement data of the charge–discharge behaviors of lead–acid batteries having nominal capacities of 90 and 68 Ah and which were mounted on the automobiles manufactured by Hyundai Motor Company. **Figure 2** shows the comparison between experimental and modeling discharge curves of a battery having a nominal capacity of 90 Ah with various discharge rates of $C/3$, $C/5$, $C/10$, and $C/20$ at a temperature of 25 °C. **Figure 3** shows the comparison between experimental and modeling charge curves of a battery having a nominal capacity of 68 Ah at a temperature of 25 °C. The battery was charged with a constant current of 30 A for 1 h and then with a constant voltage of 14.24 V. The discharge and charge curves from the experiments and modeling are in good agreement. **Figure 4** shows the distribution of the concentration of sulfuric acid within the cell of a battery having a nominal capacity of 90 Ah after 1, 4, and 8 h of discharge at rate $C/10$ and at a temperature of 25 °C. Based on the modeling, the distributions of the electrical potentials of the solid and liquid phases, the porosity of the electrodes, and the current density within the electrodes as well as the acid concentration can be predicted as a function of charge and discharge time. **Figure 5** shows the voltage profiles obtained from experiment and modeling during complex cycling protocols for a battery having a nominal capacity of 68 Ah. The profile not only contains discharge steps, but also has charging steps. It is illustrated that the modeling can reproduce well the abrupt changes of the measured voltage profile.

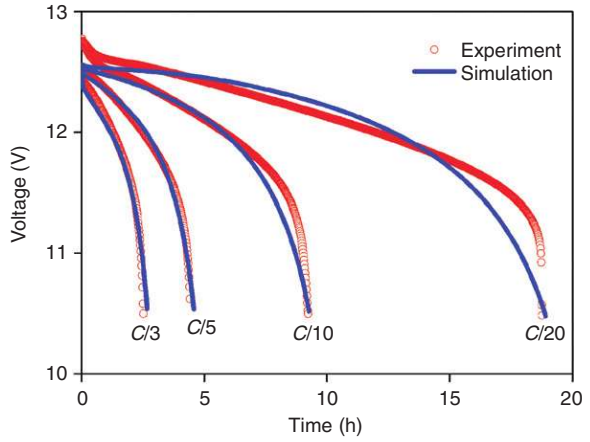

Figure 2 Comparison between experimental and modeling discharge curves at discharge rates of $C/3$, $C/5$, $C/10$, and $C/20$.

Another example to demonstrate the capabilities of the electrochemical model is given. It is the modeling of a 10 Ah lithium-ion polymer battery comprising a lithium nickel cobalt manganese oxide positive electrode, a graphite negative electrode, and a plasticized electrolyte from VK Corporation. Because the battery consists of the same repeating units of positive and negative electrode plates, polymer electrolytes, and separators, a cell composed of two parallel plate electrodes of the battery shown in **Figure 6** was chosen for modeling. In **Figure 6**, the current-collecting tabs are the current collectors extending outside from the rectangular electrodes, and they do not contain the electrode (active) material. A schematic representation of the current flow in the cell during discharge is illustrated in **Figure 6**. The distance

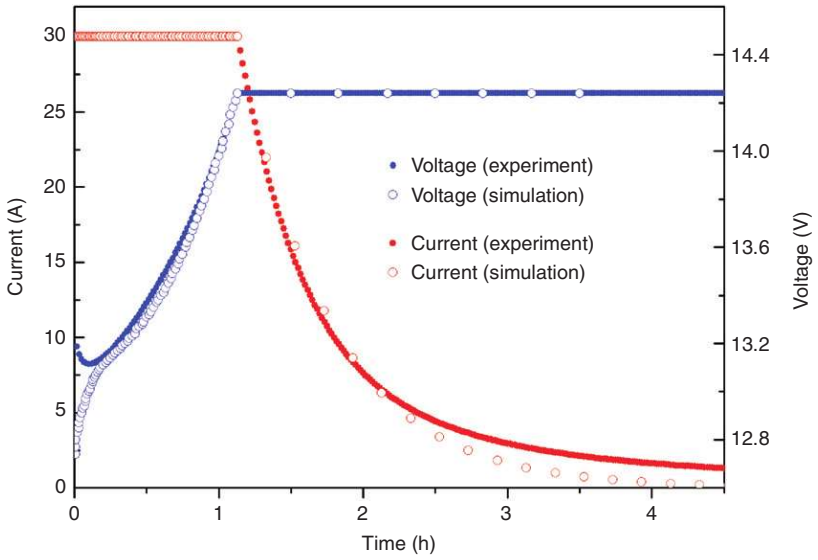

Figure 3 Comparison between experimental and modeling charge curves. The battery was charged with a constant current of 30 A for 1 h and then with a constant voltage of 14.24 V.

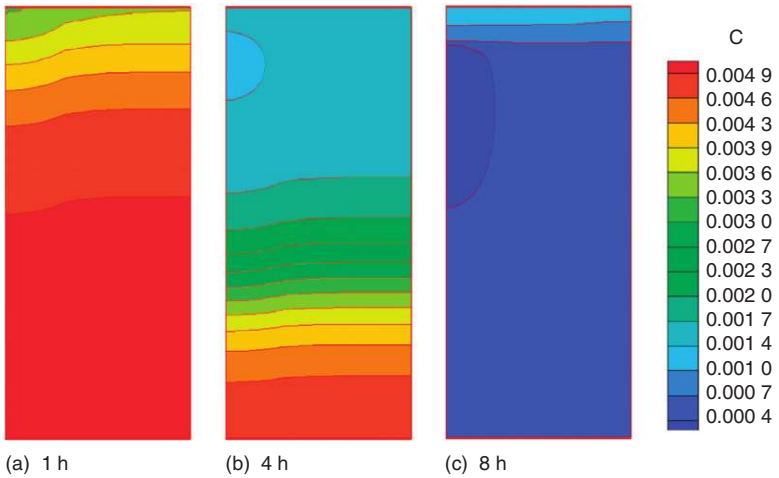

Figure 4 The distribution of the concentration of sulfuric acid within the cell after 1, 4, and 8 h of discharge with *C*/10 rate.

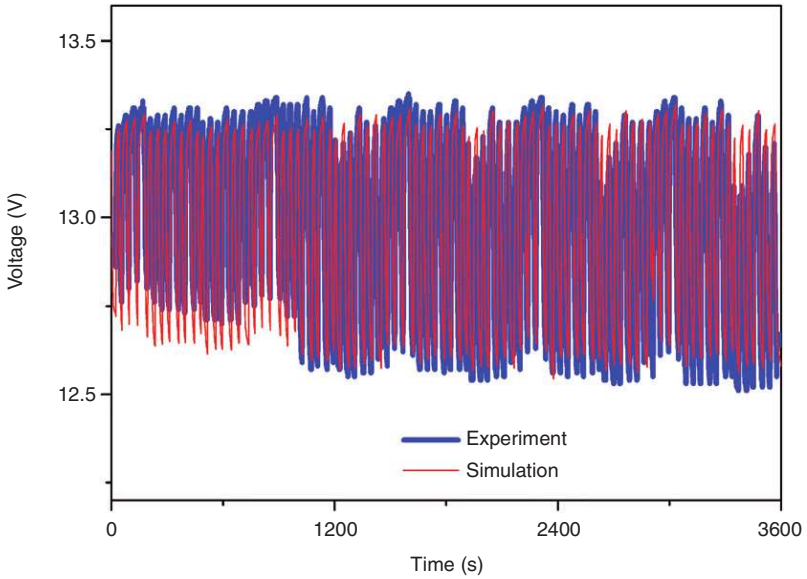

Figure 5 Comparison between the voltage profiles obtained from experiment and modeling during complex cycling protocols.

between the electrodes is assumed to be so small that the current flow between the electrodes is perpendicular to the electrodes. From the continuity of current on the electrodes, the following equations can be derived

$$\nabla \cdot \vec{i}_{\mathrm{p}} - \mathcal{J} = 0 \ \text{ in } \ \Omega_{\mathrm{p}} \qquad [8]$$

$$\nabla \cdot \vec{i}_{\mathrm{n}} + \mathcal{J} = 0 \ \text{ in } \ \Omega_{\mathrm{n}} \qquad [9]$$

where $\vec{i}_{\mathrm{p}}$ and $\vec{i}_{\mathrm{n}}$ are the linear current density vectors (current per unit length $(\mathrm{A\,m^{-1}})$) in the positive and negative electrodes, respectively, and $\mathcal{J}$ is the current density (current per unit area $(\mathrm{A\,m^{-2}})$) transferred through the separator from the negative electrode to the positive electrode. Ω_{p} and Ω_{n} denote the domains of the positive and negative electrodes, respectively. By Ohm's law, $\vec{i}_{\mathrm{p}}$ and $\vec{i}_{\mathrm{n}}$ can be written as

$$\vec{i}_{\mathrm{p}} = -\frac{1}{r_{\mathrm{p}}}\nabla V_{\mathrm{p}} \ \text{ in } \ \Omega_{\mathrm{p}} \qquad [10]$$

$$\vec{i}_{\mathrm{n}} = -\frac{1}{r_{\mathrm{n}}}\nabla V_{\mathrm{n}} \ \text{ in } \ \Omega_{\mathrm{n}} \qquad [11]$$

where r_{p} and r_{n} are the resistances (Ω) of the positive and negative electrodes, respectively, and V_{p} and V_{n} are the potentials (V) of the positive and negative electrodes, respectively. By substituting eqns [10] and [11] into eqns [8] and [9], the following Poisson equations for V_{p} and V_{n} are obtained:

$$\nabla^2 V_{\mathrm{p}} = -r_{\mathrm{p}}\mathcal{J} \ \text{ in } \ \Omega_{\mathrm{p}} \qquad [12]$$

$$\nabla^2 V_n = +r_n \mathcal{J} \text{ in } \Omega_n \quad [13]$$

The resistance, r (r_p or r_n), is calculated as follows:

$$r = \frac{1}{h_c S_c + h_e S_e} \quad [14]$$

where h_c and h_e are the thicknesses (m) of the current collector and the electrode material, respectively, and S_c and S_e are the electrical conductivities ($S\,m^{-1}$) of the current collector and the electrode material, respectively.

The current density, $\mathcal{J}$, of eqns [12] and [13] is a function of the potential difference between the positive and negative electrodes ($V_p - V_n$). The functional form depends on the polarization characteristics of the electrodes. In this study, the following polarization expression was adopted:

$$\mathcal{J} = Y(V_p - V_n - U) \quad [15]$$

where Y and U are the fitting parameters. U and Y were expressed as the functions of depth of discharge (DoD) as follows:

$$U = a_0 + a_1(\text{DoD}) + a_2(\text{DoD})^2 + a_3(\text{DoD})^3 \quad [16]$$

$$Y = a_4 + a_5(\text{DoD}) + a_6(\text{DoD})^2 \quad [17]$$

where a_0–a_6 are the constants to be determined by experiments.

By solving the equations mentioned earlier, the distribution of the current density, $\mathcal{J}$, on the electrodes can be obtained as a function of the position on the electrode and the time. Therefore, DoD varies along with the position on the electrode and the time elapsed during discharge. The distribution of DoD on the electrode can be calculated from the distribution of $\mathcal{J}$ as

$$\text{DoD} = \frac{\int_0^t \mathcal{J}\, dt}{Q_T} \quad [18]$$

where t is the discharge time (s) and Q_T is the theoretical capacity per unit area ($Ah\,m^{-2}$) of the electrodes.

The solutions to the governing equations [12] and [13] subject to the associated boundary conditions were

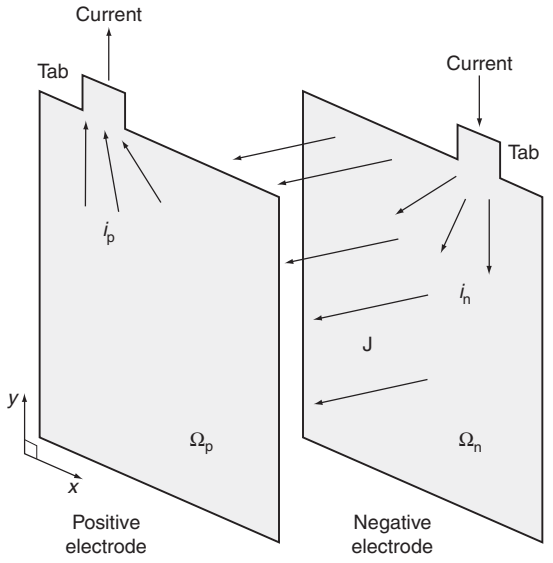

Figure 6 Schematic diagram of the current flow in the parallel plate electrodes of a battery. Reproduced with permission from Kim US, Shin CB, and Kim C-S (2008) Effect of electrode configuration on the thermal behaviour of a lithium-polymer battery. *Journal of Power Sources* 180: 909–916.

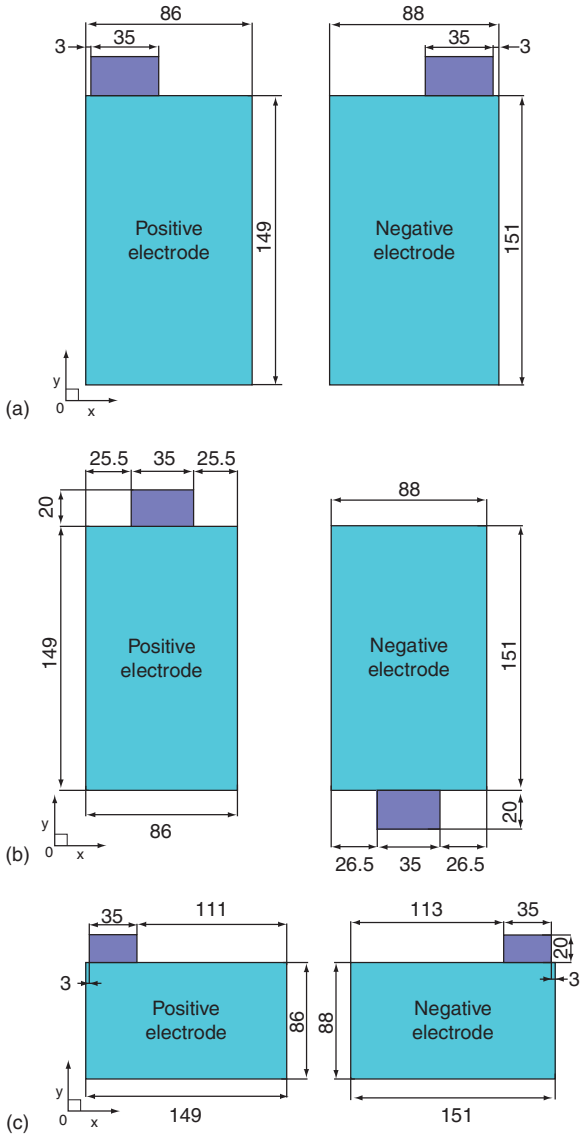

Figure 7 Schematic diagrams of the electrode shapes for (a) type A, (b) type B, and (c) type C. Reproduced with permission from Kim US, Shin CB, and Kim C-S (2008) Effect of electrode configuration on the thermal behaviour of a lithium-polymer battery. *Journal of Power Sources* 180: 909–916.

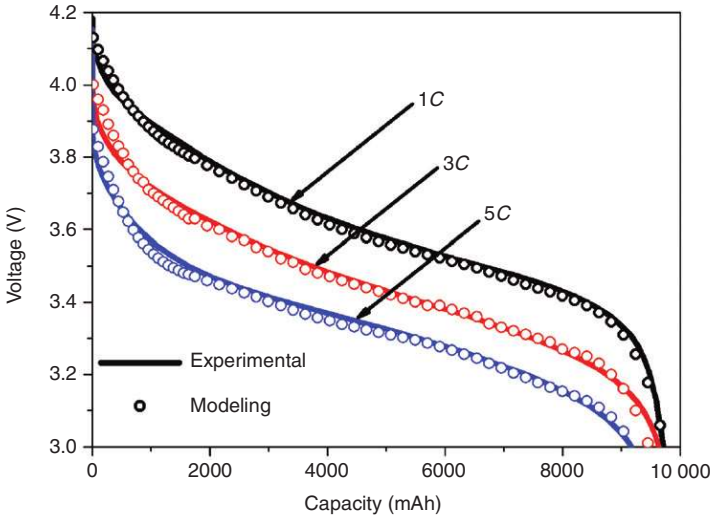

Figure 8 Comparison between experimental and modeling discharge curves for a battery with electrodes of type A at discharge rates of 1 *C*, 3 *C*, and 5 *C*. The solid lines represent experimental data and the open circles represent modeling results based on the finite element method. Reproduced with permission from Kim US, Shin CB, and Kim C-S (2008) Effect of electrode configuration on the thermal behaviour of a lithium-polymer battery. *Journal of Power Sources* 180: 909–916.

obtained by using the finite element method. Although numerical simulations were performed for electrodes of many different shapes of a lithium-ion polymer battery, the results for electrodes of three different shapes are shown because three seems to be enough to demonstrate the salient features of the modeling presented in this article. The electrodes of three different shapes are referred to as electrodes of types A, B, and C. The schematic diagrams of the electrode shapes for types A, B, and C are illustrated in **Figures 7(a), 7(b), and 7(c)**, respectively. In order to test the validity of the modeling, the calculated discharge curves based on the modeling of the 10 Ah battery fabricated by VK Corporation with electrodes of type A shown in **Figure 7(a)** are compared with the experimental data in **Figure 8**. The experiments were performed at room temperature. At various discharge rates from 1 *C* to 5 *C*, the experimental discharge curves are in good agreement with the modeling results based on the finite element method.

The distributions of the potential and current density on the electrodes during discharge are obtained as a function of time for various discharge rates. As an example, the distributions of the potential on the positive electrode, the potential on the negative electrode, and the current density for a battery with electrodes of type A at a discharge time of 30 min with 1 *C* rate are shown in **Figures 9(a), 9(b), and 9(c)**, respectively. In **Figure 9(a)**, the potential gradient on the positive electrode is seen to be most severe in the region where the tab is attached to the current collector. This is because all the current flows through the conducting current collector into the tab from the entire electrode plate. Again, the potential gradient on the negative electrode shown in **Figure 9(b)** is the highest at the region near the tab, because all the current has to flow from the tab through the entire electrode plate. **Figure 9(c)** shows the nonuniform distributions of current density transferred from the negative electrode to the positive electrode of type A during the discharge with 1 *C* rate.

Thermal Modeling

Because the primary challenge in designing lithium-ion polymer batteries is safety, thermal stability problems must be overcome. The main concern with the thermal behavior of lithium-ion polymer battery is the possible significant temperature increase during high power extraction, which may lead to degradation of the battery and thermal runaway. Thermal modeling can play a vital role in maintaining the operating temperature and temperature uniformity of lithium-ion polymer battery within a suitable range.

Based on the differential energy conservation for a battery, the transient two-dimensional equation of heat conduction can be written as follows

$$\rho C_p \frac{\partial T}{\partial t} = \frac{\partial}{\partial x}\left(k_x \frac{\partial T}{\partial x}\right) + \frac{\partial}{\partial x}\left(k_y \frac{\partial T}{\partial y}\right) + q - q_{\text{conv}} \qquad [19]$$

where ρ is the density (kg m^{-3}), C_p is the volume-averaged specific heat capacity at constant pressure ($\text{J kg}^{-1}\,^{\circ}\text{C}^{-1}$), T is the temperature (°C), k_x and k_y are the effective thermal conductivities along the x and y directions (see **Figure 6** for x and y directions) ($\text{W m}^{-1}\,^{\circ}\text{C}^{-1}$), respectively, q is the heat generation rate

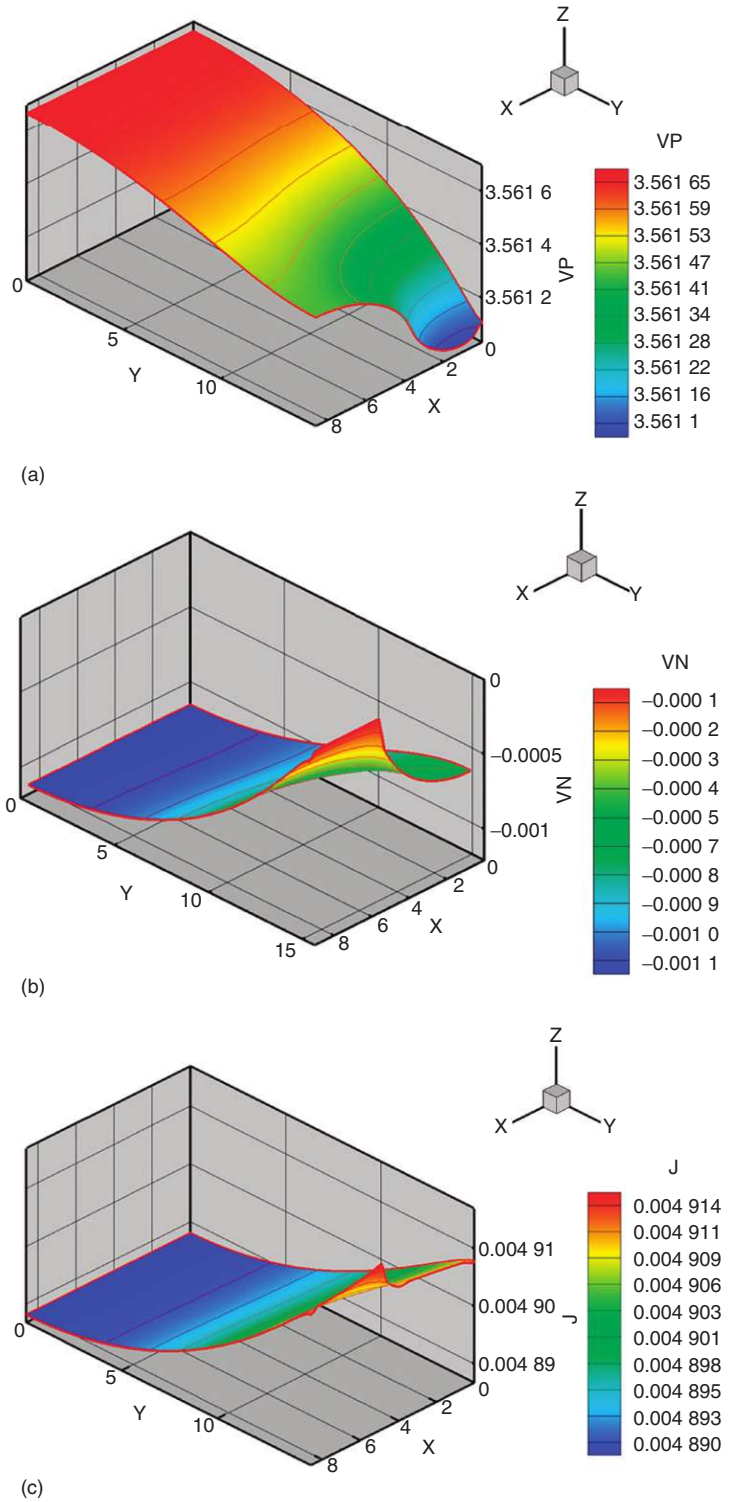

Figure 9 Distributions of (a) the potential on the positive electrode, (b) the potential on the negative electrode, and (c) the current density on electrodes of type A at a discharge time of 30 min with 1 *C* rate. Reproduced with permission from Kim US, Shin CB, and Kim C-S (2008) Effect of electrode configuration on the thermal behaviour of a lithium-polymer battery. *Journal of Power Sources* 180: 909–916.

per unit volume ($\mathrm{W\,m^{-3}}$), and q_{conv} is the heat dissipation rate ($\mathrm{W\,m^{-3}}$) through the surfaces of the battery by convection. Effective thermal conductivities of various compartments of the cell can be estimated based on the equivalent networks of parallel and series thermal resistances of cell components.

The heat generation rate, q, is given as

$$q = a\mathcal{J}\left[E_{oc} - E - T\frac{dE_{oc}}{dT}\right] + a_p r_p i_p^2 + a_n r_n i_n^2 \qquad [20]$$

where a is the specific area of the battery ($\mathrm{m^{-1}}$), $\mathcal{J}$ is the current density ($\mathrm{A\,m^{-2}}$) calculated by eqn [15], E_{oc} is the open-circuit potential of the cell (V), E is the cell voltage (V), a_p and a_n are the specific area of the positive and negative electrodes ($\mathrm{m^{-1}}$), respectively, and i_p and i_n are the magnitudes of the vectors $\vec{i}_p$ and $\vec{i}_n$ obtained from eqns [10] and [11] ($\mathrm{A\,m^{-1}}$), respectively. The first term on the right-hand side of eqn [20] is the heat generated owing to charge transfer at the electrode/electrolyte interfaces. This involves an irreversible part, representing the energy loss by the deviation of the cell potential from the open-circuit potential owing to electrochemical polarization, and a reversible part, representing the heat proportional to dE_{oc}/dT owing to entropy change. The third and fourth terms arise from ohmic heating in the positive and negative electrodes, respectively. The heat dissipation rate, q_{conv}, is derived as

$$q_{conv} = \frac{2h}{d}(T - T_{air}) \qquad [21]$$

where h is the convective heat transfer coefficient on the surfaces of the battery ($\mathrm{W\,m^{-2}\,{}^{\circ}C^{-1}}$), d is the thickness of the battery in the direction perpendicular to the parallel electrodes (m), and T_{air} is the ambient temperature (°C). This term is rendered as in eqn [21] by the approximation of a three-dimensional object into a two-dimensional object. Convective boundary condition applied on the boundaries of the electrode is written as

$$-k\frac{\partial T}{\partial n} = h_e(T - T_{air}) \qquad [22]$$

where $\partial/\partial n$ denotes the gradient in the direction of the outward normal to the boundary and h_e is the effective convective heat transfer coefficient on the edge of the battery, which is modified to accommodate the effect of the aluminum pouch enveloping the edge of the electrodes.

After obtaining the distributions of the potential and current density on the electrodes during discharge, the temperature distributions of the battery can be calculated as a function of time for various discharge rates by using eqn [19]. As a demonstration, the temperature distributions based on the experimental infrared (IR) image and the modeling after the discharge of 10.8 min with 5 *C* rate are shown in **Figure 10**. The overall appearances of

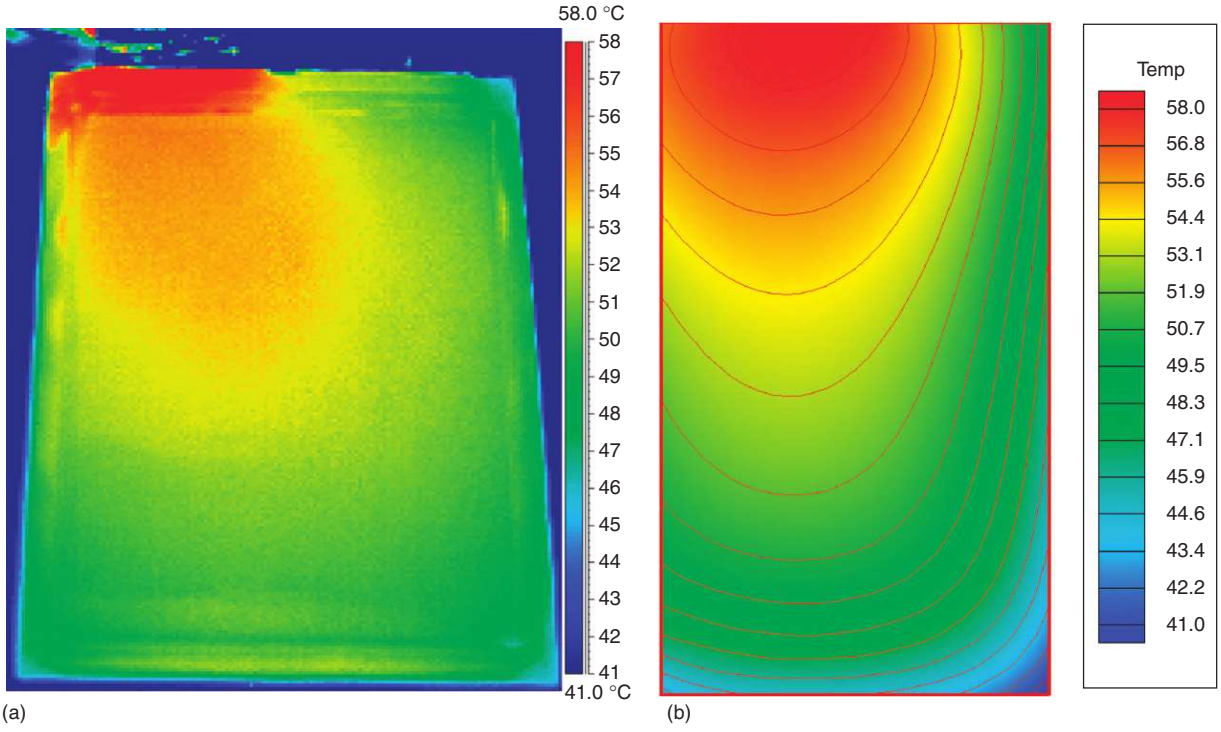

Figure 10 Temperature distributions based on (a) the experimental IR image and (b) the modeling for a battery with electrodes of type A at a discharge time of 10.8 min with 5 *C* rate. Reproduced with permission from Kim US, Shin CB, and Kim C-S (2008) Effect of electrode configuration on the thermal behaviour of a lithium-polymer battery. *Journal of Power Sources* 180: 909–916.

the temperature distributions from the experiment and modeling are in good agreement. It is observed that the temperature near the current-collecting tab of the positive electrode is higher than that of the negative electrode. This phenomenon is due to the fact that the electrical conductivity of the active material of the positive electrode is much lower than that of the negative electrode, although both the current flows near the tabs of the positive and negative electrodes are similarly high. The maximum temperatures from the experiment and modeling are close to each other near the value of 58 °C, although the minimum temperature from the experiment is a bit higher than that from the modeling.

In **Figure 11**, the temperature distributions based on the experimental IR image and the modeling after the discharge of 10.8 min with 5 *C* rate are shown for a battery with electrodes of type B. The overall appearances of the temperature distributions from the experiment and modeling for electrodes of type B are in good agreement. As in the case of electrodes of type A, it is observed that the temperature near the current-collecting tab of the positive electrode is higher than that of the negative electrode, because the electrical conductivity of the active material of the positive electrode is much lower than that of the negative electrode. The maximum temperatures (~56 °C) from the experiment and modeling are close to each other and the minimum temperatures (~43 °C) from the experiment and modeling are close to each other. For a battery with electrodes of type C, the temperature distributions based on the experimental IR image and the modeling after the discharge of 10.0 min with 5 *C* rate are shown in **Figure 12**. The overall appearances of the temperature distributions from the experiment and modeling for electrodes of type C are in good agreement. The maximum temperatures (454 °C) from the experiment and modeling are close to each other, although the minimum temperature from the experiment is a bit higher than that from the modeling as for the case of electrodes of type A. In **Table 1**, the maximum and minimum temperatures from the experimental measurement for a battery with electrodes of types A, B, and C are compared with those predicted by the modeling for a discharge rate of 5 *C*, because the discrepancy between the temperatures from the experiment and modeling would be the highest. The maximum temperatures from the experiment and modeling are in good agreement for the whole range of DoD, but there are some discrepancies between the minimum temperatures from the experiment and modeling for DoD values higher than 0.5 for batteries with different types of

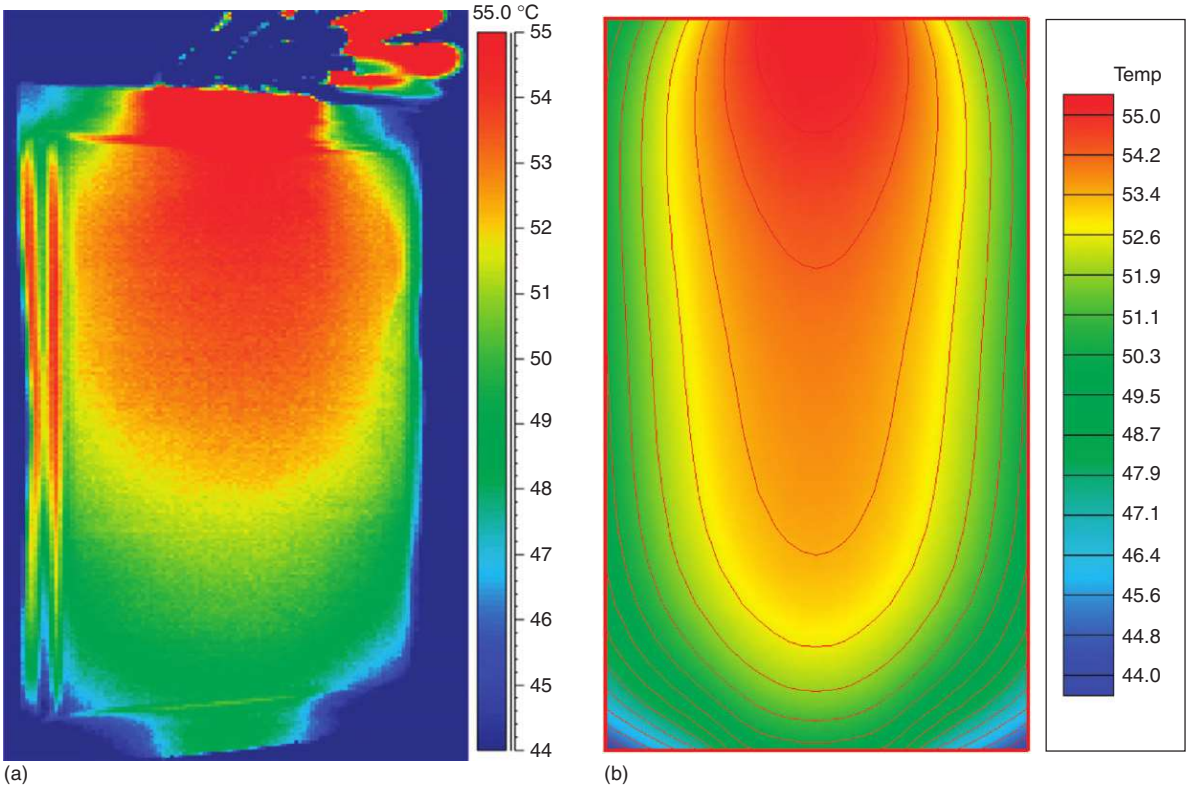

Figure 11 Temperature distributions based on (a) the experimental IR image and (b) the modeling for a battery with electrodes of type B at a discharge time of 10.8 min with 5 *C* rate. Reproduced with permission from Kim US, Shin CB, and Kim C-S (2008) Effect of electrode configuration on the thermal behaviour of a lithium-polymer battery. *Journal of Power Sources* 180: 909–916.

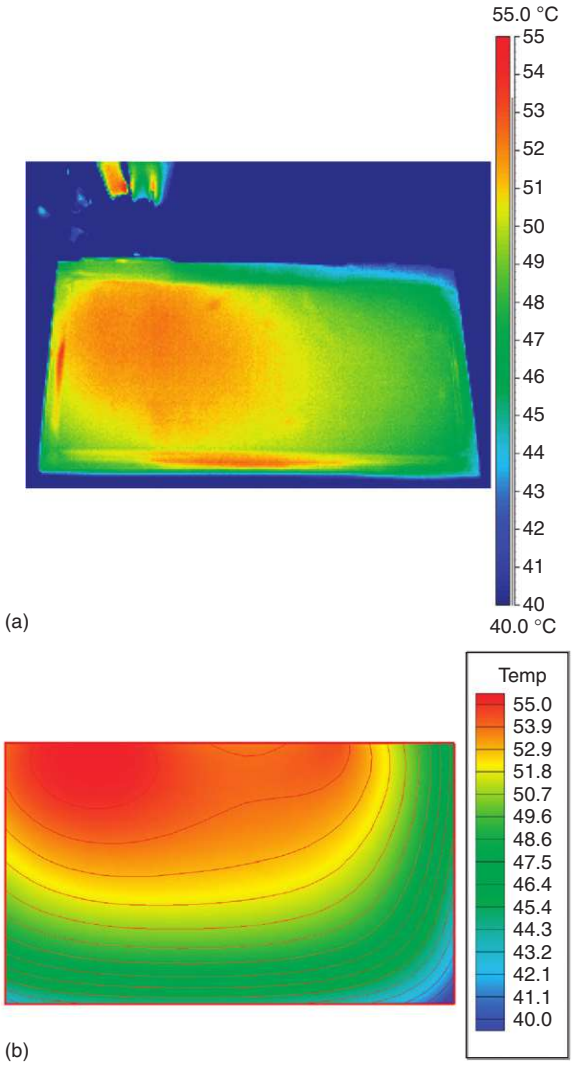

Figure 12 Temperature distributions based on (a) the experimental IR image and (b) the modeling for a battery with electrodes of type C at a discharge time of 10.0 min with 5 *C* rate. Reproduced with permission from Kim US, Shin CB, and Kim C-S (2008) Effect of electrode configuration on the thermal behaviour of a lithium-polymer battery. *Journal of Power Sources* 180: 909–916.

electrodes. If the electrodes of types A, B, and C are evaluated in terms of the lower maximum temperature during discharge, the electrode of type B, which has the current-collecting tabs on the middle of the opposite sides of the rectangular electrode, is more preferable than of types A and C, which have the current-collecting tabs at the ends of the same side of the rectangular electrode.

Concluding Remarks

The analytical and electrical models are briefly reviewed. The capability of the electrochemical model is demonstrated to predict the effect of cell design on the performance and thermal behavior of a battery. The modeling results are given for a lead–acid battery and a lithium-ion polymer battery.

For the case of a lead–acid battery, a two-dimensional modeling was carried out to predict the dynamic behaviors of a 12-V automotive lead–acid battery. The model accounted for electrochemical kinetics and ionic mass transfer in a battery cell. In order to validate the modeling, the modeling results were compared with the measurement data of the dynamic behaviors of the lead–acid batteries. The modeling results agree well with the measurement data.

For the case of a lithium-ion polymer battery, the two-dimensional potential and current density distribution on the electrodes of a lithium-ion polymer battery were predicted as a function of discharge time. Modeling was carried out for electrodes of three different geometries to check the effect of the aspect ratio of the electrodes and the placing of current-collecting tabs on the discharge behaviors of the battery. By comparing the experimental discharge curves with the modeling results at the discharge rates of 1 *C*, 3 *C*, and 5 *C*, it was confirmed that the parameters tuned for electrodes of one geometry can be applied for electrodes of other geometries as long as the materials and compositions of the electrodes and the manufacturing processes are the

Table 1 Maximum and minimum temperatures from the experiment and modeling for a discharge rate of 5*C*

Model	*DoD (%)*	*Minimum temperature (°C)*		*Maximum temperature (°C)*	
		Experimental	*Modeling*	*Experimental*	*Modeling*
Type A	30	34.4	33.5	44.5	44.5
	50	39.0	37.7	50.4	50.0
	90	47.0	40.0	57.8	58.7
Type B	30	32.9	35.3	43.7	41.9
	50	36.3	38.3	48.9	47.7
	90	42.8	43.7	57.0	55.6
Type C	30	35.7	33.6	43.0	43.1
	50	40.5	38.2	48.1	48.9
	83	45.4	38.9	53.7	55

DoD, depth of discharge.
Reproduced with permission from Kim US, Shin CB, and Kim C-S (2008) Effect of electrode configuration on the thermal behaviour of a lithium-polymer battery. *Journal of Power Sources* 180: 909–916.

same. Then, based on the results of the modeling of potential and current density distributions, the heat generation rate as a function of discharge time and the position on the electrodes was calculated to predict the thermal behavior of lithium-ion polymer battery. The two-dimensional temperature distributions from the experiment and modeling are in good agreement for batteries with three different types of electrodes.

Nomenclature

Symbols and Units

a	specific surface area of electrode (m^{-1})
a_1	volumetric change per mole of the material converted (m^3 mol^{-1})
a_2	coefficient accounting for volumetric ion production or consumption
a_n	specific area of negative electrode (m^{-1})
a_p	specific area of positive electrode (m^{-1})
A	specific electroactive area
c	acid concentration (mol m^{-3})
C_p	specific heat capacity at constant pressure (J kg^{-1} °C^{-1})
c_{ref}	reference concentration
d	thickness of the electrode (m)
D^{eff}	effective diffusivity (m^2 s^{-1})
E	cell voltage (V)
E_{oc}	open-circuit potential of the cell (V)
F	Faraday constant (96 485 °C mol^{-1})
h	convective heat transfer coefficient (W m^{-2} °C^{-1})
h_c	thickness of the current collector
h_e	thickness of the electrode material
H	convective heat transfer coefficient (Wm^{-2} °C^{-1})
i_0	exchange current density (A m^{-2})
$\vec{i}_n$	current density vector in the negative electrode
$\vec{i}_p$	current density vector in the positive electrode
I	discharge current (A)
$\mathscr{J}\|_.$	transfer current density (A m^{-3})
k	thermal conductivity (W m^{-1} °C^{-1})
k_x	effective thermal conductivity along the x direction (W m^{-1} °C^{-1})
k_y	effective thermal conductivity along the x direction (W m^{-1} °C^{-1})
n	Peukert coefficient
q	heat generation rate per unit volume (W m^{-3})
q_{conv}	heat dissipation rate (W m^{-3})
Q_{MAX}	theoretical electrode capacity
Q^T	theoretical electrode capacity per unit area (Ah m^{-2})
r	resistance(Ω)
r_n	resistance of negative electrode
r_p	resistance of positive electrode
R	universal gas constant (8.3145 J $mol^{-1}K^{-1}$)
S_c	conductivity of the current collector
S_e	conductivity of the electrode material
t	time (s)
T	absolute temperature (K)
T_{air}	ambient temperature (°C)
V_n	potential of negative electrode
V_p	potential of positive electrode
Y, U	fitting parameters
a_a	anodic transfer coefficient
a_c	cathodic transfer coefficient
ε	porosity
η	electrode overpotential (V)
k^{eff}	effective conductivity of the liquid phase (S m^{-1})
$k_D^{eff}\|_.$	effective conductivity of the liquid phase due to diffusion (S m^{-1})
Ω_p	domain of positive electrode
Ω_n	domain of negative electrode
ϕ_s	potential of the solid phase (V)
ϕ_l	potential of the liquid phase (V)
ρ	density (kg m^{-3})
σ^{eff}	effective conductivity of the solid matrix (S m^{-1})

Abbreviations and Acronyms

DoD	depth of discharge
IR	infrared
SoC	state of charge

See also: **Secondary Batteries – Lead–Acid Systems:** Modeling; **Secondary Batteries – Lithium Rechargeable Systems – Lithium-Ion:** Lithium-Ion Polymer Batteries.Overview.

Further Reading

Al-Hallaj S and Selman JR (2002) Thermal modeling of secondary lithium batteries for electric vehicle/hybrid electric vehicle applications. *Journal of Power Sources* 110: 341–348.

Arora P, Doyle M, Gozdz AS, White RE, and Newman J (2000) Comparison between computer simulations and experimental data for high-rate discharges of plastic lithium-ion batteries. *Journal of Power Sources* 88: 219–231.

Baker DR and Verbrugge MW (1999) Temperature and current distribution in thin-film batteries. *Journal of the Electrochemical Society* 146: 2413–2424.

Bernardi DM, Gu H, and Schoene AY (1993) Two-dimensional mathematical model of a lead–acid cell. *Journal of the Electrochemical Society* 140: 2250–2258.

Buller S, Thele M, Karen E, and De Doncker RW (2003) Impedance-based non-linear modeling for automotive applications. *Journal of Power Sources* 113: 422–430.

Cedar G, Doyle M, Arora P, and Fuentes Y (2002) Computational modeling and simulation for rechargeable batteries. *MRS Bulletin* 27: 619–623.

Chen SC, Wan CC, and Wang YY (2005) Thermal analysis of lithium-ion batteries. *Journal of Power Sources* 140: 111–124.

Chen Y and Evans JW (1994a) Thermal analysis of lithium polymer electrolyte batteries by a two dimensional model – thermal behaviour and design optimization. *Electrochimica Acta* 39: 517–526.

Chen Y and Evans JW (1994b) Three-dimensional thermal modeling of lithium-polymer batteries under galvanostatic discharge and dynamic power profile. *Journal of the Electrochemical Society* 141: 2947–2955.

Chen Y and Evans JW (1996) Thermal analysis of lithium-ion batteries. *Journal of the Electrochemical Society* 143: 2708–2712.

Dees DW, Battaglia VS, and Bélanger A (2002) Electrochemical modeling of lithium polymer batteries. *Journal of Power Sources* 110: 310–320.

Doerffel D and Sharkh SA (2006) A critical review of using the Peukert equation for determining the remaining capacity of lead–acid and lithium-ion batteries. *Journal of Power Sources* 155: 395–400.

Doyle M, Newman J, Gozdz AS, Schmutz CN, and Tarascon J-M (1996) Comparison of modeling predictions with experimental data from plastic lithium ion cells. *Journal of Electrochemical Society* 143: 1890–1903.

Dubarry M and Liaw BY (2007) Development of a universal modeling tool for rechargeable lithium battery. *Journal of Power Sources* 174: 856–860.

Gomadam PM, Weidner JW, Dougal RA, and White RE (2002) Mathematical modeling of lithium-ion and nickel battery systems. *Journal of Power Sources* 110: 267–284.

Gu H (1983) Mathematical analysis of a Zn/NiOOH cell. *Journal of the Electrochemical Society* 130: 1459–1464.

Gu H, Nguyen TV, and White RE (1987) A mathematical model of a lead–acid cell. *Journal of the Electrochemical Society* 134: 2953–2960.

Gu WB, Wang CY, and Liaw BY (1997) Numerical modeling of coupled electrochemical and transport processes in lead–acid batteries. *Journal of the Electrochemical Society* 144: 2053–2061.

Kim US, Shin CB, and Kim C-S (2008) Effect of electrode configuration on the thermal behavior of a lithium-polymer battery. *Journal of Power Sources* 180: 909–916.

Kwon KH, Shin CB, Kang TH, and Kim C-S (2006) A two-dimensional modeling of a lithium-polymer battery. *Journal of Power Sources* 163: 151–157.

Newman J and Tiedemann W (1993) Potential and current distribution in electrochemical cells. *Journal of the Electrochemical Society* 140: 1961–1968.

Newman J, Thomas KE, Hafezi H, and Wheeler DR (2003) Modeling of lithium-ion batteries. *Journal of Power Sources* 119–121: 838–843.

Ning G and Popov BN (2004) Cycle life modeling of lithium-ion batteries. *Journal of the Electrochemical Society* 151: A1584–A1591.

Ning G, White RE, and Popov BN (2006) A generalized cycle life model of rechargeable Li-ion batteries. *Electrochimica Acta* 51: 2012–2022.

Pals CR and Newman J (1995a) Thermal modeling of the lithium/polymer battery. I. Discharge behavior of a single cell. *Journal of the Electrochemical Society* 142: 3274–3281.

Pals CR and Newman J (1995b) Thermal modeling of the lithium/polymer battery. II. Temperature profiles in a cell stack. *Journal of the Electrochemical Society* 142: 3282–3288.

Salameh ZM, Casacca MA, and Lynch WA (1992) A mathematical model of lead–acid batteries. *IEEE Transactions on Energy Conversion* 7: 93–98.

Sikha G, Popov BN, and White RE (2004) Effect of porosity on the capacity fade of a lithium-ion battery. *Journal of the Electrochemical Society* 151: A1104–A1114.

Smith K and Wang C-Y (2006) Power and thermal characterization of a lithium-ion battery pack for hybrid-electric vehicles. *Journal of Power Sources* 160: 662–673.

Song L and Evans JW (1998) The thermal stability of lithium-polymer batteries. *Journal of the Electrochemical Society* 145: 2327–2334.

Song L and Evans JW (2000) Electrochemical–thermal model of lithium polymer batteries. *Journal of the Electrochemical Society* 147: 2086–2095.

Spotnitz RM (2005) Battery modeling. *Interface* 14: 39–42.

Srinivasan V and Wang CY (2003) Analysis of electrochemical and thermal behavior of Li-ion cells. *Journal of the Electrochemical Society* 150: A98–A106.

Verbrugge MW (1995) Primary current distribution in a thin-film battery. Application to power-density calculations for lithium batteries. *Journal of Electrostatics* 34: 61–85.

Wang CY and Srinivasan V (2000) Computational battery dynamics (CBD) – electrochemical/thermal coupled modeling and multi-scale modeling. *Journal of Power Sources* 110: 364–376.